# Prospects of higher-order statistics in the era of next-generation galaxy surveys

Dissertation

zur

Erlangung des Doktorgrades (Dr. rer. nat.)

der

Mathematisch-Naturwissenschaftlichen Fakultät

der

Rheinischen Friedrich-Wilhelms-Universität Bonn

von Davit Alkhanishvili aus Tiflis

Bonn, Oktober 2024

Angefertigt mit Geneh Friedrich-Wilhelms-U	migung der Mathematisch-Naturwissenschaftlichen Fakultät der Rheinischen niversität Bonn
Gutachter/Betreuer: Gutachter:	Prof. Dr. Cristiano Porciani Prof. Dr. Peter Schneider
Tag der Promotion: Erscheinungsjahr:	07.04.2025 2025

# **Abstract**

In the last decades, the  $\Lambda$  cold dark matter model has been recognised as the standard model of cosmology due to its remarkable accuracy in explaining cosmological observations. The measurement of clustering signal from the large-scale structure using summary statistics like the power spectrum proved to be a useful tool in constraining the parameters of this standard model of cosmology. With the advent of upcoming next-generation galaxy surveys, which boast extensive volume coverage and high galaxy number density, the importance of higher-order statistics like the bispectrum is becoming more apparent in providing the potential for greatly improving current constraints on cosmological parameters. They also present additional computational and modelling challenges which this thesis aims to tackle. The study focuses particularly on modelling the bispectrum using the perturbation theory to enhance its role in extracting cosmological information beyond two-point statistics.

At first we present findings from testing next-to-leading order perturbation theory expansions of the matter power spectrum and the bispectrum using *N*-body simulations, with a focus on the effective field theory (EFT) of large-scale structure. Results reveal EFT as having the largest range of accuracy (reach) among perturbation theory models, showcasing its capability to capture small-scale non-linear effects. The impact of systematic and statistical errors on the model's reach is also explored.

Next we introduce the use of deep neural networks to model the effect of survey geometry on galaxy power spectrum and bispectrum. The models demonstrate high accuracy (better than 0.1 per cent) and computational efficiency. The only challenge in such an approach is creating training datasets for the bispectrum, which requires significant time investment. However, this step can be accelerated using massive parallelisation and should not be a challenge in practical applications.

Lastly, the performance of a perturbative galaxy bias expansion up to third order is assessed against synthetic galaxy catalogues, which replicate the survey characteristics of the next-generation Euclid spectroscopic galaxy survey. We investigate up to which scales the combination of the real-space galaxy power spectrum and the bispectrum provide unbiased estimates of the fiducial cosmological parameters, how well these parameters are constrained. From these tests, it emerges that the combination of the galaxy power spectrum and the bispectrum modelled using the galaxy bias expansion can accurately extract the cosmological parameters up to a scale of  $0.18 \ h\,\mathrm{Mpc}^{-1}$ . The study also demonstrates between 2-5 times more gain in the ability to constrain the cosmological parameters by including the bispectrum data over just using the power spectrum.

# **Contents**

1	Introduction		
2	The	ory	5
	2.1	Cosmology	5
		2.1.1 The Cosmological Principle	5
		2.1.2 Friedmann Equations	6
		2.1.3 The matter contents of the Universe	8
		2.1.4 The ΛCDM model	10
		2.1.5 Cosmological redshift	11
	2.2	Cosmological structure formation	12
		2.2.1 Dark matter as a fluid	12
	2.3	Standard perturbation theory	16
		2.3.1 Dark-matter halos	19
	2.4	Halo and galaxy bias	20
	2.5	Cosmic fields and their statistical description	22
		2.5.1 Statistical homogeneity and isotropy	22
		2.5.2 Two-point correlation function and power spectrum	23
		2.5.3 Gaussian random fields and the Wick theorem	24
		2.5.4 Three-point correlation function and bispectrum	25
		2.5.5 Linear power spectrum	26
	2.6	One-loop standard perturbation theory	28
		2.6.1 Effective Field Theory of Large-Scale Structure	30
	2.7	Numerical simulations	32
	2.8	Bayesian statistics in cosmological parameter analysis	34
		2.8.1 Markov chain Monte Carlo method	36
	2.9	Goals and open questions addressed in this thesis	37
3	The	reach of next-to-leading-order perturbation theory for the matter bispectrum	39
4	Win	dow function convolution with deep neural network models	43
5	Euc	lid preparation. Galaxy power spectrum and bispectrum modelling in real	
	spa	ce control of the con	45
	5.1	The Euclid mission	45
	5.2	Scientific goals	46

	5.3	Data	47
		5.3.1 Flagship simulation	47
		5.3.2 Power spectrum and bispectrum measurements	48
	5.4	Theoretical model	51
	5.5	Bias relations	55
	5.6	Likelihood function	56
	5.7	Results	58
		5.7.1 The fiducial linear bias	59
		5.7.2 Testing the model with fixed cosmology	59
		5.7.3 Comparison between bias relations	61
		5.7.4 Testing model with varied cosmology	63
		5.7.5 Comparison with the P-only fits	66
	5.8	Concluding remarks	68
6	Sun	nmary	71
Bi	bliog	ıraphy	73
4	Pub	olished papers	89
	<b>A.</b> 1	The reach of next-to-leading-order perturbation theory for the matter bispectrum	89
	A.2	Window function convolution with deep neural network models	111
Lis	st of	Figures 1	117
Lis	st of	Tables 1	121
Δc	crony	vms	123

# Introduction

Since the dawn of mankind, humans have wondered about the origins of the world and the cosmos that surrounds it. In early civilisations, astronomical phenomena and stars have been attributed to religious beliefs, but they also enabled us to predict the seasons and create calendars. Centuries ago, the exploration of the skies was veiled in mysticism. A pivotal moment in astronomical advancement, occurring roughly 400 years ago, was the unveiling of Newton's law of universal gravitation. This revolutionary discovery not only laid the groundwork for modern cosmology but also expanded our understanding of the universe. Gravitation stands as the primary force shaping the Universe's structure, but its impact reaches further. It revealed a profound realisation: the same physical laws governing the Earth govern the celestial realms. The heavens, once deemed otherworldly and mystical, are now recognised as part of our shared cosmic reality, where Earth, despite its modest scale, was an equal part of it. Today, we are in an extraordinary era where the origins of the cosmos, the birth of the Earth, life, and humanity have shifted from legend to quantitative science. When employing Earth-bound telescopes with meter-size mirrors or even turning to telescopes installed in space we can observe billions of galaxies of various sizes and shapes, and at various distances away from us - we are by no means special! All of humanity lives on a tiny planet orbiting a star among the hundreds of billions of other stars in our Galaxy. To give an impression of this, in Fig. 1.1 we show the image from the James Webb Space Telescope depicting thousands of background galaxies. Considering that thirty million similar images cover the full sky, one can not comprehend the vastness of the Universe that surrounds

The science that tries to explain the Universe as a whole is the science of cosmology. It asks the most basic questions like: How did the Universe emerge? How old and how large is it? What does it contain? How will it evolve in future? Is it static? Even though these questions sound simple, the answers to them are complicated and hard to achieve due to our limited capacity to observe everything. The time scale for cosmological evolution is so much longer than that over which we can make observations, that it is impossible to completely follow the evolution of objects inside it. Furthermore, we only have access to the one realisation of the Universe and due to this it is difficult to distinguish the laws of nature from cosmic coincidences. For example, is it a coincidence that our Universe has a flat geometry, or is there some kind of physical laws behind it? Answering these questions is also complicated due to the fact that we can observe the current state of the Universe only very locally, since those events we can look at lie in our past lightcone. If a source is at distance D, for an observer it will look  $\Delta t = D/c$  younger than today. However, this fact due to the finite speed of light makes it

30th April 2025 12:58

possible to look back into the past and study the evolution of the Universe.

In the last century, despite these challenges we learned that the Universe is bigger than our galaxy and is expanding (Hubble, 1929), discovered a dark matter (DM) component that does not interact with light (Zwicky, 1933; Rubin and Ford, 1970) and detected the Cosmic Microwave Background (CMB) which confirmed the Big Bang hypothesis (Dicke et al., 1965). We discovered that while dark matter dominates the structure formation in our Universe, dark energy, abbreviated with Λ, dominates the total energy budget today and causes the accelerated expansion of the Universe (Riess et al., 1998). These discoveries formed the basis for the six-parameter model that describes the Universe as a whole - the Λ Cold Dark Matter (ΛCDM) model. It celebrated a great success for the last two decades and matches remarkably well with many observations from CMB missions like the Wilkinson Microwave Anisotropy Probe (WMAP) and Planck (Planck Collaboration et al., 2016), as well as galaxy redshift surveys like the Two-degree-Field Galaxy Survey (Colless et al., 2001) and Baryon Oscillation Spectroscopic Survey (BOSS) (Dawson et al., 2013). These measurements have given us much more precise insight into the energy content of the Universe; over two-thirds of it is dominated by dark energy, while the matter sector is taken up by dark matter, which is five times more abundant than the baryons.

Despite these successes of ACDM, it is unsatisfactory that the visible matter that can be directly observed from light sources like stars, galaxies, etc. only makes up roughly 5 per cent of the Universe. We still have to understand the nature of the rest 95 per cent and reconcile it with the existing theories of particle physics and general relativity, which currently is the biggest challenge for the ACDM model. Moreover, there are slight inconsistencies (tensions) among different data sets and numerical studies that might indicate potential problems for the model. These challenges are intended to be tackled, at least to some extent, through numerous upcoming experiments that leverage a combination of data from supernovae, gravitational lensing, the CMB, and the distribution of galaxies on a large scale. This thesis seeks to contribute to the latter field by examining three-point statistics - an analysis method that, if implemented correctly, has the potential to significantly enhance our utilisation of the data generated by these new experiments. In the following section, we will lay out the theoretical background and discuss the goals and open questions that were addressed in this thesis.

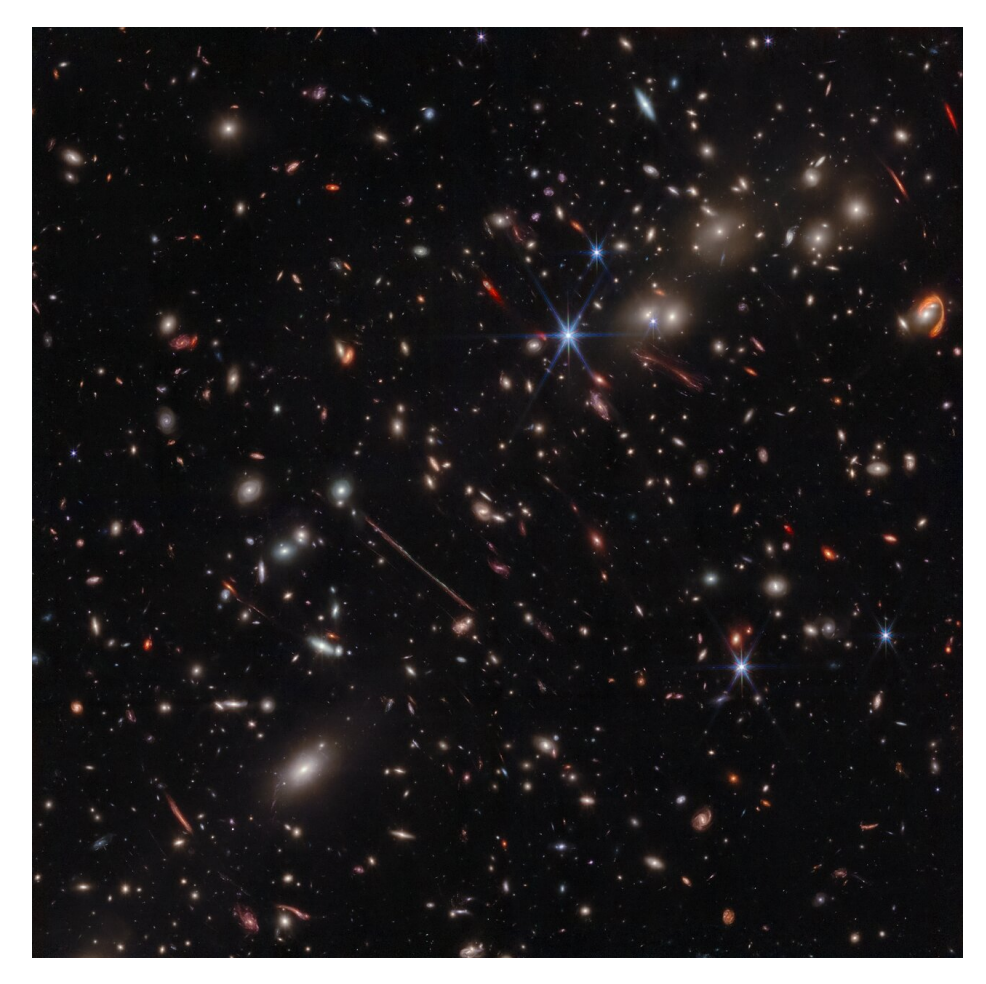


Figure 1.1: An image of the galaxy cluster known as "El Gordo" taken by the James Webb Space Telescope. El Gordo acts as a gravitational lens, distorting and magnifying the light from distant background galaxies. Credit: NASA, ESA, CSA.

# **Theory**

Studying the large scale structure (LSS) of the Universe is one of the main goals of cosmology. It has become widely accepted that gravitational instability plays a central role in giving rise to the wonderful structures seen in galaxy surveys. Extracting the wealth of information contained in galaxy clustering to learn about cosmology thus requires a quantitative understanding of the dynamics of gravitational instability and application of sophisticated statistical tools that can best be used to test theoretical models against observations.

In this chapter we will briefly review the fundamentals of cosmology and the theory of structure formation based on the use of standard perturbation theory (SPT). We will also briefly discuss the numerical and statistical methods actively used in the observational cosmology to extract the information from galaxy surveys.

# 2.1 Cosmology

# 2.1.1 The Cosmological Principle

Cosmological Principle (CP) states that on large scales, the Universe should be isotropic and homogeneous - it looks the same in every direction and it has the same properties at every point. This is *a priori* assumption about the Universe and is a reasonable postulate backed up by observations (e.g. Scaramella et al., 1991; Planck Collaboration et al., 2020a). However, in recent years some evidence has appeared against the assumption of isotropy. Namely, the Hubble constant (Luongo et al., 2022) and temperature-luminosity relation of galaxy clusters (Migkas et al., 2021, 2022) appear to be not isotropic. Even though at the moment one can not rule out systematic errors, there is a possibility the assumption of isotropy will be revised in the future.

We need to combine the CP with General Relativity (GR). According to GR space-time is described as a four-dimensional manifold and its properties are defined by metric tensor  $g_{\mu\nu}$ . It determines both the distances between two events and *geodesics* of free-falling particles, which represent straight lines (shortest path) following the manifold's curvature. Distance s is computed from the following equation:

$$ds^2 = g_{\mu\nu} dx^{\mu} dx^{\nu} , \qquad (2.1)$$

where Einstein's summation convention is used, which implies summation over the indices that

appear twice. To compute a metric that incorporates CP we need to assume the existence of a set of *fundamental observers* - who all experience the Universe in the same way if their clocks are synchronised, and who all follow the mean motion of matter and radiation. Robertson (1935) and Walker (1937) showed that by following the above conditions one arrives at the metric

$$ds^{2} = c^{2}dt^{2} - a^{2}(t) \left[ d\chi^{2} + f_{K}^{2}(\chi) \left( d\theta^{2} + \sin^{2}\theta \, d\phi^{2} \right) \right]. \tag{2.2}$$

Here, t is the cosmic time, a(t) is the *scale factor*,  $\chi$  is the comoving radial coordinate,  $\theta$  and  $\phi$  are the angular coordinates on the unit sphere. The above metric in the literature is referred to as *Friedmann-Lemaître-Robertson-Walker metric* (hereafter FLRW metric). The scale factor is normalised such that  $a(t_0) = 1$  today and allows the freedom of homogeneous spatial expansion or contraction<sup>1</sup>, i.e. it describes the relative size of the Universe. Using the scale factor we can introduce *comoving coordinates*  $\mathbf{x}$  and *physical coordinates*  $\mathbf{r}$  that are related via

$$\mathbf{r} = a(t)\,\mathbf{x}\,. \tag{2.3}$$

Two observers with no peculiar velocity will always have the same comoving distance in space-time. At last,  $f_K(\chi)$  is the *comoving angular diameter distance*, which depends on the *curvature parameter K* in the following way:

$$f_K(\chi) = \begin{cases} K^{-1/2} \sin\left(K^{1/2}\chi\right) & \text{for } K > 0\\ \chi & \text{for } K = 0\\ (-K)^{-1/2} \sinh\left[(-K)^{1/2}\chi\right] & \text{for } K < 0. \end{cases}$$
 (2.4)

The parameter K describes the curvature of the space at fixed t. The surface of a sphere with radius  $\chi$  is then given by  $4\pi f_K^2(\chi)$ , which differs from the Euclidean value  $4\pi\chi^2$  (in the case of K=0, where space becomes flat).

#### 2.1.2 Friedmann Equations

The Universe, as described by the FLRW metric, is not static; it can contract or expand (in fact, ours does the latter). If we can determine the evolution of the scale factor a(t), we can infer the dynamics of the Universe on the largest scales. To achieve this, we plug in the FLRW metric into Einstein Field Equations (EFEs), given as

$$R_{\mu\nu} - \frac{1}{2}g_{\mu\nu}R = \frac{8\pi G}{c^4}T_{\mu\nu} - \Lambda g_{\mu\nu}, \qquad (2.5)$$

where G is the gravitational constant,  $T_{\mu\nu}$  is the *stress-energy* tensor, describing the content of energy in the space-time,  $\Lambda$  is the *cosmological constant* (we will explore its meaning later on),  $R_{\mu\nu}$  and R are Ricci tensor and Ricci scalar, respectively. The latter two are computed from the Riemann

30th April 2025 12:58

<sup>&</sup>lt;sup>1</sup> The scale factor depends only on the cosmic time and can be factored out from the spatial components of the metric tensor.

<sup>&</sup>lt;sup>2</sup> Note the difference from the definition of curvature of the space-time, which in turn is described by the *Riemann curvature tensor* in *Einstein's field equations* 

curvature tensor  $R^{\gamma}_{\ \mu\nu\rho}$  via contraction of indices,

$$R_{\mu\nu} \equiv R^{\sigma}_{\ \mu\nu\sigma} \tag{2.6}$$

and

$$R \equiv R^{\mu}_{\ \mu} = g_{\mu\nu}R^{\mu\nu} \,. \tag{2.7}$$

The meaning behind the EFEs, which is the cornerstone of the GR was elegantly summed up by the physicist John Wheeler in twelve words: "Space-time tells matter how to move; matter tells space-time how to curve". In other words, the stress-energy tensor dictates what should be the curvature, and that curvature, in turn, dictates the motion of the matter described by the said tensor.

The Riemann curvature tensor consists of derivatives of the metric tensor up until the second order. Therefore, the inputs of EFEs are metric and stress-energy tensors. Plugging in the FLRW metric (2.2) it can be shown that the type of matter contents must be a homogeneous perfect fluid with the density  $\rho(t)$  and pressure p(t). From this calculation, the *Friedmann equations* can be derived:

$$\left(\frac{\dot{a}}{a}\right)^2 = \frac{8\pi G}{3}\rho - \frac{Kc^2}{a^2} + \frac{\Lambda c^2}{3},$$
 (2.8)

$$\frac{\ddot{a}}{a} = -\frac{4\pi G}{3} \left( \rho + \frac{3p}{c^2} \right) + \frac{\Lambda c^2}{3} . \tag{2.9}$$

These equations describe the evolution of the scale factor in time, which is dictated by the r.h.s., i.e. the different energy densities that were introduced by the stress-energy tensor. The density  $\rho$  and pressure p correspond to 'normal' matter (particles with or without mass, where the latter is also called radiation). The term with cosmological constant  $\Lambda$  describes a constant energy density of yet unknown physical origin. Originally, this constant was introduced by Einstein in the field equations to allow for a solution that describes a static universe.

In 1928 Edwin Hubble discovered that most galaxies move away from us with a radial velocity v which on average is proportional to their distance D,

$$v = H_0 D, (2.10)$$

where  $H_0$  is *Hubble constant*. According to equation (2.10) the Universe is expanding and it is not static. The value of  $H_0$  is usually parameterised as

$$H_0 = 100 h \,\mathrm{km \, s}^{-1} \,\mathrm{Mpc}^{-1}$$
, (2.11)

where h is a dimensionless number and accounts for the measurement uncertainty about the value of  $H_0$ . Namely, the observations of the early Universe like Baryon-acoustic-oscillation (BAO) and the CMB suggest a value of  $h = 0.68 \pm 0.09$  (Planck Collaboration et al., 2016). On the other hand, the local Universe observations like from supernovae of type Ia (Riess et al., 2022) indicate a higher value of  $h = 0.73 \pm 0.1$ . This tension is statistically significant and poses one of the challenges in modern cosmology. Therefore, since many other parameters depend on the Hubble constant, h is still kept when working in comoving space. In Fig. 2.1 we show the original plot from Hubble (1929) relating the recession velocity of galaxies to distance. The linear relation between the two is clearly detectable. However, this diagram was produced using the objects located close-by. For distant objects the relation

becomes non-linear. One can introduce the time-dependent Hubble function, or *expansion rate* of the Universe as it is referred to in the literature, H(t) by taking the time derivative of the equation (2.3). Therefore the velocity of the expansion  $\mathbf{v}$  will be

$$\mathbf{v} \equiv \mathbf{r} = \dot{a}\mathbf{x} = \frac{\dot{a}}{a}\mathbf{r}(t) = H(t)\mathbf{r}(t). \tag{2.12}$$

According to this, the Hubble constant is the present value of the expansion rate  $H_0 = H(t_0)$ . Then one can define the beginning of the Universe as the event when a(t) = 0. The evolution of the scale factor and Hubble function is determined from the Friedmann equations. The solution to these equations depends on the matter densities in the Universe.

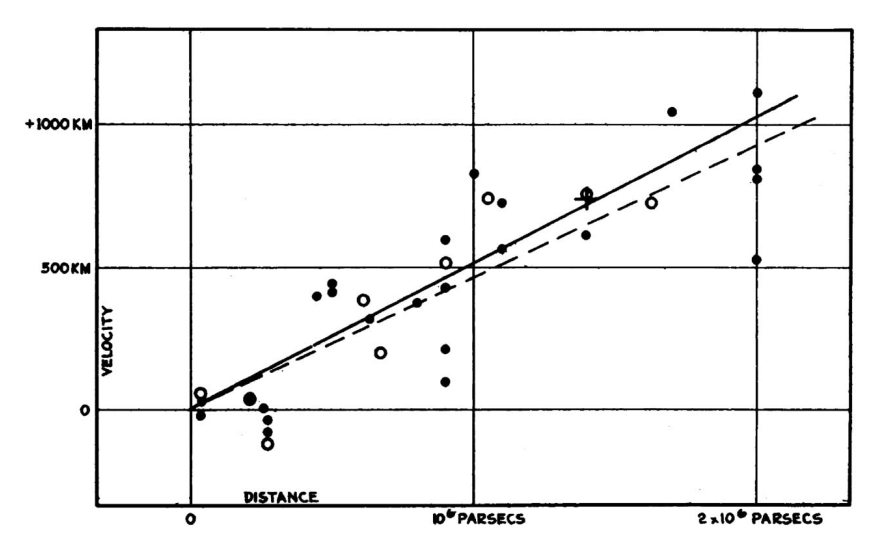


Figure 2.1: The original recession-velocity-versus-distance plot done by Hubble (1929). Plotted are galaxies (originally referred to as 'extragalactic nebulae') whose velocity has been inferred from the spectroscopy. The distances were estimated using the variable cepheid stars via their period-luminosity relation by relating the period of their pulsations to the distance modulus. The solid line is a linear fit to the filled circles that represent individual galaxies. The dashed line is a fit to the empty circles representing galaxies grouped together. The slope of the lines indicates the Hubble constant.

#### 2.1.3 The matter contents of the Universe

In addition to two Friedmann equations, following the first law of thermodynamics one can write down the third equation, the *adiabatic equation*,

$$d(\rho c^2 a^3) = -p d(a^3), \qquad (2.13)$$

which tells that the energy density  $\rho c^2$  within a comoving volume changes with the work done by its expansion or contraction. From this equation, we can determine the time dependence of the matter components. Assuming that an equation of state  $p = w \rho c^2$  holds, solving the adiabatic equation yields the solution

$$\rho(t) = \rho_0 a^{-3(w+1)} \tag{2.14}$$

which tells us that density scales with a and exact behaviour depends on w. The equation is normalised such that  $\rho_0 = \rho_0(t_0)$ , i.e. when a = 1.

In cosmology, one distinguishes between three (main) matter components: *pressureless matter*, *radiation* and *vacuum energy*.

Pressureless matter consists of particles that have mass (such as protons, neutrons, and electrons) and are characterised by vanishing pressure (p = 0 and therefore w = 0). This assumption holds if particles are non-relativistic, i.e.  $p \ll w\rho$ . Then, equation (2.14) implies that

$$\rho_{\rm m}(t) = \rho_{\rm m0} \, a^{-3}(t) \tag{2.15}$$

i.e. density times volume stays constant, a result that is intuitively apparent from matter conservation.

The next component is radiation, i.e. relativistic massless particles. Its equation of state is

The next component is radiation, i.e. relativistic massless particles. Its equation of state is characterised by w = 1/3. Therefore,

$$\rho_{\rm r}(t) = \rho_{\rm r0} \, a^{-4}(t) \,. \tag{2.16}$$

The last component is vacuum energy. It is the energy density of empty space characterised by the cosmological constant  $\Lambda$ . Its equation of state is  $p = -\rho c^2$ , which implies the unintuitive negative pressure. Following equations (2.8) and (2.14), we get

$$\rho_{\Lambda}(t) = \rho_{\Lambda 0} = \frac{\Lambda c^2}{8\pi G} \,. \tag{2.17}$$

The matter density of the Universe is then given by the sum of these three components  $\rho = \rho_{\rm m} + \rho_{\rm r} + \rho_{\Lambda}$ . We also define *critical density*  $\rho_{\rm cr}$ , which corresponds to the total density for which the Universe is flat, i.e. when K=0. Therefore, from equation (2.8) follows

$$\rho_{\rm cr} = \frac{3H_0^2}{8\pi G} \,. \tag{2.18}$$

If  $\rho > \rho_{\rm cr}$ , the Universe is positively curved, otherwise, it is curved negatively. Using this we can define the *cosmological density parameters*. These dimensionless quantities are defined as the respective matter densities relative to the critical density,

$$\Omega_i = \frac{\rho_{i0}}{\rho_{cr}} \,. \tag{2.19}$$

We can further define the total density coefficient of the Universe as  $\Omega_0 = \Omega_r + \Omega_m + \Omega_\Lambda$ , which is closely related to the global curvature of the space-time. For a flat universe  $\Omega_0 = 1$ , for a positively or negatively curved one it will be  $\Omega_0 > 1$  and  $\Omega_0 < 1$ , respectively. Using these definitions we can rewrite the Friedmann equation (2.8) as

$$H^{2}(a) = H_{0}^{2} \left[ \frac{\Omega_{\rm r}}{a^{4}} + \frac{\Omega_{\rm m}}{a^{3}} + \frac{(1 - \Omega_{0})}{a^{2}} + \Omega_{\Lambda} \right]. \tag{2.20}$$

One of the main goals of the observational side of cosmology is to determine the values of these density parameters and Hubble constant, since by knowing them we can describe the Universe's expansion

Table 2.1: Cosmological parameters as measured from the CMB (Planck Collaboration et al., 2020a) and SNeIa (Brout et al., 2022) observations.

Parameter	Planck 2018	Pantheon+
$\Omega_{ m m}$	$0.311 \pm 0.006$	$0.334 \pm 0.018$
$\Omega_{\Lambda}$	$0.689 \pm 0.006$	$0.666 \pm 0.018$
$H_0$	$67.66 \pm 0.42$	$73.6 \pm 1.1$

history as a solution to the equation (2.20). A lot of effort went into achieving this goal. Modern cosmology has access to various probes that complement each other which allows us to cross-validate the different methods for systematic errors and break degeneracies between the parameters. The basic idea is the following: cosmological observables, like the clustering of galaxies, are sensitive to cosmological parameters. Therefore, if the observables can be both accurately modeled and measured, the parameters can be inferred. Some other examples of cosmological probes are CMB, weak-lensing surveys<sup>3</sup> and Supernovae type Ia (hereafter SNeIa) observations<sup>4</sup>.

In Table 2.1 we present the results of a few selected cosmological parameters measured from the CMB (Planck Collaboration et al., 2020a) and SNeIa (Brout et al., 2022) observations, assuming a flat Universe i.e. K = 0. While the results from different probes look similar, there are still some tensions that need to be alleviated either by introducing new physics or reducing systematic errors.

#### 2.1.4 The ΛCDM model

As we already mentioned in Sect.1 it was revealed through observations that there exist two exotic matter components: dark matter (DM) and dark energy. This *dark sector* can not be observed directly, but there is a lot of indirect evidence that calls for its existence.

DM does not emit electromagnetic radiation; however, its gravitational impact manifests across various scales. The rotation curves of galaxies, for instance, deviate from the expected drop at large radii that one would anticipate based on Keplerian rotation influenced solely by visible baryonic matter (Sofue and Rubin, 2001). A similar rationale applies to hot gas in galaxy clusters — X-ray measurements infer temperatures so high that, absent the gravitational influence of DM, the gas would evaporate from the cluster (Allen et al., 2011). Moreover, the cosmic web (defined in Sect. 2.2) would not assume its observed form without a 'backbone' of DM. Clustering processes on large scales would generally be much weaker (Eisenstein et al., 2005). Theoretical considerations introduce different types of DM - called cold, warm, or hot - corresponding to non-relativistic, relativistic, or ultra-relativistic particles. When comparing quantitative predictions for various DM types against data, it is found that DM in our Universe is cold (Bardeen et al., 1986; Jenkins et al., 1998), therefore explaining the part of the current concordance model, Λ Cold Dark Matter (ΛCDM). Thus, since cold

<sup>&</sup>lt;sup>3</sup> Light is deflected by a gravitational potential, described by GR, causing *Gravitational Lensing*. Depending on the strength of the potential there are various lensing regimes. In the weak regime, where the potential is small, cosmological information is extracted using the statistical methods.

<sup>&</sup>lt;sup>4</sup> SNaIa are *standard candles* which means their luminosity and absolute magnitude can be obtained. Their distance is recovered by comparing their apparent magnitude to the absolute one. This distance is compared to the one inferred from the redshift which is cosmology-dependent.

dark matter is non-relativistic, the matter density parameter  $\Omega_m$  is the sum of parameters for DM,  $\Omega_c$ , and baryons,  $\Omega_b$ . The former was observed to be five times bigger than the latter by surveys like *Planck* and *BOSS*.

The emergence of the concept of dark energy can be traced back to the influential studies by Riess et al. (1998) and Perlmutter et al. (1999), which were later honoured with a Nobel Prize. Using SNeIa as standard candles, they demonstrated that the Universe is presently undergoing accelerated expansion. Subsequent works have corroborated this observation (for a review see Huterer and Shafer, 2018). An expansion history of this nature is only feasible if we infer a contribution to the energy budget with a density that remains constant over time and has negative pressure, a deduction supported by the Friedmann equations. Within the  $\Lambda$ CDM framework, this dark energy contribution is encapsulated through the cosmological constant  $\Lambda$ . Theoretical extensions go beyond this by describing dark energy as a dynamic, time-dependent quantity (e.g. Chevallier and Polarski, 2001) and there is a growing evidence to support such extensions according to the next-generation galaxy surveys (DESI Collaboration et al., 2024).

### 2.1.5 Cosmological redshift

We need to construct maps of astrophysical sources in three dimensions to extract cosmological information from them. While the two-dimensional position on the sky can be easily measured, more difficult is to obtain the distance along the line of sight. An additional complication arises due to the fact that we live in an expanding universe with non-Euclidean geometry and due to a finite speed of light when we observe the Universe we are actually looking back in time. Therefore, there is no unique defintion of distance. Different concepts of distance have emerged that need to be applied in the correct context. One common way of dealing with these complications is to introduce the concept of cosmological redshift as a distance indicator.

Due to the expansion of the Universe, the light the galaxies emit gets shifted towards larger wavelengths. This redshift z is defined as follows

$$z \equiv \frac{\lambda}{\lambda_0} - 1 \,, \tag{2.21}$$

where  $\lambda$  is the observed wavelength of a spectral line, whose intrinsic wavelength in a rest-frame is  $\lambda_0$ . The farther away a source is, the stronger the effect will be. We can find out how the cosmological redshift relates to scale factor a(t) and, particularly, to cosmic time t.

From FLRW metric, we find for radial light rays that

$$\chi = \int_{t}^{t_0} \frac{c \, dt'}{a(t')}, \qquad (2.22)$$

where a comoving distance  $\chi$  between a source and an observer is independent of time by definition. Since a time interval is the inverse of a frequency  $\nu$  we find that

$$\frac{\mathrm{d}t_0}{\mathrm{d}t} = \frac{v}{v_0} = \frac{a(t_0)}{a(t)} = \frac{1}{a(t)} = z + 1. \tag{2.23}$$

In the last step, we have used the equation (2.21). The redshift z can be used as a distance indicator or to quantify the time span we look in the past when observing the source. The fact that it is easily

accessible through spectroscopic measurements makes it very useful in astronomical surveys.

Astronomical surveys that span a wide portion of the sky and whose goal is the three-dimensional mapping of the cosmos are called the *redshift surveys* since the information about the line of sight distance comes from the measured redshift. Early redshift surveys were limited in size since they allowed observing one object at a time. From the 1990s, the development of fibre-optic and multi-slit spectrographs enabled the parallel observation of several hundred galaxies. The earliest example is 2dF Galaxy Redshift Survey (2dFGRS) that in the 1900s and early 2000s observed around  $2.4 \times 10^6$ galaxies in the patch of the sky of  $\approx 1500 \deg^2$  (Colless et al., 2001). A more recent one is the *Sloan* Digital Sky Survey IV (SDSS-IV; Albareti et al., 2017), the fourth stage of the custom built 2.5m telescope at Apache Point Observatory, and of particular interest is their Extended Baryon Oscillation Spectroscopic Survey (eBOSS; Dawson et al., 2016). eBOSS started in 2014 and concentrated on the observation of galaxies and quasars, in a range of redshifts (0.6 < z < 2.2) left completely unexplored by other surveys. Currently the next-generation redshift surveys like Euclid (Laureijs et al., 2011) and Dark-Energy Spectroscopic Instrument (DESI Collaboration et al., 2016) with their extensive observed volume and high galaxy number density are at the forefront of mapping the galaxy distribution on the very large scales. These missions will play an important role in understanding the nature of dark energy and structure formation on cosmological scales.

# 2.2 Cosmological structure formation

The real Universe shows structure on scales up to  $\sim 200 \, h^{-1} \rm Mpc$  (like in the form of 'Great Walls'), which was first detected in the CfA galaxy redshift survey. One of the maps from that survey is shown in Fig. 2.2.

Besides this wall-like structure, the large filaments of galaxies, and voids in between can be identified. These correlated structures are created and shaped by gravity. Just as gravity on small scales pulls together gas particles to form stars, it also pulls together galaxies and matter into patterns on large scales. These patterns of matter distribution are referred to as large scale structure (LSS) or 'the cosmic web'. The most natural explanation for the LSS seen in the galaxy surveys is that it is a result of gravitational amplification of small primordial fluctuations due to the gravitational interaction of collisionless cold dark matter (CDM) particles in an expanding universe.

All the calculations we performed in the previous sections only describe the homogeneous and isotropic Universe on the scales above  $200 \, h^{-1}$ Mpc since we invoked CP. However, when we look at the small portion of the sky we can see planets, stars, and galaxies, which break this homogeneity. At these small scales, the CP is invalid. The homogeneous Universe can be described through GR using the mathematical framework of the FLRW metric. However, such models can not account for the presence of the structure in the Universe. Hence, the homogeneous world models have to be supplemented by a description of matter inhomogeneities. In other words, we need another theory that should explain how actually galaxies, galaxy clusters, and the cosmic web form. It is possible to accomplish this within the context of the *cosmological structure formation*.

#### 2.2.1 Dark matter as a fluid

In general, structure formation is a very complicated process - it is in principle an N-body problem where an enormous amount of particles interact with each other through various forces. The

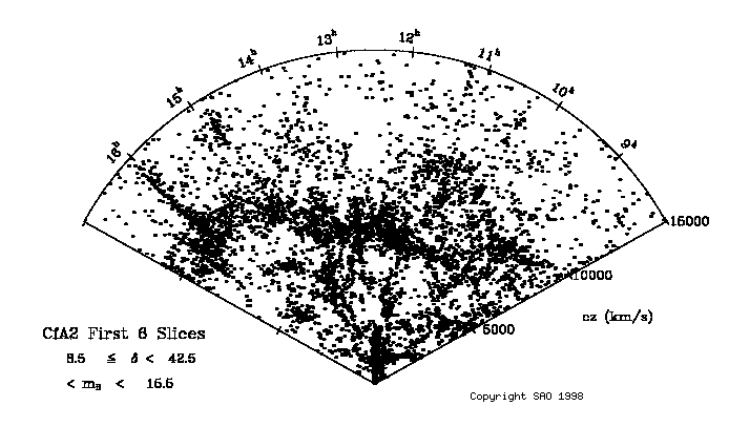


Figure 2.2: The Great Wall: in redshift surveys of galaxies with radial velocities of  $cz \le 1500$  km/s, a large galaxy structure was discovered located at a redshift of  $cz \sim 6000$  km/s. Each dot on this wedge diagram represents a galaxy. The polar angle denotes the rectascension, whereas the radial coordinate denotes the redshift of the galaxies, which measures their distances according to Hubble's law. Source: Geller and Huchra (1989)

cosmological processes happen on large scales and all forces besides gravity can be safely neglected still, it is practically impossible to treat structure formation analytically as an N-body problem. The solution is to approach this problem in the framework of hydrodynamics and treat matter as a fluid instead. Therefore, we do not need to follow individual particles, but instead describe the smooth fields of density  $\rho$  and velocity  $\mathbf{u}$ .

We can simplify the problem by concentrating on the structure formation of dark matter only and thus the pressure will be set to zero<sup>5</sup>. This is justified since the matter component of the Universe contains much more dark matter than baryons (Planck Collaboration et al., 2020a). Furthermore, we shall consider matter perturbations on scales much smaller than the horizon scale at a given epoch, since on large scales the curvature of space-time is important. This allows us to apply the simpler Newtonian gravitation and avoid the full treatment in the framework of more complicated General Relativity. Finally, we concentrate on the matter-dominated epoch of the Universe, i.e. where the matter term in the Friedmann equations dominates. This implies that  $\Omega_r = 0$ .

30th April 2025 12:58

<sup>&</sup>lt;sup>5</sup> Since the dark matter in the Universe is collisionless the fluid approximation breaks down on small scales or at late times. This means that streams of dark matter particles can cross each other without frictional interactions, therefore there is not a well-defined velocity field **u**(**r**), but multi-streams do occur. However, on large scales and at early times, such multiple streams are unimportant, and the fluid approximation applies.

Taking all these into account we can write the following fluid equations:

$$\frac{\partial \rho(\mathbf{r},t)}{\partial t} + \nabla_r \cdot [\rho \, \mathbf{u}(\mathbf{r},t)] = 0 \qquad \text{Continuity equation}$$
 (2.24)

$$\frac{\partial \mathbf{u}}{\partial t} + (\mathbf{u} \cdot \nabla_r) \mathbf{u} = -\nabla_r \phi \qquad \text{Euler equation}$$
 (2.25)

$$\nabla_r^2 \phi = 4\pi G \rho - \Lambda$$
 Poisson equation (2.26)

The continuity equation (2.24) describes the conservation of mass. The Euler equation (2.25) is the equation of motion for the fluid. The left-hand side of this equation is the Lagrangian derivative of the fluid velocity, which describes the change of velocity as measured by an observer who follows the flow. This change of flow velocity is caused by the acceleration, which in this case provided by the gravitational acceleration  $-\nabla_r \phi$ . The Poisson equation (2.26) has been modified to include the cosmological constant.

Next we rewrite the equations in terms of comoving coordinates

$$\mathbf{x} = \frac{\mathbf{r}}{a(t)} \tag{2.27}$$

For the density and velocity field we then have

$$\rho(\mathbf{r},t) = \hat{\rho}(\mathbf{x},t) \tag{2.28}$$

$$\mathbf{u}(\mathbf{r},t) = \dot{a}\,\mathbf{x} + \mathbf{v}(\mathbf{x},t) \tag{2.29}$$

As one can see the velocity field has two components: the Hubble expansion of the homogeneous Universe and the peculiar velocity  $\mathbf{v}(\mathbf{x},t)$ . Although  $\rho(\mathbf{r})$  and  $\hat{\rho}(\mathbf{x})$  describe the same density field, they are different mathematical functions. Before writing down the equations in comoving coordinates it is helpful instead of using density field to define a so-called *density contrast* as

$$\delta(\mathbf{x},t) = \frac{\hat{\rho}(\mathbf{x},t) - \bar{\rho}(t)}{\bar{\rho}(t)},$$
(2.30)

where  $\bar{\rho}(t)$  is the mean density. As we mentioned above, if this parameter is small the linear approximation can be used.

Thus, the fluid equation system in the comoving coordinates is

$$\frac{\partial \delta}{\partial t} + \frac{1}{a} \nabla_x \cdot [(1 + \delta) \mathbf{v}] = 0 \tag{2.31}$$

$$\frac{\partial \mathbf{v}}{\partial t} + \frac{\dot{a}}{a}\mathbf{v} + \frac{1}{a}(\mathbf{v} \cdot \nabla_x)\mathbf{v} = -\frac{1}{a}\nabla_x \Phi \tag{2.32}$$

$$\nabla_x^2 \Phi = \frac{3H_0^2 \Omega_{\rm m}}{2a} \delta \tag{2.33}$$

Here  $\Phi$  is the comoving gravitational potential

$$\Phi = \phi(a\mathbf{x}, t) + \frac{\ddot{a}a}{2} |\mathbf{x}|^2$$
 (2.34)

These 3 equations, (2.31), (2.32) and (2.33), form the complete set of evolution equations for the density contrast  $\delta$  and the peculiar velocity  $\mathbf{v}$ , coupled via the gravitational potential  $\Phi$ . The trivial solution  $\delta \equiv 0$ ,  $\mathbf{v} \equiv \mathbf{0}$ ,  $\Phi \equiv 0$  corresponds to the unperturbed, homogeneously expanding Universe. Hence,  $\delta$  and  $\mathbf{v}$  describe the deviations of the density and velocity field from this homogeneous expansion.

The equations written in the above form are non-linear and can not be solved analytically. If we consider small perturbations in the density field and small peculiar velocities, we can linearize the foregoing equations in the small quantities  $\delta$  and  $\mathbf{v}$ . In the continuity equation (2.31) the term  $\mathbf{v}\delta$  is of second order and will be neglected. The same is true for the term  $\frac{1}{a}(\mathbf{v} \cdot \nabla_x)\mathbf{v}$  in the Euler equation (2.32), whereas the Poisson equation (2.33) is already linear. The other two then become

$$\frac{\partial \delta}{\partial t} + \frac{1}{a} \nabla \cdot \mathbf{v} = 0, \qquad (2.35)$$

$$\frac{\partial \mathbf{v}}{\partial t} + \frac{\dot{a}}{a}\mathbf{v} = -\frac{1}{a}\nabla\Phi\,,\tag{2.36}$$

where we drop the index on  $\nabla$ -operator. since all the spatial derivatives are with respect to comoving coordinates.

Taking the time derivative of the linearized continuity equation (2.35), and the divergence of the linearized Euler equation (2.36),

$$\frac{\partial}{\partial t} \left[ \frac{\partial \delta}{\partial t} + \frac{1}{a} \nabla \cdot \mathbf{v} \right] = 0,$$

$$\frac{\nabla}{a} \cdot \left[ \frac{\partial \mathbf{v}}{\partial t} + \frac{\dot{a}}{a} \mathbf{v} = -\frac{1}{a} \nabla \Phi \right]$$

and then combining the two resulting equations, together with the Poisson equation (2.33) to replace the Laplacian of  $\Phi$  yields

$$\frac{\partial^2 \delta}{\partial t^2} + \frac{2\dot{a}}{a} \frac{\partial \delta}{\partial t} - \frac{3H_0^2 \Omega_{\rm m}}{2a^3} \delta = 0 \tag{2.37}$$

Even though the density contrast depends on the variables  $\mathbf{x}$  and t, (2.37) does not contain derivatives with respect to  $\mathbf{x}$ , nor does  $\mathbf{x}$  occurs explicitly in coefficients of this linear equation. Hence, (2.37) is an ordinary differential equation and the solution can be factorised. The general solution to this equation is

$$\delta(\mathbf{x},t) = D_{\perp}(t)\Delta_{\perp}(\mathbf{x}) + D_{\perp}(t)\Delta_{\perp}(\mathbf{x}), \qquad (2.38)$$

where  $D_{\pm}(t)$  are two linearly independent solutions and  $\Delta_{\pm}(\mathbf{x})$  are two arbitrary functions of position describing the initial density field configuration. Equation (2.37) together with Friedmann equation (2.20) determines the growth of density perturbations in the linear regime as a function of cosmology.  $D_{+}$  grows with cosmic time, whereas  $D_{-}$  is a decreasing function. Thus, if at some early time, both modes were present, the  $D_{-}$  mode would have died away quickly. Therefore, only the growing mode is relevant for structure formation. The  $D_{+}$  is called a *growth factor*.

A closed-form solution for the  $D_{\pm}$  does not exist, but there are some important cases that can be considered.

• When  $\Omega_{\rm m}$  = 1,  $\Omega_{\Lambda}$  = 0 (Einstein-de Sitter (EdS) universe), we have the simple solution

$$D_{+} = a(t), \qquad D_{-} = a(t)^{-\frac{3}{2}},$$
 (2.39)

thus density fluctuations grow as the scale factor.

• In the case where there is only matter and vacuum energy, the linear growth admits the integral representation as a function of  $\Omega_{\rm m}$  and  $\Omega_{\Lambda}$ :

$$D_{+} = a^{3}H(a)\frac{5\Omega_{\rm m}}{2} \int_{0}^{a} \frac{\mathrm{d}a'}{\left[a'H(a')\right]^{3}}$$
 (2.40)

In general, it is not possible analytically to solve this integral, but an approximate form of the growth factor has been derived in Carroll et al. (1992),

$$D_{+}(a) = \frac{5 a \Omega_{\rm m}(a)}{2} \left[ \Omega_{\rm m}^{4/7}(a) - \Omega_{\Lambda}(a) + \left( 1 + \frac{\Omega_{\rm m}(a)}{2} \right) \left( 1 + \frac{\Omega_{\Lambda}(a)}{70} \right) \right]^{-1}. \tag{2.41}$$

# 2.3 Standard perturbation theory

We will now consider the evolution of density and velocity field beyond the linear approximation. To do so, we will make an approximation, that is, we will characterise the velocity field by its divergence,  $\theta = \nabla \cdot \mathbf{v}$ , and neglect the vorticity degrees of freedom. From equation (2.32) we can write the evolution equation for vorticity,  $\mathbf{w} = \nabla \times \mathbf{v}$ , as

$$\frac{\partial \mathbf{w}}{\partial t} + \frac{\dot{a}}{a} \mathbf{w} - \frac{1}{a} \nabla \times [\mathbf{v} \times \mathbf{w}] = \frac{1}{a} \nabla \times \left( \frac{1}{\rho} \nabla \cdot \sigma \right), \tag{2.42}$$

where we have temporarily restored the stress tensor contribution  $(\sigma_{ij})$  to the conservation of momentum. We see that if  $\sigma_{ij}\approx 0$ , as in the case of a pressureless ideal fluid, if the primordial vorticity vanishes, it remains zero at all times. On the other hand, if the initial vorticity is non-zero, in the linear regime it decays due to the expansion of the universe; however, it can be amplified non-linearly through the third term in equation (2.42). In what follows, we will assume that initial vorticity vanishes, thus equation (2.42) together with the equation of state  $\sigma_{ij}\approx 0$  guarantees that vorticity stays zero throughout the evolution. It must be noted, that this assumption is only valid as long as the condition  $\sigma_{ij}\approx 0$  remains true; in particular, multi-streaming and shocks can generate vorticity. This is expected to happen at small enough scales.

The general assumption of standard perturbation theory (SPT) is that the linear density field still dominates on intermediate scales, and non-linear gravitational interaction between particles imposes only small corrections onto it. Thus it is possible to expand the density and velocity fields about the linear solutions. Linear solutions correspond to simple (time-dependent) scaling of the initial density field; thus we can write

$$\delta(\mathbf{x},t) = \sum_{n=1}^{\infty} \delta^{(n)}(\mathbf{x},t), \qquad \theta(\mathbf{x},t) = \sum_{n=1}^{\infty} \theta^{(n)}(\mathbf{x},t), \qquad (2.43)$$

where  $\delta^{(1)}$  and  $\theta^{(1)}$  are linear in the initial density field,  $\delta^{(2)}$  and  $\theta^{(2)}$  are quadratic in the initial density field, etc..

On large scales, when fluctuations are small, linear perturbation theory (PT) provides an adequate description of cosmological fields. In this regime, different Fourier modes evolve independently (they do not couple) conserving the primordial statistics. Therefore, it is natural to Fourier transform equation (2.31), (2.32) and (2.33) and work in Fourier space. Convention for the Fourier transform of an arbitrary field  $A(\mathbf{x}, t)$  throughout this work will be

$$\tilde{A}(\mathbf{k},t) = \int d^3 \mathbf{x} \, e^{-i\mathbf{k}\cdot\mathbf{x}} A(\mathbf{x},t) \,. \tag{2.44}$$

When non-linear terms in the perturbation series are taken into account, the equations of motion in Fourier space show the coupling between different Fourier modes characteristic of non-linear theories. Taking the divergence of equation (2.32) and Fourier transforming the resulting equations of motion we get

$$\frac{\partial \tilde{\delta}(\mathbf{k},t)}{\partial t} + \tilde{\theta}(\mathbf{k},t) = -\int \frac{\mathrm{d}^3 \mathbf{k}_1 \mathrm{d}^3 \mathbf{k}_2}{(2\pi)^3} \delta_{\mathrm{D}}(\mathbf{k} - \mathbf{k}_{12}) \,\alpha(\mathbf{k}_1, \mathbf{k}_2) \,\tilde{\theta}(\mathbf{k}_1, t) \,\tilde{\delta}(\mathbf{k}_2, t) \,, \tag{2.45}$$

$$\frac{\partial \tilde{\theta}(\mathbf{k},t)}{\partial t} + H(t) \,\tilde{\theta}(\mathbf{k},t) + \frac{3}{2} \Omega_{\mathrm{m}} H^{2}(t) \,\tilde{\delta}(\mathbf{k},t) = -\int \frac{\mathrm{d}^{3} \mathbf{k}_{1} \mathrm{d}^{3} \mathbf{k}_{2}}{(2\pi)^{3}} \delta_{\mathrm{D}}(\mathbf{k} - \mathbf{k}_{12}) 
\times \beta(\mathbf{k}_{1},\mathbf{k}_{2}) \,\tilde{\theta}(\mathbf{k}_{1},t) \,\tilde{\theta}(\mathbf{k}_{2},t),$$
(2.46)

 $(\delta_{\rm D}$  denotes the three dimensional Dirac delta function,  $\mathbf{k}_{12} = \mathbf{k}_1 + \mathbf{k}_2)$  where the functions

$$\alpha(\mathbf{k}_1, \mathbf{k}_2) = \frac{\mathbf{k}_{12} \cdot \mathbf{k}_1}{k_1^2}, \qquad \beta(\mathbf{k}_1, \mathbf{k}_2) = \frac{k_{12}^2(\mathbf{k}_1 \cdot \mathbf{k}_2)}{2k_1^2 k_2^2}$$
(2.47)

encode the non-linearity of the evolution (mode coupling) and come from the non-linear terms in the fluid equations (2.31), (2.32). From (2.45) and (2.46) we see that the evolution of  $\tilde{\delta}(\mathbf{k}, t)$  and  $\tilde{\theta}(\mathbf{k}, t)$  is determined by the mode coupling of the fields at all pairs of wave vector  $\mathbf{k}_1$  and  $\mathbf{k}_2$  whose sum is  $\mathbf{k}$ .

Let us first consider the EdS universe, for which  $\Omega_{\rm m}=1$  and  $\Omega_{\Lambda}=0$ . In this case the equations (2.45) and (2.46) can be formally solved with the following perturbative expansion:

$$\tilde{\delta}(\mathbf{k},t) = \sum_{n=1}^{\infty} a^n(t) \, \delta^{(n)}(\mathbf{k},t) \,, \qquad \tilde{\theta}(\mathbf{k},t) = -H(t) \sum_{n=1}^{\infty} a^n(t) \, \theta^{(n)}(\mathbf{k},t) \,, \tag{2.48}$$

where only the fastest-growing mode is taken into account. At small a, the series are dominated by their first term, and since  $\theta^{(1)}(\mathbf{k}) = \delta^{(1)}(\mathbf{k})$  from the continuity equation,  $\delta^{(1)}(\mathbf{k})$  completely characterises the linear fluctuations.

The equations of motion (2.45) and (2.46) determine  $\delta^{(n)}(\mathbf{k})$  and  $\theta^{(n)}(\mathbf{k})$  in terms of the linear

fluctuations to be

$$\delta^{(n)}(\mathbf{k}) = \int \frac{d^3 \mathbf{q}_1 \cdots d^3 \mathbf{q}_n}{(2\pi)^{3(n-1)}} \delta_{\mathcal{D}}(\mathbf{k} - \mathbf{q}_{1\dots n}) F_n(\mathbf{q}_1, \dots, \mathbf{q}_n) \delta^{(1)}(\mathbf{q}_1) \cdots \delta^{(1)}(\mathbf{q}_n), \qquad (2.49)$$

$$\theta^{(n)}(\mathbf{k}) = \int \frac{\mathrm{d}^3 \mathbf{q}_1 \cdots \mathrm{d}^3 \mathbf{q}_n}{(2\pi)^{3(n-1)}} \delta_{\mathrm{D}}(\mathbf{k} - \mathbf{q}_{1\cdots n}) G_n(\mathbf{q}_1, \dots, \mathbf{q}_n) \delta^{(1)}(\mathbf{q}_1) \cdots \delta^{(1)}(\mathbf{q}_n), \qquad (2.50)$$

where  $F_n$  and  $G_n$  are homogeneous functions, which are constructed from the fundamental mode coupling functions  $\alpha(\mathbf{k}_1, \mathbf{k}_2)$  and  $\beta(\mathbf{k}_1, \mathbf{k}_2)$  according to recursion relations

$$F_{n}(\mathbf{q}_{1},...,\mathbf{q}_{n}) = \sum_{m=1}^{n-1} \frac{G_{m}(\mathbf{q}_{1},...,\mathbf{q}_{m})}{(2n+3)(n-1)} [(2n+1)\alpha(\mathbf{k}_{1},\mathbf{k}_{2})F_{n-m}(\mathbf{q}_{m+1},...,\mathbf{q}_{n}) + 2\beta(\mathbf{k}_{1},\mathbf{k}_{2})G_{n-m}(\mathbf{q}_{m+1},...,\mathbf{q}_{n})],$$
(2.51)

$$G_{n}(\mathbf{q}_{1},...,\mathbf{q}_{n}) = \sum_{m=1}^{n-1} \frac{G_{m}(\mathbf{q}_{1},...,\mathbf{q}_{m})}{(2n+3)(n-1)} [3\alpha(\mathbf{k}_{1},\mathbf{k}_{2})F_{n-m}(\mathbf{q}_{m+1},...,\mathbf{q}_{n}) + 2n\beta(\mathbf{k}_{1},\mathbf{k}_{2})G_{n-m}(\mathbf{q}_{m+1},...,\mathbf{q}_{n})],$$
(2.52)

where  $\mathbf{k}_1 = \mathbf{q}_1 + \cdots + \mathbf{q}_m$ ,  $\mathbf{k}_2 = \mathbf{q}_{m+1} + \cdots + \mathbf{q}_n$ ,  $\mathbf{k} = \mathbf{k}_1 + \mathbf{k}_2$  and  $F_1 = G_1 = 1$ . Particularly, for n = 2 we have

$$F_2(\mathbf{q}_1, \mathbf{q}_2) = \frac{5}{7} + \frac{1}{2} \frac{\mathbf{q}_1 \cdot \mathbf{q}_2}{q_1 q_2} \left( \frac{q_1}{q_2} + \frac{q_2}{q_1} \right) + \frac{2}{7} \left( \frac{\mathbf{q}_1 \cdot \mathbf{q}_2}{q_1 q_2} \right)^2, \tag{2.53}$$

$$G_2(\mathbf{q}_1, \mathbf{q}_2) = \frac{3}{7} + \frac{1}{2} \frac{\mathbf{q}_1 \cdot \mathbf{q}_2}{q_1 q_2} \left( \frac{q_1}{q_2} + \frac{q_2}{q_1} \right) + \frac{4}{7} \left( \frac{\mathbf{q}_1 \cdot \mathbf{q}_2}{q_1 q_2} \right)^2. \tag{2.54}$$

In general, the SPT expansion is more complicated because the solutions at each order become non-separable functions of t and k. In particular, the growing mode at order n does not scale as  $D_+^n(t)$  or  $a^n(t)$  as in (2.48). It was shown in Scoccimarro et al. (1998) that a simple approximation to the equations of motion for general  $\Omega_{\rm m}$  and  $\Omega_{\Lambda}$  leads to separable solutions to arbitrary order in SPT and the same recursion relations (2.51) and (2.52) as in the EdS case. Thus, for the arbitrary cosmology, the perturbative solution will be

$$\tilde{\delta}(\mathbf{k},t) = \sum_{n=1}^{\infty} D_{+}^{n}(t) \, \delta^{(n)}(\mathbf{k},t) \,, \qquad \tilde{\theta}(\mathbf{k},t) = -H(t) f(\Omega_{\mathrm{m}}, \Omega_{\Lambda}) \sum_{n=1}^{\infty} D_{+}^{n}(t) \, \theta^{(n)}(\mathbf{k},t) \,, \qquad (2.55)$$

where  $f(\Omega_{\rm m}, \Omega_{\Lambda}) = {\rm d} \ln D_+/{\rm d} \ln a$ . All the information on the dependence of the SPT solutions on the cosmological parameters  $\Omega_{\rm m}$  and  $\Omega_{\Lambda}$  is then encoded in the linear growth factor,  $D_+(t)$ . Although, this approximation was shown to generate systematic shifts at the per cent level when applied to three-point statistics like bispectrum (Steele and Baldauf, 2021).

Given knowledge of  $\delta^{(1)}$ , we can construct the density field at a specific time up to an arbitrary order and incorporate non-linear gravitational clustering to our desired level of accuracy. However, this will lead to exceedingly intricate analytical expressions. Moreover, it is unclear until which scale  $k_{\text{max}}$  this

methodology remains valid and precisely models the actual density field since, at extremely non-linear scales, multi-streaming will occur and invalidate the fluid approximation on which the entire treatment is based. We cannot determine this threshold using first principles, so we must compare our theoretical framework with empirical data to address this issue. This difficulty can be tackled using numerical *N*-body simulations, which we will explain in Sect. 2.7. For the time being, we will shift our attention away from larger scales (and the fluid approximation) towards strongly non-linear scales, where we will explore a potential theoretical approach in greater detail.

#### 2.3.1 Dark-matter halos

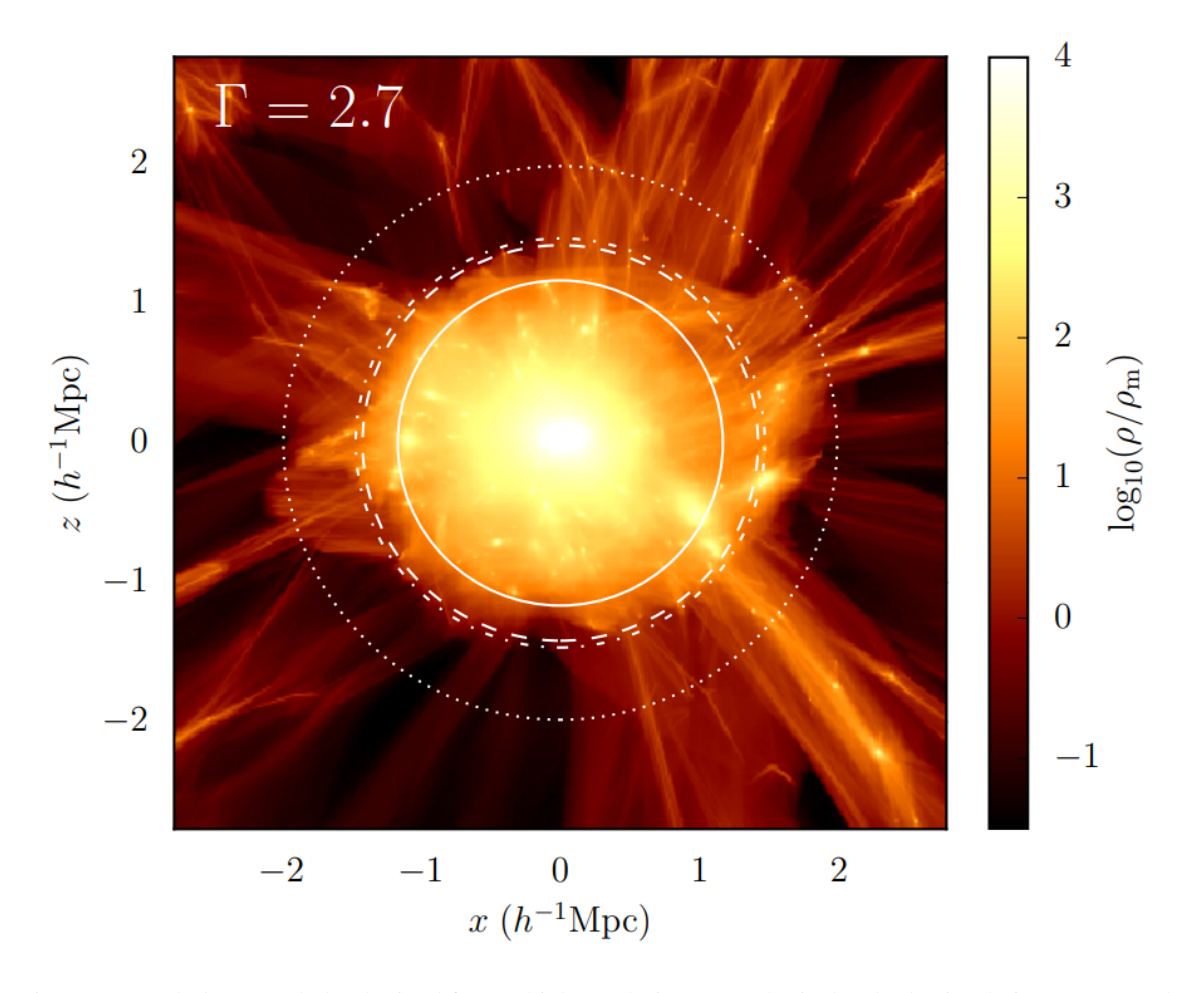


Figure 2.3: A dark-matter halo obtained from a high-resolution cosmological *N*-body simulation (More et al., 2015). The halo has an approximately spherical shape and is supplied with matter from the outer regions via anisotropic filaments. The density of the halo is greatest at its center and gradually decreases towards the outskirts. The white lines visible in the image correspond to different physical criteria utilised to establish the boundaries of the halo.

At the smallest scales of the cosmic web, where collapse in all three dimensions takes place, the gravitational *N*-body interaction is difficult to describe analytically due to limited possibilities.

To overcome this issue, one way is to utilise the *spherical collapse model* (Gunn and Gott, 1972), which assumes a spherically-symmetric mass overdensity in an otherwise uniform universe. This model proposes that during early times, shells of matter recede from the center of mass due to the Hubble expansion, causing the physical radius of the overdensity to increase with time. However, the gravitational attraction of the shells stalls the recession process, and thus the comoving radius decreases with time. If the initial perturbation is dense enough, the shells will eventually reach a maximum physical size, known as the *turn-around radius*, and then collapse. The result of this collapse is a virialised object of finite size in equilibrium, which is referred to as a *dark-matter halo*.

The average density of the halo  $\rho_{\rm vir}$  can be computed as  $\rho_{\rm vir} = \Delta_{\rm vir} \bar{\rho}_{\rm m}(t)$  where  $\bar{\rho}_{\rm m}(t)$  is the mean matter density of the Universe and the overdensity  $\Delta_{\rm vir}$  depends on the cosmological parameters and in general on time. For an EdS universe it is  $\Delta_{\rm vir} \approx 178$  for all t, for  $\Lambda \rm CDM$  universe the values vary between the EdS value at very high redshifts and increases as we approach the current epoch. It can be shown that collapse happens when the initial overdensity field  $\delta \geq 1.68$ , which means that already in the linear regime we can identify the locations of halo formation.

The idealised model presented earlier is just a simplification, as reality is a much more complex process. In actuality, a density perturbation will not exist in isolation, but rather within the intricate environment of the cosmic web. To account for this, the ellipsoidal collapse model was introduced (Bond and Myers, 1996), which relaxes the assumption of spherical symmetry. The formation process and internal structure of haloes remain active fields of research and are investigated using both analytical and numerical approaches (e.g. Borzyszkowski et al., 2014; More et al., 2015; Borzyszkowski et al., 2017). Fig. 2.3 shows a halo from an *N*-body simulation, which is being assembled through anisotropic streams of matter from the outer regions. The density of the halo is highest at the center and gradually decreases towards the outskirts. For more details on simulations, please refer to Sect. 2.7.

Rather than delving into the details of halo formation, our study focuses on larger scales, with an emphasis on haloes that are modeled as point-like objects and serve as tracers of the LSS. Since we lack direct access to DM and the cosmic web, which primarily comprises it, we instead observe discrete objects that follow the LSS due to their physical formation process. Under the assumptions that DM haloes form in dense regions of the LSS (with denser regions having more massive and denser haloes; Kaiser, 1984; Bardeen et al., 1986), and that galaxies subsequently form in DM haloes (where baryons cool and fall into the gravitational potential; Mo et al., 2010), we can utilize this relationship to make inferences about cosmology from galaxy surveys. This connection between discrete objects and an underlying continuous distribution is referred to as *tracer bias* or more specifically *halo and galaxy bias* (Desjacques et al., 2018). A more comprehensive and quantitative description of this concept will be explored in the following section.

# 2.4 Halo and galaxy bias

Moving from the DM distribution to galaxies generally involves two distinct steps. Initially, we require a method to connect the DM density field to the DM haloes, followed by another process to populate these haloes with galaxies (Fry and Gaztanaga, 1993; Cooray and Sheth, 2002; Berlind and Weinberg, 2002). This two-step approach is necessary because a single DM halo may contain multiple galaxies of varying masses and luminosities, which cannot be directly inferred from the halo's properties alone.

There are two possible approaches to address this issue. Firstly, one can try to comprehend the

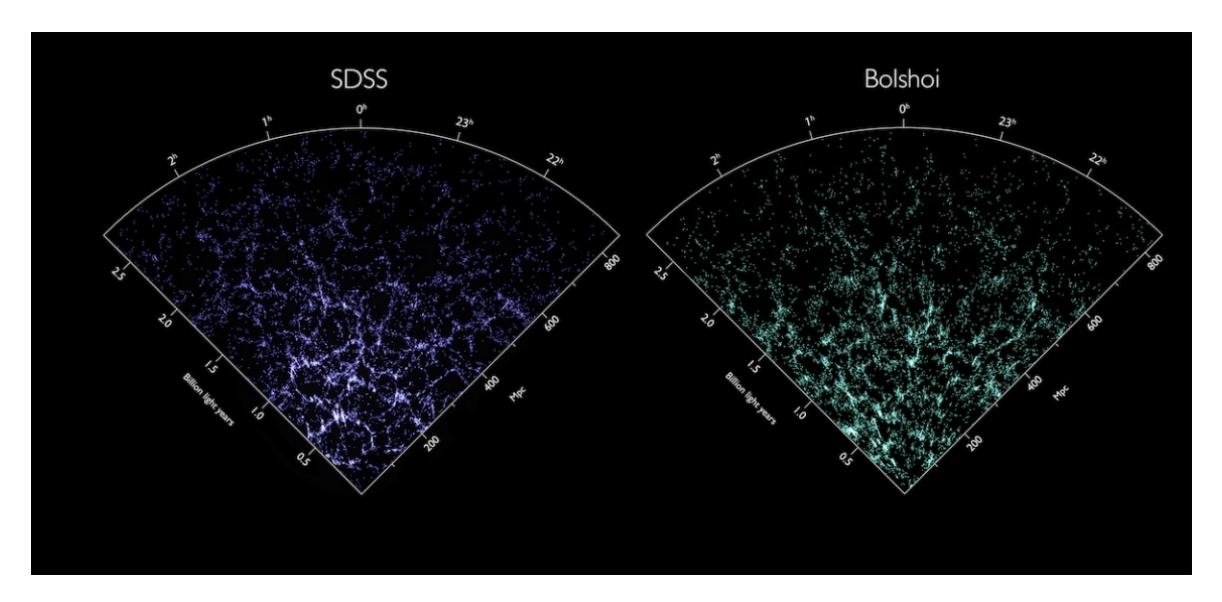


Figure 2.4: The maps of the galaxy distribution observed by SDSS and the one extracted from the Bolshoi simulation. Credit: Bettoni (2013).

physical mechanisms that cause bias. This method necessitates a thorough understanding of the halo formation process (or the arrangement of *peaks*, which are points in space where the density field exceeds a particular threshold). Alternatively, one can take a more phenomenological approach, based on fundamental physical principles, but with the primary aim of developing a practical method for application in observations. In this study, we will mainly concentrate on the latter approach. Such a phenomenological model that connects haloes (or tracers in general) to the underlying matter distribution is called a Eulerian biasing scheme (McDonald and Roy, 2009; Baldauf et al., 2011; Desjacques, 2013).

The basic assumption is that the overdensity field of galaxies  $\delta_g(\mathbf{x})$  is related to the matter density field  $\delta(\mathbf{x})$  in some general form  $\delta_g(\mathbf{x}) = \mathcal{F}[\delta]$ , where  $\mathcal{F}$  is a functional. In Fig. 2.4 we illustrate the motivation for this assumption: if one puts the map of the survey over the map predicted by the N-body simulation, they will exhibit remarkable visual statistical similarity. The most simple relation between these two fields is expressed through *linear bias* model, i.e.  $\delta_g = b_1 \delta$  (Kaiser, 1984). This relation only holds true on the very large scales (Gaztanaga and Frieman, 1994).

A biasing scheme is called *local* if it can be written down in the form of an expansion,

$$\delta_{\mathbf{g}}(\mathbf{x},t) = \sum_{O} b_{O}(t) O(\mathbf{x},t), \qquad (2.56)$$

where O denotes an bias operator and  $b_O$  the respective bias parameter. The former describes the properties of the galaxies' environment on which their density can depend, and the latter are numbers that do not depend on spatial coordinates, but may certainly depend on galaxy properties like colour or luminosity. The parameters can be positive or negative, and the larger the absolute value of a bias parameter is, the more importance the respective operator has for describing the galaxy field. Historically, the operators O would just be taken as powers of the density field, i.e.  $\delta_g = b_1 \delta + b_2 \delta^2 + b_3 \delta^3 + \dots$  (Fry and Gaztanaga, 1993). Research has revealed that these models

do not entirely capture the halo field. To obtain a more accurate representation, one should consider other factors, such as different combinations of density field derivatives or even the peculiar velocity field (Mirbabayi et al., 2015).

Typically, the exact values of bias parameters are not of utmost importance. Instead, in observations such as galaxy clustering surveys, a bias model is assumed, and the bias parameters are considered as free parameters of that model, which will be marginalised during the data analysis process (Cole et al., 2005; Percival et al., 2007; Blake et al., 2010; Granett et al., 2012; Alam et al., 2017). The primary challenge is to identify a bias model that accurately describes real-world conditions, which is not a simple task. Equation (2.56) provides a lot of freedom, which must be reduced using reasonable arguments. While it is mathematically feasible to formulate a comprehensive set of operators or basis up to a certain expansion order, determining which operators are necessary for a practical physical context is crucial. Additionally, the minimum scale that one is attempting to model will likely dictate the need for specific operators. Moreover, one must determine how to link the operators to cosmology or how to model the operators themselves such that they rely on cosmological parameters.

# 2.5 Cosmic fields and their statistical description

Until this point, we discussed how the density field evolves in time, and gave the equations that describe gravitational clustering. In the following section, we shall derive the explicit spatial dependency, i.e.  $\delta(\mathbf{x})$ . The current explanation of the LSS of the Universe is that the present distribution of matter on cosmological scales results from the growth of primordial, small, seed fluctuations on an otherwise homogeneous universe amplified by gravitational instability. Tests of cosmological theories which characterise these primordial seeds are not deterministic in nature but rather statistical, for the following reasons:

- We do not have direct observational access to primordial fluctuations, which would provide definite initial conditions for the deterministic evolution equations.
- The time scale for cosmological evolution is so much longer than that over which we can make observations, that it is impossible to follow the evolution of single systems. In other words, what we observe through our past light cone is different objects at different times of their evolution; therefore, testing the evolution of structure must be done statistically.

The observable Universe is modelled as a stochastic *realisation* of a statistical ensemble of possibilities. The goal is to make statistical predictions, which in turn depend on the statistical properties of the primordial perturbations leading to the formation of LSS.

### 2.5.1 Statistical homogeneity and isotropy

A random field is characterised by the probability that a specific realisation  $\delta(\mathbf{x})$  of the density fluctuations occurs. Abstractly a random field can be better described as follows. We assume that all possible realisations of the density field are smooth so that  $\delta(\mathbf{x})$  can be described, with sufficient accuracy, by its values on a regular grid in  $\mathbf{x}$ . Let  $\mathbf{x}_i$  be as set of appropriately numbered grid-points, and let  $\delta_i = \delta(\mathbf{x}_i)$  be the density contrast at  $\mathbf{x}_i$ . The realization of the random field is then described by the set of the  $\delta_i$ , and the random field is characterized by the joint probability distribution

$$p(\delta_1, \delta_2, \dots) \, \mathrm{d}\delta_1 \mathrm{d}\delta_2 \, \dots \tag{2.57}$$

that  $\delta(\mathbf{x}_i)$  lies within  $d\delta_i$  of  $\delta_i$ . Hence, the description of the random fields reduces to a joint probability distribution of discrete random variables.

We stated in Sect. 2.1 that on large enough scales the Universe is homogeneous and isotropic; therefore, the density field should share these properties. This is formulated by the requirement that if all grid points are translated and rotated in the same way,  $\mathbf{x} \longrightarrow \mathcal{R}(\mathbf{x} + \mathbf{y})$ , where  $\mathcal{R}$  is a rotation matrix and  $\mathbf{y}$  a translation vector, the probability density p must remain unchanged. Thus, the probabilities depend only on the relative positions.

#### 2.5.2 Two-point correlation function and power spectrum

Given that we are approaching the issue of structure formation from a statistical perspective, it is logical to incorporate statistical quantities that enable us to provide accurate details regarding the statistical properties of the random field. Our aim is to establish the mathematical tools necessary for a precise and quantitative analysis.

We shall now consider second-order statistical properties of a density field  $\delta(\mathbf{x})$ . The *two-point* correlation function is defined as the joint ensemble average of the density at two different locations,

$$\xi(r) = \langle \delta(\mathbf{x}) \, \delta(\mathbf{x} + \mathbf{r}) \rangle, \qquad (2.58)$$

which depends only on the distance r between the two points due to statistical homogeneity and isotropy. Here  $\langle \cdots \rangle$  denotes the average over the ensemble of realisations of the random field. In practice, the ensemble average can be replaced with a volume average. In the limit  $r \to 0$  it coincides with the variance of the field

$$\lim_{r \to 0} \xi(r) = \langle \delta^2(\mathbf{x}, t) \rangle. \tag{2.59}$$

The density contrast  $\delta(\mathbf{x})$  is usually written in terms of its Fourier components,

$$\delta(\mathbf{x}) = \int \frac{\mathrm{d}^3 \mathbf{k}}{(2\pi)^3} \,\tilde{\delta}(\mathbf{k}) \,\mathrm{e}^{\mathrm{i}\mathbf{k}\cdot\mathbf{x}} \,. \tag{2.60}$$

The quantities  $\tilde{\delta}(\mathbf{k})$  are then complex random variables. As  $\delta(\mathbf{x})$  is real, it follows that

$$\tilde{\delta}(\mathbf{k}) = \tilde{\delta}^*(-\mathbf{k}). \tag{2.61}$$

The density field is, therefore, determined entirely by the statistical properties of the random variable  $\tilde{\delta}(\mathbf{k})$ . We can compute the correlators in Fourier space,

$$\langle \tilde{\delta}(\mathbf{k})\tilde{\delta}(\mathbf{k}')\rangle = \int d^3\mathbf{x} d^3\mathbf{r} \langle \delta(\mathbf{x})\delta(\mathbf{x}+\mathbf{r})\rangle e^{-i(\mathbf{k}+\mathbf{k}')\cdot\mathbf{x}-i\mathbf{k}'\cdot\mathbf{x}}, \qquad (2.62)$$

30th April 2025 12:58

which gives,

$$\langle \tilde{\delta}(\mathbf{k}) \tilde{\delta}(\mathbf{k}') \rangle = \int d^3 \mathbf{x} d^3 \mathbf{r} \, \xi(r) \, e^{-i(\mathbf{k} + \mathbf{k}') \cdot \mathbf{x} - i\mathbf{k}' \cdot \mathbf{r}}$$

$$= (2\pi)^3 \delta_{\mathrm{D}}(\mathbf{k} + \mathbf{k}') \int d^3 \mathbf{r} \, \xi(r) \, e^{i\mathbf{k} \cdot \mathbf{r}}$$

$$= (2\pi)^3 \delta_{\mathrm{D}}(\mathbf{k} + \mathbf{k}') P(k) \,, \tag{2.63}$$

where P(k) is by definition the density *power spectrum* and  $k = |\mathbf{k}|$ . The inverse relation between two-point correlation function and power spectrum reads

$$\xi(r) = \int \frac{\mathrm{d}^3 \mathbf{k}}{(2\pi)^3} P(k) \,\mathrm{e}^{\mathrm{i}\mathbf{k}\cdot\mathbf{r}} \,. \tag{2.64}$$

Hence, the power spectrum and the two-point correlation function are Fourier transform pairs. Both of these functions give information about how strongly clustered the field is depending on the scale. In order to extract cosmological insights from the power spectrum, the conventional approach involves modelling it using a physical framework that incorporates cosmological parameters. Subsequently, a comparison is made between the modelled power spectrum and the observed power spectrum. Alternatively, one can utilise the two-point correlation function which contains identical information. However, performing numerical calculations in Fourier space is frequently preferred due to its reduced complexity and computational cost.

#### 2.5.3 Gaussian random fields and the Wick theorem

The power spectrum is a well-defined quantity for almost all homogeneous random fields. This concept becomes extremely useful when one considers a *Gaussian* field. It means that any joint probability distribution  $p(\delta_1, \delta_2, ...)$  of local densities  $\delta_i$  follows the Gaussian normal distribution.

A Gaussian random field is characterised by the properties:

- the Fourier components  $\tilde{\delta}(\mathbf{k})$  are mutually statistically independent,
- the probability density for  $\tilde{\delta}(\mathbf{k})$  is described by Gaussian,
- the joint probability distribution of a number N of linear combinations of the random variables  $\delta(\mathbf{x}_i)$  is a multivariate Gaussian.

For Gaussian fields any ensemble average of the product of variables can be obtained by the product of ensemble averages of pairs. This rule written explicitly for the Fourier modes of density field  $\delta(\mathbf{x})$  is

$$\langle \tilde{\delta}(\mathbf{k}_{1}) \cdots \tilde{\delta}(\mathbf{k}_{2N+1}) \rangle = 0,$$

$$\langle \tilde{\delta}(\mathbf{k}_{1}) \cdots \tilde{\delta}(\mathbf{k}_{2N}) \rangle = \sum_{\text{all pair associations } N \text{ pairs } (i,j)} \langle \tilde{\delta}(\mathbf{k}_{i}) \tilde{\delta}(\mathbf{k}_{j}) \rangle$$

$$= \sum_{\text{all pair associations } N \text{ pairs } (i,j)} (2\pi)^{3} P(\mathbf{k}_{i}) \delta_{D}(\mathbf{k}_{i} + \mathbf{k}_{j}),$$

$$(2.66)$$

where we used (2.63) to express the correlators  $\langle \tilde{\delta}(\mathbf{k}_i) \tilde{\delta}(\mathbf{k}_j) \rangle$  using the power spectrum  $P(\mathbf{k}_i)$ . This is the *Wick theorem*. Hence, according to this theorem, the correlator vanishes for any odd number of variables. This theorem is very convenient for quantitative considerations. Therefore, the statistical properties of the Gaussian random variables  $\tilde{\delta}(\mathbf{k})$  are fully specified by its power spectrum.

General random fields are not Gaussian and to specify a random field, one needs to specify all N-point correlation functions. Throughout this work, we assume that the density fluctuations in the early Universe are a realisation of a Gaussian random field, which is justified by observations, since CMB, which essentially tells us the initial conditions of structure formation, is indeed very close to Gaussian random field (Planck Collaboration et al., 2020b). However, non-linear evolution of the density fields due to gravitational instability (i.e. the formation of the LSS and DM haloes) turns it into a highly non-Gaussian field at the present epoch – this can also be understood from the SPT equations: At next-to-leading order, i.e. for the calculation of  $\delta_{n\geq 2}$ , integrals need to be computed that couple the density fields at different scales  $\mathbf{k}$  to each other, whereas for Guassian random field the modes evolve independently.

# 2.5.4 Three-point correlation function and bispectrum

The three-point correlation function is the lowest-order statistic sensitive to non-Gaussianity. It is defined similarly to two-point correlation function, by taking an ensemble average of the field at three different locations,

$$\xi_3(x_1, x_2, x_3) = \langle \delta(\mathbf{x}_1) \delta(\mathbf{x}_2) \delta(\mathbf{x}_3) \rangle \tag{2.67}$$

The Fourier equivalent of the three-point correlation function is the bispectrum  $B(k_1, k_2, k_3)$ , defined by

$$(2\pi)^{3}\delta_{\mathcal{D}}(\mathbf{k}_{1}+\mathbf{k}_{2}+\mathbf{k}_{3})B(k_{1},k_{2},k_{3}) = \langle \tilde{\delta}(\mathbf{k}_{1})\tilde{\delta}(\mathbf{k}_{2})\tilde{\delta}(\mathbf{k}_{3})\rangle. \tag{2.68}$$

As one can notice, the bispectrum is defined only for closed triangles of wavevectors, i.e. where  $\mathbf{k}_1 + \mathbf{k}_2 + \mathbf{k}_3 = 0$ . Some of the triangular configurations are shown in Fig. 2.5.

As the bispectrum is a function of both the size and shape of triangles formed by a closed loop of k-vectors, there is more information encoded in the bispectrum compared to the power spectrum. Historically, the bispectrum has been considered as a useful tool to learn about the statistical properties of the primordial density perturbations that seeded structure formation (their degree of non-Gaussianity, in particular) and to study non-linear physical processes like gravitational dynamics and galaxy biasing. Furthermore, the bispectrum can be used as an independent statistic to complement the power spectrum when inferring the cosmological parameters.

Correlation functions are directly related to the multi-point probability function. The physical interpretation of the two-point correlation function is that it measures the excess over the random probability that two particles at volume elements  $dV_1$  and  $dV_2$  are separated by distance  $x_{12} = |\mathbf{x}_1 - \mathbf{x}_2|$ ,

$$dP_{12} = n^2 [1 + \xi(x_{12})] dV_1 dV_2, \qquad (2.69)$$

where *n* is the mean density. If there is no clustering (random distribution),  $\xi = 0$  and the probability of having a pair of particles is just given by the mean density squared, independent of distance. If objects are clustered ( $\xi > 0$ ), the probability is enhanced, whereas if objects are anti-correlated ( $\xi < 0$ ) the probability is suppressed. Similarly, for the three-point case, the probability of having three objects

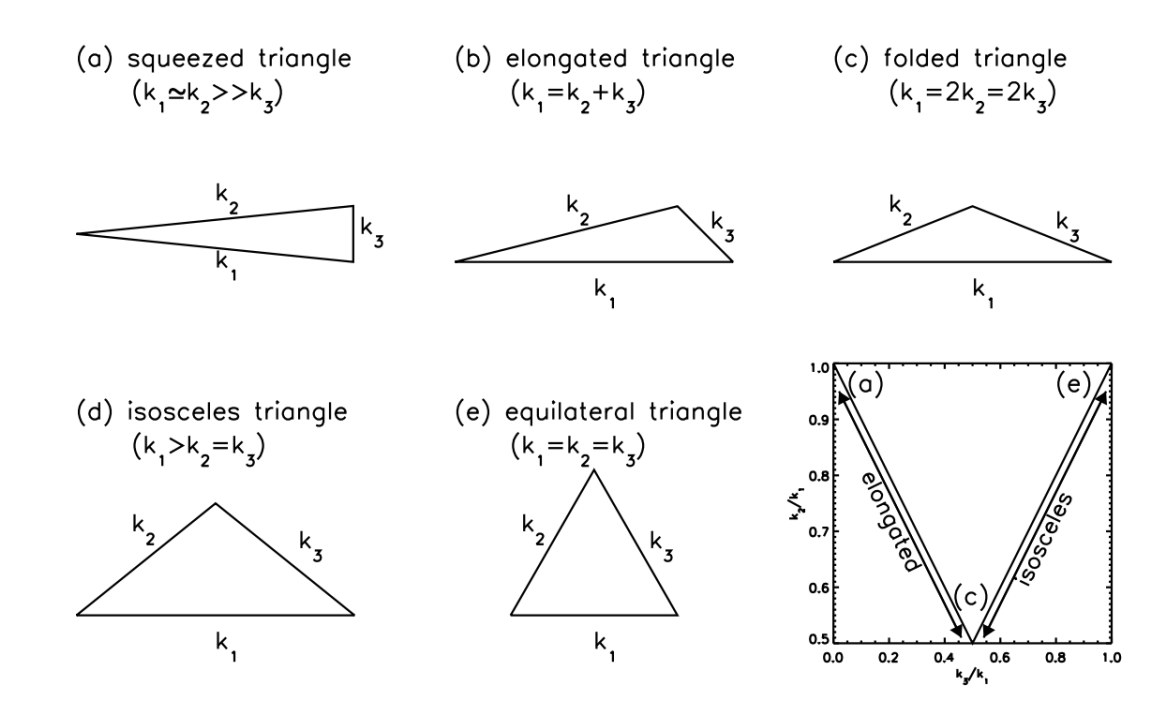


Figure 2.5: Visual representations of triangles forming the bispectrum,  $B(k_1, k_2, k_3)$ , with various combinations of triangles satisfying  $k_3 \le k_2 \le k_1$ . Source: Jeong and Komatsu (2009)

is given by

$$dP_{123} = n^3 [1 + \xi(x_{12}) + \xi(x_{23}) + \xi(x_{31}) + \xi_3(x_{12}, x_{23}, x_{31})] dV_1 dV_2 dV_3.$$
 (2.70)

If the density field is Gaussian  $\xi_3 = 0$ , and all probabilities are determined by  $\xi(r)$  alone.

# 2.5.5 Linear power spectrum

Now we concentrate on the time evolution of the cosmic fields during the matter-dominated epoch. In this case, as we discussed in Sect. 2.3, diffusion effects are negligible and the evolution can be expressed in terms of ideal fluid equations that describe the conservation of mass and momentum. As a result, the evolution of the power spectrum is given by a simple time-dependent scaling of the linear power spectrum

$$P(k,z) = D^{2}(z)P_{L}(k)$$
, (2.71)

where D(z) is the growth factor. One must note, however, that the linear power spectrum specified by  $P_{\rm L}(k)^6$  derives from the linear evolution of density fluctuations through the radiation domination era and the resulting decoupling of matter from radiation. This evolution must be followed by using general relativistic Boltzmann numerical code (Ma and Bertschinger, 1995), although analytic results

<sup>&</sup>lt;sup>6</sup> We denote the linear power spectrum interchangeably by  $P_{\rm I}(k)$  or by  $P_{\rm O}(k)$ 

can be used to understand quantitatively the results. The end result is that

$$P_{\rm L}(k) = A_{\rm s} k^{n_{\rm s}} T^2(k) , \qquad (2.72)$$

where  $n_s$  is the primordial spectral index,  $A_s$  is the normalization of power spectrum, T(k) is the transfer function. The transfer function describes how structures grow differently depending on scale in linear theory. The growth of fluctuations at a certain scale, denoted as k, relies on when they enter the horizon. This timing, whether during the radiation-dominated or matter-dominated era, affects the outcome. In other words, it depends on which term dominates in the Friedmann equation. When small perturbations enter during the radiation-dominated era, their growth is prevented until the Universe transitions into the matter-dominated phase. Additionally, the transfer function takes into account the impact of *free-streaming*. This effect varies depending on the type of DM, whether it is cold, warm, or hot. Different DM particles exhibit varying velocities, where faster particles cluster less than slower ones and tend to free-stream. Consequently, hot and warm DM lead to a decrease in small-scale power compared to CDM. This is encoded in the transfer function and depends on the cosmological parameters in a complicated way, although in cases when the baryonic content is negligible it can be approximated by a fitting function that depends on the shape parameter  $\Gamma = \Omega_{\rm m} h$  (Bardeen et al., 1986). Once the perturbations grow sufficiently, linear theory breaks down, and one needs to follow the evolution of the density by numerical methods. The initial conditions for these simulations are provided by (2.72).

The theory provides the basis for understanding the shape of the power spectrum, but the actual measurement of the fluctuations' strength, represented by the normalisation constant  $A_s$ , is necessary. In the past, a specific parametrisation was developed based on observations. It was discovered that when counting galaxies within a sphere of  $8 h^{-1}$  Mpc, the variance of their number N was remarkably close to one, i.e.

$$\frac{\langle (N - \langle N \rangle)^2 \rangle}{\langle N \rangle^2} \approx 1. \tag{2.73}$$

According to the latest data (see below), it has been confirmed that the value is actually less than one. However, the initial concept of quantifying the level of structure by counting collapsed objects within a specific radius has been retained. One employs the dispersion  $\sigma^2(R)$  of the density field  $\delta_R(\mathbf{x})$  when smoothed at a certain radius R,

$$\sigma^{2}(R) \equiv \langle \delta_{R}^{2}(\mathbf{x}) \rangle = \int |\tilde{W}(kR)|^{2} P(k) \frac{d^{3}k}{(2\pi)^{3}} = \frac{1}{2\pi^{2}} \int_{0}^{\infty} |\tilde{W}(kR)|^{2} P(k) dk$$
 (2.74)

where  $\tilde{W}(kR)$  is the Fourier representation of a top-hat filter function that smoothes the density field. Setting  $R=8\,h^{-1}$  Mpc gives the cosmological parameter  $\sigma_8$  that is constrained to be  $\sigma_8\approx 0.8$  by current surveys (e.g. Planck Collaboration et al., 2020a). We see that  $\sigma_8\propto A_s$ , so fixing either of them uniquely defines the normalisation of the power spectrum.

30th April 2025 12:58

<sup>&</sup>lt;sup>7</sup> The horizon represents the furthest distance a photon can cover within a specified time period. In other words, it signifies the maximum spatial separation between two points that allows them to remain causally connected during that time interval.

# 2.6 One-loop standard perturbation theory

As we saw in Sect. 2.3, the dynamics of gravitational instability are non-linear, and therefore non-linear evolution inevitably leads to the development of non-Gaussian features.

The statistical characterisation of non-Gaussian fields is, in general, a non-trivial subject. The situation is somewhat different for gravitational clustering from Gaussian initial conditions, which we deal with in this work. Here it is possible to calculate in a model-independent way how the non-Gaussian features arise, and what is the most natural statistical description. In particular, since the non-linearities in the equations of motion are quadratic, gravitational instability generates connected high-order correlation functions that scale as  $\xi_N \propto \xi_2^{N-1}$  at large scales, where  $\xi_2 \ll 1$  and perturbation theory applies. This scaling can be represented by connected *tree diagrams*, where each link represents a two-point function (or power spectrum in Fourier space), since for N points (N-1) links are necessary to connect them in a tree-like fashion. In the framework of SPT we found that non-linear gravitational evolution of the density field can be derived as a perturbative expansion given by the equation (2.48), which we can use to build the correlators in Fourier space.

$$<\!\!\delta(1)\delta(2)\delta(3)_{\widehat{\mathbf{c}}}= \qquad \qquad <\!\!\delta(1)\delta(2)\delta(3)\delta(4)_{\widehat{\mathbf{c}}}= \qquad \qquad + \qquad \qquad + \qquad \qquad \qquad +$$

Figure 2.6: Tree diagrams for bispectrum (left diagram) and trispectrum (right diagram) or three-point and four-point functions in a real space. Here dots represent the density fields and lines represent the power spectrums (two-point function in a real space). Source: Bernardeau et al. (2002)

Fig. 2.6 show the tree diagrams that describe the three- and four-point function induced by gravity. The number of lines coming out of the given vertex is the order in PT that gives rise to such a diagram. For example, the diagram for bispectrum requires linear and second-order PT, representing  $\langle \tilde{\delta}_2(\mathbf{k}_1) \tilde{\delta}_1(\mathbf{k}_2) \tilde{\delta}_1(\mathbf{k}_3) \rangle^8$ . On the other hand, the diagrams for trispectrum require up to third order in PT. The first term represents  $\langle \tilde{\delta}_1(\mathbf{k}_1) \tilde{\delta}_2(\mathbf{k}_2) \tilde{\delta}_2(\mathbf{k}_3) \tilde{\delta}_1(\mathbf{k}_4) \rangle$  whereas the second describes  $\langle \tilde{\delta}_1(\mathbf{k}_1) \tilde{\delta}_3(\mathbf{k}_2) \tilde{\delta}_1(\mathbf{k}_3) \tilde{\delta}_1(\mathbf{k}_4) \rangle$ .

In general, a consistent calculation of the p-point function induced by gravity to leading order (tree-level) requires from first to (p-1)th order in PT. At short scales as  $\xi_2 \longrightarrow 1$ , there are corrections to tree-level PT. These are naturally described in terms of diagrams as well, in particular, next to leading order contributions (*one-loop corrections*) require from first to (p+1)th order in PT. These are represented by one-loop diagrams, i.e. diagrams where there is one closed loop.

Figs. 2.7 and 2.8 show the one-loop diagrams for the power spectrum and bispectrum. The one-loop corrections to the power spectrum describe the non-linear corrections to the linear evolution, that is, the effects of mode coupling and the onset of non-linear structure growth.

We can write the power spectrum up to one-loop corrections as

$$P_{\text{SPT}}(k, z) \simeq P_{\text{SPT}}^{\text{tree}}(k, z) + P_{\text{SPT}}^{1-\text{loop}}(k, z)$$
. (2.75)

<sup>&</sup>lt;sup>8</sup> Subscripts represent the order in perturbation theory

$$\langle \delta(1)\delta(2)\rangle_{c} = -$$
 +  $\left[$  +  $\left[$ 

Figure 2.7: Diagrams for the two-point correlation or power spectrum up to one-loop. The terms in the square brackets represent one-loop correction terms given by Eqs. (2.77) and (2.78). Source: Bernardeau et al. (2002)

Under the assumption of Gaussian intial conditions, the leading-order term coincides with the linear power spectrum,  $P_{\text{SPT}}^{\text{tree}}(k,z) = [D(z)]^2 P_{\text{L}}(k)$ , and the one-loop contribution consists of two terms,

$$P^{(1)}(k,z) = D^{2}(z) \left[ P_{22}(k) + P_{13}(k) \right], \qquad (2.76)$$

with

$$P_{22}(k,z) = 2 \int \frac{d^3 \mathbf{q}}{(2\pi)^3} [F_{2,\text{sym}}(\mathbf{k} - \mathbf{q}, \mathbf{q})]^2 P_{L}(|\mathbf{k} - \mathbf{q}|) P_{L}(q), \qquad (2.77)$$

$$P_{13}(k,\tau) = 6 \int \frac{d^3 \mathbf{q}}{(2\pi)^3} F_{3,\text{sym}}(\mathbf{k}, \mathbf{q}, -\mathbf{q}) P_{L}(k) P_{L}(q) . \tag{2.78}$$

Here  $P_{ij}$  denotes the amplitude given by a loop diagram representing the contribution from  $\langle \delta_i \delta_j \rangle$  to the power spectrum. Since we have assumed Gaussian initial conditions  $P_{ij}$  vanishes if i+j is odd. Equation (2.77) is positive definite and describes the mode coupling between wave vectors  $\mathbf{k} - \mathbf{q}$  and  $\mathbf{q}$ . On the other hand, (2.77) is in general negative and does not describe mode coupling, i.e. it is proportional to  $P_{\mathrm{L}}(k,\tau)$ .

The one-loop expansion for the bispectrum,  $B_{SPT}(k_1, k_2, k_3, z) \simeq B_{SPT}^{tree}(k_1, k_2, k_3, z) + B_{SPT}^{1-loop}(k_1, k_2, k_3, z)$ , is given by the tree-level part in terms of a single diagram from second order SPT (Fig. 2.6) plus its permutations over external momenta:

$$B_{\rm SPT}^{\rm tree}(k_1,k_2,k_3,z) = D^2(z) \left[ 2 \, F_{\rm 2,sym}({\bf k}_1,{\bf k}_2) P_{\rm L}(k_1) P_{\rm L}(k_2) + {\rm perms.} \right] \, . \label{eq:BSPT}$$

The one-loop contribution consists of four distinct diagrams involving up to fourth-order solutions,

$$<\delta(1)\delta(2)\delta(3)_{\stackrel{>}{c}}=$$
 + + + + + +

Figure 2.8: Diagrams for the three-point correlation or bispectrum one-loop corrections. Source: Bernardeau et al. (2002)

$$B_{\text{SPT}}^{\text{1-loop}} = D^{6}(z) \left[ B_{222} + B_{123}^{I} + B_{123}^{II} + B_{411}^{II} \right], \tag{2.79}$$

30th April 2025 12:58

where

$$B_{222} = 8 \int \frac{d^3 \mathbf{q}}{(2\pi)^3} F_{2,\text{sym}}(\mathbf{k}_1 + \mathbf{q}, -\mathbf{q}) F_{2,\text{sym}}(-\mathbf{k}_1 - \mathbf{q}, \mathbf{q} - \mathbf{k}_2) F_{2,\text{sym}}(\mathbf{k}_2 - \mathbf{q}, \mathbf{q})$$
(2.80)

$$\times P_{\mathrm{L}}(|\mathbf{k}_{2}-\mathbf{q}|)P_{\mathrm{L}}(|\mathbf{k}_{1}+\mathbf{q}|),$$

$$B_{123}^{I} = 6P_{L}(k_{3}) \int \frac{d^{3}\mathbf{q}}{(2\pi)^{3}} F_{3,\text{sym}}(\mathbf{q} - \mathbf{k}_{2}, -\mathbf{k}_{3}, -\mathbf{q}) F_{2,\text{sym}}(\mathbf{q}, \mathbf{k}_{2} - \mathbf{q})$$
(2.81)

$$\times P_{L}(|\mathbf{k}_{2} - \mathbf{q}|)P_{L}(q) + 5 \text{ perms.},$$

$$B_{123}^{II} = 6P_{L}(k_{2})P_{L}(k_{3})F_{2,\text{sym}}(\mathbf{k}_{2}, \mathbf{k}_{3}) \int \frac{d^{3}\mathbf{q}}{(2\pi)^{3}}F_{3,\text{sym}}(\mathbf{k}, \mathbf{q}, -\mathbf{q})P_{L}(q) + 5 \text{ perms.}$$
 (2.82)

= 
$$F_{2,\text{sym}}(\mathbf{k}_2, \mathbf{k}_3)[P_L(k_1)P_{13}(k_2) + P_L(k_2)P_{13}(k_1)] + 2 \text{ perms.}$$
,

$$B_{411} = 12P_{L}(k_2)P_{L}(k_3) \int \frac{d^3\mathbf{q}}{(2\pi)^3} F_{4,\text{sym}}(\mathbf{q}, -\mathbf{q}, -\mathbf{k}_2, -\mathbf{k}_3) P_{L}(q) + 2 \text{ perms.}.$$
 (2.83)

At early times and on large scales, the tree-level SPT accurately describes both the matter power spectrum and bispectrum. However, in later stages, one-loop corrections lead to an overestimation of the power spectrum on mildly non-linear scales ( $k \sim 0.1~h\,\mathrm{Mpc}^{-1}$ , Crocce and Scoccimarro, 2006; Carlson et al., 2009; Taruya et al., 2009), and including higher-order terms does not improve the accuracy of the predictions (e.g. Blas et al., 2014). The reason behind the failure of SPT is well understood: the loop integrals encompass scales where the assumptions of the theory are no longer valid, such as the generation of vorticity and velocity dispersion during orbit crossing (e.g., Pueblas and Scoccimarro, 2009), resulting in a non-perturbative regime of physics. Consequently, the breakdown of SPT on small scales compromises its predictions for the larger scales.

## 2.6.1 Effective Field Theory of Large-Scale Structure

The fact that two well-separated scales characterise the Universe, the Hubble scale, over which perturbations are linear, and the non-linear scale, which marks the scale over which the gravitational collapse overtakes the Hubble expansion, makes the problem of structure formation suitable for Effective Field Theory (EFT) treatment. In a system characterised by a wide range of scales, such theories isolate a set of degrees of freedom and describe them with a simplified model without having to deal with the complex (and often unknown) underlying dynamics. The impact of physics one intends to neglect on the degrees of freedom one aims to study is computed as a perturbation theory in terms of expansion parameters.

The EFT for large-scale structure (Baumann et al., 2012; Carrasco et al., 2012, 2014a,b; Hertzberg, 2014; Porto et al., 2014; Senatore and Zaldarriaga, 2015) aims to provide a concise representation of the matter density field's long-wavelength modes by integrating out the shorter-wavelength ones. Unlike the SPT, the EFT does not rely on the single-stream approximation. Instead, it considers an effective stress tensor that incorporates all operators involving the long-wavelength density and velocity fields, along with their derivatives, as permitted by the symmetries of the problem, namely the equivalence principle, statistical isotropy, and homogeneity. To describe the behaviour of the system, the effective stress tensor is expanded in a Taylor series with respect to the long-wavelength fluctuations. This expansion generates an infinite series of unknown parameters, with each parameter

associated with a specific perturbative order. The parameters of the effective theory serve two purposes. Firstly, they generate 'counterterms' in the expressions for observables in the EFT, allowing for the cancellation of the ultraviolet (UV) sensitivity of loop integrals in SPT, meaning their dependence on the cutoff scale. This cancellation process can be carried out systematically in perturbation theory, order by order. Secondly, the remaining part of the counterterms, which is independent of the cutoff, plays a crucial role in quantifying the influence of non-perturbative physics on the long-wavelength modes. This is achieved by introducing new 'effective' interactions among these modes. However, the amplitude of this part can not be determined directly from the effective field theory itself, as it is unable to account for small-scale physics. Therefore, it must be determined through empirical means, such as comparison with numerical simulations, or it may be marginalised over during the analysis of observational data (see, e.g. Ivanov et al., 2020; d'Amico et al., 2020).

The EFT framework postulates the presence of a scale, commonly represented by the wavenumber  $k_{\rm NL}$ , where the physics transitions into a non-perturbative regime, rendering the effective description invalid. Multiple lines of reasoning indicate that the expansion of the low-frequency fields can be systematically organized, such that the expansion parameter of the perturbation theory becomes  $k/k_{\rm NL}$ . This implies that as the wavenumber k approaches  $k_{\rm NL}$ , an increasing number of terms need to be taken into account to obtain precise expressions for the matter field correlators.

In this thesis, we consider the specific parametrisation of the counterterms appearing in the one-loop expression for the matter power spectrum and bispectrum presented in (Angulo et al., 2015a). Namely,

$$P_{\text{EFT}}(k, z) = P_{\text{SPT}}(k, z) + P_{c_0}(k, z),$$
 (2.84)

where the tree-level counterterm is given by

$$P_{c_0}(k,z) = -2c_0(z) [D(z)]^2 k^2 P_{L}(k) , \qquad (2.85)$$

and  $c_0$  is undetermined by the theory. In terms of the effective speed of sound for the perturbations,  $c_{s(1)}(z)$ , we have  $\bar{c}_0 \equiv (2\pi) \left[D(z)\right]^\zeta \left[c_{s(1)}(z)\right]^2/k_{\rm NL}^2$  (where  $\zeta$  denotes a real constant arising from the time dependence of the effective stress tensor, see below for further details). Parameter  $c_0$  can be related to  $\bar{c}_1$  introduced by Angulo et al. (2015a) in the following manner:  $c_0$  is defined as  $\bar{c}_1 \left[D(z)\right]^\zeta$ , where  $\left[D(z)\right]^{n+\zeta}$  corresponds to the assumed growth factor of the EFT corrections to the SPT density fluctuations of order n.

Similarly, for the one-loop bispectrum EFT introduces four counterterms

$$B_{\text{EFT}} = B_{\text{SPT}} + B_{c_0} + B_{c_1} + B_{c_2} + B_{c_3}, \qquad (2.86)$$

where one of them is also proportional to  $c_0$ 

$$B_{c_0} = c_0(z) \left[ D(z) \right]^4 \left[ 2 P_{\rm L} \left( k_1 \right) P_{\rm L} \left( k_2 \right) \tilde{F}_2^{(s)} \left( \mathbf{k}_1, \mathbf{k}_2 \right) + 2 \text{ perms.} \right] - 2 k_1^2 P_{\rm L} \left( k_1 \right) P_{\rm L} \left( k_2 \right) F_2 \left( \mathbf{k}_1, \mathbf{k}_2 \right) + 5 \text{ perms.} \right], \tag{2.87}$$

with

$$\tilde{F}_{2}^{(s)}(\mathbf{k}_{1}, \mathbf{k}_{2}) = -\frac{1}{(1+\zeta)(7+2\zeta)} \left[ \left( 5 + \frac{113\zeta}{14} + \frac{17\zeta^{2}}{7} \right) (k_{1}^{2} + k_{2}^{2}) + \left( 7 + \frac{148\zeta}{7} + \frac{48\zeta^{2}}{7} \right) \mathbf{k}_{1} \cdot \mathbf{k}_{2} \right] \\
+ \left( 2 + \frac{59\zeta}{7} + \frac{18\zeta^{2}}{7} \right) \left( \frac{1}{k_{1}^{2}} + \frac{1}{k_{2}^{2}} \right) (\mathbf{k}_{1} \cdot \mathbf{k}_{2})^{2} + \left( \frac{7}{2} + \frac{9\zeta}{2} + \zeta^{2} \right) \left( \frac{k_{1}^{2}}{k_{2}^{2}} + \frac{k_{2}^{2}}{k_{1}^{2}} \right) \mathbf{k}_{1} \cdot \mathbf{k}_{2} \\
+ \left( \frac{20\zeta}{7} + \frac{8\zeta^{2}}{7} \right) \frac{(\mathbf{k}_{1} \cdot \mathbf{k}_{2})^{3}}{k_{1}^{2}k_{2}^{2}} \right] . \tag{2.88}$$

As suggested by some theoretical considerations and fits to simulations  $\zeta = 3.1$  (Foreman and Senatore, 2016). Quadratic contributions from the long-wavelength perturbations to the effective stress-energy tensor expansion lead to three additional counterterms with the following forms:

$$B_{c_1} = -2 c_1(z) [D(z)]^4 k_1^2 P_L(k_2) P_L(k_3) + 2 \text{ perms.},$$
(2.89)

$$B_{c_2} = -2c_2(z) \left[D(z)\right]^4 k_1^2 \frac{(\mathbf{k}_2 \cdot \mathbf{k}_3)^2}{k_2^2 k_3^2} P_{\mathcal{L}}(k_2) P_{\mathcal{L}}(k_3) + 2 \text{ perms.},$$
 (2.90)

$$B_{c_3} = -c_3(z) \left[ D(z) \right]^4 (\mathbf{k}_2 \cdot \mathbf{k}_3) \left[ \frac{\mathbf{k}_1 \cdot \mathbf{k}_2}{k_2^2} + \frac{\mathbf{k}_1 \cdot \mathbf{k}_3}{k_3^2} \right] P_{\mathcal{L}}(k_2) P_{\mathcal{L}}(k_3) + 2 \text{ perms.},$$
 (2.91)

where alongside  $c_0$  we have additional constants  $c_1$ ,  $c_2$  and  $c_3$  (similar to  $c_0$ , the  $[D(z)]^{\zeta}$  scaling is absorbed in their definition) that need to be either fit to simulations or marginalised over in the analysis of actual observational data.

While some authors argue that EFT offers a convergent perturbative framework for  $k < k_{\rm NL}$  (e.g. Carrasco et al., 2014a), there are indications that it resembles SPT since it also forms an asymptotic expansion. This expansion loses accuracy when incorporating higher-order loop corrections, reaching a point where it no longer aligns with numerical simulations (e.g. Pajer and van der Woude, 2018; Konstandin et al., 2019). The breakdown of the theory is not caused by short-distance physics but rather by large contributions arising from mildly non-linear scales.

Ultimately, EFT can be perceived as an enhanced version of SPT, wherein counterterms are introduced to regulate the UV-sensitive components.

#### 2.7 Numerical simulations

Cosmological simulations or N-body simulations have become a unique testbed to follow the structure formation in the Universe, and the size and sophistication of these simulations have steeply grown in the last decades. We have the capability to investigate the development of the cosmic web across various length scales, ranging from several hundred  $h^{-1}$  Mpc to smaller sub-kpc scales encompassing individual DM haloes and their constituent galaxies. However, it is not feasible to encompass this wide range of scales within a single simulation. Instead, a decision must be made regarding the specific problem to be addressed, and the simulation setup must be tailored accordingly. In this particular study, our interest lies not in examining the intricate details of the internal structure of individual DM haloes or galaxies. Rather, our focus is on the cosmic scales and the statistics derived from them.

Consequently, we will concentrate on DM-only simulations and omit the inclusion of baryons.

N-body simulations study the behaviour (meaning tracing their position and velocity in time) of a large number of particles under the influence of the gravitational force in a cubic box of some size which represents a part of the observable universe. Obviously, when we deal with DM actual elementary particles can not be simulated since that would require enormous computational power and in fact is not required to achieve results of cosmological relevance. Instead one uses the representative particles in the mass range of  $10^7$ - $10^{11} \, \mathrm{M}_{\odot}$ .

To set up a simulation one has to fix a few external parameters - the number of DM particles N, the comoving side length L of the simulation box, and the cosmological parameters. For example, common numbers are  $N=1024^3$  and L=1  $h^{-1}$  Gpc. The matter content of the Universe is  $\Omega_{\rm m}\approx 0.3$  and the critical density is  $\rho_{\rm cr}\approx 27.8\times 10^{10}h^{-2}{\rm M}_{\odot}\,{\rm Mpc}^{-3}$ . Following this a particle mass  $m_{\rm p}$  is of the order of  $10^{10}$   $h^{-1}$   ${\rm M}_{\odot}$ , i.e. that of a small galaxy. More particles give better resolution, but such simulations are more expensive to run. In order to implement the CP and to allow the application of Fourier transformations, it is common to use the *periodic boundary conditions*. This means the particles close to one side of the box will feel the force from the opposite side, and they will enter from that side when leaving the box.

The force experienced by the i-th particle from the j-th particle can be mathematically expressed as

$$\mathbf{F}_{i} = G \sum_{i \neq j} \frac{m_{p}^{2} \left(\mathbf{r}_{j} - \mathbf{r}_{i}\right)}{\left|\mathbf{r}_{j} - \mathbf{r}_{i}\right|^{3}}.$$
(2.92)

This direct approach of calculating the sum of forces for all N particles at a specific time step and using it to accelerate them according to the force they feel is the simplest method. Subsequently, in the next time step, this process is repeated with updated positions and velocities. However, this method becomes impractical for large N due to its computational cost, which scales quadratically as  $N^2$ . To address this challenge, modern N-body codes, such as the Gadget-2 (Springel, 2005) code, employ a hybrid technique known as the TreePM method. This approach divides the force calculation into two components, targeting large and small scales respectively.

For large scales, the *Particle-Mesh* method (referred to as the PM method) is utilised. In this approach, the mass of the point-like DM particles is distributed across a grid using an interpolation technique<sup>9</sup>. This allows the computation of the potential by solving the Poisson equation. The force can be easily determined by performing a Fast Fourier Transform (FFT) and multiplying it with *i* **k**. The positions and velocities of the particles are then updated by applying this force using the same grid interpolation. This method is efficient in terms of speed and memory usage. However, it lacks accuracy when the separation between particles is only a few grid cells. In such cases, a slower but more precise Tree algorithm is employed. This algorithm divides the particle distribution into successively smaller cubes (the initial one being the tree node and the subsequent ones referred to as leaves) with increasing particle density. The force acting on the particles within these cubes is calculated using a multipole expansion. Since this method requires a significant amount of memory, it is reasonable to apply it only to the smallest scales.

In a cosmological simulation, it is necessary to establish the initial density and velocity field, known as the initial conditions (IC), which can then evolve over time. To determine these IC, we must select

<sup>&</sup>lt;sup>9</sup> A widely used method is *Cloud-In-Cell* (CIC), where the mass of one particle is distributed over the adjacent eight grid points, weighted with the distance to the grid point (Efstathiou et al., 1985).

an initial redshift, denoted as  $z_{\rm IC}$ , during the matter-dominated epoch. It is crucial to choose  $z_{\rm IC}$  appropriately, ensuring that the random field remains Gaussian while avoiding excessively high values that would lead to decreased accuracy for small  $\delta$ . Moreover, choosing an excessively high  $z_{\rm IC}$  would result in unnecessary computational time. Typically, a commonly used value for  $z_{\rm IC}$  is approximately 50. For each  ${\bf k}$ , the amplitude of the Fourier modes  $\tilde{\delta}({\bf k})$  are sampled from the following Gaussian distribution:

$$p[\tilde{\delta}(\mathbf{k})] = \frac{1}{\pi \sigma^2(k)} \exp\left[-\frac{\tilde{\delta}^2(\mathbf{k})}{\sigma^2(k)}\right]. \tag{2.93}$$

Here  $\sigma(k) \propto P_{\rm L}(k)$  and the theoretical linear power spectrum can be computed numerically from Boltzmann solvers such as the CAMB (Lewis et al., 2000a; Howlett et al., 2012) at the respective  $z_{\rm IC}$  for a certain input cosmology. This way for the IC we obtain a Gaussian random field with the correct power spectrum. The next step is to obtain the particle distribution that gives exactly this density field. To achieve this, we can start by positioning the N particles on a uniform grid. Then, we apply a slight positional shift to each particle, ensuring that they have the correct Fourier modes  $\delta(k)$ , employing a technique known as the Zel'dovich approximation (ZA; Zel'dovich, 1970). The shifted position  $\mathbf{x}(\mathbf{q},t)$  for a particle at initial position  $\mathbf{q}$  is given as

$$\mathbf{x}(\mathbf{q},t) = \mathbf{q} + D(t)\Psi_1(\mathbf{q}), \qquad (2.94)$$

where  $\Psi_1(\mathbf{q})$  is called displacement field and is described by its Fourier modes

$$\Psi_1(\mathbf{q}) = -i\,\mathbf{k}\frac{\tilde{\delta}(\mathbf{k})}{k^2}\,. (2.95)$$

The ZA is the first-order term within the broader expansion of the displacement field in the context of Lagrangian Perturbation Theory (LPT). In LPT, the trajectory of each fluid element is traced by considering its displacement from the initial position  $\mathbf{q}$  caused by the complete displacement field  $\Psi$ , which can be expressed as:

$$\Psi(\mathbf{q},t) = \sum_{n=1}^{\infty} \Psi_n(\mathbf{q},t).$$
 (2.96)

Utilizing solely ZA introduces undesirable artefacts in the low-redshift power spectrum, impacting it at a per cent level. However, these spurious effects can be mitigated by employing higher-order LPT methods, such as 2LPT (White, 2014), for generating the IC.

# 2.8 Bayesian statistics in cosmological parameter analysis

Much of this work is dedicated to performing or preparing a cosmological parameter analysis. Hence, in this section, we want to detail the basic foundations of such an analysis.

In the real-world scenario, we collect some data from a survey and estimate a particular statistic **X** (e.g. the power spectrum of galaxies in 20 bins). We wish to interpret this data in terms of a *model* **M**. It will typically depend on some parameters  $\theta$ , which we want to determine. The goal of the parameter analysis is to provide estimates of the parameters and their uncertainties, or ideally the whole probability distribution of  $\theta$ , given the data **X**. The latter is called the *posterior distribution*  $p(\theta \mid \mathbf{X})$  i.e. the probability that the measured parameters take certain values after doing the experiment (as

well as assuming some prior knowledge about the parameters). From  $p(\theta \mid \mathbf{X})$  one can calculate the expectation values of the parameters and their errors.

Often, what may be easily calculable is not this, but rather the opposite,  $p(\mathbf{X} \mid \boldsymbol{\theta})$  - i.e. if we know what parameters are, we can compute the expected distribution of the data. This is the same as the likelihood that the model parameters describe a given observation,  $\mathcal{L}(\boldsymbol{\theta} \mid \mathbf{X})$ . However, the likelihood should not be confused with the probability density over  $\boldsymbol{\theta}$ , which is the posterior distribution  $p(\boldsymbol{\theta} \mid \mathbf{X})$  and is related to the likelihood through *Bayes' theorem* 

$$p(\theta \mid \mathbf{X}) = \frac{\mathcal{L}(\theta \mid \mathbf{X}) p(\theta)}{p(\mathbf{X})}.$$
 (2.97)

Here,  $p(\theta)$  is called the *prior* and expresses what we know about the parameters prior to the experiment being done. This may be the result of previous experiments, or theory (e.g. some parameters, such as the age of the Universe, may have to be positive). In the absence of any previous information, the prior is often assumed to be a constant (a 'flat prior'), meaning all parameters are equally likely.  $p(\mathbf{X})$  is called the *evidence* and simply acts to normalise the posterior distribution,

$$p(\mathbf{X}) = \int d\theta \mathcal{L}(\theta \mid \mathbf{X}) p(\theta). \qquad (2.98)$$

Since it does not depend on the model parameters it is often ignored when doing a parameter estimation. However, the evidence does play a role in model selection when more than one theoretical model is being considered, and one wants to choose which model is most likely to describe the data.

In cosmology, due to the central limit theorem, it is a reasonable assumption that the probability distribution of  $\mathbf{X}$  follows a multivariate Gaussian with a covariance matrix  $\mathbf{C}$ . Therefore the likelihood is

$$\mathcal{L}(\boldsymbol{\theta} \mid \mathbf{X}) \propto \exp\left[-\frac{\chi^2(\mathbf{X}, \boldsymbol{\theta})}{2}\right],$$
 (2.99)

with

$$\chi^{2}(\mathbf{X}, \boldsymbol{\theta}) = [\mathbf{M}(\boldsymbol{\theta}) - \mathbf{X}]^{\mathrm{T}} \mathbf{C}^{-1} [\mathbf{M}(\boldsymbol{\theta}) - \mathbf{X}].$$
 (2.100)

We can thus calculate the posterior distribution for our cosmological parameters via

$$\ln p(\boldsymbol{\theta} \mid \mathbf{X}) = \ln \mathcal{L}(\boldsymbol{\theta} \mid \mathbf{X}) + \ln p(\boldsymbol{\theta}) + \text{const} = -\frac{\chi^2(\mathbf{X}, \boldsymbol{\theta})}{2} + \ln p(\boldsymbol{\theta}) + \text{const}.$$
 (2.101)

After we have computed a posterior  $p(\theta \mid \mathbf{X})$ , we are often interested in the *marginalised posterior* of a certain subset  $\{\theta_i\}_{i\in I}$  of parameters (for example, we wish to know the one-dimensional marginalised posterior of the parameter  $\Omega_{\rm m}$ ). We can achieve that by integrating the posterior over all remaining parameters

$$p(\{\theta_i\} \mid \mathbf{X}) = \prod_{i \notin I} \int d\theta_j \ p(\boldsymbol{\theta} \mid \mathbf{X}). \tag{2.102}$$

When performing a cosmological parameter analysis, we mostly want to report constraints on the individual marginalised parameters. Usually, we cite a mean of a marginalised posterior and a corresponding 68.3 per cent credible interval, which corresponds to the interval within one standard deviation of a Gaussian distribution.

#### 2.8.1 Markov chain Monte Carlo method

After we have established how to compute the posterior distribution of cosmological parameters, a cosmological parameter analysis appears feasible. If the problem has two or three parameters, then it may be possible to evaluate the likelihood on a sufficiently fine grid, locate the peak and estimate the errors. However, usually, the dimensions of the parameter space in cosmology are larger. Therefore, as the number of grid points grows exponentially with dimension, it becomes rapidly unfeasible to do it this way. In fact, it is also very inefficient to do it this way, since most of the hypervolume has a very small likelihood so is of little interest.

There are various ways to sample the posterior distribution more efficiently, concentrating the points more densely where the probability is high. The most common method is the Markov Chain Monte Carlo (MCMC). The aim of MCMC is to generate a set of point whose distribution function is proportional to the posterior distribution. MCMC makes random draws, by moving in parameter space in a Markov process - i.e. the next sample depends only on the present one. The resulting Markov chain of points samples the posterior, so we can estimate all the usual quantities of interest like mean and variance from it. Furthermore, marginalisation is extremely easy: Instead of taking a high-dimensional integral, one can ignore the marginalised dimensions of the sampled random walk, which produces a projected posterior distribution along the parameter axis we are interested in.

The basic procedure to make the chain is to generate a new point  $\theta^*$  by taking some step from the present point  $\theta$  and accepting it as a new point in the chain based on some criteria. The most popular algorithm is the *Metropolis-Hastings* algorithm which has the following steps:

• Choose a random initial starting point  $\theta$  in parameter space and compute the target probability density.

#### Then at each iteration:

- Generate a step in parameter space from a so-called *proposal distribution*<sup>10</sup> and a new trial point  $\theta^*$  using this step.
- Compute the acceptance ratio:

$$\alpha = \frac{p(\boldsymbol{\theta}^* \mid \mathbf{X})}{p(\boldsymbol{\theta} \mid \mathbf{X})} \tag{2.103}$$

• Draw a uniform random number u between 0 and 1. If  $u < \alpha$ , the point  $\theta^*$  gets accepted and we repeat the iteration with  $\theta^*$  as the initial point. Otherwise, the point  $\theta^*$  gets rejected, and we repeat the procedure from the start.

The downsides of the Metropolis-Hastings algorithm are choosing the efficient proposal distribution and the fact that convergence is only ensured after an infinite number of evaluations. If the algorithm is stopped early, there is a danger that one mistakes a local maximum for a global one and believes that the random walk has already converged. One method to avoid this is to compute the multiple random walks with different starting points in parallel. Still, convergence can require many evaluations of the likelihood function, which can be prohibitive if it is numerically expensive to compute.

30th April 2025 12:58

 $<sup>^{10}</sup>$  Usually, but not necessarily, this distribution is chosen to be a multivariate Gaussian distribution.

# 2.9 Goals and open questions addressed in this thesis

In this introduction, we have provided an overview of the current state of theory and methodology in the field of precision cosmology, which seeks to comprehend the entire Universe. We have outlined the fundamental principles that underpin our prevailing cosmological model, known as the  $\Lambda$ CDM model. This six-parameter model encompasses the history and composition of the Universe, including the densities of enigmatic entities called DM and dark energy. We have underscored the significance of the close relationship between theory, observations, and numerical simulations as the essential foundations for scientific advancements in cosmology. The interdependence of these distinct branches is vital for progress in the field.

In the rest of the study, we will focus in particular on the issue of theoretical modelling of summary statistics like the power spectrum and the bispectrum. Only an accurate model across a broad range of scales will allow access to the cosmological information contained in the DM distribution. Our research can be broken down into three aspects:

- 1. Up to which scale are the state-of-the-art perturbation theory models (e.g. EFT) for the matter power spectrum and the bispectrum valid when tested against a very large set of *N*-body simulations? How does this scale depend on the assumed survey volume and the systematic errors introduced by the *N*-body technique?
- 2. How well can a deep neural network (DNN) approach model the influence of the survey geometry on the estimated galaxy power spectrum and the bispectrum?
- 3. In view of the forthcoming analysis of the *Euclid* spectroscopic galaxy sample what is the accuracy of the perturbative galaxy bias expansion in the description of the real-space galaxy power spectrum and the bispectrum? How well can this model can infer the fiducial bias and cosmological parameters? How well are these parameters constrained depending on the assumed scale cuts on the data vectors? Which bias relations allow unbiased parameter inference?

# The reach of next-to-leading-order perturbation theory for the matter bispectrum

The following summary is based on the publication

 Alkhanishvili, D., Porciani, C., Sefusatti, E., Biagetti, M., Lazanu, A., Oddo, A., and Yankelevich, V. (2022). The reach of next-to-leading-order perturbation theory for the matter bispectrum. *MNRAS*, 512(4):4961–4981

https://doi.org/10.1093/mnras/stac567

For this work, I led the data analysis and implemented the pipelines that computed the theoretical models for the power spectrum and bispectrum. Cristiano Porciani provided invaluable insight into many aspects of goodness-of-fit tests and measured statistics. Emiliano Sefusatti provided the measured power spectrum and the bispectrum from the Minerva suite. Matteo Biagetti provided the Eos simulation suite which was used to cross-validate the primary results. Andrei Lazanu assisted in the cross-validation of the perturbation theory models. Andrea Oddo and Victoria Yankelevich provided auxiliary data to estimate the modelled power spectrum and the bispectrum. Of course, many ideas and analysis choices resulted from discussions with the collaborators, so it is impossible to disentangle the individual contributions perfectly.

The published paper can be found in App. A.1.

The perturbation theory of the large-scale structure of the Universe is the widely used method of obtaining predictions with analytical control. Even though convergence properties of such theories are still a matter of debate, there is growing evidence that including just the first few terms provides an accurate approximation of the exact solution. Modern approaches come in various flavours and sometimes contain free parameters (e.g. EFT). Therefore, it is crucial to identify the range of validity (or reach as they refer to in the literature) and accuracy before applying them to the observational data. *N*-body simulations of CDM are the standard test bed to achieve this.

In this paper, we have used a very large set of *N*-body simulations (the Minerva suite)<sup>1</sup> to test the next-to-leading-order expansions for the matter power spectrum and bispectrum in five different

<sup>&</sup>lt;sup>1</sup> The suite consists of 300 comoving boxes of side length  $L = 1500 \ h^{-1} \ \mathrm{Mpc}$ .

implementations of perturbation theory. Specifically, we have studied how the different models match the measurements from the simulations as a function of the maximum wavenumber considered  $k_{\rm max}$ . Considering the next generation of surveys, such as those to be conducted by DESI and the *Euclid* mission, we specifically focus on data at redshift z=1. The reach of a model is determined as the minimum value of  $k_{\rm max}$  where the null hypothesis that the *N*-body data are consistent with the model predictions is rejected using a  $\chi^2$  goodness-of-fit test with a significance level of 0.05. To carry out this analysis, certain assumptions about the covariance matrix of the measurements are necessary. In both cases, a dedicated version of the  $\chi^2$  test is employed to ensure that these expressions accurately approximate the covariance matrix of the measurements extracted from the simulations.

The first part of the paper concentrates on employing the full MINERVA suite while neglecting the systematic errors in the simulations. The results can be summarised as follows.

- 1. By analysing the simulation data as a function of  $k_{\rm max}$  and fitting the EFT parameters governing the counterterms' amplitude, we observe their stability up to a certain maximum wavenumber, after which they change, indicating that perturbative expansion breaks down beyond this scale and higher-order corrections become important. The stability region ends at  $k_{\rm max} = 0.14~h\,{\rm Mpc}^{-1}$  for the power spectrum and 0.125  $h\,{\rm Mpc}^{-1}$  for the bispectrum. These specific values define the default range of scales ( $k < k_{\rm fit}$ ) used for fitting the EFT parameters.
- 2. The  $\chi^2$  goodness-of-fit test for the power spectrum demonstrates that EFT accurately match the simulations up to  $k_{\text{max}} = 0.14 \ h \, \text{Mpc}^{-1}$ , while all models without free parameters fail at larger scales, around  $k_{\text{max}} = 0.06 \ h \, \text{Mpc}^{-1}$ .
- 3. Performing the same test for the bispectrum allows us to rank the models based on their accuracy range. EFT models have the widest accuracy range, reaching  $k_{\rm max} \simeq 0.16$   $0.19 \, h \, {\rm Mpc}^{-1}$  (depending on data binning). RegPT and RLPT follow with a slightly lower range of accuracy  $(k_{\rm max} \simeq 0.10 0.14 \, h \, {\rm Mpc}^{-1})$ , while SPT has the narrowest range of accuracy  $(k_{\rm max} \simeq 0.08 \, h \, {\rm Mpc}^{-1})$ . It's worth noting that the nominal reach of EFT extends beyond  $k_{\rm fit}$ , indicating that the model with counterterms fixed using triangle configurations with side length  $k < k_{\rm fit} = 0.125 \, h \, {\rm Mpc}^{-1}$  continues to provide a good fit on slightly smaller scales.

Current surveys of the LSS cover volumes which are one to two orders of magnitude smaller than the total volume of the Minerva simulations. This translates to larger statistical uncertainty around the measurements of the power spectrum and the bispectrum and thus into more extended ranges of accuracy for the models. Therefore, we have sub-sampled the Minerva suite to investigate how the reach of the models depends on the total volume covered by the simulations. This is useful to gauge the range of scales that can be probed in the actual galaxy redshift surveys. We have also approximately accounted for systematic effects introduced by the *N*-body technique using different methods. Our main findings are as follows.

4. As expected, due to the larger statistical error bars the reach of the models improves for smaller volumes as it becomes easier to fit to the data. Considering a Euclid-like survey volume at z = 1 gives a median reach for SPT of approximately 0.12  $h \,\mathrm{Mpc}^{-1}$  for the power spectrum and 0.15  $h \,\mathrm{Mpc}^{-1}$  for the bispectrum. On the other hand, for EFT we obtain 0.25  $h \,\mathrm{Mpc}^{-1}$  for the power spectrum and 0.18  $h \,\mathrm{Mpc}^{-1}$  for the bispectrum. All other models fall in between these extremes.

- 5. The estimated accuracy range of EFT predictions is significantly influenced by the chosen procedure for fitting the counterterms. When considering the volume of the Euclid-like shell, using  $k_{\rm fit} = 0.22 \, h \, {\rm Mpc}^{-1}$  extends the median reach of the EFT model to  $0.33 \, h \, {\rm Mpc}^{-1}$  for the power spectrum and  $0.25 \, h \, {\rm Mpc}^{-1}$  for the bispectrum. However, this extension comes at the cost of degradation in accuracy for the full Minerva set. Regarding the bispectrum, fitting only the  $c_0$  parameter from the power spectrum and setting the other three counterterms to zero provides the highest reach for  $V < 100, h^{-3} \, {\rm Mpc}^3$ . On the other hand, fitting all four parameters is preferred for larger volumes. Consequently, defining a definitive reach for the models with free parameters becomes challenging due to these complexities.
- 6. Accounting for a scale- and shape-dependent bias resulting from the finite mass resolution of the *N*-body simulations has a minimal impact on the results, with changes observed to be less than 10 per cent.
- 7. On the other hand, a significant difference arises when uncorrelated systematic errors are added in quadrature to the statistical uncertainties. In such cases, the reach of EFT is dramatically extended due to the freedom provided by the counterterms. For instance, when considering the entire Minerva suite, the EFT model demonstrates a good fit up to scales of 0.40 and 0.27 h Mpc<sup>-1</sup> for the power spectrum and the bispectrum, respectively. More modest changes are observed for the models with no fixed parameters, particularly for larger volumes.

# Window function convolution with deep neural network models

The following summary is based on the publication

• Alkhanishvili, D., Porciani, C., and Sefusatti, E. (2023). Window function convolution with deep neural network models. *A&A*, 669:L2

https://doi.org/10.1051/0004-6361/202245156

For this work, I led the data analysis and implemented the pipelines that trained and tested the deep neural network models for the power spectrum and bispectrum. Cristiano Porciani and Emiliano Sefusatti provided invaluable insight into many aspects of the effects of the survey geometry on the observed power spectrum and the bispectrum. Of course, many ideas and analysis choices resulted from discussions with the collaborators, so it is impossible to disentangle the individual contributions perfectly.

The published paper can be found in App. A.2.

Conventional estimators of the galaxy power spectrum and bispectrum are susceptible to the influence of the survey geometry. Due to the convolution with the survey's window function, they produce spectra that deviate from the true underlying signal. Especially on large scales, this bias becomes statistically significant for current and future generations of experiments. Consequently, it is crucial to precisely model the impact of the window function on the summary statistics of the galaxy distribution. Furthermore, to enable the sampling of posterior probabilities during the Bayesian estimation of cosmological parameters, it is essential that this process remains computationally efficient. To meet these demands, we have developed a DNN that emulates the convolution with the window function, and we show that it offers fast and precise predictions.

The purpose of our DNN model is to serve as a proof of concept and to achieve this objective, we made certain simplifications in our study. Firstly, we utilised the linear power spectrum and tree-level bispectrum for matter fluctuations. Secondly, we considered a top-hat window function with a fixed volume, where the number density of tracers remains constant across radial distances from the observer. While this ideal scenario allowed us to demonstrate the effectiveness of our DNN model, we believe there is no reason why it cannot accurately predict the effects of more realistic survey masks.

Building a DNN model requires a training set to fit the model parameters. For this purpose, we have used the suite of 2000 linear power spectra in the Quijote database (Villaescusa-Navarro et al., 2020) to build the training set for our DNNs. These spectra were obtained by sampling five cosmological parameters on a Latin hypercube. From these linear power spectra via convolution, we obtained the power spectrum and the bispectrum as observed in the survey whose geometry follows the top-hat window function. In order to benchmark the trained DNN model we also randomly generated 200 samples by employing the same procedure used for the training data set.

It takes less than 10 microseconds to generate DNN predictions for either the power spectrum or the bispectrum. This is ideal for sampling posterior distributions in Bayesian parameter inference. Overall, the DNN provides models for the power spectrum and the bispectrum that are accurate to better than 0.1 per cent.

Generation of the training data set is the bottleneck operation in the DNN approach. It requires a considerable time investment in the case of the bispectrum. In our case, generating 2000 convolved bispectra using 64 processor cores took approximately one month of wall-clock time. This phase can be expedited through extensive parallelisation and potentially by adopting more computationally efficient formulations for the convolution integral, as proposed by Pardede et al. (2022). However, the time investment in constructing the training set shouldn't be a deterrent to adopting the DNN approach. Even for the relatively straightforward case of the isotropic bispectrum of matter-density fluctuations in real space, obtaining posterior distributions for the five considered cosmological parameters would necessitate significantly more than 2000 evaluations of the window-convolved signal. Thus, employing the DNN model would invariably result in a noticeable speedup. To sum up, we find that utilising the DNN model is advantageous, as long as the size of the training set remains substantially smaller than the number of necessary likelihood evaluations in the Bayesian estimation of the model parameters.

# Euclid preparation. Galaxy power spectrum and bispectrum modelling in real space

This chapter is part of the not-yet published article **Euclid Collaboration: Pardede et al., in prep.** which deals with the analysis of the galaxy power spectrum and the bispectrum in real space. Since the article is in preparation, the results presented here are not yet approved by the Euclid Consortium. For this work, I led the data analysis and implemented the pipelines for the real-space galaxy power spectrum and the bispectrum. The Flaghsip I simulations and the measured power spectrum and the bispectrum were provided by the members of Euclid Consortium. Of course, many ideas and analysis choices resulted from discussions with the collaborators, so it is impossible to disentangle the individual contributions perfectly.

#### 5.1 The Euclid mission

In the previous chapters, we discussed cosmology and expansion history of the Universe, the power spectrum, the bispectrum, galaxy bias, etc. To measure all of these features, one needs to have a specific survey, which covers a large sky area and redshift range. In this section, we introduce a promising instrument for such observations - the *Euclid* satellite Laureijs et al. (2011). The main goal of *Euclid* is to understand the physical origin of the accelerated expansion of the Universe. The mission observes the evolution of cosmic structures by measuring the shapes and redshifts of galaxies over a large fraction of the sky. With the new observational data, we should be able to better understand the properties of dark energy, test models of the origin of dark energy, and test GR on different scales. It is hoped that the mission will aid in understanding dark energy and predicting the future evolution of the Universe. Another important goal is to explore the nature and properties of dark matter. A final goal is to reconstruct the initial conditions which led to the present cosmic structure of the Universe.

Euclid is a medium-class mission of the European Space Agency (ESA). The satellite was launched by a SpaceX Falcon 9 rocket from Cape Canaveral, Florida, on July 1<sup>st</sup> 2023 and transferred to the Lagrange point L2 of the Sun-Earth system. The planned mission timeline is 6 years and it will cover  $15000 \text{ deg}^2$  of the sky in a redshift range  $z \approx 0.9 - 1.8$ .

*Euclid* consists of a 1.2-meter Korsch telescope equipped with imaging and spectroscopic instruments, VIS and NISP, working in the visible and near-infrared wavelength ranges, respectively.

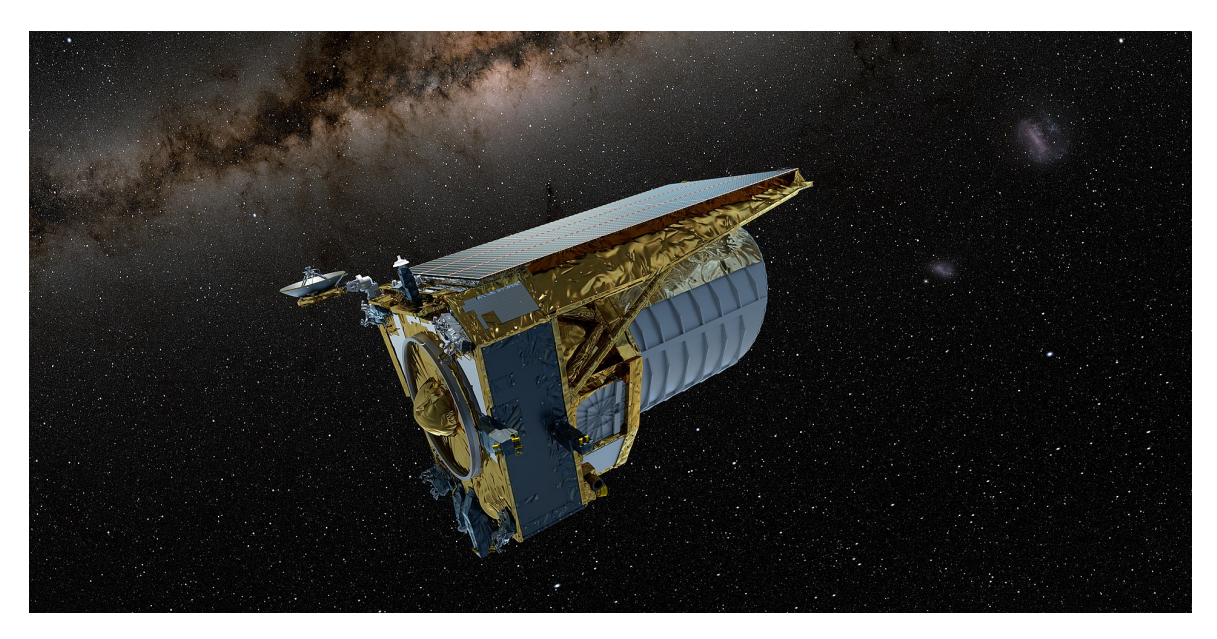


Figure 5.1: The artist's view of the ESA medium class astronomy and astrophysics space mission *Euclid* . Credit: ESA

The VIS works in the wavelength range from 500 to 900 nm and has a pixel resolution of 0.1 arcseconds. The large VIS images with their fine angular resolution will be used for many different purposes, but VIS has been built specifically to make shape measurements of distant galaxies. Their distortions resulting from weak gravitational lensing by intervening matter allow the matter distribution to be mapped. Therefore, the dark matter distribution and its changes over the last 10 billion years will be reconstructed.

The Near Infrared Spectrometer and Photometer (NISP) consists of 16 near-infrared detectors and covers the same field of view as VIS. The wavelength range of the instrument is between 900 and 2000 nm. The near-infrared photometry data will be combined with the VIS data to derive the photometric redshifts and rough estimates of the distances of galaxies observed by the VIS. On the other hand, the spectrometer will accurately measure the distances of  $\approx 50$  million galaxies. NISP slitless spectroscopic observations will be able to detect Lyman-alpha emission lines across the Universe, out to redshifts of 1.9, when the Universe was only 3.5 billion years old. The power of this mode is the combination of good sensitivity to detect an emission line from even very compact distant galaxies and covering an area corresponding to almost 3 times the area of the full moon on the sky in every observation.

# 5.2 Scientific goals

In this chapter in preparation for the analysis of the *Euclid* spectroscopic sample we explore the limits of validity of the perturbative galaxy bias model applied to the joint analysis of the power spectrum and bispectrum (P + B) in real space.

Several recent works provided comparisons of the matter and halo/galaxy bispectrum theoretical predictions in real space against measurements from *N*-body simulations, at leading order (Oddo

h	$\Omega_{ m c}$	$\Omega_{\mathrm{b}}$	$10^{-9} \times A_s$	$n_s$	$M_{\nu}$	$L$ [ $h^{-1}$ Mpc]	F
0.67	0.27	0.049	2.0943	0.97	0	3780	2.3

Table 5.1: Cosmological and structural parameters of Flagship I simulation.

et al., 2020a; Bose et al., 2020; Oddo et al., 2021; Moradinezhad Dizgah et al., 2021; Ivanov et al., 2022) and higher order (Baldauf et al., 2015a; Angulo et al., 2015b; Lazanu et al., 2016; Bose and Taruya, 2018; Eggemeier et al., 2021; Steele and Baldauf, 2021; Baldauf et al., 2021; Alkhanishvili et al., 2022; Philcox et al., 2022; D'Amico et al., 2022). The most stringent of these tests, involving simulation volumes of the order of hundreds of cubic Gigaparsec, indicate that the leading-order, i.e. tree-level prediction for the galaxy bispectrum has a reach of about  $k_{\rm max} \lesssim 0.08 \, h \, {\rm Mpc}^{-1}$  at any relevant redshift, while it can provide a good fit to simulations up to  $k_{\rm max} \lesssim 0.15 \, h \, {\rm Mpc}^{-1}$  for volumes comparable to those that will be probed by the *Euclid* mission.

Much of these results assumed dark matter halo catalogues or galaxy catalogues constructed to reproduce the samples characterising the *eBOSS* surveys. Here we revisit these earlier investigations focusing on a galaxy population that we expect to be a fair description of the *Euclid* spectroscopic sample. We explore the scale cuts for a joint analysis of the galaxy power spectrum and bispectrum in real space, as defined by two wavenumbers  $k_{\text{max}}^P$  and  $k_{\text{max}}^B$ . We will consider a one-loop prediction in perturbation theory for the power spectrum while we will limit ourselves to the tree-level description for the bispectrum. We will study the possibility of reducing the parameter space offered by imposing relations among the bias parameters and how these may lead to systematic errors in the determination of cosmological parameters.

## 5.3 Data

In order to determine the range of validity of our reference theoretical models for the real-space power spectrum and the bispectrum, we require the mock galaxy catalogue generated from the *N*-body simulation which spans the same redshift range that will be observed by *Euclid*. We have used the real-space galaxy power spectrum and bispectrum estimated from this catalogue to study the range of validity of our reference theoretical models. In this section, we introduce and discuss this data.

### 5.3.1 Flagship simulation

Flagship I simulation spans the same redshift range that will be observed by *Euclid*. Namely, we have four snapshots that cover the redshift range  $z \in [0.9, 1.8]$  and were generated using the PKDGRAV3 (Potter et al., 2017) *N*-body code. The latter simulated approximately 2 trillion dark matter particles in a periodic cubic box with a side length of  $L = 3780 \ h^{-1}$  Mpc assuming flat  $\Lambda$ CDM cosmological model with parameters given in Table 5.1. The mass resolution of the simulation  $m_p \approx 2.398 \times 10^9 \ h^{-1} \ M_{\odot}$  allows to resolve the halos with a mass of few  $10^{10} \ h^{-1} \ M_{\odot}$ , which host the majority of  $H\alpha$  emission line galaxies that are going to be the main observation targets of the *Euclid* survey.

Table 5.2: Specifications for the HOD galaxy samples used in this analysis. The table lists the total number of objects  $N_g$  and the mean number density  $\bar{n}$  of the sample. All the considered samples share the same volume, which coincides with the one of the Flagship I comoving outputs, i.e.,  $3780 \, h^{-3} \, \text{Mpc}^3$ .

z	HOD	$N_{ m g}$	$\bar{n}$
	Model		$\left[10^{-3} h^3 \mathrm{Mpc}^{-3}\right]$
0.9	1	201 816 513	3.7
	3	110 321 755	2
1.2	1	108 057 141	2
	3	55 563 490	0.0010
1.5	1	69 132 138	1.3
	3	31 613 213	0.6
1.8	1	24 553 758	0.5
	3	16 926 864	0.3

In each snapshot, galaxies were populated through a two-step process. Initially, friend-of-friend (FOF)<sup>1</sup> halos were selected with a minimum mass equivalent to that of 10 matter particles. Subsequently, these halos were assigned galaxies using the halo occupation distribution (HOD) algorithm, aligning with the central and satellite fractions found in the primary Flagship 1 lightcone catalogue. This lightcone catalogue, in turn, was designed to replicate the number density and clustering characteristics based on two distinct H $\alpha$  profiles referred to as Model 1 and Model 3 in Pozzetti et al. (2016). These two models are defined by different templates for the evolution of the luminosity function  $\phi(L,z)^2$ . Model 1 employs a conventional Schechter parametrisation (Schechter, 1976), while Model 3 directly fits real observations. As a result, the Model 1 sample contains nearly twice as many objects as Model 3, which is more conservative in selecting H $\alpha$  emitters. From now on these models will be referred to as HOD1 and HOD3.

The total numbers of galaxies for each sample, their number density, and the associated Poisson shot-noise contribution, defined as the inverse of the sample mean number density,  $1/\bar{n}$ , are listed in Table 5.2.

#### 5.3.2 Power spectrum and bispectrum measurements

Given the Fourier transform of the galaxy overdensity field  $\delta_g(\mathbf{k})$ , the galaxy power spectrum,  $P_g(k)$ , and the bispectrum,  $B_g(\mathbf{k}_1, \mathbf{k}_2, \mathbf{k}_3)$ , can be defined in terms of the two- and three-point correlators as

$$\langle \delta_{\mathbf{g}}(\mathbf{k}_1) \, \delta_{\mathbf{g}}(\mathbf{k}_2) \rangle = (2\pi)^3 \delta_{\mathbf{D}}(\mathbf{k}_{12}) \, P_{\mathbf{g}}(k_1) \,, \tag{5.1}$$

<sup>&</sup>lt;sup>1</sup> The FOF algorithm uniquely defines groups that contain all particles separated by distance less than a given so-called linking length.

<sup>&</sup>lt;sup>2</sup> The luminosity function is a fundamental concept in astronomy and cosmology, particularly in the study of galaxies and their distribution of brightness (luminosity) in the Universe. The luminosity function tells us how many objects of a particular luminosity are present in a given volume of space.

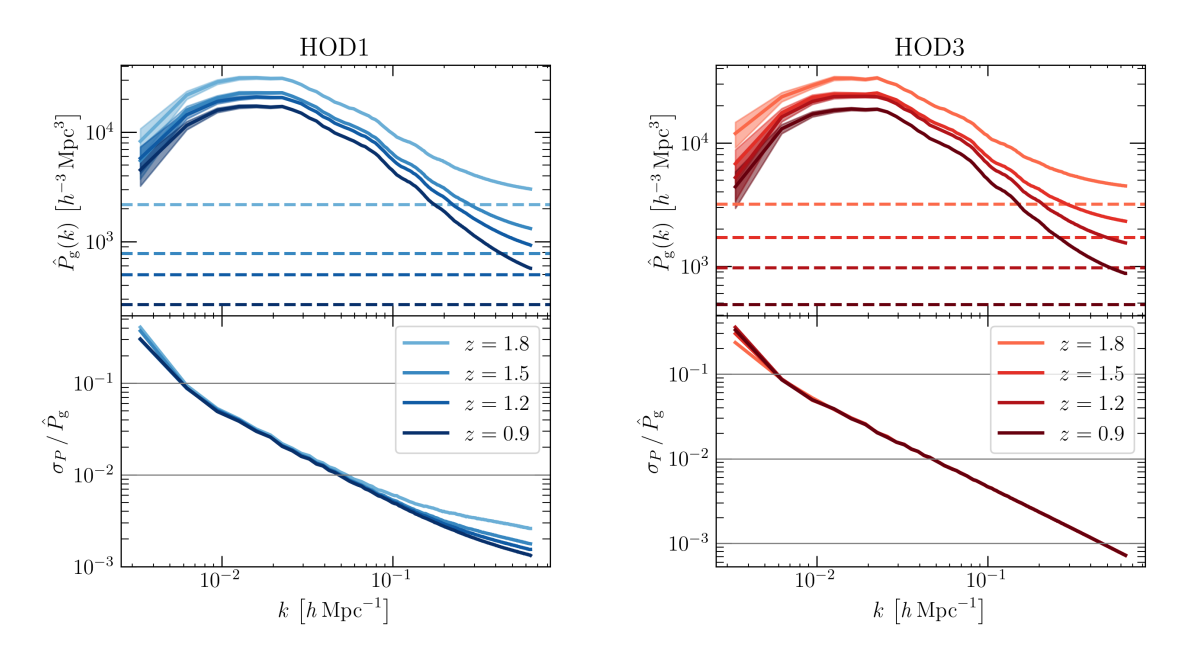


Figure 5.2: The galaxy power spectrum extracted from the Flagship 1 simulation (top) and corresponding relative statistical uncertainty (bottom). The colour gradient indicates the different redshifts of the snapshots. The shaded areas indicate the assumed statistical errors of the measurements and the horizontal dashed lines indicate the Poissonian shot noise.

and

$$\langle \delta_{\mathbf{g}}(\mathbf{k}_1) \, \delta_{\mathbf{g}}(\mathbf{k}_2) \, \delta_{\mathbf{g}}(\mathbf{k}_3) \rangle = (2\pi)^3 \delta_{\mathbf{D}}(\mathbf{k}_{123}) \, B_{\mathbf{g}}(\mathbf{k}_1, \mathbf{k}_2, \mathbf{k}_3) \,, \tag{5.2}$$

where the angle brackets denote averaging over an ensemble of realisations,  $\delta_D$  is the Dirac delta function, and  $\mathbf{k}_{i...j} \equiv \mathbf{k}_i + \cdots + \mathbf{k}_j$ .

The PowerI4 (Sefusatti et al., 2016) code was used to estimate the galaxy density in a regular Cartesian grid of  $1024^3$  cells from the galaxy positions. From this field, one obtains the Fourier-space galaxy density  $\delta_{\rm g}({\bf q})$  sampled at the wavevectors  ${\bf q}$  whose components are integer multiples of the fundamental frequency  $k_{\rm F}=2\pi/L$ . The power-spectrum estimator is

$$\hat{P}_{g}(k) = \frac{1}{L^{3} N_{P}} \sum_{\mathbf{q} \in k} |\delta_{g}(\mathbf{q})|^{2}, \qquad (5.3)$$

where  $N_P$  is the number of  $\mathbf{q}$  vectors lying in a bin centered at k and of width  $\Delta k$ . The sum is carried out over all discrete  $\mathbf{q}$  vectors satisfying the condition  $k - \Delta k/2 \le q < k + \Delta k/2$ , which is denoted as  $\mathbf{q} \in k$ . Similarly, the bispectrum estimator is

$$\hat{B}(k_1, k_2, k_3) = \frac{1}{L^3 N_B} \sum_{\mathbf{q}_1 \in k_1} \sum_{\mathbf{q}_2 \in k_2} \sum_{\mathbf{q}_3 \in k_3} \delta_K(\mathbf{q}_{123}) \ \delta_g(\mathbf{q}_1) \ \delta_g(\mathbf{q}_2) \ \delta_g(\mathbf{q}_3) \ , \tag{5.4}$$

where  $\delta_K(\mathbf{q}_{123})$  is a Kronecker symbol equal to one when  $\mathbf{q}_1$ ,  $\mathbf{q}_2$  and  $\mathbf{q}_3$  satisfy the triangle condition  $\mathbf{q}_{123} = 0$  (vanishing otherwise) and  $N_B$  is the number of  $\{\mathbf{q}_1, \mathbf{q}_2, \mathbf{q}_3\}$  triangles located in the 'triangle

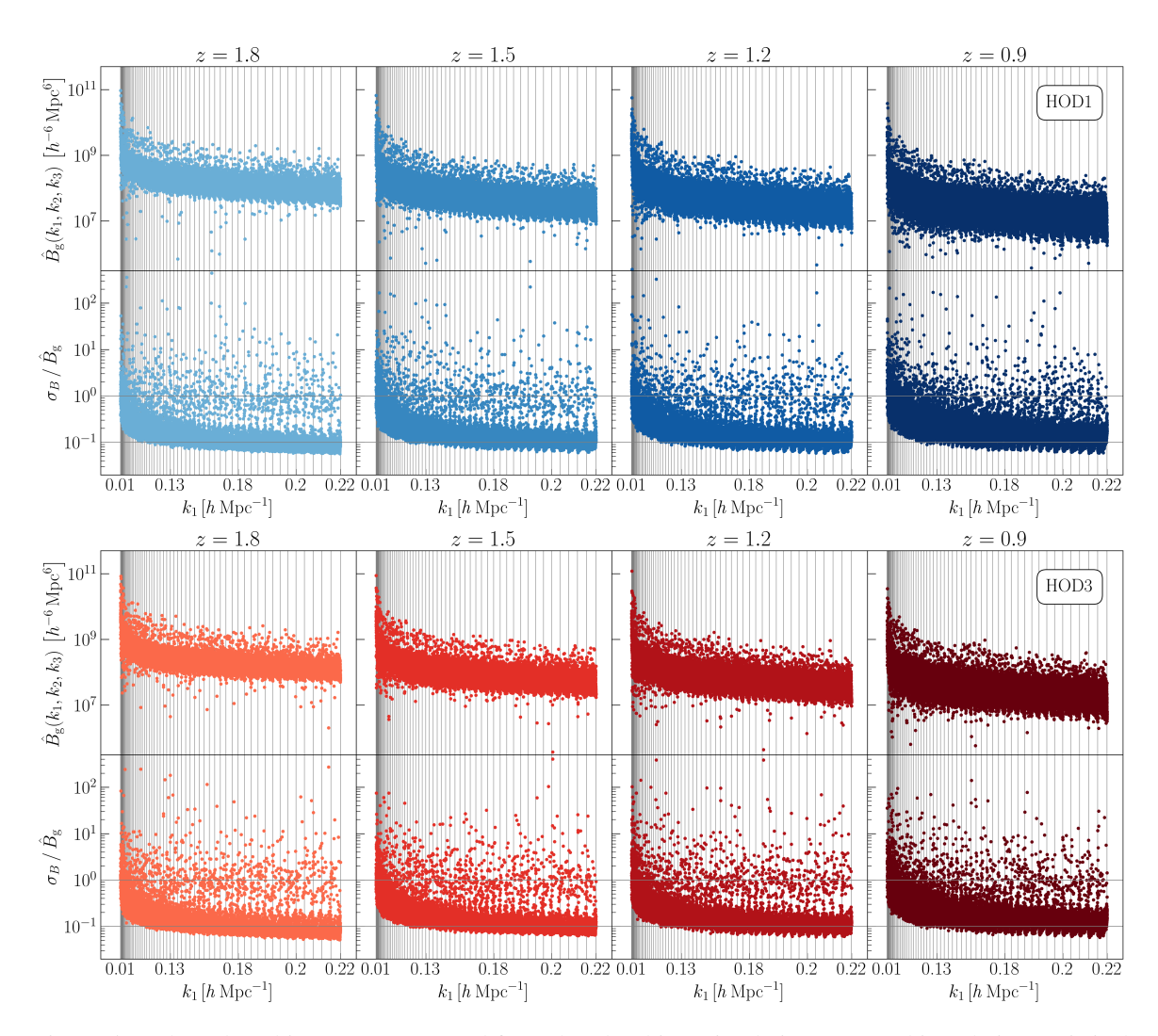


Figure 5.3: The galaxy bispectrum extracted from the Flagship 1 simulation (top) and its relative statistical uncertainty (bottom). Results are plotted by ordering the triangular configurations according to condition  $k_1 \ge k_2 \ge k_3$ . In between the two consecutive vertical lines all dots correspond to triangle bins with the same longest side  $k_1$ , whereas  $k_2$  and  $k_3$  take all allowed values.

bin' defined by the sides  $k_1 \ge k_2 \ge k_3$ . For this work, we adopt wavenumber bins of width  $\Delta k = 2 k_F$ , which in the case of Flagship 1 simulation approximately equals to 0.003  $h \, \text{Mpc}^{-1}$ .

Since we only have a single realization of the simulation and consider relatively large scales, we approximate the covariance matrices associated with the power spectrum and bispectrum measurements with their Gaussian contribution, which is limited to the diagonal component, that is the variance. In the power spectrum case this is (Feldman et al., 1994; Meiksin and White, 1999)

$$\sigma_P^2(k) = \frac{2}{N_P} \overline{P_g^2(k)} ,$$
 (5.5)

where overline indicates the average over the bin defined by the wavenumber k of the power spectrum  $P_{\rm g}(q)$ , evaluated at the discrete values of  $q \equiv |{\bf q}|$ . To compute this expression we use the theoretical  $P_{\rm g}$  obtained after the first iteration of the fitting procedure to the Flagship measurements.

Similarly, the Gaussian contribution for the bispectrum is given by (see e.g. Scoccimarro et al., 1998; Chan and Blot, 2017)

$$\sigma_B^2(k_1, k_2, k_3) = \frac{6L^3}{N_B} \overline{P_g(k_1) P_g(k_2) P_g(k_3)} . \tag{5.6}$$

Here overline indicates the average over the triangle bin defined by the sides  $k_1$ ,  $k_2$  and  $k_3$  of the three power spectra evaluated at the discrete values  $q_1$ ,  $q_2$  and  $q_3$ .

The top panel of Fig. 5.2 shows the measurements of the galaxy power spectrum for the different snapshots of the Flagship 1 simulation at redshift z = 0.9, 1.2, 1.5 and 1.8. The bottom panel shows the relative standard deviation, which is below the percent level for  $k > 0.05 \ h \, \text{Mpc}^{-1}$ . Note that, opposite to the evolution of matter power spectrum, the amplitude of the galaxy power spectrum is higher as you increase the redshift. This is caused by the presence of a larger galaxy bias at higher redshift.

Fig. 5.3 shows the measured bispectrum  $\hat{B}$  (top panels) and its relative statistical error (bottom panels) for all the considered redshifts. We account for all bins  $\{k_1, k_2, k_3\}$  that include a closed triangle  $\{\mathbf{q}_1, \mathbf{q}_2, \mathbf{q}_3\}$  with the constraint  $k_1 \leq k_2 \leq k_3$  to avoid double counting and ordered for increasing values of the wavenumbers. On average the relative errors range between several percent and 100 depending on the triangle configuration.

#### 5.4 Theoretical model

The theoretical model we use for the galaxy power spectrum depends on the assumed model for the matter power spectrum for which we adopt the one-loop expression in Standard Perturbation Theory (SPT, see Bernardeau et al., 2002, for a review) with a counterterm accounting for the impact of the short-scale perturbations as described in the Effective Field Theory of Large Scale Structure (EFTofLSS, Baumann et al., 2012; Carrasco et al., 2012). As we discussed in the Sect. 2.4 the general perturbative expansion of the galaxy density field  $\delta_g$  is based on the sum of all the individual operators that are a function of properties of the environment in which galaxies reside, such as the matter density field and the large-scale tidal field. Specifically, the sum includes all those operators that source by the gravity and velocity potentials,  $\Phi$  and  $\Phi_{\nu}$  (see Desjacques et al., 2018, for a review).

The bias expansion for the galaxy overdensity  $\delta_g(\mathbf{x})$  up to third order is given by

$$\delta_{\mathbf{g}}(\mathbf{x}) = b_1 \,\delta(\mathbf{x}) + \frac{b_2}{2} \delta^2(\mathbf{x}) + b_{\mathcal{G}_2} \mathcal{G}_2(\Phi \mid \mathbf{x}) + b_{\Gamma_3} \Gamma_3(\mathbf{x}) + b_{\nabla^2 \delta} \nabla^2 \delta(\mathbf{x}) + \epsilon(\mathbf{x}) , \qquad (5.7)$$

where  $\delta$  is the matter overdensity,  $\mathcal{G}_2$  and  $\Gamma_3$  are relevant non-local operators. Each operator is multiplied by a bias parameter that determines its amplitude. From the equation (5.7) one can identify the following terms:

- 1. At leading order the relationship between  $\delta_g$  and  $\delta$  is linear and local, and it is characterised by a linear bias parameter  $b_1$ .
- 2. Higher order contributions appear as we move to mildly non-linear scales, starting with a term proportional to  $\delta^2$ , characterised by a quadratic local bias  $b_2$ . During a spherically-symmetric gravitational collapse terms with higher powers of  $\delta$  become more important and it is expected for such terms to appear on progressively smaller scales.
- 3. Even if at the time of formation the relation between the matter and galaxy density fields is local, non-linear evolution generates the tidal fields. At leading order, the correction to the bias expansion due to the tidal stress tensor is given by a non-local quadratic bias,  $b_{\mathcal{G}_2}$ , and by the so-called second-order Galileon operator,  $\mathcal{G}_2$ , defined as

$$\mathcal{G}_2(\Phi \mid \mathbf{x}) = \left[\partial_i \partial_j \Phi(\mathbf{x})\right]^2 - \left[\nabla^2 \Phi(\mathbf{x})\right]^2 . \tag{5.8}$$

The contribution due to the next-to-leading order correction to the tidal field is represented by an additional non-local cubic bias,  $b_{\Gamma_2}$ , and by the operator

$$\Gamma_3(\mathbf{x}) = \mathcal{G}_2(\Phi \mid \mathbf{x}) - \mathcal{G}_2(\Phi_v \mid \mathbf{x}). \tag{5.9}$$

- 4. The impact of short-range non-local effects in the galaxy formation process is marked by the existence of higher derivatives of the gravitational potential. At leading order, the only non-zero term is proportional to the Laplacian of the matter density field,  $\nabla^2 \delta$ , and its amplitude is controlled by a bias parameter  $b_{\nabla^2 \delta}$ .
- 5. The influence of small-scale fluctuations on the galaxy density field at large separations is governed by an additional stochastic field, denoted as  $\epsilon$ . Under the assumption of Gaussian initial conditions, this field is entirely uncorrelated with large-scale perturbations. In the case of randomly distributed galaxies, the contribution to the galaxy power spectrum arising from this stochasticity takes the familiar form of the Poisson shot noise, expressed as  $1/\bar{n}$ , where  $\bar{n}$  represents the mean number density of the selected sample

Using the above bias expansion one can write the galaxy power spectrum in real space as the sum of the SPT model plus the matter power spectrum counterterm  $P_{\rm ct}(k)$ , correction from higher-derivative bias  $P_{\rm h.d.}(k)$ , and term describing the stochastic contributions  $P_{\epsilon}(k)$ 

$$P_{\rm g}(k) = P_{\rm SPT}(k) + P_{\rm ct}(k) + P_{\rm h.d.}(k) + P_{\epsilon}(k)$$
 (5.10)

The SPT expression  $P_{SPT}(k)$  is given by

$$P_{\text{SPT}}(k) = b_1^2 P_{\text{L}}(k) + P_{1-\text{loop}}(k)$$
, (5.11)

where

$$P_{1-\text{loop}}(k) = 2 \int d^3 \mathbf{q} \left[ K_2(\mathbf{q}, \mathbf{k} - \mathbf{q}) \right]^2 P_L(q) P_L(|\mathbf{k} - \mathbf{q}|) + 6 b_1 P_L(k) \int d^3 \mathbf{q} K_3(\mathbf{k}, \mathbf{q}, -\mathbf{q}) P_L(q)$$
(5.12)

and  $P_L(k)$  is the linear matter power spectrum and  $K_n$  kernels are defined as

$$K_2(\mathbf{k}_1, \mathbf{k}_2) = b_1 F_2(\mathbf{k}_1, \mathbf{k}_2) + \frac{b_2}{2} + b_{\mathcal{G}_2} S(\mathbf{k}_1, \mathbf{k}_2) ,$$
 (5.13)

$$K_{3}(\mathbf{k}_{1}, \mathbf{k}_{2}, \mathbf{k}_{3}) = b_{1} F_{3}(\mathbf{k}_{1}, \mathbf{k}_{2}, \mathbf{k}_{3}) + \frac{b_{2}}{3} [F_{2}(\mathbf{k}_{1}, \mathbf{k}_{2}) + \text{cyc.}] - \frac{4}{21} b_{\Gamma_{3}} [S(\mathbf{k}_{1}, \mathbf{k}_{23}) S(\mathbf{k}_{2}, \mathbf{k}_{3}) + \text{cyc.}] + \frac{2}{3} b_{\mathcal{G}_{2}} [S(\mathbf{k}_{1}, \mathbf{k}_{23}) F_{2}(\mathbf{k}_{2}, \mathbf{k}_{3}) + \text{cyc.}].$$
(5.14)

Here  $F_n$  are the usual matter SPT kernels in the Einstein-de Sitter approximation and

$$S(\mathbf{k}_1, \mathbf{k}_2) = \frac{(\mathbf{k}_1 \cdot \mathbf{k}_2)^2}{k_1^2 k_2^2} - 1.$$
 (5.15)

The higher-derivative corrections lead to the following term for the galaxy power spectrum:

$$P_{\rm h,d}(k) = -2b_1 b_{\nabla^2 s} k^2 P_{\rm L}(k) . \tag{5.16}$$

This has the similar scale dependence as EFTofLSS counterterm

$$P_{\rm ct}(k) = -2b_1^2 c_s^2 k^2 P_{\rm L}(k) , \qquad (5.17)$$

where  $c_s^2$  is the effective sound speed of the matter fluid. Unless we provide extra information on the above model parameters, the EFT counterterm and higher-derivative correction are degenerate. In this case, we can define the combination

$$c_0 := b_1^2 c_s^2 + b_1 b_{\nabla^2 \delta} , \qquad (5.18)$$

which reduces the dimension of the parameter space. Finally, the stochastic contribution is given by

$$P_{\epsilon}(k) = \frac{1}{\bar{n}} \left( 1 + \alpha_P + \epsilon_{k^2} k^2 \right) \tag{5.19}$$

which introduces two free parameters  $\alpha_P$  and  $\epsilon_{k^2}$  that describe constant and scale-dependent corrections to the Poissonian shot noise  $\bar{n}^{-1}$ .

We also account for the fact that large-scale bulk flows damp and broaden the BAO feature imprinted on  $P_{\rm L}$  during early epochs. This is done by implementing the so-called infrared (IR) resummation procedure. We follow the strategy delineated in Baldauf et al. (2015b) and further developed in

Blas et al. (2016) and Ivanov and Sibiryakov (2018). The starting point to this is to split the linear power spectrum into a smooth (no-wiggle) part  $P_{\rm nw}(k)$ , capturing the broadband shape of the power spectrum, and an oscillating (wiggly) part  $P_{\rm w}(k)$ , describing the BAO,

$$P_{\rm L}(k) = P_{\rm nw}(k) + P_{\rm w}(k) . {(5.20)}$$

In order to obtain this decomposition, we use one-dimensional Gaussian smoothing described in Vlah et al. (2016, appendix A) and Osato et al. (2019). The leading-order matter power spectrum reads then

$$P_{\rm m}^{\rm LO}(k) = \left[ P_{\rm nw}(k) + e^{-k^2 \Sigma^2} P_{\rm w}(k) \right] ,$$
 (5.21)

and the corresponding leading-order galaxy power spectrum (without the stochastic term) is  $P_{\rm g}^{\rm LO} = b_1^2 P_{\rm m}^{\rm LO}$ . In equation (5.21) the factor  ${\rm e}^{-k^2 \Sigma^2}$  accounts for suppression of the wiggle feature. Here  $\Sigma$  is defined as

$$\Sigma^{2} = \frac{1}{6\pi^{2}} \int_{0}^{k_{S}} dq \ P_{\text{nw}} \left[ 1 - j_{0}(q/k_{\text{osc}}) + 2 j_{2}(q/k_{\text{osc}}) \right] , \tag{5.22}$$

where  $j_n$  is the n-th order spherical Bessel function,  $k_{\rm osc}$  is the wavenumber corresponding to the BAO scale 110  $h^{-1}$  Mpc and  $k_{\rm S}$  is an arbitrary cut-off scale that separates short and long modes. According to Ivanov and Sibiryakov (2018) it can be shown that  $\Sigma^2$  is weakly dependent on the choice of  $k_{\rm S}$  and approaches asymptotic value for  $k_{\rm S}\approx 0.2~h\,{\rm Mpc}^{-1}$ , which we assume in equation (5.22). Finally, in all loop corrections coming from equation (5.11), we replace the  $P_{\rm L}$  with equation (5.21) to obtain the IR-resummed loop corrections  $P_{\rm I-loop}^{\rm IR}(k)$ . Therefore this leads to the IR-resummed next-to-leading-order galaxy power spectrum

$$P_{\rm g}^{\rm NLO}(k) = b_1^2 \left[ P_{\rm nw}(k) + e^{-k^2 \Sigma^2} \left( 1 + k^2 \Sigma^2 \right) P_{\rm w}(k) \right] + P_{\rm 1-loop}^{\rm IR}(k) - 2 c_0 k^2 P_{\rm m}^{\rm LO}(k) + P_{\epsilon}(k) . \tag{5.23}$$

The tree-level galaxy bispectrum in real space can be written as the sum of the SPT model  $B_{\text{SPT}}(\mathbf{k}_1, \mathbf{k}_2, \mathbf{k}_3)$  plus the stochastic term  $B_{\epsilon}(\mathbf{k}_1, \mathbf{k}_2, \mathbf{k}_3)$ . Therefore,

$$B_{\sigma}(\mathbf{k}_{1}, \mathbf{k}_{2}, \mathbf{k}_{3}) = B_{SPT}(\mathbf{k}_{1}, \mathbf{k}_{2}, \mathbf{k}_{3}) + B_{\epsilon}(\mathbf{k}_{1}, \mathbf{k}_{2}, \mathbf{k}_{3}), \qquad (5.24)$$

where

$$B_{\text{SPT}}(\mathbf{k}_1, \mathbf{k}_2, \mathbf{k}_3) = 2 b_1^2 K_2(\mathbf{k}_1, \mathbf{k}_2) P_{\text{I}}(k_1) P_{\text{I}}(k_2) + \text{cyc.}$$
 (5.25)

and

$$B_{\epsilon}(\mathbf{k}_{1}, \mathbf{k}_{2}, \mathbf{k}_{3}) = \frac{1 + \alpha_{1}}{\bar{n}} b_{1}^{2} \left[ P_{L}(k_{1}) + P_{L}(k_{2}) + P_{L}(k_{3}) \right] + \frac{1 + \alpha_{2}}{\bar{n}^{2}} .$$

The parameters  $\alpha_1$  and  $\alpha_2$  represent the corrections to the Poisson shot noise.

Like the case with the power spectrum, IR-resummation here is done by replacing the instances of the linear matter power spectrum  $P_{\rm L}$  with its IR-resummed variant, the leading-order power spectrum  $P_{\rm m}^{\rm LO}$ .

## 5.5 Bias relations

In order to reduce the dimensionality of the parameter space and increase the constraining power of the summary statistics, it has become standard practice in real data analysis to fix some of parameters to physically motivated values. In our case, the relations between the bias coefficients can prove useful. These relations can also help to break the degeneracy between some parameters which makes the determination of cosmological parameters easier and yields tighter constraints on them.

In this work we test the following bias relations with joint fits of the power spectrum and bispectrum:

1. Since we are analysing synthetic data vectors obtained using a known HOD model, it is possible to derive a relation for the quadratic local bias  $b_2$ , from a combination of halo mass function n(M), the particular HOD model used to populate halos with galaxies, and the halo quadratic bias. For the latter, we have used the halo quadratic bias relation from Lazeyras et al. (2016). In this way, it follows that

$$b_2^{\text{sph}} := b_2 - \frac{4}{3}b_{\mathcal{G}_2} = \begin{cases} -0.484 - 0.822 \, b_1 + 0.444 \, b_1^2 + 0.08 \, b_1^3, & \text{HOD1} \\ -0.015 - 1.58 \, b_1 + 0.809 \, b_1^2 + 0.025 \, b_1^3, & \text{HOD3} \end{cases}; \tag{5.26}$$

Since this relation is based on the particular numbers defining the HOD of our synthetic galaxy samples, its applicability to real observations is limited. However, this relation can still be used as a way to determine the consistency among the parameters of the standard one-loop bias expansion.

2. The influence of nonlinear gravitational evolution in generating a large-scale tidal field is a well-established phenomenon, even when starting from an initial local relationship  $\delta_g(\delta)$  (Fry, 1996; Chan et al., 2012). This implies that even if we initially express the density field of galaxies assuming a purely spherically symmetric gravitational collapse, which involves only local bias parameters denoted as  $b_n \neq 0$ , tidal contributions emerge at subsequent times due to gravitational evolution. As a result, this leads to the presence of non-negligible tidal biases. Assuming that the total number of objects is conserved in time, it is possible to find a relationship between the late-time non-local parameters and lower order bias parameters, such that:

$$b_{\mathcal{G}_2} = -\frac{2}{7} (b_1 - 1) + b_{\mathcal{G}_2, \mathcal{L}}, \qquad (5.27)$$

$$b_{\Gamma_3} = -\frac{1}{6}(b_1 - 1) - \frac{5}{2}b_{\mathcal{G}_2} + b_{\Gamma_3, \mathcal{L}}, \qquad (5.28)$$

where the bias parameters with a subscript  $\mathcal{L}$  stand for the corresponding Lagrangian quantities, i.e., at the time of formation. The previous relations are commonly referred to as *coevolution*, or *local Lagrangian* relations when setting to zero the Lagrangian bias, and have been extensively used in most real data analyses to fix one or both non-local parameters (see e.g. Feldman et al., 2001; Gil-Marín et al., 2015; Sánchez et al., 2016; Grieb et al., 2017).

3. An alternative method for determining  $b_{\mathcal{G}_2}$ , which has demonstrated greater accuracy when compared to results obtained from *N*-body simulations and is derived using the excursion set

Parameter	Uniform prior ranges
$b_1$	[0.25, 4.00]
$b_2$	[-10, 10]
$b_{\mathcal{G}_2}$	[-5, 5]
$b_{\Gamma_3}$	[-8,8]
$c_0 \left[ h^{-2} \mathrm{Mpc}^2 \right]$	[-500, 500]
$\alpha_P$	[-1,2]
$\epsilon_{k^2} \left[ h^{-2} \mathrm{Mpc}^2 \right]$	[-500, 500]
$\alpha_1$	[-1,2]
$lpha_2$	[-1,2]
$\omega_{\rm c} := \Omega_{\rm c} h^2$	[0.08, 0.18]
h	[0.5, 1.0]
$A_s/A_s^{\mathrm{fid}}$	[0.5, 1.5]

Table 5.3: The list of model parameters and assumed uniform prior ranges.

formalism<sup>3</sup>, has been proposed by Sheth et al. (2013). In this approach,  $b_{\mathcal{G}_2}$  can be expressed as a quadratic expression involving the linear bias term  $b_1$ , leading to the following relationship

$$b_{\mathcal{G}_2} = 0.524 - 0.547 \, b_1 + 0.046 \, b_1^2 \,. \tag{5.29}$$

In Fig. 5.4 we plot the above relations alongside the marginalised posterior distribution contours obtained by fitting the theoretical model from Sect. 5.4 with cosmological parameters fixed to its actual values.

### 5.6 Likelihood function

We make the simplest and most commonly used assumption to treat the data as generated by an unbiased estimator with Gaussian measurement errors. Therefore, the likelihood function  $\mathcal{L}$  in logarithmic space can be written as

$$\ln \mathcal{L}(\boldsymbol{\theta} \mid \mathbf{X}) = -\frac{1}{2} (\mathbf{M}(\boldsymbol{\theta}) - \mathbf{X})^{\mathrm{T}} \mathbf{C}^{-1} (\mathbf{M}(\boldsymbol{\theta}) - \mathbf{X}) + \text{const} = -\frac{\chi^{2}}{2} + \text{const}, \qquad (5.30)$$

where  $\mathbf{M}(\boldsymbol{\theta})$  is the theoretical model, which is the function of a set of model parameters  $\boldsymbol{\theta}$ , and explains the measured data  $\mathbf{X}$  with the corresponding covariance matrix  $\mathbf{C}$ .

<sup>&</sup>lt;sup>3</sup> The excursion set method is a cosmological framework used to model the formation of large-scale structures like galaxies and dark matter halos. It involves smoothing initial density perturbations, tracking their evolution via a random walk, and determining when regions exceed a critical threshold for collapse, forming bound structures. This method, often linked to the Press-Schechter formalism, helps predict the distribution of dark matter halos and is integral to understanding cosmic structure formation and evolution. Extensions include ellipsoidal collapse and merger trees for tracking halo growth.

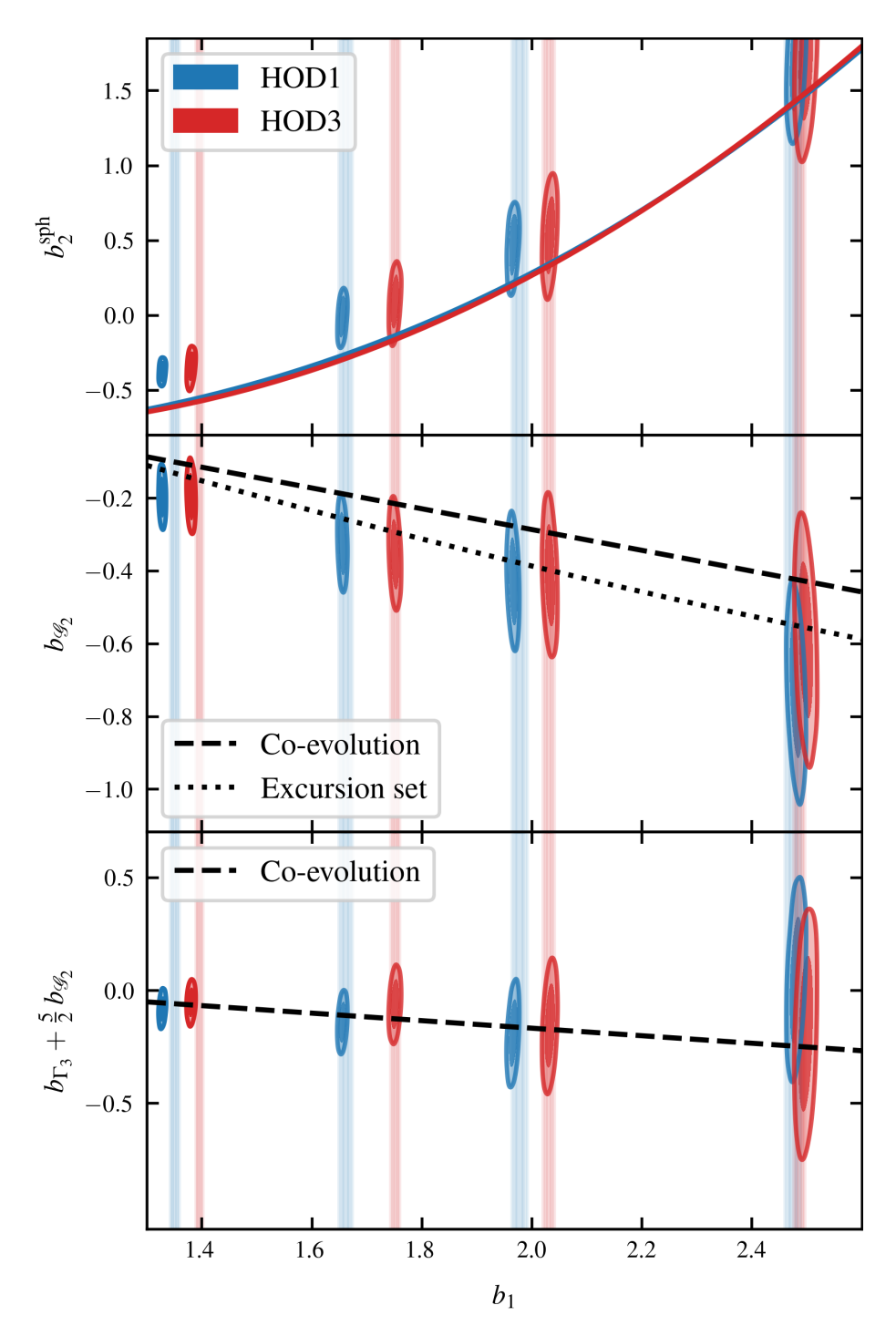


Figure 5.4: The bias relations described in Sect. 5.5. Here blue and red contours depict marginalised posterior contours obtained from fitting to HOD1 and HOD3 Flagship simulation mock galaxy catalogues. The same-coloured bands mark the  $1\,\sigma$  and  $2\,\sigma$  errors of the fiducial  $b_1$  obtained by fitting the linear spectrum to the large-scale limit of the measured power spectrum from these catalogues.

In this work, we perform the joint fit of the galaxy power spectrum and the bispectrum. Therefore,  $\mathbf{X} = \{\hat{P}_g, \hat{B}_g\}$  and  $\mathbf{M}(\boldsymbol{\theta})$  is the corresponding theoretical model described in Sect. 5.4. As we discussed in Sect. 5.3 the covariance matrix  $\mathbf{C}$  we consider contains only the leading-order Gaussian contributions, which have only the diagonal components described by the equations (5.5) and (5.6).

We perform two types of analysis. In the first, we fix the cosmological parameters to the values used in the Flagship 1 simulation listed in Table 5.1. This allows us to test whether the models are able to constrain the fiducial bias coefficients obtained from Flagship simulation HOD and what is the range of validity of these models. Fixing the cosmology helps to improve the precision and accuracy of the bias coefficients since they are degenerate with the cosmological parameters, particularly  $A_s$ . When the cosmological parameters are fixed, the set of 9 parameters of the model is  $\{b_1, b_2, b_{\mathcal{G}_2}, b_{\Gamma_3}, c_0, \alpha_P, \epsilon_{k^2}, \alpha_1, \alpha_2\}$ . We refer to this model as "maximal model", since some of them can be set to zero or fixed using the bias relations. The priors on these parameters are assumed to be uniform and are given in Table 5.3. In the second type of analysis, we also vary three cosmological parameters h,  $A_s$ , and  $\omega_c$  to see if the models are able to constrain their fiducial values in an unbiased way. Introducing these parameters can complicate the sampling of the posterior with the MCMC due to the strong degeneracy between the bias parameters and  $A_s$ . Therefore, we choose to sample the combinations of the two. Instead of sampling  $A_s$  directly we sample the ratio  $A \equiv A_s/A_s^{\rm fid}$  and the following redefined bias parameters:

$$\bar{b}_1 = A^{1/2} b_1, \quad \bar{b}_2 = A b_2, \quad \bar{b}_{\mathcal{G}_2} = A b_{\mathcal{G}_2}, \quad \bar{b}_{\Gamma_3} = A^{3/2} b_{\Gamma_3},$$
 (5.31)

adopting the same uniform priors. This is a consequence of the fact that the n-th order bias operators in the equation (5.7) scale proportionally to  $A^{n/2}$ . We keep the spectral index  $n_s$  and the baryon content  $\Omega_b$  fixed, as these parameters are constrained well by CMB observations.

With fixed cosmological parameters, we evaluate the posterior distributions using the emcee (Foreman-Mackey et al., 2013) with the 25 walkers and the affine invariant "stretch move" method from Goodman and Weare (2010). The number of steps the chains are run is equal to  $\min(10^5, 100\tau)$ , where  $\tau$  is the integrated autocorrelation time. To compute the power spectrum and bispectrum models, at each step we require the linear power spectrum, which is generated from Boltzmann solver CAMB (Lewis et al., 2000b). The loop corrections to the power spectrum are computed from the custom implementation of the FAST-PT code (McEwen et al., 2016). When we vary the cosmological parameters, we use the nested sampler code MultiNest (Feroz et al., 2019). We change the sampler due to longer running times when varying the cosmological parameters. To speed up the sampling even more we use the COMET (Eggemeier et al., 2022), which can emulate the one-loop level galaxy power spectrum and the tree-level bispectrum in the order of milliseconds.

#### 5.7 Results

In this section, the results of our analysis are presented. We first assess the accuracy of the PT-based theoretical model for P+B by carrying out the fits at fixed cosmology. In this way, we can focus on modelling the one-loop galaxy bias, test up to which  $k_{\rm max}$  the reference model can still provide a good fit to the data, and compare the performance of the bias relations listed in the Sect. 5.5. Next we repeat the same by also varying the cosmological parameters h,  $\omega_{\rm c}$  and  $A_{\rm s}$ .

Table 5.4: Marginalised mean values of the linear bias  $b_1$  and the shot-noise parameter  $\alpha_P$  measured using the large-scale limit of the ratio  $P_{\rm g}/P_{\rm m}$  presented in equation (5.32).

z	HOD	$b_1$	$\alpha_P$
	Model		$\left[ ar{n}^{-1} ight]$
0.9	1	$1.350 \pm 0.004$	$0.220 \pm 0.220$
	3	$1.395 \pm 0.003$	$0.253 \pm 0.079$
1.2	1	$1.661 \pm 0.006$	$0.424 \pm 0.152$
	3	$1.751 \pm 0.004$	$0.289 \pm 0.057$
1.5	1	$1.977 \pm 0.007$	$0.386 \pm 0.104$
	3	$2.030 \pm 0.005$	$0.219 \pm 0.032$
1.8	1	$2.474 \pm 0.007$	$0.257 \pm 0.039$
	3	$2.486 \pm 0.005$	$0.346 \pm 0.018$

#### 5.7.1 The fiducial linear bias

The validation of the model with fixed cosmology is carried out against the fiducial values of the linear bias  $b_1$ , which is determined by making use of the large-scale limit of the measured galaxy and matter power spectrum. In this regime, we can assume the data is described by the linear power spectrum and use the simple two-parameter model defined as

$$P_{\rm g}(k) = b_1^2 P_{\rm m}(k) + \frac{1 + \alpha_P}{\bar{n}}$$
 (5.32)

The latter is used to fit the data on scales  $k_{\rm max} < 0.08~h\,{\rm Mpc}^{-1}$ , which justifies the use of the linear approximation. The fitted values of  $b_1$  and  $\alpha_P$  are listed in the Table 5.4.

#### 5.7.2 Testing the model with fixed cosmology

We first perform a joint analysis of the power spectrum and bispectrum using the models described in Sect. 5.4 which have 12 free parameters listed in the Table 5.3. In this section, we consider the models with cosmological parameters fixed to their fiducial values.

We start by assessing the goodness-of-fit of the models by calculating the corresponding p-values using the posterior-averaged reduced  $\chi^2$  for each considered Flagship snapshot and various scale cuts imposed on the P and B statistics indicated by  $k_{\text{max}}^P$  and  $k_{\text{max}}^B$  from the hereafter. In Fig. 5.5 we plot these p-values in four separate panels corresponding to the Flagship snapshots at z=1.8, 1.5, 1.2, and 0.9. With white we indicate that p-value is less than 0.05, meaning that the model is rejected as a good fit to the data with a 95 per cent confidence level. According to this test, the goodness of fit is mostly determined by the  $k_{\text{max}}^B$  and is insensitive to the chosen  $k_{\text{max}}^P$ . This is expected since the bispectrum has many more data points than the power spectrum and therefore the computed  $\chi^2$  value is mostly determined by the former. Overall, one can say that the maximal P + B model with

<sup>&</sup>lt;sup>4</sup> A p-value, or probability value, is a number describing how likely it is that your data is a good fit to the model.

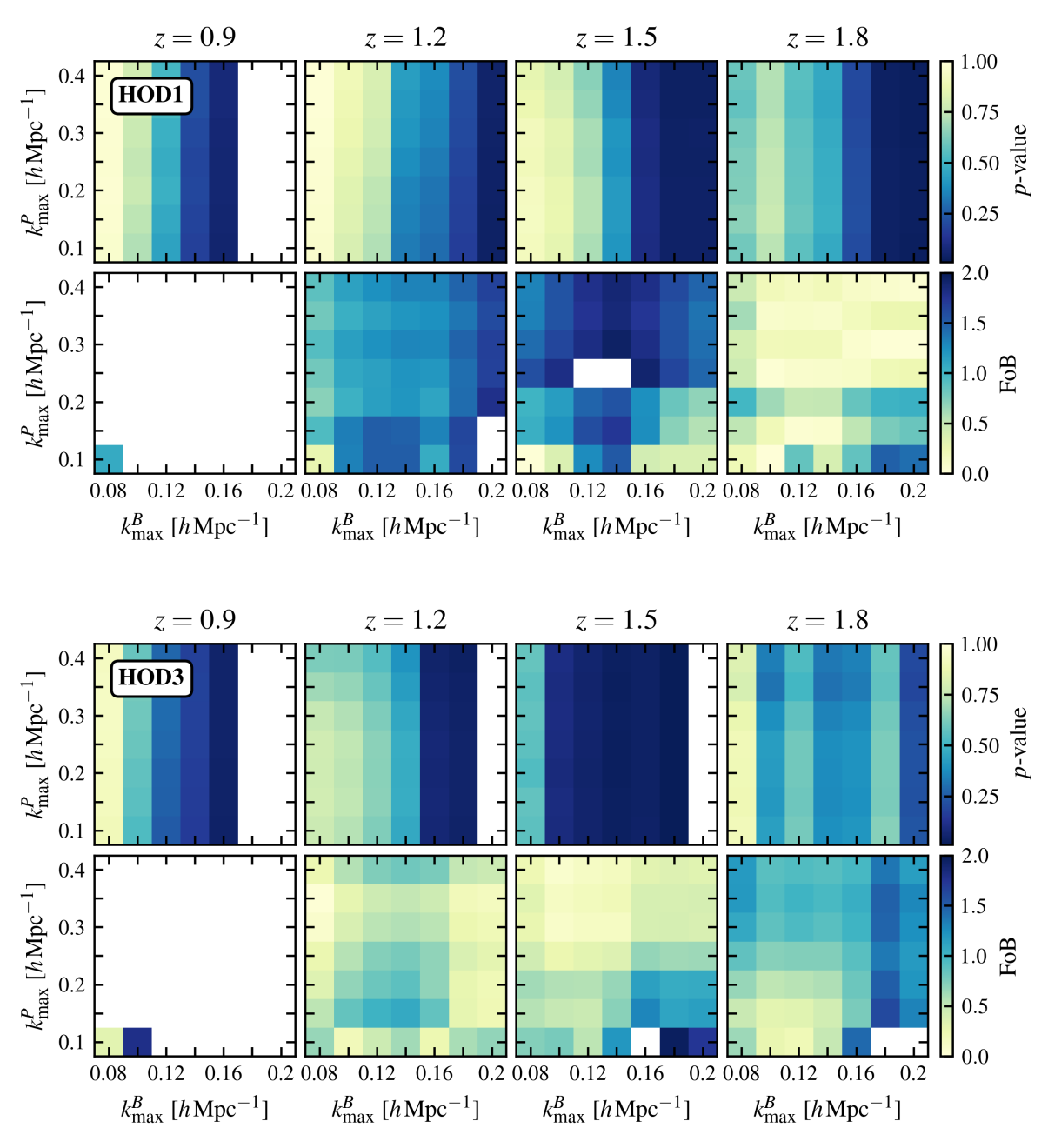


Figure 5.5: The goodness of fit test of galaxy P+B model (with fixed cosmology) against the Flagship simulation mock galaxy catalogues HOD1 and HOD3. Each panel indicates a different snapshot of the simulation and on the x and y-axis, we indicate the assumed scale cuts on the data vectors. The colours represent the corresponding p-values (top panels) and FoB with respect to parameter  $b_1$  (bottom panels). If the p-value is less than 0.05, the model is a bad fit to the data and we do not plot the corresponding p-value. Similarly, if the FoB is above 2  $\sigma$  critical level, we do not plot the corresponding value.

 $k_{\rm max}^P \le 0.4~h\,{\rm Mpc}^{-1}$  and  $k_{\rm max}^B \le 0.22~h\,{\rm Mpc}^{-1}$  provides a good fit to the Flagship simulation data for the redshift z=1.8 and below that one needs to restrict the bispectrum data up to  $0.16~h\,{\rm Mpc}^{-1}$  to maintain a good fit.

As a next step, in the same figure, we also quantify how close is the fitted linear bias parameter  $b_1$  to the fiducial one with respect to the statistical errors. This is done by computing the figure of bias (FoB) with respect to  $b_1$  as,

$$FoB = \sqrt{\sum_{ij} \Delta \theta_i \, \mathbf{S}_{ij}^{-1} \, \Delta \theta_j}, \qquad (5.33)$$

where  $\Delta\theta_i$  is the difference between the fitted and fiducial parameters and **S** is the covariance matrix of the considered parameters<sup>5</sup>. Therefore, FoB corresponds to the distance between true and estimated parameters normalised by their uncertainties. Since the fiducial parameter also has a certain variance we consider it by adding this variance to the diagonal part of **S**. We plot the obtained FoB values for different choices of scale cuts and redshifts. In the panels, the white colour indicates that FoB is above the value corresponding to  $2\sigma$  deviation between fiducial and fitted bias parameters. According to this analysis, there is no significant difference between the two for snapshots corresponding to redshifts above 0.9, whereas, for the latter case, one has to restrict the bispectrum data below  $k_{\text{max}}^B = 0.1 \ h \, \text{Mpc}^{-1}$  to be consistent with the analysis done using the Flagship HOD. This indicates the need to include the higher-order PT terms in the theoretical bispectrum to model the stronger non-linear clustering appearing at lower redshifts.

#### 5.7.3 Comparison between bias relations

We now discuss the performances of bias relations listed in Sect. 5.5. We take the maximal model with fixed cosmology and impose each of the relations to reduce the number of free parameters from nine to eight. Since we assume that bias coefficients are physical parameters rather than nuisance ones, any valid physical relation should not create a significant deviation compared to values recovered using the maximal model. In Figs. 5.6 and 5.7 for each considered catalogue we plot the fitted linear bias coefficients,  $b_1$ , with its marginalised 68 per cent credibility limits and compare them against the fiducial  $b_1$ . For these runs we vary the  $k_{\text{max}}^B$  and fix  $k_{\text{max}}^P$  to 0.15 k Mpc<sup>-1</sup>. At redshift  $k_{\text{max}}^B$  are 1.2 every model underestimates the fiducial  $k_{\text{max}}^B$  except when using the  $k_{\text{max}}^B$  and  $k_{\text{max}}^B$  to 0.15 k mpc<sup>-1</sup>. At redshift  $k_{\text{max}}^B$  relations. Particularly, in the case of  $k_{\text{max}}^B$  all models except one assuming the  $k_{\text{max}}^B$  relation from the equation (5.26) significantly underestimate  $k_{\text{max}}^B$ . This is expected since the  $k_{\text{max}}^B$  relation was obtained from fitting to the data points derived from the Flagship HOD. Overall one can say that for  $k_{\text{max}}^B$  to 0.15  $k_{\text{max}}^B$  relation tends to agree with the maximal model the most and does not induce the noticeable deviations among the recovered bias coefficients.

We further quantify the performance of the bias relations by computing the difference in Deviance Information Criterion (DIC) with respect to the maximal model with nine parameters, which we take as a reference. DIC is defined as

$$DIC = \langle D \rangle_{\text{post}} + p_V, \qquad (5.34)$$

where  $D = -2 \ln \mathcal{L}$  (deviance, which is averaged over the posterior) and  $p_V = 0.5 \text{Var}(D)$  (effective number of parameters that are constrained by the chain). The difference  $\Delta \text{DIC}$  below -5 indicates a

30th April 2025 12:58

<sup>&</sup>lt;sup>5</sup> In this particular case we are considering only one parameter,  $b_1$ , so the covariance matrix will just simply be the variance of  $b_1$ .

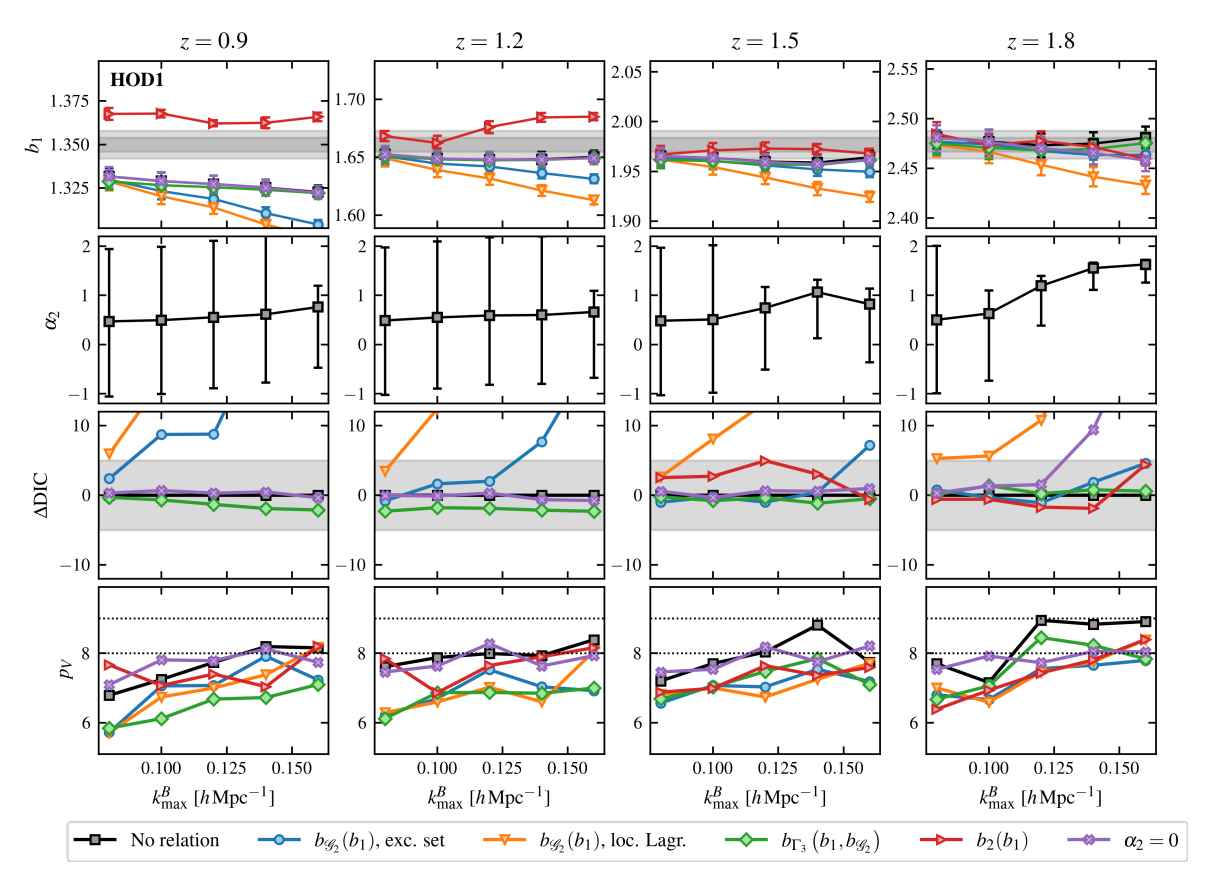


Figure 5.6: First row: comparison of bias parameter  $b_1$  obtained by fitting the galaxy P+B model (with fixed cosmology) assuming various bias relations, which are indicated using different colours and error bars depict the 68 percent credibility intervals. The grey bands mark the 1 and 2  $\sigma$  regions of the fiducial  $b_1$  obtained by fitting the linear spectrum to the large-scale limit of the measured power spectrum. Second row: the fitted values of the bispectrum Poisson shot noise correction  $\alpha_2$  and corresponding 68 percent credibility intervals when fitting the maximal model i.e. the model with only the cosmological parameters fixed. Third row: the difference in DIC with respect to the reference maximal model with nine parameters when assuming the various bias relations. The difference  $\Delta \text{DIC} < -5$  indicates a strong preference against the reference model. Fourth row: the effective number of parameters  $p_V$  that is constrained by the chain when imposing bias relations. The horizontal dotted lines indicate the actual number of parameters 9 and 8 with and without imposed bias relation, respectively. For reference, we also plot the model with  $\alpha = 0$  in violet.

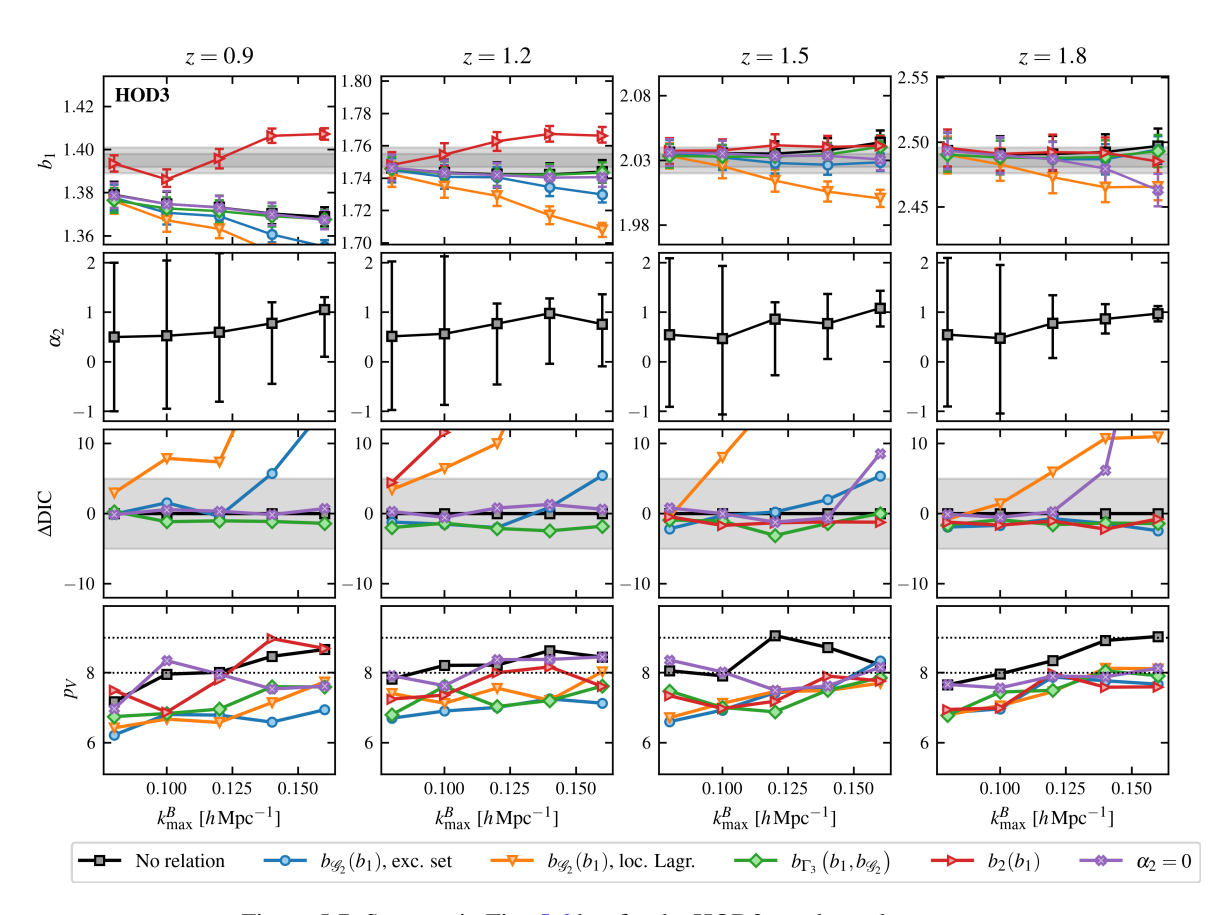


Figure 5.7: Same as in Fig. 5.6 but for the HOD3 mock catalogue case.

strong preference against the reference model. We plot this quantity alongside  $p_V$  for various redshifts and over a range of  $k_{\max}^B$  in Figs. 5.6 and 5.7. Looking at values of  $\Delta \text{DIC}$  only the co-evolution relation  $b_{\Gamma_3}(b_1)$  is favoured consistently over all the considered redshifts with respect to the reference model. The  $b_2(b_1)$  relation is only favoured for higher redshifts z=1.8 and 1.5, while at the later times, it is shown to be not consistent with the reference model. This is also evident from the fact that the recovered linear bias  $b_1$  between these two models differs significantly. The local Lagrangian bias relation  $b_{\mathcal{G}_2}(b_1)$  is strongly disfavoured compared to the reference model on the shorter scales. This was also confirmed from the bispectrum-only likelihood analysis performed in Oddo et al. (2020b). The values of  $p_V$  indicate that on large scales one parameter always remains unconstrained, which turns out to be  $\alpha_2$  as it is evident from the bottom panels. Its marginalised posterior distribution fills up the whole prior range between -1 and 2 for  $k_{\max}^B < 0.12$  h Mpc $^{-1}$ . When setting  $\alpha_2 = 0$  (cyan curves) the value of  $p_V$  is closer to the actual number of model parameters, indicating that the Markov chain can constrain all the model parameters.

#### 5.7.4 Testing model with varied cosmology

After investigating the performance of the joint fit of the galaxy power spectrum and bispectrum in real space at fixed cosmology, we investigate the possibility of these models to recover the cosmological parameters in an unbiased way. The theoretical model is described in Sect. 5.4 which depends on the 8

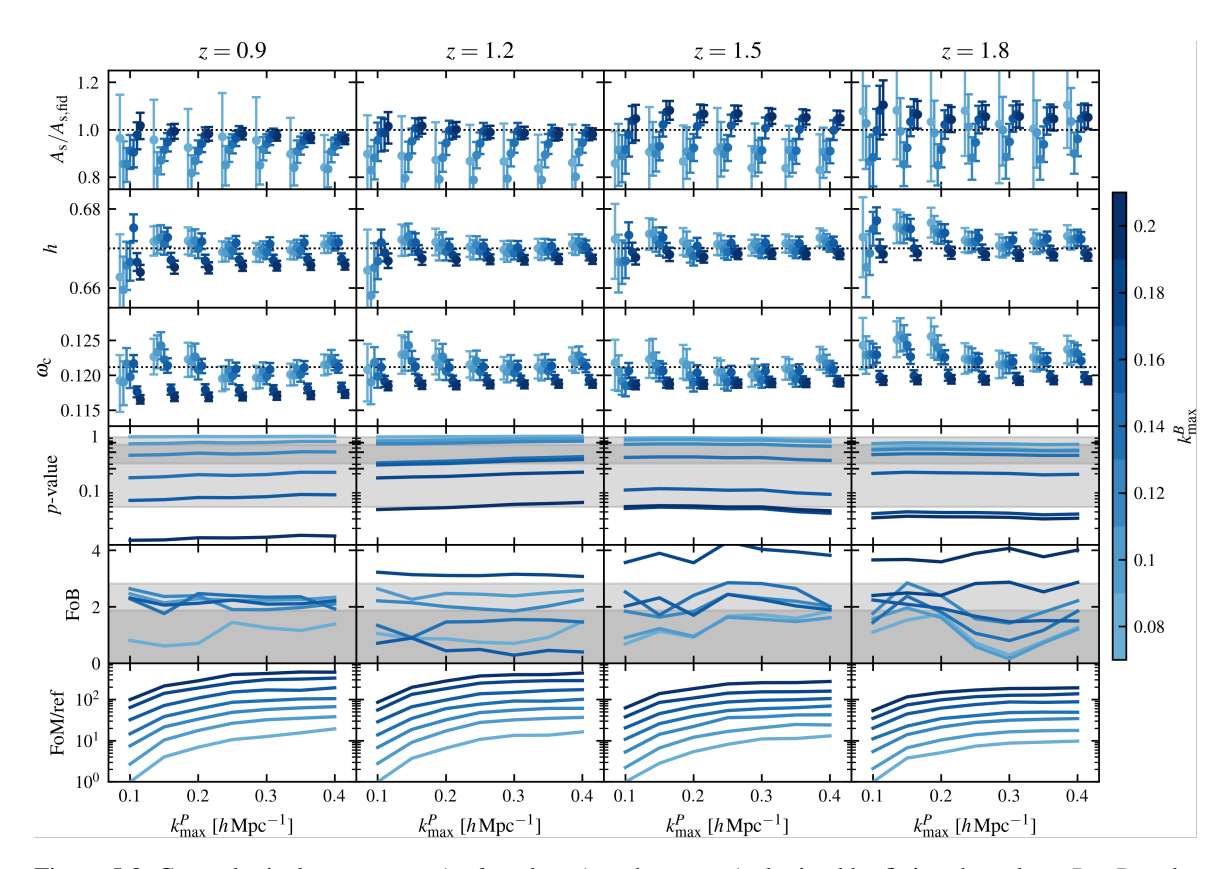


Figure 5.8: Cosmological parameters  $A_s$ , h and  $\omega_c$  (top three rows) obtained by fitting the galaxy P+B to the same statistics measured from the HOD1 snapshot as a function of the scale cut imposed on the power spectrum,  $k_{\max}^P$ . The performance metrics - goodness of fit (in terms of p-values), figure of bias, and figure of merit are plotted in the bottom three panels, respectively. The last two metrics were computed with respect to the parameters  $A_s$ , h, and  $\omega_c$ . The color gradient indicates the different scale cut on the bispectrum,  $k_{\max}^B$ . The grey band in the p-value indicates the critical value of 0.05 below which the model is rejected as a good fit to the data. The same bands in FoB panels represent the 68 and 95 percentiles of the corresponding distribution, indicating 1 and 2  $\sigma$  deviations of the fitted cosmological parameters from the actual their values. The FoM panels show the figure of merit normalized to the one computed at  $k_{\max}^P = 0.1 \ h \, \text{Mpc}^{-1}$  and  $k_{\max}^B = 0.08 \ h \, \text{Mpc}^{-1}$ .

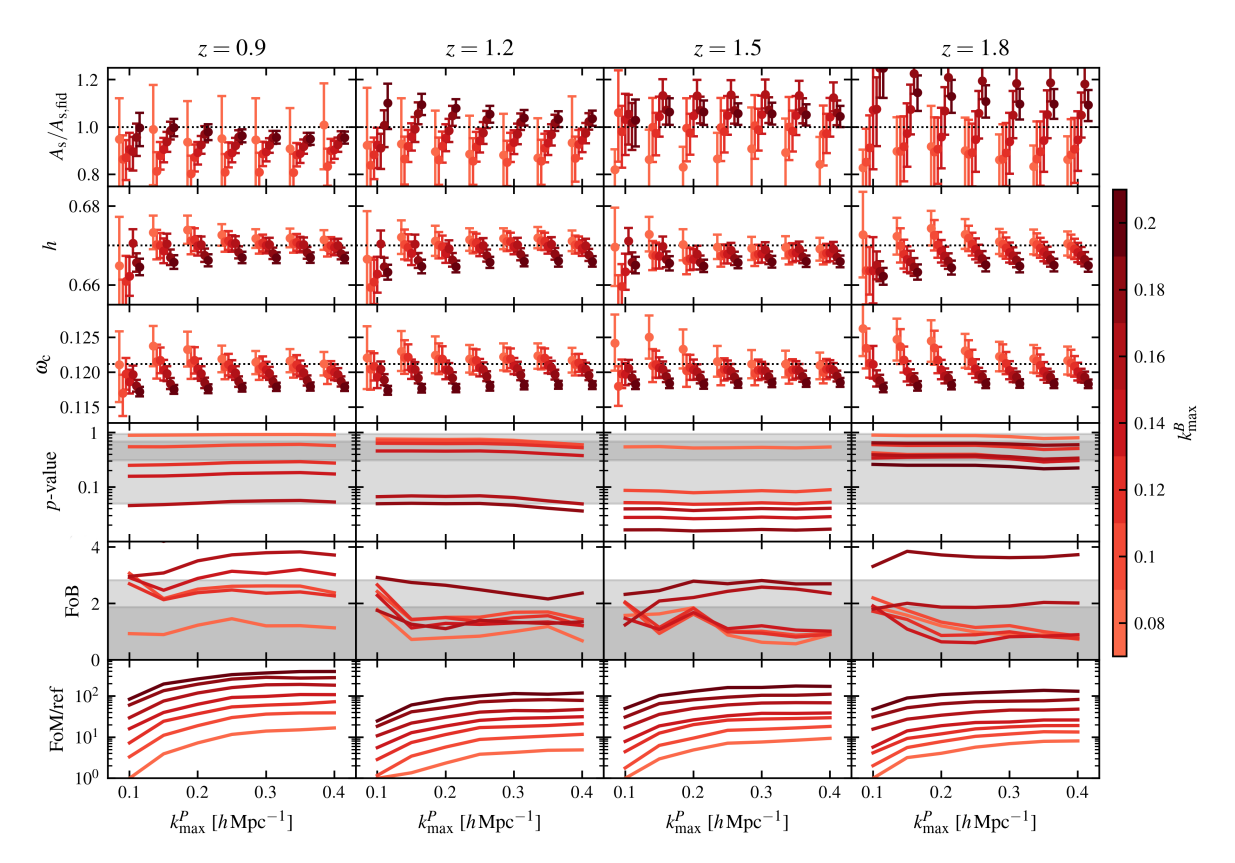


Figure 5.9: Same as in Fig. 5.8 but for the HOD3 catalogue.

bias and shot-noise parameters listed in Table 5.3 except setting  $\alpha_2 = 0$  since it remains unconstrained as we have discussed in Sect. 5.7.3. However, this time we also vary three cosmological parameters  $A_s$ ,  $\omega_c$ , and h within uniform prior ranges defined in Table 5.3 and others we fix to their fiducial values defined in Table 5.1. Notice that, in practice, we vary the combination of parameters defined by equations (5.31), but present the actual bias parameters when discussing the results. This is done to alleviate degeneracies present between the bias parameters and  $A_s$  in real space, which in turn speeds up the convergence of MCMC chains.

In Fig. 5.8 we show the fitted cosmological parameters with their marginalised 68 per cent credibility limits and corresponding metrics for goodness-of-fit, FoB, and figure of merit (FoM). The latter determines the statistical power in constraining the parameters and for a given set of model parameters  $\theta$  it is defined in the following way:

$$FoM = \frac{1}{\sqrt{\det[S(\theta)]}}.$$
 (5.35)

Here  $S(\theta)$ , as in the case of the FoB, is defined as the matrix containing the covariance of the model parameters, and det(S) is the determinant of S. The latter represents the hyper-volume contained in the hyper-surface defined by the covariance matrix S. Therefore, the high value of FoM corresponds to tighter constraints of the model parameters.

The FoB and FoM were obtained with respect to the three varied cosmological parameters. As

expected, the primordial scalar amplitude  $A_s$  remains the most problematic to obtain the unbiased fit for. The constraining power for this parameter is increased by including the short-scale information coming from the bispectrum, although, in some cases producing biased results due to strong  $A_s$  -  $b_1$  degeneracy in real space. In redshift space, the strong degeneracy can be broken since these two parameters have a distinct impact on multipoles of the power spectrum and bispectrum. The matter density parameter  $\omega_c$  remains biased on large scales, which is reduced by including the short-scale information on higher-order bias parameters. For example, including the short-scale information coming from the one-loop galaxy power spectrum helps to break the degeneracy between  $\omega_c$  and high-order bias parameters, which in turn improves the constraints on  $\omega_c$ . This feature is also reflected on the FoB, particularly, for redshifts 1.8 and 1.5 in Fig. 5.9. For these snapshots when  $k_{\text{max}}^P > 0.1 \, h \, \text{Mpc}^{-1}$  and  $k_{\text{max}}^B < 0.18 \, h \, \text{Mpc}^{-1}$  the values of FoB are reduced.

The goodness-of-fit metric p-value is consistent with what was observed with the fixed cosmology case. Namely, it weakly depends on the chosen  $k_{\text{max}}^P$  and one has to restrict  $k_{\text{max}}^B$  up to 0.12 h Mpc<sup>-1</sup> for all the considered snapshots to obtain a good fit.

The FoM increases monotonically with respect to the reference case of the fit assuming  $k_{\text{max}}^P = 0.1 \, h \, \text{Mpc}^{-1}$  and  $k_{\text{max}}^B = 0.08 \, h \, \text{Mpc}^{-1}$ . This increase is larger when moving towards lower redshifts and adding more nonlinear scales. However, it plateaus after  $k_{\text{max}}^P = 0.25 \, h \, \text{Mpc}^{-1}$  due to entering the shot-noise-dominated region of the power spectrum where the signal on the cosmological parameters diminishes.

### 5.7.5 Comparison with the P-only fits

We now compare the P+B results with the results from the companion paper Euclid Collaboration et al. (2023), where a similar analysis was performed with the galaxy power spectrum only, modelled with the same 1-loop galaxy bias model. In the latter case, only the h and  $\omega_c$  parameters were varied. Different from our analysis the primordial amplitude  $A_s$  was fixed to its fiducial value. We repeat the same for P+B case and in Fig. 5.10 we compare it to the power-spectrum-only fits in terms of their one-dimensional marginalised constraints, goodness-of-fit, FoB, and FoM (the latter w.r.t. h and  $\omega_c$ ).

Adding the extra information from the bispectrum to the power spectrum breaks the nontrivial degeneracies between second-order and leading-order bias parameters, which biases the marginalised constraints on these parameters. As a result, in Fig. 5.10 one can observe the improved agreement of the linear bias  $b_1$  with its fiducial value on large scales when combining the power spectrum and bispectrum. The same phenomenon is observed for  $\omega_c$ , whose marginalised constraints are biased for the P-only fits on large scales, but in agreement with its fiducial value when performing P + B fits.

The goodness-of-fit computed in terms of p-values simply demonstrates that due to larger degrees of freedom, the P+B finds it easier to pass that test, demonstrated by its corresponding p-value, which is above 0.05 for the considered redshifts. The FoB for both P and P+B fits are below the critical  $2\sigma$  limit, with P+B slightly favoured on the large scales due to reasons discussed in the previous paragraph. Finally, as expected the FoM is increased by approximately between 2-5 times when adding the extra information from the bispectrum. However, we should expect less constraining power from the actual surveys when including the bispectrum due to redshift-space distortions, systematic errors, and smaller survey volume than what is considered in this analysis.

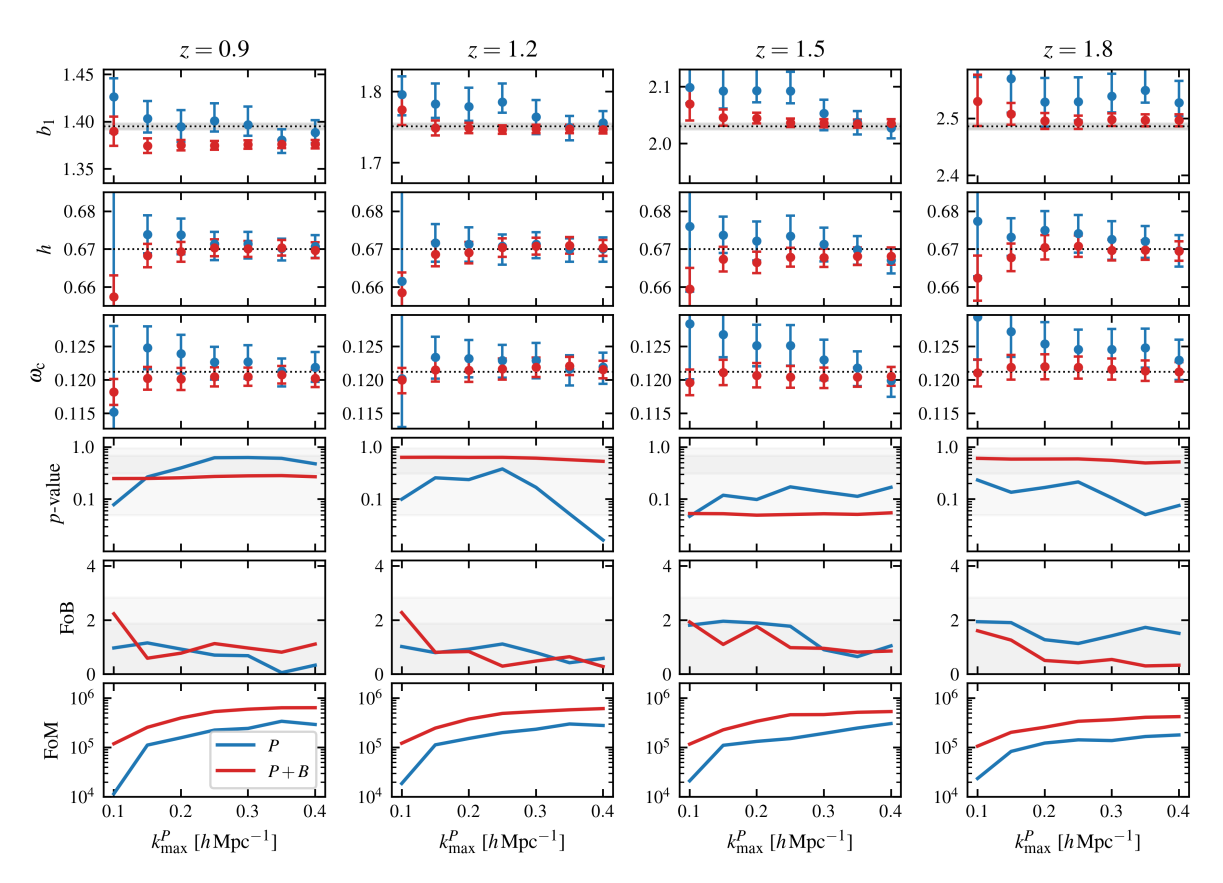


Figure 5.10: Cosmological parameters h and  $\omega_{\rm c}$  (top two rows) obtained by fitting the galaxy P and P+B to the same statistics measured from the HOD3 catalogue snapshots as a function of the scale cut  $k_{\rm max}^P$  imposed on the power spectrum while the scale cut on the bispectrum  $k_{\rm max}^B=0.12~h\,{\rm Mpc}^{-1}$ . The performance metrics goodness of fit (in terms of p-values), figure of bias, and figure of merit are plotted in the bottom three panels, respectively. The last two metrics were computed with respect to the parameters h, and  $\omega_{\rm c}$ . The grey bands in the p-value panels indicate the critical value of 0.05 below which the model is rejected as a good fit to the data. The same bands in FoB panels represent the 68 and 95 percentiles of the corresponding distribution, indicating 1 and 2  $\sigma$  deviations of the fitted cosmological parameters from the actual their values.

#### 5.8 Concluding remarks

In this chapter, we carried out an analysis meant to assess the performance of the model for one-loop galaxy bias over a redshift range that is representative of the spectroscopic galaxy sample that will be measured but *Euclid*. We have used a set of four halo catalogues from comoving snapshots of the Flagship I simulation, at z = (0.9, 1.2, 1.5, 1.8). These snapshots were subsequently populated with H $\alpha$  galaxies using HOD procedures based on the Model 1 and 3 from Pozzetti et al. (2016). Each snapshot has an outstanding volume of  $3780^3 \ h^{-3} \ \text{Mpc}^3$  and high comoving number density, allowing us to assess the accuracy of the perturbative bias expansion with a high level of precision.

We tested galaxy bias models for the full shape of the real-space galaxy power spectrum and the bispectrum. This model adopts an Eulerian bias expansion and it is based on the recently developed EFT modelling, in which the impact of the small-scale physics can be captured by a set of counterterms. The final parameter space consists of three cosmological parameters: the Hubble parameter h, the primordial scalar amplitude  $A_s$ , the cold dark matter density parameter  $\omega_c$ , plus a set of nine nuisance parameters, consisting of bias, EFT counterterm and extra parameters representing deviations from the Poissonian shot-noise.

We first analysed the performance of the combined power spectrum and the bispectrum models, or P+B, by fixing the cosmological parameters to the input cosmology of the Flagship I simulation. This way, we focused on modelling the one-loop galaxy bias and compared the performance of the well-known bias relations, which help to reduce the dimension of the parameter space. Next, we focused on how well the cosmological parameters are determined using the one-loop galaxy bias. In all the cases, we determined the range of validity of the model using three different performance metrics: the goodness of fit, figure of bias (FoB), and the figure of merit (FoM). The last two metrics were computed on the h,  $A_s$ ,  $\omega_c$  combination. The results can be summarised as follows:

- 1. When we fix the cosmology, the goodness of fit is mostly determined by  $k_{\rm max}^B$  and is insensitive to the chosen  $k_{\rm max}^P$ . One needs to restrict the former up to 0.16  $h\,{\rm Mpc}^{-1}$  to maintain a good fit. On the other hand, the FoB computed on the fiducial  $b_1$  requires to restriction the bispectrum data up to  $k_{\rm max}^B = 0.1 \, h\,{\rm Mpc}^{-1}$ .
- 2. When performing analysis using the P+B model with fixed cosmology, the co-evolution bias relation  $b_{\Gamma_3}(b_1)$  is favoured consistently over all the considered redshifts. The  $b_2(b_1)$  relation is shown to be only favoured for higher redshift z=1.8 and 1.5, and the local Lagrangian relation  $b_{G_2}(b_1)$  is strongly disfavoured on the shorter scales.
- 3. When we also vary the three cosmological parameters mentioned above, the constraining power of  $A_s$  is increased by including the bispectrum, but in some cases produces biased results due to strong  $A_s$   $b_1$  degeneracy in real space. Including the short-scale information coming from the one-loop power spectrum reduces the bias for  $\omega_c$ . We have to restrict the data vectors according to limits  $k_{\text{max}}^P \leq 0.2 \ h \, \text{Mpc}^{-1}$  and  $k_{\text{max}}^B \leq 0.18 \ h \, \text{Mpc}^{-1}$  to maintain the FoB under the  $2 \, \sigma$  limit.
- 4. The FoM increases monotonically as we add more short-scale information from the power spectrum and the bispectrum, but plateaus after  $k_{\text{max}}^P = 0.25 \ h \, \text{Mpc}^{-1}$  due to entering the shot-noise dominated region of the power spectrum.

5. When comparing the fits from P+B to P-only, while varying only  $\omega_c$  and h, the extra information coming from the bispectrum reduces a bias in  $\omega_c$  on large scales. Furthermore, as expected, the FoM is increased by factor of 2-5, indicating tighter fits on these parameters.

These results are part of a series of works meant to validate the theoretical framework that will be used to analyse the large-scale galaxy distribution as observed in the actual measurements of *Euclid*. Here we have focused on analysing the performance of the joint fit of the real-space galaxy power spectrum and the bispectrum, something that stands as an important test for the complementary analysis that is going to be carried out by *Euclid*. In parallel, in Euclid Collaboration et al. (2023) we have focused on modelling of the real-space galaxy power spectrum and found that overall, the one-loop galaxy bias expansion is sufficiently accurate on the redshift range  $1 \le z \le 2$ , even deep in the mildly non-linear regime, at  $k_{\text{max}}$  0.4 h Mpc<sup>-1</sup>. Two additional instalments of the series (Euclid Collaboration: Camacho et al., in prep., Euclid Collaboration: Pardede et al., in prep.) will extend the modelling tests to redshift space. In parallel, a different set of papers will be devoted to a similar analysis of configuration space statistics (Euclid Collaboration: Guidi et al., in prep., Euclid Collaboration: Kärcher et al., in prep., Euclid Collaboration: Pugno et al., in prep.).

## **Summary**

Due to the non-linear growth of the structure, the cosmic density field typically deviates from Gaussian distribution. Exploring statistical measures beyond the two-point correlation function presents new opportunities to harness a wealth of cosmological information. In particular, next-generation galaxy surveys with their extensive coverage and a high galaxy number density hold the potential for increasingly precise determinations of the galaxy three-point correlation function and bispectrum. Analysing these three-point correlation functions can enhance our comprehension of structure growth, galaxy bias, and primordial non-Gaussianity.

Extracting information from the galaxy bispectrum requires accurate modelling of the bispectrum of the dark matter density field. In chapter 3 we have summarised the results from Alkhanishvili et al. (2022), where we have used a very large set of N-body simulations to test the next-to-leading order perturbation theory expansions for the matter power spectrum and bispectrum in five different implementations of perturbation theory. Specifically, we studied up to which maximum wavenumber (scale)  $k_{\text{max}}$  the models provide a good fit to the simulations. This scale is also referred to as reach in the literature. We found that the state-of-the-art model Effective Field Theory (EFT) has the largest reach  $(k_{\text{max}} \approx 0.14 \ h \, \text{Mpc}^{-1})$  among other perturbation theory models. This is partly owed to the free parameters that this model has that allow to capture the influence of short-scale non-linear effects on the large-scale fluctuations. We have also looked at how these results change when one considers smaller volumes since the volumes observed by current and upcoming surveys are one or two magnitudes lower than the total volume of the simulations we have considered. As expected, due to larger error bars around the measurements of the power spectrum and the bispectrum the reach is dramatically improved. For example, in the case of EFT we obtained the reach of  $0.25 \ h \,\mathrm{Mpc}^{-1}$ for the power spectrum and 0.18 h Mpc<sup>-1</sup> for the bispectrum. Furthermore, the impact of systematic errors of the N-body simulations on the above results was tested. We have found that adding small uncorrelated systematic errors to the statistical ones dramatically extended the reach of EFT model due to the freedom provided by the counterterms. On the other hand, we found that the correlated errors like one coming from the finite mass resolution have a minimal impact on the results.

Traditional estimators of the galaxy power spectrum and bispectrum are sensitive to the survey geometry. They yield spectra that differ from the true underlying signal since they are convolved with the window function of the survey. For the current and future generations of experiments, this bias is statistically significant on large scales. It is thus imperative that the effect of the window function on the summary statistics of the galaxy distribution and their covariance is accurately modelled.

Moreover, this operation must be computationally efficient to allow sampling posterior probabilities while performing Bayesian estimation of the cosmological parameters. In chapter 4 we demonstrated how DNNs can be used to achieve this goal. We trained two models, one for the power spectrum and another for the bispectrum, which emulate the convolution with the window function. These models turned out to be accurate to better than 0.1 per cent on a timescale of 10 microseconds. The bottleneck operation in the DNN approach is the creation of the training data set, which requires a significant time investment in the case of the bispectrum. We thus conclude that using the DNN model would be advantageous as long as the size of the necessary training set is substantially smaller than the number of the required likelihood evaluations in the Bayesian estimation of the model parameters.

In chapter 5 we have assessed the performance of a model for one-loop galaxy bias against the synthetic data from Flagship I simulation that is representative of the Euclid survey spectroscopic galaxy sample. We tested galaxy bias models for the full shape of the real-space galaxy power spectrum and the bispectrum. Namely, we analysed how well the combined two and three-point statistics in Fourier space can constrain the bias and cosmological parameters. At first, we fixed the cosmological parameters to the input cosmology of the Flagship I simulation. That way we have focused on how well the one-loop galaxy bias describes the summary statistics. We found that one needs to restrict the range of considered wavenumbers for the bispectrum  $k_{\text{max}}^{B}$  up to 0.16 h Mpc<sup>-1</sup> to maintain a good fit. Additionally, we investigated which bias relations can help to reduce the dimensions of the parameter space without degrading the constraining power of the model. We have found that co-evolution bias relation  $b_{\Gamma_2}(b_1)$  is favoured over all the considered redshifts. Next, we have focused on how well the cosmological parameters are determined by the same model. Namely, we have focused on the Hubble parameter h, the primordial scalar amplitude  $A_s$ , and the cold dark matter density parameter  $\omega_c$ . In this case, the constraining power of  $A_s$  is increased by including more bispectrum data, but in some cases, this produces biased results due to strong  $A_s$ - $b_1$  degeneracy. This degeneracy is not an issue in redshift space and only exists in real space. On the other hand, the constraining power of these parameters increases as one adds more short-scale information but it plateaues after  $k_{\text{max}}^P = 0.25 \text{ h Mpc}^{-1}$  due to entering the shot-noise dominated region of the power spectrum. Lastly, we demonstrated that including the galaxy bispectrum on top of the galaxy power spectrum reduces the bias of  $\omega_c$  on large scales and the constraints on the parameters are improved by 2-5 times. Overall, our analysis shows promising results that three-point statistics will drastically improve the information harvested from the next-generation surveys and more effort needs to be made to model it accurately.

### **Bibliography**

Alam, S., Ata, M., Bailey, S., Beutler, F., Bizyaev, D., Blazek, J. A., Bolton, A. S., Brownstein, J. R., Burden, A., Chuang, C.-H., Comparat, J., Cuesta, A. J., Dawson, K. S., Eisenstein, D. J., Escoffier, S., Gil-Marín, H., Grieb, J. N., Hand, N., Ho, S., Kinemuchi, K., Kirkby, D., Kitaura, F., Malanushenko, E., Malanushenko, V., Maraston, C., McBride, C. K., Nichol, R. C., Olmstead, M. D., Oravetz, D., Padmanabhan, N., Palanque-Delabrouille, N., Pan, K., Pellejero-Ibanez, M., Percival, W. J., Petitjean, P., Prada, F., Price-Whelan, A. M., Reid, B. A., Rodríguez-Torres, S. A., Roe, N. A., Ross, A. J., Ross, N. P., Rossi, G., Rubiño-Martín, J. A., Saito, S., Salazar-Albornoz, S., Samushia, L., Sánchez, A. G., Satpathy, S., Schlegel, D. J., Schneider, D. P., Scóccola, C. G., Seo, H.-J., Sheldon, E. S., Simmons, A., Slosar, A., Strauss, M. A., Swanson, M. E. C., Thomas, D., Tinker, J. L., Tojeiro, R., Magaña, M. V., Vazquez, J. A., Verde, L., Wake, D. A., Wang, Y., Weinberg, D. H., White, M., Wood-Vasey, W. M., Yèche, C., Zehavi, I., Zhai, Z., and Zhao, G.-B. (2017). The clustering of galaxies in the completed SDSS-III Baryon Oscillation Spectroscopic Survey: cosmological analysis of the DR12 galaxy sample. MNRAS, 470(3):2617–2652.

Albareti, F. D., Allende Prieto, C., Almeida, A., Anders, F., Anderson, S., Andrews, B. H., Aragón-Salamanca, A., Argudo-Fernández, M., Armengaud, E., Aubourg, E., Avila-Reese, V., Badenes, C., Bailey, S., Barbuy, B., Barger, K., Barrera-Ballesteros, J., Bartosz, C., Basu, S., Bates, D., Battaglia, G., Baumgarten, F., Baur, J., Bautista, J., Beers, T. C., Belfiore, F., Bershady, M., Bertran de Lis, S., Bird, J. C., Bizyaev, D., Blanc, G. A., Blanton, M., Blomqvist, M., Bolton, A. S., Borissova, J., Bovy, J., Brandt, W. N., Brinkmann, J., Brownstein, J. R., Bundy, K., Burtin, E., Busca, N. G., Camacho Chavez, H. O., Cano Díaz, M., Cappellari, M., Carrera, R., Chen, Y., Cherinka, B., Cheung, E., Chiappini, C., Chojnowski, D., Chuang, C.-H., Chung, H., Cirolini, R. F., Clerc, N., Cohen, R. E., Comerford, J. M., Comparat, J., Correa do Nascimento, J., Cousinou, M.-C., Covey, K., Crane, J. D., Croft, R., Cunha, K., Darling, J., Davidson, James W., J., Dawson, K., Da Costa, L., Da Silva Ilha, G., Deconto Machado, A., Delubac, T., De Lee, N., De la Macorra, A., De la Torre, S., Diamond-Stanic, A. M., Donor, J., Downes, J. J., Drory, N., Du, C., Du Mas des Bourboux, H., Dwelly, T., Ebelke, G., Eigenbrot, A., Eisenstein, D. J., Elsworth, Y. P., Emsellem, E., Eracleous, M., Escoffier, S., Evans, M. L., Falcón-Barroso, J., Fan, X., Favole, G., Fernandez-Alvar, E., Fernandez-Trincado, J. G., Feuillet, D., Fleming, S. W., Font-Ribera, A., Freischlad, G., Frinchaboy, P., Fu, H., Gao, Y., Garcia, R. A., Garcia-Dias, R., Garcia-Hernández, D. A., Garcia Pérez, A. E., Gaulme, P., Ge, J., Geisler, D., Gillespie, B., Gil Marin, H., Girardi, L., Goddard, D., Gomez Maqueo Chew, Y., Gonzalez-Perez, V., Grabowski, K., Green, P., Grier, C. J., Grier, T., Guo, H., Guy, J., Hagen, A., Hall, M., Harding, P., Harley, R. E., Hasselquist, S., Hawley, S., Hayes, C. R., Hearty, F., Hekker, S., Hernandez Toledo, H., Ho, S., Hogg, D. W., Holley-Bockelmann, K., Holtzman, J. A., Holzer, P. H., Hu, J., Huber, D., Hutchinson, T. A.,

Hwang, H. S., Ibarra-Medel, H. J., Ivans, I. I., Ivory, K., Jaehnig, K., Jensen, T. W., Johnson, J. A., Jones, A., Jullo, E., Kallinger, T., Kinemuchi, K., Kirkby, D., Klaene, M., Kneib, J.-P., Kollmeier, J. A., Lacerna, I., Lane, R. R., Lang, D., Laurent, P., Law, D. R., Leauthaud, A., Le Goff, J.-M., Li, C., Li, C., Li, N., Li, R., Liang, F.-H., Liang, Y., Lima, M., Lin, L., Lin, L., Lin, Y.-T., Liu, C., Long, D., Lucatello, S., MacDonald, N., MacLeod, C. L., Mackereth, J. T., Mahadevan, S., Maia, M. A. G., Maiolino, R., Majewski, S. R., Malanushenko, O., Malanushenko, V., Mallmann, N. D., Manchado, A., Maraston, C., Marques-Chaves, R., Martinez Valpuesta, I., Masters, K. L., Mathur, S., McGreer, I. D., Merloni, A., Merrifield, M. R., Mészáros, S., Meza, A., Miglio, A., Minchey, I., Molaverdikhani, K., Montero-Dorta, A. D., Mosser, B., Muna, D., Myers, A., Nair, P., Nandra, K., Ness, M., Newman, J. A., Nichol, R. C., Nidever, D. L., Nitschelm, C., O'Connell, J., Oravetz, A., Oravetz, D. J., Pace, Z., Padilla, N., Palanque-Delabrouille, N., Pan, K., Parejko, J., Paris, I., Park, C., Peacock, J. A., Peirani, S., Pellejero-Ibanez, M., Penny, S., Percival, W. J., Percival, J. W., Perez-Fournon, I., Petitjean, P., Pieri, M., Pinsonneault, M. H., Pisani, A., Prada, F., Prakash, A., Price-Jones, N., Raddick, M. J., Rahman, M., Raichoor, A., Barboza Rembold, S., Reyna, A. M., Rich, J., Richstein, H., Ridl, J., Riffel, R. A., Riffel, R., Rix, H.-W., Robin, A. C., Rockosi, C. M., Rodríguez-Torres, S., Rodrigues, T. S., Roe, N., Roman Lopes, A., Román-Zúñiga, C., Ross, A. J., Rossi, G., Ruan, J., Ruggeri, R., Runnoe, J. C., Salazar-Albornoz, S., Salvato, M., Sanchez, S. F., Sanchez, A. G., Sanchez-Gallego, J. R., Santiago, B. X., Schiavon, R., Schimoia, J. S., Schlafly, E., Schlegel, D. J., Schneider, D. P., Schönrich, R., Schultheis, M., Schwope, A., Seo, H.-J., Serenelli, A., Sesar, B., Shao, Z., Shetrone, M., Shull, M., Silva Aguirre, V., Skrutskie, M. F., Slosar, A., Smith, M., Smith, V. V., Sobeck, J., Somers, G., Souto, D., Stark, D. V., Stassun, K. G., Steinmetz, M., Stello, D., Storchi Bergmann, T., Strauss, M. A., Streblyanska, A., Stringfellow, G. S., Suarez, G., Sun, J., Taghizadeh-Popp, M., Tang, B., Tao, C., Tayar, J., Tembe, M., Thomas, D., Tinker, J., Tojeiro, R., Tremonti, C., Troup, N., Trump, J. R., Unda-Sanzana, E., Valenzuela, O., Van den Bosch, R., Vargas-Magaña, M., Vazquez, J. A., Villanova, S., Vivek, M., Vogt, N., Wake, D., Walterbos, R., Wang, Y., Wang, E., Weaver, B. A., Weijmans, A.-M., Weinberg, D. H., Westfall, K. B., Whelan, D. G., Wilcots, E., Wild, V., Williams, R. A., Wilson, J., Wood-Vasey, W. M., Wylezalek, D., Xiao, T., Yan, R., Yang, M., Ybarra, J. E., Yeche, C., Yuan, F.-T., Zakamska, N., Zamora, O., Zasowski, G., Zhang, K., Zhao, C., Zhao, G.-B., Zheng, Z., Zheng, Z., Zhou, Z.-M., Zhu, G., Zinn, J. C., and Zou, H. (2017). The 13th Data Release of the Sloan Digital Sky Survey: First Spectroscopic Data from the SDSS-IV Survey Mapping Nearby Galaxies at Apache Point Observatory. *ApJS*, 233(2):25.

Alkhanishvili, D., Porciani, C., and Sefusatti, E. (2023). Window function convolution with deep neural network models. *A&A*, 669:L2.

Alkhanishvili, D., Porciani, C., Sefusatti, E., Biagetti, M., Lazanu, A., Oddo, A., and Yankelevich, V. (2022). The reach of next-to-leading-order perturbation theory for the matter bispectrum. *MNRAS*, 512(4):4961–4981.

Allen, S. W., Evrard, A. E., and Mantz, A. B. (2011). Cosmological Parameters from Observations of Galaxy Clusters. *ARA&A*, 49(1):409–470.

Angulo, R. E., Foreman, S., Schmittfull, M., and Senatore, L. (2015a). The one-loop matter bispectrum in the Effective Field Theory of Large Scale Structures. *J. Cosmology Astropart. Phys.*, 10:039.

- Angulo, R. E., Foreman, S., Schmittfull, M., and Senatore, L. (2015b). The one-loop matter bispectrum in the Effective Field Theory of Large Scale Structures. *J. Cosmology Astropart. Phys.*, 10:039.
- Baldauf, T., Garny, M., Taule, P., and Steele, T. (2021). Two-loop bispectrum of large-scale structure. *Phys. Rev. D*, 104(12):123551.
- Baldauf, T., Mercolli, L., Mirbabayi, M., and Pajer, E. (2015a). The bispectrum in the Effective Field Theory of Large Scale Structure. *J. Cosmology Astropart. Phys.*, 5:007.
- Baldauf, T., Mirbabayi, M., Simonović, M., and Zaldarriaga, M. (2015b). Equivalence principle and the baryon acoustic peak. *Phys. Rev. D*, 92(4):043514.
- Baldauf, T., Seljak, U., Senatore, L., and Zaldarriaga, M. (2011). Galaxy bias and non-linear structure formation in general relativity. *J. Cosmology Astropart. Phys.*, 2011(10):031.
- Bardeen, J. M., Bond, J. R., Kaiser, N., and Szalay, A. S. (1986). The statistics of peaks of gaussian random fields. *ApJ*, 304:15–61.
- Bardeen, J. M., Bond, J. R., Kaiser, N., and Szalay, A. S. (1986). The Statistics of Peaks of Gaussian Random Fields. *ApJ*, 304:15.
- Baumann, D., Nicolis, A., Senatore, L., and Zaldarriaga, M. (2012). Cosmological non-linearities as an effective fluid. *J. Cosmology Astropart. Phys.*, 2012(7):051.
- Berlind, A. A. and Weinberg, D. H. (2002). The Halo Occupation Distribution: Toward an Empirical Determination of the Relation between Galaxies and Mass. *ApJ*, 575(2):587–616.
- Bernardeau, F., Colombi, S., Gaztañaga, E., and Scoccimarro, R. (2002). Large-scale structure of the Universe and cosmological perturbation theory. *Phys. Rep.*, 367:1–248.
- Bettoni, D. (2013). Framing the Dark: Theory and phenomenology of a non-minimally coupled dark matter fluid. PhD thesis.
- Blake, C., Brough, S., Colless, M., Couch, W., Croom, S., Davis, T., Drinkwater, M. J., Forster, K., Glazebrook, K., Jelliffe, B., Jurek, R. J., Li, I. H., Madore, B., Martin, C., Pimbblet, K., Poole, G. B., Pracy, M., Sharp, R., Wisnioski, E., Woods, D., and Wyder, T. (2010). The WiggleZ Dark Energy Survey: the selection function and z = 0.6 galaxy power spectrum. *MNRAS*, 406(2):803–821.
- Blas, D., Garny, M., Ivanov, M. M., and Sibiryakov, S. (2016). Time-sliced perturbation theory II: baryon acoustic oscillations and infrared resummation. *J. Cosmology Astropart. Phys.*, 2016(7):028.
- Blas, D., Garny, M., and Konstandin, T. (2014). Cosmological perturbation theory at three-loop order. *J. Cosmology Astropart. Phys.*, 2014(1):010.
- Bond, J. R. and Myers, S. T. (1996). The Peak-Patch Picture of Cosmic Catalogs. I. Algorithms. *ApJS*, 103:1.

- Borzyszkowski, M., Ludlow, A. D., and Porciani, C. (2014). The formation of cold dark matter haloes II. Collapse time and tides. *MNRAS*, 445(4):4124–4136.
- Borzyszkowski, M., Porciani, C., Romano-Díaz, E., and Garaldi, E. (2017). ZOMG I. How the cosmic web inhibits halo growth and generates assembly bias. *MNRAS*, 469(1):594–611.
- Bose, B., Byun, J., Lacasa, F., Moradinezhad Dizgah, A., and Lombriser, L. (2020). Modelling the matter bispectrum at small scales in modified gravity. *J. Cosmology Astropart. Phys.*, 2020(2):025.
- Bose, B. and Taruya, A. (2018). The one-loop matter bispectrum as a probe of gravity and dark energy. *J. Cosmology Astropart. Phys.*, 2018(10):019.
- Brout, D., Scolnic, D., Popovic, B., Riess, A. G., Carr, A., Zuntz, J., Kessler, R., Davis, T. M., Hinton, S., Jones, D., Kenworthy, W. D., Peterson, E. R., Said, K., Taylor, G., Ali, N., Armstrong, P., Charvu, P., Dwomoh, A., Meldorf, C., Palmese, A., Qu, H., Rose, B. M., Sanchez, B., Stubbs, C. W., Vincenzi, M., Wood, C. M., Brown, P. J., Chen, R., Chambers, K., Coulter, D. A., Dai, M., Dimitriadis, G., Filippenko, A. V., Foley, R. J., Jha, S. W., Kelsey, L., Kirshner, R. P., Möller, A., Muir, J., Nadathur, S., Pan, Y.-C., Rest, A., Rojas-Bravo, C., Sako, M., Siebert, M. R., Smith, M., Stahl, B. E., and Wiseman, P. (2022). The Pantheon+ Analysis: Cosmological Constraints. *ApJ*, 938(2):110.
- Carlson, J., White, M., and Padmanabhan, N. (2009). Critical look at cosmological perturbation theory techniques. *Phys. Rev. D*, 80(4):043531.
- Carrasco, J. J. M., Foreman, S., Green, D., and Senatore, L. (2014a). The 2-loop matter power spectrum and the IR-safe integrand. *J. Cosmology Astropart. Phys.*, 7:56.
- Carrasco, J. J. M., Foreman, S., Green, D., and Senatore, L. (2014b). The Effective Field Theory of Large Scale Structures at two loops. *J. Cosmology Astropart. Phys.*, 7:57.
- Carrasco, J. J. M., Hertzberg, M. P., and Senatore, L. (2012). The effective field theory of cosmological large scale structures. *Journal of High Energy Physics*, 2012:82.
- Carroll, S. M., Press, W. H., and Turner, E. L. (1992). The cosmological constant. 30:499–542.
- Chan, K. C. and Blot, L. (2017). Assessment of the information content of the power spectrum and bispectrum. *Phys. Rev. D*, 96(2):023528.
- Chan, K. C., Scoccimarro, R., and Sheth, R. K. (2012). Gravity and large-scale nonlocal bias. *Physical Review D*, 85(8).
- Chevallier, M. and Polarski, D. (2001). Accelerating Universes with Scaling Dark Matter. *International Journal of Modern Physics D*, 10(2):213–223.
- Cole, S., Percival, W. J., Peacock, J. A., Norberg, P., Baugh, C. M., Frenk, C. S., Baldry, I., Bland-Hawthorn, J., Bridges, T., Cannon, R., Colless, M., Collins, C., Couch, W., Cross, N. J. G., Dalton, G., Eke, V. R., De Propris, R., Driver, S. P., Efstathiou, G., Ellis, R. S., Glazebrook, K., Jackson, C., Jenkins, A., Lahav, O., Lewis, I., Lumsden, S., Maddox, S., Madgwick, D., Peterson, B. A., Sutherland, W., and Taylor, K. (2005). The 2dF Galaxy Redshift Survey: power-spectrum analysis of the final data set and cosmological implications. *MNRAS*, 362(2):505–534.

- Colless, M., Dalton, G., Maddox, S., Sutherland, W., Norberg, P., Cole, S., Bland-Hawthorn, J., Bridges, T., Cannon, R., Collins, C., Couch, W., Cross, N., Deeley, K., De Propris, R., Driver, S. P., Efstathiou, G., Ellis, R. S., Frenk, C. S., Glazebrook, K., Jackson, C., Lahav, O., Lewis, I., Lumsden, S., Madgwick, D., Peacock, J. A., Peterson, B. A., Price, I., Seaborne, M., and Taylor, K. (2001). The 2df galaxy redshift survey: spectra and redshifts. *MNRAS*, 328:1039–1063.
- Colless, M. et al. (2001). The 2dF Galaxy Redshift Survey: Spectra and redshifts. *Mon. Not. Roy. Astron. Soc.*, 328:1039.
- Cooray, A. and Sheth, R. (2002). Halo models of large scale structure. Phys. Rep., 372(1):1–129.
- Crocce, M. and Scoccimarro, R. (2006). Renormalized cosmological perturbation theory. *Phys. Rev. D*, 73(6):063519.
- D'Amico, G., Donath, Y., Lewandowski, M., Senatore, L., and Zhang, P. (2022). The BOSS bispectrum analysis at one loop from the Effective Field Theory of Large-Scale Structure. *arXiv e-prints*, page arXiv:2206.08327.
- d'Amico, G., Gleyzes, J., Kokron, N., Markovic, K., Senatore, L., Zhang, P., Beutler, F., and Gil-Marín, H. (2020). The cosmological analysis of the SDSS/BOSS data from the Effective Field Theory of Large-Scale Structure. *J. Cosmology Astropart. Phys.*, 2020(5):005.
- Dawson, K. S., Kneib, J.-P., Percival, W. J., Alam, S., Albareti, F. D., Anderson, S. F., Armengaud, E., Aubourg, É., Bailey, S., Bautista, J. E., Berlind, A. A., Bershady, M. A., Beutler, F., Bizyaev, D., Blanton, M. R., Blomqvist, M., Bolton, A. S., Bovy, J., Brandt, W. N., Brinkmann, J., Brownstein, J. R., Burtin, E., Busca, N. G., Cai, Z., Chuang, C.-H., Clerc, N., Comparat, J., Cope, F., Croft, R. A. C., Cruz-Gonzalez, I., da Costa, L. N., Cousinou, M.-C., Darling, J., de la Macorra, A., de la Torre, S., Delubac, T., du Mas des Bourboux, H., Dwelly, T., Ealet, A., Eisenstein, D. J., Eracleous, M., Escoffier, S., Fan, X., Finoguenov, A., Font-Ribera, A., Frinchaboy, P., Gaulme, P., Georgakakis, A., Green, P., Guo, H., Guy, J., Ho, S., Holder, D., Huehnerhoff, J., Hutchinson, T., Jing, Y., Jullo, E., Kamble, V., Kinemuchi, K., Kirkby, D., Kitaura, F.-S., Klaene, M. A., Laher, R. R., Lang, D., Laurent, P., Le Goff, J.-M., Li, C., Liang, Y., Lima, M., Lin, Q., Lin, W., Lin, Y.-T., Long, D. C., Lundgren, B., MacDonald, N., Geimba Maia, M. A., Malanushenko, E., Malanushenko, V., Mariappan, V., McBride, C. K., McGreer, I. D., Ménard, B., Merloni, A., Meza, A., Montero-Dorta, A. D., Muna, D., Myers, A. D., Nandra, K., Naugle, T., Newman, J. A., Noterdaeme, P., Nugent, P., Ogando, R., Olmstead, M. D., Oravetz, A., Oravetz, D. J., Padmanabhan, N., Palanque-Delabrouille, N., Pan, K., Parejko, J. K., Pâris, I., Peacock, J. A., Petitjean, P., Pieri, M. M., Pisani, A., Prada, F., Prakash, A., Raichoor, A., Reid, B., Rich, J., Ridl, J., Rodriguez-Torres, S., Carnero Rosell, A., Ross, A. J., Rossi, G., Ruan, J., Salvato, M., Sayres, C., Schneider, D. P., Schlegel, D. J., Seljak, U., Seo, H.-J., Sesar, B., Shandera, S., Shu, Y., Slosar, A., Sobreira, F., Streblyanska, A., Suzuki, N., Taylor, D., Tao, C., Tinker, J. L., Tojeiro, R., Vargas-Magaña, M., Wang, Y., Weaver, B. A., Weinberg, D. H., White, M., Wood-Vasey, W. M., Yeche, C., Zhai, Z., Zhao, C., Zhao, G.-b., Zheng, Z., Ben Zhu, G., and Zou, H. (2016). The SDSS-IV Extended Baryon Oscillation Spectroscopic Survey: Overview and Early Data. AJ, 151(2):44.
- Dawson, K. S., Schlegel, D. J., Ahn, C. P., Anderson, S. F., Aubourg, É., Bailey, S., Barkhouser, R. H., Bautista, J. E., Beifiori, A., Berlind, A. A., Bhardwaj, V., Bizyaev, D., Blake, C. H., Blanton, M. R.,

Blomqvist, M., Bolton, A. S., Borde, A., Bovy, J., Brandt, W. N., Brewington, H., Brinkmann, J., Brown, P. J., Brownstein, J. R., Bundy, K., Busca, N. G., Carithers, W., Carnero, A. R., Carr, M. A., Chen, Y., Comparat, J., Connolly, N., Cope, F., Croft, R. A. C., Cuesta, A. J., da Costa, L. N., Davenport, J. R. A., Delubac, T., de Putter, R., Dhital, S., Ealet, A., Ebelke, G. L., Eisenstein, D. J., Escoffier, S., Fan, X., Filiz Ak, N., Finley, H., Font-Ribera, A., Génova-Santos, R., Gunn, J. E., Guo, H., Haggard, D., Hall, P. B., Hamilton, J.-C., Harris, B., Harris, D. W., Ho, S., Hogg, D. W., Holder, D., Honscheid, K., Huehnerhoff, J., Jordan, B., Jordan, W. P., Kauffmann, G., Kazin, E. A., Kirkby, D., Klaene, M. A., Kneib, J.-P., Le Goff, J.-M., Lee, K.-G., Long, D. C., Loomis, C. P., Lundgren, B., Lupton, R. H., Maia, M. A. G., Makler, M., Malanushenko, E., Malanushenko, V., Mandelbaum, R., Manera, M., Maraston, C., Margala, D., Masters, K. L., McBride, C. K., McDonald, P., McGreer, I. D., McMahon, R. G., Mena, O., Miralda-Escudé, J., Montero-Dorta, A. D., Montesano, F., Muna, D., Myers, A. D., Naugle, T., Nichol, R. C., Noterdaeme, P., Nuza, S. E., Olmstead, M. D., Oravetz, A., Oravetz, D. J., Owen, R., Padmanabhan, N., Palanque-Delabrouille, N., Pan, K., Parejko, J. K., Pâris, I., Percival, W. J., Pérez-Fournon, I., Pérez-Ràfols, I., Petitjean, P., Pfaffenberger, R., Pforr, J., Pieri, M. M., Prada, F., Price-Whelan, A. M., Raddick, M. J., Rebolo, R., Rich, J., Richards, G. T., Rockosi, C. M., Roe, N. A., Ross, A. J., Ross, N. P., Rossi, G., Rubiño-Martin, J. A., Samushia, L., Sánchez, A. G., Sayres, C., Schmidt, S. J., Schneider, D. P., Scóccola, C. G., Seo, H.-J., Shelden, A., Sheldon, E., Shen, Y., Shu, Y., Slosar, A., Smee, S. A., Snedden, S. A., Stauffer, F., Steele, O., Strauss, M. A., Streblyanska, A., Suzuki, N., Swanson, M. E. C., Tal, T., Tanaka, M., Thomas, D., Tinker, J. L., Tojeiro, R., Tremonti, C. A., Vargas Magaña, M., Verde, L., Viel, M., Wake, D. A., Watson, M., Weaver, B. A., Weinberg, D. H., Weiner, B. J., West, A. A., White, M., Wood-Vasey, W. M., Yeche, C., Zehavi, I., Zhao, G.-B., and Zheng, Z. (2013). The Baryon Oscillation Spectroscopic Survey of SDSS-III. AJ, 145(1):10.

DESI Collaboration, Adame, A. G., Aguilar, J., Ahlen, S., Alam, S., Alexander, D. M., Alvarez, M., Alves, O., Anand, A., Andrade, U., Armengaud, E., Avila, S., Aviles, A., Awan, H., Bahr-Kalus, B., Bailey, S., Baltay, C., Bault, A., Behera, J., BenZvi, S., Bera, A., Beutler, F., Bianchi, D., Blake, C., Blum, R., Brieden, S., Brodzeller, A., Brooks, D., Buckley-Geer, E., Burtin, E., Calderon, R., Canning, R., Carnero Rosell, A., Cereskaite, R., Cervantes-Cota, J. L., Chabanier, S., Chaussidon, E., Chaves-Montero, J., Chen, S., Chen, X., Claybaugh, T., Cole, S., Cuceu, A., Davis, T. M., Dawson, K., de la Macorra, A., de Mattia, A., Deiosso, N., Dey, A., Dey, B., Ding, Z., Doel, P., Edelstein, J., Eftekharzadeh, S., Eisenstein, D. J., Elliott, A., Fagrelius, P., Fanning, K., Ferraro, S., Ereza, J., Findlay, N., Flaugher, B., Font-Ribera, A., Forero-Sánchez, D., Forero-Romero, J. E., Frenk, C. S., Garcia-Quintero, C., Gaztañaga, E., Gil-Marín, H., Gontcho, S. G. A., Gonzalez-Morales, A. X., Gonzalez-Perez, V., Gordon, C., Green, D., Gruen, D., Gsponer, R., Gutierrez, G., Guy, J., Hadzhiyska, B., Hahn, C., Hanif, M. M. S., Herrera-Alcantar, H. K., Honscheid, K., Howlett, C., Huterer, D., Iršič, V., Ishak, M., Juneau, S., Karaçaylı, N. G., Kehoe, R., Kent, S., Kirkby, D., Kremin, A., Krolewski, A., Lai, Y., Lan, T. W., Landriau, M., Lang, D., Lasker, J., Le Goff, J. M., Le Guillou, L., Leauthaud, A., Levi, M. E., Li, T. S., Linder, E., Lodha, K., Magneville, C., Manera, M., Margala, D., Martini, P., Maus, M., McDonald, P., Medina-Varela, L., Meisner, A., Mena-Fernández, J., Miquel, R., Moon, J., Moore, S., Moustakas, J., Mudur, N., Mueller, E., Muñoz-Gutiérrez, A., Myers, A. D., Nadathur, S., Napolitano, L., Neveux, R., Newman, J. A., Nguyen, N. M., Nie, J., Niz, G., Noriega, H. E., Padmanabhan, N., Paillas, E., Palanque-Delabrouille, N., Pan, J., Penmetsa, S., Percival, W. J., Pieri, M. M., Pinon, M., Poppett,

- C., Porredon, A., Prada, F., Pérez-Fernández, A., Pérez-Ràfols, I., Rabinowitz, D., Raichoor, A., Ramírez-Pérez, C., Ramirez-Solano, S., Ravoux, C., Rashkovetskyi, M., Rezaie, M., Rich, J., Rocher, A., Rockosi, C., Roe, N. A., Rosado-Marin, A., Ross, A. J., Rossi, G., Ruggeri, R., Ruhlmann-Kleider, V., Samushia, L., Sanchez, E., Saulder, C., Schlafly, E. F., Schlegel, D., Schubnell, M., Seo, H., Shafieloo, A., Sharples, R., Silber, J., Slosar, A., Smith, A., Sprayberry, D., Tan, T., Tarlé, G., Taylor, P., Trusov, S., Ureña-López, L. A., Vaisakh, R., Valcin, D., Valdes, F., Vargas-Magaña, M., Verde, L., Walther, M., Wang, B., Wang, M. S., Weaver, B. A., Weaverdyck, N., Wechsler, R. H., Weinberg, D. H., White, M., Yu, J., Yu, Y., Yuan, S., Yèche, C., Zaborowski, E. A., Zarrouk, P., Zhang, H., Zhao, C., Zhao, R., Zhou, R., Zhuang, T., and Zou, H. (2024). DESI 2024 VI: Cosmological Constraints from the Measurements of Baryon Acoustic Oscillations. *arXiv e-prints*, page arXiv:2404.03002.
- DESI Collaboration, Aghamousa, A., Aguilar, J., Ahlen, S., Alam, S., Allen, L. E., Allende Prieto, C., Annis, J., Bailey, S., Balland, C., and et al. (2016). The DESI Experiment Part I: Science, Targeting, and Survey Design. *ArXiv e-prints*.
- Desjacques, V. (2013). Local bias approach to the clustering of discrete density peaks. *Phys. Rev. D*, 87(4):043505.
- Desjacques, V., Jeong, D., and Schmidt, F. (2018). Large-scale galaxy bias. Phys. Rep., 733:1–193.
- Desjacques, V., Jeong, D., and Schmidt, F. (2018). Large-scale galaxy bias. *Physics Reports*, 733:1–193.
- Dicke, R. H., Peebles, P. J. E., Roll, P. G., and Wilkinson, D. T. (1965). Cosmic Black-Body Radiation. *ApJ*, 142:414–419.
- Efstathiou, G., Davis, M., White, S. D. M., and Frenk, C. S. (1985). Numerical techniques for large cosmological N-body simulations. *ApJS*, 57:241–260.
- Eggemeier, A., Camacho-Quevedo, B., Pezzotta, A., Crocce, M., Scoccimarro, R., and Sánchez, A. G. (2022). Comet: Clustering observables modelled by emulated perturbation theory.
- Eggemeier, A., Scoccimarro, R., Smith, R. E., Crocce, M., Pezzotta, A., and Sánchez, A. G. (2021). Testing one-loop galaxy bias: Joint analysis of power spectrum and bispectrum. *Phys. Rev. D*, 103(12):123550.
- Eisenstein, D. J., Zehavi, I., Hogg, D. W., Scoccimarro, R., Blanton, M. R., Nichol, R. C., Scranton, R., Seo, H.-J., Tegmark, M., Zheng, Z., Anderson, S. F., Annis, J., Bahcall, N. A., Brinkmann, J., Burles, S., Castander, F. J., Connolly, A., Csabai, I., Doi, M., Fukugita, M., Frieman, J. A., Glazebrook, K., Gunn, J. E., Hendry, J. S., Hennessy, G., Ivezić, Z., Kent, S., Knapp, G. R., Lin, H., Loh, Y.-S., Lupton, R. H., Margon, B., McKay, T. A., Meiksin, A., Munn, J. A., Pope, A., Richmond, M. W., Schlegel, D., Schneider, D. P., Shimasaku, K., Stoughton, C., Strauss, M. A., SubbaRao, M., Szalay, A. S., Szapudi, I., Tucker, D. L., Yanny, B., and York, D. G. (2005). Detection of the baryon acoustic peak in the large-scale correlation function of sdss luminous red galaxies. *ApJ*, 633:560–574.

Euclid Collaboration, Pezzotta, A., Moretti, C., Zennaro, M., Moradinezhad Dizgah, A., Crocce, M., Sefusatti, E., Ferrero, I., Pardede, K., Eggemeier, A., Barreira, A., Angulo, R. E., Marinucci, M., Camacho Quevedo, B., de la Torre, S., Alkhanishvili, D., Biagetti, M., Breton, M. A., Castorina, E., D'Amico, G., Desjacques, V., Guidi, M., Kärcher, M., Oddo, A., Pellejero Ibanez, M., Porciani, C., Pugno, A., Salvalaggio, J., Sarpa, E., Veropalumbo, A., Vlah, Z., Amara, A., Andreon, S., Auricchio, N., Baldi, M., Bardelli, S., Bender, R., Bodendorf, C., Bonino, D., Branchini, E., Brescia, M., Brinchmann, J., Camera, S., Capobianco, V., Carbone, C., Cardone, V. F., Carretero, J., Casas, S., Castander, F. J., Castellano, M., Cavuoti, S., Cimatti, A., Congedo, G., Conselice, C. J., Conversi, L., Copin, Y., Corcione, L., Courbin, F., Courtois, H. M., Da Silva, A., Degaudenzi, H., Di Giorgio, A. M., Dinis, J., Dupac, X., Dusini, S., Ealet, A., Farina, M., Farrens, S., Fosalba, P., Frailis, M., Franceschi, E., Galeotta, S., Gillis, B., Giocoli, C., Granett, B. R., Grazian, A., Grupp, F., Guzzo, L., Haugan, S. V. H., Hormuth, F., Hornstrup, A., Jahnke, K., Joachimi, B., Keihänen, E., Kermiche, S., Kiessling, A., Kilbinger, M., Kitching, T., Kubik, B., Kunz, M., Kurki-Suonio, H., Ligori, S., Lilje, P. B., Lindholm, V., Lloro, I., Maiorano, E., Mansutti, O., Marggraf, O., Markovic, K., Martinet, N., Marulli, F., Massey, R., Medinaceli, E., Mellier, Y., Meneghetti, M., Merlin, E., Meylan, G., Moresco, M., Moscardini, L., Munari, E., Niemi, S. M., Padilla, C., Paltani, S., Pasian, F., Pedersen, K., Percival, W. J., Pettorino, V., Pires, S., Polenta, G., Pollack, J. E., Poncet, M., Popa, L. A., Pozzetti, L., Raison, F., Renzi, A., Rhodes, J., Riccio, G., Romelli, E., Roncarelli, M., Rossetti, E., Saglia, R., Sapone, D., Sartoris, B., Schneider, P., Schrabback, T., Secroun, A., Seidel, G., Seiffert, M., Serrano, S., Sirignano, C., Sirri, G., Stanco, L., Surace, C., Tallada-Crespí, P., Taylor, A. N., Tereno, I., Toledo-Moreo, R., Torradeflot, F., Tutusaus, I., Valentijn, E. A., Valenziano, L., Vassallo, T., Wang, Y., Weller, J., Zamorani, G., Zoubian, J., Zucca, E., Biviano, A., Bozzo, E., Burigana, C., Colodro-Conde, C., Di Ferdinando, D., Mainetti, G., Martinelli, M., Mauri, N., Sakr, Z., Scottez, V., Tenti, M., Viel, M., Wiesmann, M., Akrami, Y., Allevato, V., Anselmi, S., Baccigalupi, C., Ballardini, M., Bernardeau, F., Blanchard, A., Borgani, S., Bruton, S., Cabanac, R., Cappi, A., Carvalho, C. S., Castignani, G., Castro, T., Ca\{n}as-Herrera, G., Chambers, K. C., Contarini, S., Cooray, A. R., Coupon, J., Davini, S., De Lucia, G., Desprez, G., Di Domizio, S., Dole, H., Díaz-Sánchez, A., Escartin Vigo, J. A., Escoffier, S., Ferreira, P. G., Finelli, F., Gabarra, L., Ganga, K., García-Bellido, J., Giacomini, F., Gozaliasl, G., Hall, A., Ilić, S., Joudaki, S., Kajava, J. J. E., Kansal, V., Kirkpatrick, C. C., Legrand, L., Loureiro, A., Macias-Perez, J., Magliocchetti, M., Mannucci, F., Maoli, R., Martins, C. J. A. P., Matthew, S., Maurin, L., Metcalf, R. B., Migliaccio, M., Monaco, P., Morgante, G., Nadathur, S., Walton, N. A., Patrizii, L., Popa, V., Potter, D., Pourtsidou, A., Pöntinen, M., Risso, I., Rocci, P. F., Sánchez, A. G., Sahlén, M., Schneider, A., Sereno, M., Simon, P., Spurio Mancini, A., Steinwagner, J., Testera, G., Teyssier, R., Toft, S., Tosi, S., Troja, A., Tucci, M., Valiviita, J., Vergani, D., Verza, G., and Vielzeuf, P. (2023). Euclid preparation. TBD. Galaxy power spectrum modelling in real space. arXiv e-prints, page arXiv:2312.00679.

Feldman, H. A., Frieman, J. A., Fry, J. N., and Scoccimarro, R. (2001). Constraints on galaxy bias, matter density, and primordial non-gaussianity from the PSCz galaxy redshift survey. *Phys. Rev. Lett.*, 86:1434–1437.

Feldman, H. A., Kaiser, N., and Peacock, J. A. (1994). Power-Spectrum Analysis of Three-dimensional Redshift Surveys. *ApJ*, 426:23.

- Feroz, F., Hobson, M. P., Cameron, E., and Pettitt, A. N. (2019). Importance Nested Sampling and the MultiNest Algorithm. *The Open Journal of Astrophysics*, 2(1):10.
- Foreman, S. and Senatore, L. (2016). The EFT of Large Scale Structures at all redshifts: analytical predictions for lensing. *J. Cosmology Astropart. Phys.*, 2016(4):033.
- Foreman-Mackey, D., Hogg, D. W., Lang, D., and Goodman, J. (2013). emcee: The MCMC Hammer. *PASP*, 125(925):306.
- Fry, J. N. (1996). The evolution of bias. *ApJ*, 461:L65.
- Fry, J. N. and Gaztanaga, E. (1993). Biasing and Hierarchical Statistics in Large-Scale Structure. *ApJ*, 413:447.
- Gaztanaga, E. and Frieman, J. A. (1994). Bias and High-Order Galaxy Correlation Functions in the APM Galaxy Survey. *ApJ*, 437:L13.
- Geller, M. J. and Huchra, J. P. (1989). Mapping the universe. Science, 246(4932):897–903.
- Gil-Marín, H., Noreña, J., Verde, L., Percival, W. J., Wagner, C., Manera, M., and Schneider, D. P. (2015). The power spectrum and bispectrum of SDSS DR11 BOSS galaxies I. Bias and gravity. *MNRAS*, 451(1):539–580.
- Goodman, J. and Weare, J. (2010). Ensemble samplers with affine invariance. *Communications in Applied Mathematics and Computational Science*, 5(1):65–80.
- Granett, B. R., Guzzo, L., Coupon, J., Arnouts, S., Hudelot, P., Ilbert, O., McCracken, H. J., Mellier, Y., Adami, C., Bel, J., Bolzonella, M., Bottini, D., Cappi, A., Cucciati, O., de la Torre, S., Franzetti, P., Fritz, A., Garilli, B., Iovino, A., Krywult, J., Le Brun, V., Le Fevre, O., Maccagni, D., Malek, K., Marulli, F., Meneux, B., Paioro, L., Polletta, M., Pollo, A., Scodeggio, M., Schlagenhaufer, H., Tasca, L., Tojeiro, R., Vergani, D., and Zanichelli, A. (2012). The power spectrum from the angular distribution of galaxies in the CFHTLS-Wide fields at redshift ~0.7. *MNRAS*, 421(1):251–261.
- Grieb, J. N., Sánchez, A. G., Salazar-Albornoz, S., Scoccimarro, R., Crocce, M., Vecchia, C. D., Montesano, F., Gil-Marín, H., Ross, A. J., Beutler, F., Rodríguez-Torres, S., Chuang, C.-H., Prada, F., Kitaura, F.-S., Cuesta, A. J., Eisenstein, D. J., Percival, W. J., Vargas-Magaña, M., Tinker, J. L., Tojeiro, R., Brownstein, J. R., Maraston, C., Nichol, R. C., Olmstead, M. D., Samushia, L., Seo, H.-J., Streblyanska, A., and bo Zhao, G. (2017). The clustering of galaxies in the completed SDSS-III baryon oscillation spectroscopic survey: Cosmological implications of the fourier space wedges of the final sample. *Monthly Notices of the Royal Astronomical Society*, page stw3384.
- Gunn, J. E. and Gott, J. Richard, I. (1972). On the Infall of Matter Into Clusters of Galaxies and Some Effects on Their Evolution. *ApJ*, 176:1.
- Hertzberg, M. P. (2014). Effective field theory of dark matter and structure formation: Semianalytical results. *Phys. Rev. D*, 89(4):043521.
- Howlett, C., Lewis, A., Hall, A., and Challinor, A. (2012). CMB power spectrum parameter degeneracies in the era of precision cosmology. *J. Cosmology Astropart. Phys.*, 2012(4):027.

- Hubble, E. (1929). A Relation between Distance and Radial Velocity among Extra-Galactic Nebulae. *Proceedings of the National Academy of Science*, 15(3):168–173.
- Huterer, D. and Shafer, D. L. (2018). Dark energy two decades after: observables, probes, consistency tests. *Reports on Progress in Physics*, 81(1):016901.
- Ivanov, M. M., Philcox, O. H. E., Nishimichi, T., Simonović, M., Takada, M., and Zaldarriaga, M. (2022). Precision analysis of the redshift-space galaxy bispectrum. *Phys. Rev. D*, 105(6):063512.
- Ivanov, M. M. and Sibiryakov, S. (2018). Infrared resummation for biased tracers in redshift space. *J. Cosmology Astropart. Phys.*, 2018(7):053.
- Ivanov, M. M., Simonović, M., and Zaldarriaga, M. (2020). Cosmological parameters from the BOSS galaxy power spectrum. *J. Cosmology Astropart. Phys.*, 2020(5):042.
- Jenkins, A., Frenk, C. S., Pearce, F. R., Thomas, P. A., Colberg, J. M., White, S. D. M., Couchman, H. M. P., Peacock, J. A., Efstathiou, G., and Nelson, A. H. (1998). Evolution of Structure in Cold Dark Matter Universes. *ApJ*, 499:20.
- Jeong, D. and Komatsu, E. (2009). Primordial Non-Gaussianity, Scale-dependent Bias, and the Bispectrum of Galaxies. *ApJ*, 703:1230–1248.
- Kaiser, N. (1984). On the spatial correlations of Abell clusters. ApJ, 284:L9–L12.
- Konstandin, T., Porto, R. A., and Rubira, H. (2019). The effective field theory of large scale structure at three loops. *J. Cosmology Astropart. Phys.*, 2019(11):027.
- Laureijs, R., Amiaux, J., Arduini, S., Auguères, J. L., Brinchmann, J., Cole, R., Cropper, M., Dabin, C., Duvet, L., Ealet, A., and et al. (2011). Euclid Definition Study Report. page arXiv:1110.3193.
- Lazanu, A., Giannantonio, T., Schmittfull, M., and Shellard, E. P. S. (2016). Matter bispectrum of large-scale structure: Three-dimensional comparison between theoretical models and numerical simulations. *Phys. Rev. D*, 93(8):083517.
- Lazeyras, T., Wagner, C., Baldauf, T., and Schmidt, F. (2016). Precision measurement of the local bias of dark matter halos. *J. Cosmology Astropart. Phys.*, 2:018.
- Lewis, A., Challinor, A., and Lasenby, A. (2000a). Efficient Computation of Cosmic Microwave Background Anisotropies in Closed Friedmann-Robertson-Walker Models. *ApJ*, 538(2):473–476.
- Lewis, A., Challinor, A., and Lasenby, A. (2000b). Efficient Computation of Cosmic Microwave Background Anisotropies in Closed Friedmann-Robertson-Walker Models. *ApJ*, 538(2):473–476.
- Luongo, O., Muccino, M., Colgáin, E. Ó., Sheikh-Jabbari, M. M., and Yin, L. (2022). Larger H<sub>0</sub> values in the CMB dipole direction. *Phys. Rev. D*, 105(10):103510.
- Ma, C.-P. and Bertschinger, E. (1995). Cosmological Perturbation Theory in the Synchronous and Conformal Newtonian Gauges. *ApJ*, 455:7.
- McDonald, P. and Roy, A. (2009). Clustering of dark matter tracers: generalizing bias for the coming era of precision LSS. *J. Cosmology Astropart. Phys.*, 2009(8):020.

- McEwen, J. E., Fang, X., Hirata, C. M., and Blazek, J. A. (2016). FAST-PT: a novel algorithm to calculate convolution integrals in cosmological perturbation theory. *J. Cosmology Astropart. Phys.*, 2016(9):015.
- Meiksin, A. and White, M. (1999). The growth of correlations in the matter power spectrum. *MNRAS*, 308:1179–1184.
- Migkas, K., Pacaud, F., Schellenberger, G., Erler, J., Nguyen-Dang, N. T., Reiprich, T. H., Ramos-Ceja, M. E., and Lovisari, L. (2021). Cosmological implications of the anisotropy of ten galaxy cluster scaling relations. *A&A*, 649:A151.
- Migkas, K., Reiprich, T., Pacaud, F., Lovisari, L., and Schellenberger, G. (2022). Probing the isotropy of the late Universe with galaxy clusters. In *44th COSPAR Scientific Assembly. Held 16-24 July*, volume 44, page 2988.
- Mirbabayi, M., Schmidt, F., and Zaldarriaga, M. (2015). Biased tracers and time evolution. *J. Cosmology Astropart. Phys.*, 2015(7):030–030.
- Mo, H., van den Bosch, F. C., and White, S. (2010). Galaxy Formation and Evolution.
- Moradinezhad Dizgah, A., Biagetti, M., Sefusatti, E., Desjacques, V., and Noreña, J. (2021). Primordial non-Gaussianity from biased tracers: likelihood analysis of real-space power spectrum and bispectrum. *J. Cosmology Astropart. Phys.*, 2021(5):015.
- More, S., Diemer, B., and Kravtsov, A. V. (2015). The Splashback Radius as a Physical Halo Boundary and the Growth of Halo Mass. *ApJ*, 810(1):36.
- Oddo, A., Rizzo, F., Sefusatti, E., Porciani, C., and Monaco, P. (2021). Cosmological parameters from the likelihood analysis of the galaxy power spectrum and bispectrum in real space. *J. Cosmology Astropart. Phys.*, 2021(11):038.
- Oddo, A., Sefusatti, E., Porciani, C., Monaco, P., and Sánchez, A. G. (2020a). Toward a robust inference method for the galaxy bispectrum: likelihood function and model selection. *J. Cosmology Astropart. Phys.*, 2020(3):056.
- Oddo, A., Sefusatti, E., Porciani, C., Monaco, P., and Sánchez, A. G. (2020b). Toward a robust inference method for the galaxy bispectrum: likelihood function and model selection. *J. Cosmology Astropart. Phys.*, 2020(3):056.
- Osato, K., Nishimichi, T., Bernardeau, F., and Taruya, A. (2019). Perturbation theory challenge for cosmological parameters estimation: Matter power spectrum in real space. *Phys. Rev. D*, 99(6):063530.
- Pajer, E. and van der Woude, D. (2018). Divergence of perturbation theory in large scale structures. *J. Cosmology Astropart. Phys.*, 2018(5):039.
- Pardede, K., Rizzo, F., Biagetti, M., Castorina, E., Sefusatti, E., and Monaco, P. (2022). Bispectrum-window convolution via Hankel transform. *J. Cosmology Astropart. Phys.*, 2022(10):066.

- Percival, W. J., Nichol, R. C., Eisenstein, D. J., Frieman, J. A., Fukugita, M., Loveday, J., Pope, A. C., Schneider, D. P., Szalay, A. S., Tegmark, M., Vogeley, M. S., Weinberg, D. H., Zehavi, I., Bahcall, N. A., Brinkmann, J., Connolly, A. J., and Meiksin, A. (2007). The Shape of the Sloan Digital Sky Survey Data Release 5 Galaxy Power Spectrum. *ApJ*, 657(2):645–663.
- Perlmutter, S., Aldering, G., Goldhaber, G., Knop, R. A., Nugent, P., Castro, P. G., Deustua, S., Fabbro, S., Goobar, A., Groom, D. E., Hook, I. M., Kim, A. G., Kim, M. Y., Lee, J. C., Nunes, N. J., Pain, R., Pennypacker, C. R., Quimby, R., Lidman, C., Ellis, R. S., Irwin, M., McMahon, R. G., Ruiz-Lapuente, P., Walton, N., Schaefer, B., Boyle, B. J., Filippenko, A. V., Matheson, T., Fruchter, A. S., Panagia, N., Newberg, H. J. M., Couch, W. J., and Supernova Cosmology Project (1999). Measurements of Omega and Lambda from 42 High-Redshift Supernovae. *ApJ*, 517:565–586.
- Philcox, O. H. E., Ivanov, M. M., Cabass, G., Simonović, M., Zaldarriaga, M., and Nishimichi, T. (2022). Cosmology with the redshift-space galaxy bispectrum monopole at one-loop order. *Phys. Rev. D*, 106(4):043530.
- Planck Collaboration, Ade, P. A. R., Aghanim, N., Arnaud, M., Ashdown, M., Aumont, J., Baccigalupi, C., Banday, A. J., Barreiro, R. B., Bartlett, J. G., and et al. (2016). Planck 2015 results. XIII. Cosmological parameters. *aap*, 594:A13.
- Planck Collaboration, Aghanim, N., Akrami, Y., Ashdown, M., Aumont, J., Baccigalupi, C., Ballardini, M., Banday, A. J., Barreiro, R. B., Bartolo, N., Basak, S., Battye, R., Benabed, K., Bernard, J. P., Bersanelli, M., Bielewicz, P., Bock, J. J., Bond, J. R., Borrill, J., Bouchet, F. R., Boulanger, F., Bucher, M., Burigana, C., Butler, R. C., Calabrese, E., Cardoso, J. F., Carron, J., Challinor, A., Chiang, H. C., Chluba, J., Colombo, L. P. L., Combet, C., Contreras, D., Crill, B. P., Cuttaia, F., de Bernardis, P., de Zotti, G., Delabrouille, J., Delouis, J. M., Di Valentino, E., Diego, J. M., Doré, O., Douspis, M., Ducout, A., Dupac, X., Dusini, S., Efstathiou, G., Elsner, F., Enßlin, T. A., Eriksen, H. K., Fantaye, Y., Farhang, M., Fergusson, J., Fernandez-Cobos, R., Finelli, F., Forastieri, F., Frailis, M., Fraisse, A. A., Franceschi, E., Frolov, A., Galeotta, S., Galli, S., Ganga, K., Génova-Santos, R. T., Gerbino, M., Ghosh, T., González-Nuevo, J., Górski, K. M., Gratton, S., Gruppuso, A., Gudmundsson, J. E., Hamann, J., Handley, W., Hansen, F. K., Herranz, D., Hildebrandt, S. R., Hivon, E., Huang, Z., Jaffe, A. H., Jones, W. C., Karakci, A., Keihänen, E., Keskitalo, R., Kiiveri, K., Kim, J., Kisner, T. S., Knox, L., Krachmalnicoff, N., Kunz, M., Kurki-Suonio, H., Lagache, G., Lamarre, J. M., Lasenby, A., Lattanzi, M., Lawrence, C. R., Le Jeune, M., Lemos, P., Lesgourgues, J., Levrier, F., Lewis, A., Liguori, M., Lilje, P. B., Lilley, M., Lindholm, V., López-Caniego, M., Lubin, P. M., Ma, Y. Z., Macías-Pérez, J. F., Maggio, G., Maino, D., Mandolesi, N., Mangilli, A., Marcos-Caballero, A., Maris, M., Martin, P. G., Martinelli, M., Martínez-González, E., Matarrese, S., Mauri, N., McEwen, J. D., Meinhold, P. R., Melchiorri, A., Mennella, A., Migliaccio, M., Millea, M., Mitra, S., Miville-Deschênes, M. A., Molinari, D., Montier, L., Morgante, G., Moss, A., Natoli, P., Nørgaard-Nielsen, H. U., Pagano, L., Paoletti, D., Partridge, B., Patanchon, G., Peiris, H. V., Perrotta, F., Pettorino, V., Piacentini, F., Polastri, L., Polenta, G., Puget, J. L., Rachen, J. P., Reinecke, M., Remazeilles, M., Renzi, A., Rocha, G., Rosset, C., Roudier, G., Rubiño-Martín, J. A., Ruiz-Granados, B., Salvati, L., Sandri, M., Savelainen, M., Scott, D., Shellard, E. P. S., Sirignano, C., Sirri, G., Spencer, L. D., Sunyaev, R., Suur-Uski, A. S., Tauber, J. A., Tavagnacco, D., Tenti, M., Toffolatti, L., Tomasi, M., Trombetti, T., Valenziano, L., Valiviita, J., Van Tent, B., Vibert, L., Vielva, P., Villa, F., Vittorio, N., Wandelt, B. D., Wehus, I. K.,

- White, M., White, S. D. M., Zacchei, A., and Zonca, A. (2020a). Planck 2018 results. VI. Cosmological parameters. *A&A*, 641:A6.
- Planck Collaboration, Akrami, Y., Arroja, F., Ashdown, M., Aumont, J., Baccigalupi, C., Ballardini, M., Banday, A. J., Barreiro, R. B., Bartolo, N., Basak, S., Benabed, K., Bernard, J. P., Bersanelli, M., Bielewicz, P., Bond, J. R., Borrill, J., Bouchet, F. R., Bucher, M., Burigana, C., Butler, R. C., Calabrese, E., Cardoso, J. F., Casaponsa, B., Challinor, A., Chiang, H. C., Colombo, L. P. L., Combet, C., Crill, B. P., Cuttaia, F., de Bernardis, P., de Rosa, A., de Zotti, G., Delabrouille, J., Delouis, J. M., Di Valentino, E., Diego, J. M., Doré, O., Douspis, M., Ducout, A., Dupac, X., Dusini, S., Efstathiou, G., Elsner, F., Enßlin, T. A., Eriksen, H. K., Fantaye, Y., Fergusson, J., Fernandez-Cobos, R., Finelli, F., Frailis, M., Fraisse, A. A., Franceschi, E., Frolov, A., Galeotta, S., Galli, S., Ganga, K., Génova-Santos, R. T., Gerbino, M., González-Nuevo, J., Górski, K. M., Gratton, S., Gruppuso, A., Gudmundsson, J. E., Hamann, J., Handley, W., Hansen, F. K., Herranz, D., Hivon, E., Huang, Z., Jaffe, A. H., Jones, W. C., Jung, G., Keihänen, E., Keskitalo, R., Kiiveri, K., Kim, J., Krachmalnicoff, N., Kunz, M., Kurki-Suonio, H., Lamarre, J. M., Lasenby, A., Lattanzi, M., Lawrence, C. R., Le Jeune, M., Levrier, F., Lewis, A., Liguori, M., Lilje, P. B., Lindholm, V., López-Caniego, M., Ma, Y. Z., Macías-Pérez, J. F., Maggio, G., Maino, D., Mandolesi, N., Marcos-Caballero, A., Maris, M., Martin, P. G., Martínez-González, E., Matarrese, S., Mauri, N., McEwen, J. D., Meerburg, P. D., Meinhold, P. R., Melchiorri, A., Mennella, A., Migliaccio, M., Miville-Deschênes, M. A., Molinari, D., Moneti, A., Montier, L., Morgante, G., Moss, A., Münchmeyer, M., Natoli, P., Oppizzi, F., Pagano, L., Paoletti, D., Partridge, B., Patanchon, G., Perrotta, F., Pettorino, V., Piacentini, F., Polenta, G., Puget, J. L., Rachen, J. P., Racine, B., Reinecke, M., Remazeilles, M., Renzi, A., Rocha, G., Rubiño-Martín, J. A., Ruiz-Granados, B., Salvati, L., Savelainen, M., Scott, D., Shellard, E. P. S., Shiraishi, M., Sirignano, C., Sirri, G., Smith, K., Spencer, L. D., Stanco, L., Sunyaev, R., Suur-Uski, A. S., Tauber, J. A., Tavagnacco, D., Tenti, M., Toffolatti, L., Tomasi, M., Trombetti, T., Valiviita, J., Van Tent, B., Vielva, P., Villa, F., Vittorio, N., Wandelt, B. D., Wehus, I. K., Zacchei, A., and Zonca, A. (2020b). Planck 2018 results. IX. Constraints on primordial non-Gaussianity. A&A, 641:A9.
- Porto, R. A., Senatore, L., and Zaldarriaga, M. (2014). The Lagrangian-space Effective Field Theory of large scale structures. *J. Cosmology Astropart. Phys.*, 5:22.
- Potter, D., Stadel, J., and Teyssier, R. (2017). PKDGRAV3: beyond trillion particle cosmological simulations for the next era of galaxy surveys. *Computational Astrophysics and Cosmology*, 4(1):2.
- Pozzetti, L., Hirata, C. M., Geach, J. E., Cimatti, A., Baugh, C., Cucciati, O., Merson, A., Norberg, P., and Shi, D. (2016). Modelling the number density of htters for future spectroscopic near-ir space missions. *A&A*, 590:A3.
- Pueblas, S. and Scoccimarro, R. (2009). Generation of vorticity and velocity dispersion by orbit crossing. *Phys. Rev. D*, 80(4):043504.
- Riess, A. G., Filippenko, A. V., Challis, P., Clocchiatti, A., Diercks, A., Garnavich, P. M., Gilliland, R. L., Hogan, C. J., Jha, S., Kirshner, R. P., Leibundgut, B., Phillips, M. M., Reiss, D., Schmidt, B. P., Schommer, R. A., Smith, R. C., Spyromilio, J., Stubbs, C., Suntzeff, N. B., and Tonry, J. (1998). Observational Evidence from Supernovae for an Accelerating Universe and a Cosmological Constant. *AJ*, 116:1009–1038.

- Riess, A. G., Yuan, W., Macri, L. M., Scolnic, D., Brout, D., Casertano, S., Jones, D. O., Murakami, Y., Anand, G. S., Breuval, L., Brink, T. G., Filippenko, A. V., Hoffmann, S., Jha, S. W., D'arcy Kenworthy, W., Mackenty, J., Stahl, B. E., and Zheng, W. (2022). A Comprehensive Measurement of the Local Value of the Hubble Constant with 1 km s<sup>-1</sup> Mpc<sup>-1</sup> Uncertainty from the Hubble Space Telescope and the SH0ES Team. *ApJ*, 934(1):L7.
- Robertson, H. P. (1935). Kinematics and World-Structure. ApJ, 82:284.
- Rubin, V. C. and Ford, W. Kent, J. (1970). Rotation of the Andromeda Nebula from a Spectroscopic Survey of Emission Regions. *ApJ*, 159:379.
- Sánchez, A. G., Scoccimarro, R., Crocce, M., Grieb, J. N., Salazar-Albornoz, S., Vecchia, C. D., Lippich, M., Beutler, F., Brownstein, J. R., Chuang, C.-H., Eisenstein, D. J., Kitaura, F.-S., Olmstead, M. D., Percival, W. J., Prada, F., Rodríguez-Torres, S., Ross, A. J., Samushia, L., Seo, H.-J., Tinker, J., Tojeiro, R., Vargas-Magaña, M., Wang, Y., and Zhao, G.-B. (2016). The clustering of galaxies in the completed SDSS-III baryon oscillation spectroscopic survey: Cosmological implications of the configuration-space clustering wedges. *Monthly Notices of the Royal Astronomical Society*, 464(2):1640–1658.
- Scaramella, R., Vettolani, G., and Zamorani, G. (1991). The Distribution of Clusters of Galaxies within 300 MPC H -1 and the Crossover to an Isotropic and Homogeneous Universe. *ApJ*, 376:L1.
- Schechter, P. (1976). An analytic expression for the luminosity function for galaxies. *ApJ*, 203:297–306.
- Schneider, P. (2009). Cosmology Lecture Notes WS 2009/10.
- Scoccimarro, R., Colombi, S., Fry, J. N., Frieman, J. A., Hivon, E., and Melott, A. (1998). Nonlinear Evolution of the Bispectrum of Cosmological Perturbations. *Astrophys. J.*, 496:586–604.
- Scoccimarro, R., Colombi, S., Fry, J. N., Frieman, J. A., Hivon, E., and Melott, A. (1998). Nonlinear evolution of the bispectrum of cosmological perturbations. *ApJ*, 496:586.
- Sefusatti, E., Crocce, M., Scoccimarro, R., and Couchman, H. M. P. (2016). Accurate estimators of correlation functions in Fourier space. *MNRAS*, 460(4):3624–3636.
- Senatore, L. and Zaldarriaga, M. (2015). The IR-resummed Effective Field Theory of Large Scale Structures. *J. Cosmology Astropart. Phys.*, 2015(2):013.
- Sheth, R. K., Chan, K. C., and Scoccimarro, R. (2013). Nonlocal lagrangian bias. *Phys. Rev. D*, 87:083002.
- Sofue, Y. and Rubin, V. (2001). Rotation Curves of Spiral Galaxies. ARA&A, 39:137–174.
- Springel, V. (2005). The cosmological simulation code GADGET-2. MNRAS, 364:1105–1134.
- Steele, T. and Baldauf, T. (2021). Precise calibration of the one-loop bispectrum in the effective field theory of large scale structure. *Phys. Rev. D*, 103(2):023520.

- Taruya, A., Nishimichi, T., Saito, S., and Hiramatsu, T. (2009). Nonlinear evolution of baryon acoustic oscillations from improved perturbation theory in real and redshift spaces. *Phys. Rev. D*, 80(12):123503.
- Villaescusa-Navarro, F., Hahn, C., Massara, E., Banerjee, A., Delgado, A. M., Ramanah, D. K., Charnock, T., Giusarma, E., Li, Y., Allys, E., Brochard, A., Uhlemann, C., Chiang, C.-T., He, S., Pisani, A., Obuljen, A., Feng, Y., Castorina, E., Contardo, G., Kreisch, C. D., Nicola, A., Alsing, J., Scoccimarro, R., Verde, L., Viel, M., Ho, S., Mallat, S., Wandelt, B., and Spergel, D. N. (2020). The Quijote Simulations. *ApJS*, 250(1):2.
- Vlah, Z., Seljak, U., Yat Chu, M., and Feng, Y. (2016). Perturbation theory, effective field theory, and oscillations in the power spectrum. *J. Cosmology Astropart. Phys.*, 2016(3):057.
- Walker, A. G. (1937). On Milne's Theory of World-Structure. *Proceedings of the London Mathematical Society*, 42:90–127.
- White, M. (2014). The Zel'dovich approximation. MNRAS, 439(4):3630–3640.
- Zel'dovich, Y. B. (1970). Gravitational instability: An approximate theory for large density perturbations. *A&A*, 5:84–89.
- Zwicky, F. (1933). Die Rotverschiebung von extragalaktischen Nebeln. *Helvetica Physica Acta*, 6:110–127.

## APPENDIX A

## **Published papers**

A.1 The reach of next-to-leading-order perturbation theory for the matter bispectrum

Advance Access publication 2022 March 4



# The reach of next-to-leading-order perturbation theory for the matter bispectrum

Davit Alkhanishvili, <sup>1,2\*</sup> Cristiano Porciani, <sup>1\*</sup> Emiliano Sefusatti, <sup>3,4,5\*</sup> Matteo Biagetti, <sup>3,4,5,6</sup> Andrei Lazanu <sup>0</sup>, <sup>7</sup> Andrea Oddo <sup>4,6</sup> and Victoria Yankelevich <sup>08</sup>

Accepted 2022 February 28. Received 2022 February 23; in original form 2021 July 16

#### **ABSTRACT**

We provide a comparison between the matter bispectrum derived with different flavours of perturbation theory at next-to-leading order and measurements from an unprecedentedly large suite of N-body simulations. We use the  $\chi^2$  goodness-of-fit test to determine the range of accuracy of the models as a function of the volume covered by subsets of the simulations. We find that models based on the effective field theory (EFT) approach have the largest reach, standard perturbation theory has the shortest, and 'classical' resummed schemes lie in between. The gain from EFT, however, is less than in previous studies. We show that the estimated range of accuracy of the EFT predictions is heavily influenced by the procedure adopted to fit the amplitude of the counterterms. For the volumes probed by galaxy redshift surveys, our results indicate that it is advantageous to set three counterterms of the EFT bispectrum to zero and measure the fourth from the power spectrum. We also find that large fluctuations in the estimated reach occur between different realizations. We conclude that it is difficult to unequivocally define a range of accuracy for the models containing free parameters. Finally, we approximately account for systematic effects introduced by the N-body technique either in terms of a scale- and shape-dependent bias or by boosting the statistical error bars of the measurements (as routinely done in the literature). We find that the latter approach artificially inflates the reach of EFT models due to the presence of tunable parameters.

**Key words:** methods: statistical – theory – large-scale structure of Universe.

#### 1 INTRODUCTION

The three-point correlation function or its Fourier counterpart, the bispectrum, are the lowest-order clustering statistics that characterize departures from Gaussianity in the galaxy distribution. Although these statistics have a long history dating back to the earliest galaxy redshift surveys (Peebles & Groth 1975; Gaztanaga 1994; Scoccimarro et al. 2001; Verde et al. 2002; Gaztañaga et al. 2005; Pan & Szapudi 2005; Kulkarni et al. 2007; McBride et al. 2011; Gil-Marín et al. 2015a, b, 2017; Slepian et al. 2017a, b, 2018; Pearson & Samushia 2018; Gualdi et al. 2019), their importance has always been rather marginal. On the contrary, they are expected to play a key role to fully exploit the potential of forthcoming observations such as those conducted with the Dark-Energy Spectroscopic Instrument (DESI; DESI Collaboration 2016) and the *Euclid* satellite (Laureijs et al. 2011) by improving the estimation of cosmological parameters and breaking degeneracies that emerge from the analysis of the power

spectrum (e.g Chudaykin & Ivanov 2019; Yankelevich & Porciani 2019; Barreira 2020; Gualdi & Verde 2020; Heinrich & Doré 2020; Agarwal et al. 2021; Eggemeier et al. 2021; Hahn & Villaescusa-Navarro 2021; Moradinezhad Dizgah et al. 2021; Samushia, Slepian & Villaescusa-Navarro 2021).

In order to achieve this goal, it is crucial that accurate theoretical models are available in the mildly non-linear regime of perturbation growth. The information we want to retrieve, in fact, is distributed over many triangular configurations the number of which grows rapidly with the minimum considered length scale (Sefusatti & Scoccimarro 2005; Sefusatti et al. 2006; Chan & Blot 2017). Therefore, an essential feature of the models is that they give accurate predictions over the widest possible range of scales. In this paper, we investigate the accuracy of perturbative models for the bispectrum of the matter density field against large suites of *N*-body simulations. This way we test the primary building block of models for the galaxy bispectrum that should also address additional sources of non-linearities (e.g. galaxy biasing and redshift-space distortions) and discreteness effects.

<sup>&</sup>lt;sup>1</sup>Argelander Institut für Astronomie der Universität Bonn, Auf dem Hügel 71, D-53121 Bonn, Germany

<sup>&</sup>lt;sup>2</sup>Member of the International Max Planck Research School (IMPRS) for Astronomy and Astrophysics at the Universities of Bonn and Cologne, Germany

<sup>&</sup>lt;sup>3</sup>Istituto Nazionale di Astrofisica, Osservatorio Astronomico di Trieste, via Tiepolo 11, I-34143 Trieste, Italy

<sup>&</sup>lt;sup>4</sup>Institute for Fundamental Physics of the Universe, via Beirut 2, I-34151 Trieste, Italy

<sup>&</sup>lt;sup>5</sup>Istituto Nazionale di Fisica Nucleare, Sezione di Trieste, Via Valerio 2, I-34127 Trieste, Italy

<sup>&</sup>lt;sup>6</sup>SISSA - International School for Advanced Studies, Via Bonomea 265, I-34136 Trieste, Italy

Laboratoire de Physique de l'Ecole normale supérieure, ENS, Université PSL, CNRS, Sorbonne Université, Université de Paris, F-75005 Paris, France

<sup>&</sup>lt;sup>8</sup>Astrophysics Research Institute, Liverpool John Moores University, Liverpool L3 5RF, UK

<sup>\*</sup>E-mail: daalkh@astro.uni-bonn.de (DA); cporcian@uni-bonn.de (CP); emiliano.sefusatti@inaf.it (ES)

#### 4962 D. Alkhanishvili et al.

Standard perturbation theory (SPT; see Bernardeau et al. 2002, for a review) has long been the workhorse for theoretical predictions on clustering statistics in cosmology. Based on the socalled single-stream approximation (in which velocity dispersion is neglected), it expands the fluid equations for a self-gravitating pressureless fluid in terms of the linear density contrast and velocity potential. The evolution of the bispectrum generated from Gaussian initial conditions to the lowest non-vanishing order in SPT was pioneered by Fry (1984). Next-to-leading-order (NLO) corrections were then discussed in Scoccimarro (1997) and Scoccimarro et al. (1998). Over the years, alternative schemes have been developed to model the growth of cosmological perturbations and the calculation of the matter bispectrum has been combined with techniques that resum infinite subsets of perturbative contributions in both the Eulerian (Crocce & Scoccimarro 2006a, b; Bernardeau, Crocce & Scoccimarro 2008, 2012; Crocce, Scoccimarro & Bernardeau 2012) and the Lagrangian descriptions (Matsubara 2008; Rampf & Wong 2012). More recently, following a general trend in theoretical physics, an effective field theory (EFT) that approximately describes gravitational instability on 'perturbative' scales and averages over small-scale fluctuations provided a new framework to model the matter bispectrum (Angulo et al. 2015; Baldauf et al. 2015c). In this case, feedback from the small scales to the large scales is expressed in terms of a number of parameters that are fit to observational data or numerical simulations. This construction appears to be successful in extending the range of accuracy of the models. In this work, we compare the different approaches ranging from SPT to EFT with two large suites of N-body simulations. Since many of the forthcoming observational probes will concentrate on intermediate redshifts, we only consider data at redshift z = 1.

Although several authors already tried to determine the domain of accuracy (sometimes dubbed the reach or k-reach) of different perturbative predictions for the bispectrum (e.g. Angulo et al. 2015; Baldauf, Mercolli & Zaldarriaga 2015b; Lazanu et al. 2016; Steele & Baldauf 2021), our work critically evidences that the results depend on a number of factors that have been rarely explored in depth. In the first place, they depend on the overall volume covered by the N-body simulations which determines the size of the statistical uncertainty affecting the measurements. Besides, when these random errors are small, estimates of the reach are influenced by systematic shifts due to imperfections of the Nbody technique (which are not easy to model and to account for). Furthermore, in the case of the EFT, on top of the sheer goodnessof-fit criterion, one should also consider the consistency (as a function of the minimum length scale under study) of the bestfitting values for the parameters that determine the amplitude of the EFT corrections. In addition, the number of free parameters and the range of scales used in the fitting procedure might influence the inferred range of accuracy. By considering all these effects, we provide a much more comprehensive investigation of the reach of perturbative models for the matter bispectrum at NLO than what is already available in the literature. As a byproduct of our study, we also obtain analogous results for the matter power spectrum which we use in order to calibrate the EFT corrections for the bispectrum.

This paper is organized as follows. In Section 2, we briefly review the PT models we use while, in Section 3, we introduce the simulation suites and the bispectrum measurements. In Section 4, we describe how the perturbative models are implemented in practice and how we use the  $\chi^2$  goodness-of-fit test to determine their range of accuracy.

Our results are presented and critically discussed in Section 5. Finally, we summarize our findings in Section 6.

#### 2 PERTURBATION THEORY

Given the Fourier transform of the mass-density contrast at redshift z,  $\delta(\mathbf{k}, z)$ , the matter power spectrum, P(k, z), and the bispectrum,  $B(\mathbf{k}_1, \mathbf{k}_2, \mathbf{k}_3, z)$ , can be defined in terms of the two- and three-point equal-time correlators as

$$\langle \delta(\mathbf{k}_1, z) \, \delta(\mathbf{k}_2, z) \rangle = (2\pi)^3 \delta_{\mathcal{D}}(\mathbf{k}_{12}) \, P(k_1, z), \tag{1}$$

and

$$\langle \delta(\mathbf{k}_1, z) \, \delta(\mathbf{k}_2, z) \, \delta(\mathbf{k}_3, z) \rangle = (2\pi)^3 \delta_{D}(\mathbf{k}_{123}) \, B(\mathbf{k}_1, \mathbf{k}_2, \mathbf{k}_3, z), \tag{2}$$

where the angle brackets denote averaging over an ensemble of realizations,  $\delta_D$  is the Dirac delta function, and  $\mathbf{k}_{i...j} \equiv \mathbf{k}_i + \cdots + \mathbf{k}_j$ . In this section, we briefly review a number of perturbative methods that have been used to model P(k, z) and  $B(\mathbf{k}_1, \mathbf{k}_2, \mathbf{k}_3, z)$  on quasilinear scales and that we will test against numerical simulations.

#### 2.1 Standard perturbation theory

In the standard model of cosmology, the formation of the large-scale structure of the Universe is dominated by a dark-matter component. Although the physical origin of dark matter is still unclear, it is generally assumed that, on macroscopic scales, it can be modelled as a self-gravitating medium governed by the collisionless Boltzmann (or Vlasov) equation in a cosmological background. The Vlasov–Poisson system can be written as a hierarchy of coupled evolution equations for the velocity moments of the phase-space distribution function (the so-called macroscopic transport equations).

SPT assumes that the dark matter can be treated as a pressureless ideal fluid governed by the continuity, Euler, and Poisson equations. These are obtained by setting to zero the second velocity moment of the phase-space distribution function and thus correspond to considering the so-called 'single-stream' regime in which there is a well-defined velocity everywhere.

By considering irrotational flows only, the dynamic equations are written in terms of two scalar fields, namely the matter-density contrast and the divergence of the peculiar velocity. The solution of the linearized transport equations is  $\delta^{(1)}(\mathbf{k},z) \equiv D(z)\,\delta_{\mathrm{L}}(\mathbf{k})$ , where D(z) denotes the linear growth factor and  $\delta_{\mathrm{L}}(\mathbf{k})$  is the linear solution at the time in which D=1. Following an established practice, we set D=1 at the present time, corresponding to z=0.

The fastest growing solution for  $\delta(\mathbf{k},z)$  is written as an expansion in terms of the linear density contrast. In particular, if we consider the Einstein-de Sitter (EdS) cosmological model, it follows that

$$\delta(\mathbf{k}, z) = \sum_{n=1}^{\infty} [D(z)]^n \, \delta^{(n)}(\mathbf{k}), \tag{3}$$

with

$$\delta^{(n)}(\mathbf{k}) = \int \frac{\mathrm{d}^3 \mathbf{k}_1 \cdots \mathrm{d}^3 \mathbf{k}_n}{(2\pi)^{3(n-1)}} \, \delta_{\mathrm{D}}(\mathbf{k} - \mathbf{k}_{1\cdots n}) \, F_n(\mathbf{k}_1, \dots, \mathbf{k}_n)$$

$$\times \, \delta_{\mathrm{L}}(\mathbf{k}_1) \cdots \delta_{\mathrm{L}}(\mathbf{k}_n), \tag{4}$$

where the (symmetrized) kernels  $F_n$  describe the gravitational coupling between Fourier modes of the linear solution and can be obtained by recursion relations (Goroff et al. 1986).

Once the statistical properties of  $\delta_L(\mathbf{k})$  have been specified, the expressions above allow us to derive perturbative expansions for the power spectrum and the bispectrum of the matter density contrast.

These are conveniently computed by following a diagrammatic approach which is analogous to the Feynman diagrams in quantum electrodynamics (e.g. Bernardeau et al. 2002). We classify as 'tree-level' all terms associated with tree diagrams (in the sense of graph theory) and as 'loop corrections' those associated with diagrams containing *n*-loops (and that require *n* 3D integrations).

Under the assumption that  $\delta_L(\mathbf{k})$  is a Gaussian random field, the leading-order term for P(k, z) coincides with the linear power spectrum,  $P_{\text{SPT}}^{\text{tree}}(k, z) = [D(z)]^2 P_L(k)$ , where  $\langle \delta_L(\mathbf{k}) \delta_L(\mathbf{k}') \rangle = (2\pi)^3 \delta_D(\mathbf{k} + \mathbf{k}') P_L(k)$ , while, for the bispectrum, we have

$$B_{\text{SPT}}^{\text{tree}}(\mathbf{k}_1, \mathbf{k}_2, \mathbf{k}_3, z) = 2 [D(z)]^4 F_2(\mathbf{k}_1, \mathbf{k}_2) P_{\text{L}}(k_1) P_{\text{L}}(k_2)$$

$$+ 2 \text{ perms.}$$
 (5)

Accounting for the NLO corrections, we obtain

$$P_{\rm SPT}(k,z) \simeq P_{\rm SPT}^{\rm tree}(k,z) + P_{\rm SPT}^{\rm 1-loop}(k,z), \tag{6}$$

$$B_{\text{SPT}}(\mathbf{k}_1, \mathbf{k}_2, \mathbf{k}_3, z) \simeq B_{\text{SPT}}^{\text{tree}}(\mathbf{k}_1, \mathbf{k}_2, \mathbf{k}_3, z)$$

+ 
$$B_{\text{SPT}}^{\text{1-loop}}(\mathbf{k}_1, \mathbf{k}_2, \mathbf{k}_3, z)$$
. (7)

Their explicit expressions are given in Appendix A.

On large scales and at early times, tree-level SPT provides an accurate description of both the matter power spectrum and bispectrum. At late times, however, one-loop corrections overpredict P on mildly non-linear scales ( $k \sim 0.1\,h\,{\rm Mpc}^{-1}$ , Crocce & Scoccimarro 2006a; Carlson, White & Padmanabhan 2009; Taruya et al. 2009) and higher-order terms do not improve the quality of the predictions (e.g. Blas, Garny & Konstandin 2014). The reason for the breakdown of SPT is well understood: loop integrals extend to scales at which the assumptions of the theory do not apply (e.g. due to the generation of vorticity and velocity dispersion at orbit crossing, Pueblas & Scoccimarro 2009) and physics becomes non-perturbative. The failure of SPT on small scales thus corrupts its predictions for the large scales.

#### 2.2 Renormalized perturbation theory

Higher-order SPT corrections in the expansions for the matter power spectrum and the bispectrum may have larger amplitudes than lowerorder ones. In other words, increasing the order of the expansions does not necessarily improve their accuracy (Crocce & Scoccimarro 2006a; Blas et al. 2014). Renormalized perturbation theory (RPT; Crocce & Scoccimarro 2006a, b, 2008; Bernardeau et al. 2008, 2012; Crocce et al. 2012) forms one of the first attempts to overcome the shortcomings of SPT (for an approach based on the renormalization group, see Matarrese & Pietroni 2007; Pietroni 2008). In RPT, infinite subsets of SPT diagrams are resummed and organized in terms of multipoint propagators defined as the ensemble average of the infinitesimal variation of the evolved cosmic fields with respect to the linear solutions (see Appendix B). A key property is that all the statistical quantities, such as the power spectra and the bispectra, can be expressed in terms of the multipoint propagators. This is known as the multipoint-propagator expansion or  $\Gamma$ -expansion.

RPT has two main advantages over SPT. First, all the contributions to the power spectrum are positive and adding higher-order terms improves the range of accuracy of the theory as no cancellations occur between successive loop corrections. Secondly, the exponential factor appearing in the high-*k* limit of the multipoint propagators effectively damps the contributions to the loop integrals outside the range of validity of the expansion, thus preventing some of the issues which occur in SPT.

One can construct a matching scheme for any multipoint propagator which smoothly interpolates between the resummed behaviour in the high-k limit and the SPT results at low k (Bernardeau et al. 2012; Crocce et al. 2012; Taruya et al. 2012). In this paper, we adopt the form derived in Taruya et al. (2012) which is known as regularized PT (REGPT). An alternative matching scheme (dubbed MPTBREEZE) has been proposed by Crocce et al. (2012) and implemented for the bispectrum in Lazanu et al. (2016). We have verified that REGPT and MPTBREEZE give nearly identical results and, for this reason, there is no point in considering both here.

#### 2.3 Lagrangian perturbation theory

In the Lagrangian approach to fluid dynamics, the trajectories of the fluid elements are characterized in terms of the displacement field  $\Psi(\mathbf{p},t)$  which links the Lagrangian position  $\mathbf{p}$  and the Eulerian position  $\mathbf{x}$  (at time t) through the relation  $\mathbf{x}(\mathbf{p},t) = \mathbf{p} + \Psi(\mathbf{p},t)$ . Lagrangian perturbation theory (LPT) is derived by using  $\Psi(\mathbf{p},t)$  as a perturbative variable (e.g. Zel'dovich 1970; Moutarde et al. 1991; Catelan 1995). In this framework, the Eulerian matter density can be expressed as

$$\delta(\mathbf{k}) = \int d^3 \mathbf{p} \, e^{-i\mathbf{k}\cdot\mathbf{p}} \left[ e^{-i\mathbf{k}\cdot\Psi(\mathbf{p})} - 1 \right], \tag{8}$$

(where we do not write the time dependence explicitly to simplify notation) which allows us to write an expression for the power spectrum

$$P(\mathbf{k}) = \int d^3 \Delta_{12} \, e^{-i\mathbf{k}\cdot\Delta_{12}} \left[ \langle e^{-i\mathbf{k}\cdot[\Psi(\mathbf{p_1})-\Psi(\mathbf{p_2})]} \rangle - 1 \right], \tag{9}$$

and the bispectrum

$$B(\mathbf{k}_{1}, \mathbf{k}_{2}, \mathbf{k}_{3}) = \int d^{3} \Delta_{12} \int d^{3} \Delta_{13} e^{-i\mathbf{k}\cdot(\Delta_{12} + \Delta_{13})}$$

$$\times \left[ \langle e^{-i\mathbf{k}_{2}\cdot[\Psi(\mathbf{p}_{1}) - \Psi(\mathbf{p}_{2})] - i\mathbf{k}_{3}\cdot[\Psi(\mathbf{p}_{1}) - \Psi(\mathbf{p}_{3})]} \rangle - 1 \right], \quad (10)$$

where  $\Delta_{ij} \equiv \mathbf{p_i} - \mathbf{p_j}$ , and the expectation value only depends on the separation  $\Delta_{12}$ ,  $\Delta_{13}$  due to homogeneity (Fisher & Nusser 1996; Taylor & Hamilton 1996; Matsubara 2008; Rampf & Wong 2012). A perturbative expansion of equations (9) and (10) can then be obtained by means of the cumulant expansion theorem

$$\langle e^{-iX} \rangle = \exp\left[\sum_{N=1}^{\infty} \frac{(-i)^N}{N!} \langle X^N \rangle_c\right],$$
 (11)

where  $\langle X^N \rangle_c$  represents the  $N^{\text{th}}$  order cumulant of the random variable X. Expanding the powers of X with the binomial theorem, two types of terms are obtained: those depending on  $\Psi$  at one point, and those depending on  $\Psi$  at multiple points. It turns out that, if both sets of terms are expanded to the same perturbative order, the 'classical' LPT results coincide with the SPT expressions for both the power spectrum and the bispectrum (Matsubara 2008; Rampf & Wong 2012).

#### 2.4 Resummed Lagrangian perturbation theory

On closer inspection, it emerges the classical LPT predictions for P and B can be improved by reorganizing the perturbative expansion. The key issue is that, for large Lagrangian separations, the terms depending on  $\Psi$  at one point are much larger than those depending on  $\Psi$  at multiple points. It thus makes sense to keep the first set of terms inside the argument of the exponential and use the cumulant expansion only for the second set (Matsubara 2008; Rampf & Wong

2012). This approach is generally referred to as resummed LPT (RLPT) as it corresponds to a partial resummation of the perturbative expansion. The resulting formulae for calculating P and B to NLO are presented in Appendix C. In Lazanu et al. (2016), it has been shown that the RLPT predictions are similar to those of MPTBREEZE.

#### 2.5 Effective field theory of large-scale structure

Effective theories have become a widely used tool in modern physics. In a system characterized by a wide range of scales, they isolate a set of degrees of freedom and describe them with a simplified model without having to deal with the complex (and often unknown) underlying dynamics. The impact of the physics one wishes to neglect on the degrees of freedom one desires to study is computed as a perturbation theory in terms of one or more expansion parameters.

The EFT of large-scale structure (EFT; Baumann et al. 2012; Carrasco, Hertzberg & Senatore 2012; Carrasco et al. 2014a, b; Hertzberg 2014; Porto, Senatore & Zaldarriaga 2014; Senatore & Zaldarriaga 2015) attempts to provide an effective description of the long-wavelength modes of the matter density field by integrating out (i.e. averaging over) the short-wavelength ones. Contrary to the models introduced in the previous sections, the EFT does not rely on the single-stream approximation and considers an effective stress tensor that is expressed in terms of all operators of the longwavelength density and velocity fields (and their derivatives) allowed by the symmetries of the problem: the equivalence principle, along with the assumption of statistical isotropy and homogeneity. The effective stress tensor is Taylor expanded in the long-wavelength fluctuations giving rise to an infinite series of unknown parameters each associated with a perturbative order. These parameters can be treated as coupling constants in the Wilsonian approach to renormalization. We can imagine that the theory contains a cutoff (i.e. the loop corrections are integrated up to a maximum wavenumber) and the couplings of the effective theory can be changed to enforce that the physics at low k is always the same when the cutoff is changed. Therefore, the parameters of the effective theory fulfil two purposes. In the EFT expressions for observables, they generate 'counterterms' which can be used to cancel out the ultraviolet (UV) sensitivity of the loop integrals in SPT (i.e. their dependence on the cutoff scale). This can be done order by order in perturbation theory. Moreover, the remaining cutoff-independent part of the counterterms should actually quantify the impact of the non-perturbative physics on the long-wavelength modes by introducing new 'effective' interactions among long-wavelength modes. The amplitude of this part, however, cannot be derived from the EFT (which is blind to smallscale physics) and must be fixed empirically by comparison with numerical simulations or marginalized over in the analysis of actual observational data (see e.g. d'Amico et al. 2020; Ivanov, Simonović & Zaldarriaga 2020).

EFT assumes the existence of a scale, generally indicated in terms of the wavenumber  $k_{\rm NL}$ , around which physics becomes non-perturbative and the effective description becomes meaningless. Several lines of reasoning suggest that the derivative expansion of the long-wavelength fields can be organized so that the expansion parameter of the perturbation theory is  $k/k_{\rm NL}$ , meaning that more and more terms should be considered to get accurate expressions for the correlators of the matter field as k approaches  $k_{\rm NL}$ .

The fact that perturbations of all wavelengths (barring virialized structures) evolve on similar time-scales constitutes a complication of the theory. It follows from this that the EFT is non-local in time, i.e. the long-wavelength perturbations depend on the entire past history of the short-wavelength modes. This is difficult to treat and, in practical applications, the local-in-time approximation is almost invariably invoked. We adopt the same strategy in our study. In particular, we focus on the specific parametrization of the counterterms appearing in the one-loop expressions for the matter power spectrum and bispectrum presented in Angulo et al. (2015). Considering the linear Taylor approximation of the effective stress tensor in the long-wavelength perturbations gives the EFT power spectrum to NLO (Carrasco et al. 2014b)

$$P_{\text{EFT}}(k, z) = P_{\text{SPT}}(k, z) + P_{c_0}(k, z),$$
 (12)

where the tree-level counterterm is given by

$$P_{c_0}(k, z) = -2 c_0(z) [D(z)]^2 k^2 P_{L}(k), \qquad (13)$$

and  $c_0$  is undetermined by the theory. In terms of the effective speed of sound for the perturbations,  $c_{s(1)}(z)$ , we have  $\bar{c}_0 \equiv (2\pi) \, [D(z)]^\zeta \, [c_{s(1)}(z)]^2 / k_{\rm NL}^2$  (where  $\zeta$  denotes a real constant arising from the time dependence of the effective stress tensor, see below for further details). Note that our  $c_0$  relates to the parameter  $\bar{c}_1$  introduced by Angulo et al. (2015) as  $c_0 \equiv \bar{c}_1 \, [D(z)]^\zeta$ , where  $[D(z)]^{n+\zeta}$  is the assumed growth factor of the EFT corrections to the SPT density fluctuations of order n.

Similarly, for the bispectrum to NLO, EFT gives four counterterms (Angulo et al. 2015; Baldauf et al. 2015b)

$$B_{\text{EFT}} = B_{\text{SPT}} + B_{c_0} + B_{c_1} + B_{c_2} + B_{c_3}. \tag{14}$$

(where the dependence on  $\mathbf{k}_1$ ,  $\mathbf{k}_2$ ,  $\mathbf{k}_3$  and z is left implicit to simplify notation), one of which is also proportional to  $c_0$ 

$$B_{c_0} = c_0(z) [D(z)]^4 \left[ 2 P_{L}(k_1) P_{L}(k_2) \tilde{F}_2^{(s)}(\mathbf{k}_1, \mathbf{k}_2) + 2 \text{ perms.} \right]$$

$$- 2 k_1^2 P_{L}(k_1) P_{L}(k_2) F_2(\mathbf{k}_1, \mathbf{k}_2) + 5 \text{ perms.} , \qquad (15)$$

with

$$\tilde{F}_{2}^{(s)}(\mathbf{k}_{1}, \mathbf{k}_{2}) = -\frac{1}{(1+\zeta)(7+2\zeta)} \left[ \left( 5 + \frac{113\zeta}{14} + \frac{17\zeta^{2}}{7} \right) \right] \\
\times \left( k_{1}^{2} + k_{2}^{2} \right) + \left( 7 + \frac{148\zeta}{7} + \frac{48\zeta^{2}}{7} \right) \mathbf{k}_{1} \cdot \mathbf{k}_{2} \\
+ \left( 2 + \frac{59\zeta}{7} + \frac{18\zeta^{2}}{7} \right) \left( \frac{1}{k_{1}^{2}} + \frac{1}{k_{2}^{2}} \right) (\mathbf{k}_{1} \cdot \mathbf{k}_{2})^{2} \\
+ \left( \frac{7}{2} + \frac{9\zeta}{2} + \zeta^{2} \right) \left( \frac{k_{1}^{2}}{k_{2}^{2}} + \frac{k_{2}^{2}}{k_{1}^{2}} \right) \\
\times \mathbf{k}_{1} \cdot \mathbf{k}_{2} + \left( \frac{20\zeta}{7} + \frac{8\zeta^{2}}{7} \right) \frac{(\mathbf{k}_{1} \cdot \mathbf{k}_{2})^{3}}{k_{1}^{2}k_{2}^{2}} \right]. \tag{16}$$

Following Angulo et al. (2015), we assume  $\zeta = 3.1$  as suggested by some theoretical considerations and fits to simulations (Foreman & Senatore 2016). We note that Baldauf et al. (2015c) find no appreciable difference between using  $\zeta = 2$  or 3.1. Quadratic contributions from the long-wavelength perturbations to the effective-stress-tensor expansion lead to four additional counterterms, only three of which

<sup>&</sup>lt;sup>1</sup>Note that RLPT is different from the so-called convolution LPT (e.g. Carlson, Reid & White 2013) which further extends the partial resummation but has not yet been applied to the bispectrum.

are independent. They have the following forms:

$$B_{c_1} = -2c_1(z)[D(z)]^4 k_1^2 P_L(k_2) P_L(k_3) + 2 \text{ perms.},$$
 (17)

$$B_{c_2} = -2 c_2(z) [D(z)]^4 k_1^2 \frac{(\mathbf{k}_2 \cdot \mathbf{k}_3)^2}{k_2^2 k_3^2} P_{L}(k_2) P_{L}(k_3) + 2 \text{ perms.}, (18)$$

$$B_{c_3} = -c_3(z) [D(z)]^4 (\mathbf{k}_2 \cdot \mathbf{k}_3) \left[ \frac{\mathbf{k}_1 \cdot \mathbf{k}_2}{k_2^2} + \frac{\mathbf{k}_1 \cdot \mathbf{k}_3}{k_3^2} \right] P_{\mathbf{L}}(k_2) P_{\mathbf{L}}(k_3)$$

$$+2 \text{ perms.},$$
 (19)

where the effective coupling constants  $c_1$ ,  $c_2$ , and  $c_3$  are unknown (similar to  $c_0$ , we absorb the  $[D(z)]^{\zeta}$  scaling in their definition).

Although some authors claim that EFT provides a manifestly convergent perturbative scheme for  $k < k_{\rm NL}$  (e.g. Carrasco et al. 2014a), there are indications that, like SPT, it forms an asymptotic expansion in which adding higher and higher-loop corrections, at a certain point, deteriorates the agreement with numerical simulations (e.g. Pajer & van der Woude 2018; Konstandin, Porto & Rubira 2019). The break down of the theory should not be caused by the influence of short-distance physics but rather to large contributions coming from mildly non-linear scales.

At the end of the day, EFT can also be simply seen as an improved version of SPT in which counterterms are added to regularize the UV-sensitive contributions.

#### 2.6 IR resummation

Large-scale flows broaden and damp the baryon acoustic oscillation (BAO) feature imprinted in  $P_{\rm L}$  at early epochs. These effects are poorly captured by Eulerian perturbation theories and are more easily understood in the Lagrangian framework (Meiksin, White & Peacock 1999; Crocce & Scoccimarro 2008; Taruya et al. 2009). It turns out that it is possible to account for them by resumming the perturbative predictions to all orders, a procedure known as 'IR resummation' (e.g. Senatore & Zaldarriaga 2015). In the framework of EFT, this is often implemented following the strategy delineated by Baldauf et al. (2015a) and further developed in Blas et al. (2016, the method we use) and Ivanov & Sibiryakov (2018). In order to decompose the linear power spectrum in smooth and oscillating parts, we use 1D Gaussian smoothing as described in Vlah et al. (2016, appendix A) and Osato et al. (2019).

#### 2.7 Time evolution

In all the results described above, time evolution is entirely captured by the function D(z). This directly follows from equation (3) and its analogue for the EFT corrections<sup>2</sup> which hold true in the EdS universe only. In general, the second-order SPT solution has the form  $D_{2A}(z) A(\mathbf{k}) + D_{2B}(z) B(\mathbf{k})$ , where  $D_{2A}(z)$  and  $D_{2B}(z)$  slightly differ from  $[D(z)]^2$  (for their explicit expressions see e.g. appendix A in Takahashi 2008). Similarly, the third-order solution contains six different growth factors that deviate a little from  $[D(z)]^3$ . Previous studies have shown that assuming the  $[D(z)]^n$  scaling provides rather accurate approximations to the matter power spectrum and bispectrum in the  $\Lambda$ CDM model (e.g. Scoccimarro et al. 1998; Bernardeau et al. 2002). For P(k), the leading-order contribution is unaffected since it only depends on the linear density fluctuations. Moreover, in the relevant range of wavenumbers, deviations from the exact solution for the one-loop corrections are well below

the per cent level at z=1 (Takahashi 2008). For these reasons, we can safely set  $D_{2A}(z)=D_{2B}(z)=D(z)$  in our analysis of the power spectrum. On the contrary, we use the exact  $F_2$  kernel

$$F_{2,\text{ACDM}}(\mathbf{k}_1, \mathbf{k}_2) = \frac{5}{7} \frac{D_{2A}(z)}{D(z)^2} \frac{(\mathbf{k}_1 + \mathbf{k}_2) \cdot \mathbf{k}_1}{k_1^2} + \frac{2}{7} \frac{D_{2B}(z)}{D(z)^2} \frac{(\mathbf{k}_1 + \mathbf{k}_2)^2 \mathbf{k}_1 \cdot \mathbf{k}_2}{2k_1^2 k_2^2},$$
(20)

to compute the tree-level bispectrum in SPT and EFT (but not for the loop corrections). This is necessary because adopting the EdS approximation would generate systematic shifts at the per cent level (Steele & Baldauf 2021) which are comparable with the statistical errors of the measurements extracted from our very large suites of simulations (see Section 3). We revisit this issue in Section 5.3.

Since we only consider the matter density field at z = 1, from now on, we drop the dependence on z of all functions.

#### 3 N-BODY SIMULATIONS

In this section, we introduce the *N*-body simulations and the estimators we use to test the theoretical models introduced above.

#### 3.1 Simulation suites

We use two sets of N-body simulations, named MINERVA and EOS, run using the GADGET-2 code (Springel 2005). Our main investigation is based on the MINERVA set (first presented in Grieb et al. 2016) which consists of 300 simulations each following the evolution of  $1000^3$  dark-matter particles in a periodic cubic box with a side length of  $1500 \, h^{-1}$  Mpc. In order to perform some additional tests in Section 5, we complement the MINERVA suite with a subset of the EOS suite composed of 10 realizations each containing  $1536^3$  particles in a periodic cubic box with a side length of  $2000 \, h^{-1}$  Mpc.

The simulations follow the formation of the large-scale structure in flat  $\Lambda$  CDM cosmological models with parameters given in Table 1. The linear transfer functions are obtained from the Boltzmann codes CAMB (Lewis, Challinor & Lasenby 2000; Howlett et al. 2012) and CLASS (Blas, Lesgourgues & Tram 2011) for the MINERVA and EOS simulations, respectively. In all cases, the initial particle displacements are computed using the publicly available code 2LPTIC (Crocce, Pueblas & Scoccimarro 2006) starting from Gaussian initial conditions.

#### 3.2 Power spectrum and bispectrum estimators

We use the POWERI4 code (Sefusatti et al. 2016) to estimate the matter density in a regular Cartesian grid containing  $512^3$  cells from the particle positions. With the FFT algorithm, we obtain the Fourier-space overdensity  $\delta_{\bf q}$  sampled at the wavevectors  ${\bf q}$  with Cartesian components that are integer multiples of the fundamental frequency  $k_{\rm F}=2\pi/L_{\rm box}$ . Our power-spectrum estimator is

$$\hat{P}(k) = \frac{1}{L_{\text{box}}^3 N_P} \sum_{\mathbf{q} \in k} |\delta_{\mathbf{q}}|^2, \tag{21}$$

where  $N_P$  is the number of  $\mathbf{q}$  vectors lying in a bin centred at wavenumber k and of width  $\Delta k$ . The notation  $\mathbf{q} \in k$  means that k

<sup>&</sup>lt;sup>2</sup>I.e.  $\delta_{\text{EFT}}(\mathbf{k}, z) = \sum_{n=1}^{\infty} [D(z)]^{n+\zeta} \, \delta_{\text{EFT}}^{(n)}(\mathbf{k})$  where  $\delta = \delta_{\text{SPT}} + \delta_{\text{EFT}}$ .

<sup>&</sup>lt;sup>3</sup>Information on the EOS suite is available in Biagetti et al. (2017) and at https://mbiagetti.gitlab.io/cosmos/nbody/eos/.

#### 4966 D. Alkhanishvili et al.

Table 1. Cosmological and structural parameters for the MINERVA and EOS simulations.

Name	$n_{s}$	h	$\Omega_b$	$\Omega_m$	$\sigma_8$	# sims	$N_{\rm p}^{1/3}$	$L_{\rm box}$ $(h^{-1}{ m Mpc})$	$V_{\text{tot}}$ $(h^{-3}  \text{Gpc}^3)$	$m_{\rm p} (10^{10}  h^{-1} M_{\odot})$	IC	Zinitial
MINERVA	0.9632	0.695	0.044	0.285	0.828	300	1000	1500	1012	26.7	2LPT	63
EOS	0.967	0.7	0.045	0.3	0.85	10	1536	2000	80	18.3	2LPT	99

**Table 2.** Main characteristics of our binning schemes – see equation (23). The total number of measurements for  $\hat{P}$  and  $\hat{B}$  are indicated with  $N_k$  and  $N_t$ , respectively, while  $k_{\text{max}}$  gives the maximum wavenumber reached.

s	С	$N_k$	$N_{\mathrm{t}}$	$k_{\rm max}(h{ m Mpc}^{-1})$
1	2.0	48	11757	0.20
2	2.5	28	2513	0.24
3	3.0	28	2513	0.36

 $-\Delta k/2 \le q < k + \Delta k/2$ . Similarly, for the bispectrum, we use

$$\hat{B}(k_1, k_2, k_3) = \frac{1}{L_{\text{box}}^3 N_B} \sum_{\mathbf{q}_1 \in k_1} \sum_{\mathbf{q}_2 \in k_2} \sum_{\mathbf{q}_3 \in k_3} \delta_{\mathbf{q}_1} \delta_{\mathbf{q}_2} \delta_{\mathbf{q}_3}, \tag{22}$$

where  $\mathbf{q}_1$ ,  $\mathbf{q}_2$ , and  $\mathbf{q}_3$  satisfy the triangle condition  $\mathbf{q}_{123} = 0$  and  $N_B$  denotes the number of triangles contributing to a given 'triangle bin' defined by the sides  $k_1 \ge k_2 \ge k_3$  (which do not necessarily form a closed triangle; Oddo et al. 2020). We consider different binning schemes characterized by the bin width  $s = \Delta k/k_F$  and the central wavenumber of the first bin c (also expressed in units of  $k_F$ ) so that the centres of all bins are given by

$$k_i = [c + (i - 1)s]k_F, i = 1, 2, ..., N_k.$$
 (23)

The parameters we use for the different power-spectrum and bispectrum measurements and the maximum wavenumber they reach are summarized in Table 2. It is worth stressing that we subtract from  $\hat{P}$  and  $\hat{B}$  the systematic contributions due to Poissonian shot noise which are anyway smaller than the statistical uncertainties.

Fig. 1 shows the average  $\hat{P}$  obtained from the MINERVA simulations for the three bin sizes (top panel) and the relative standard error of the mean (bottom panel). Note that, due to the large number of realizations we consider, we achieve better than 1 per cent (one per mille) precision for  $k > 0.01 h \, \mathrm{Mpc^{-1}} \, (k > 0.1 h \, \mathrm{Mpc^{-1}})$ . Similarly, Fig. 2 shows the mean  $\hat{B}$  (top panels) and its standard deviation (bottom panels). In this case, the relative errors range between 10 per cent and one per mille depending on the triangular configuration and the bin size. Dealing with such unusually small random errors (which cannot be obtained from current observations of galaxy clustering) calls for a consistent treatment of the systematic errors introduced by the *N*-body method (see Section 5.4).

#### 4 MATCHING THE MODELS TO SIMULATIONS

In this section, we explain how we compare the perturbative models to the measurements extracted from the *N*-body simulations.

#### 4.1 Binning of theoretical predictions

In order to compare the theoretical predictions with the measurements, we need to account for the finite bin sizes assumed by the power-spectrum and bispectrum estimators and, possibly, for the discreteness characterizing the Fourier-space density grid. The most

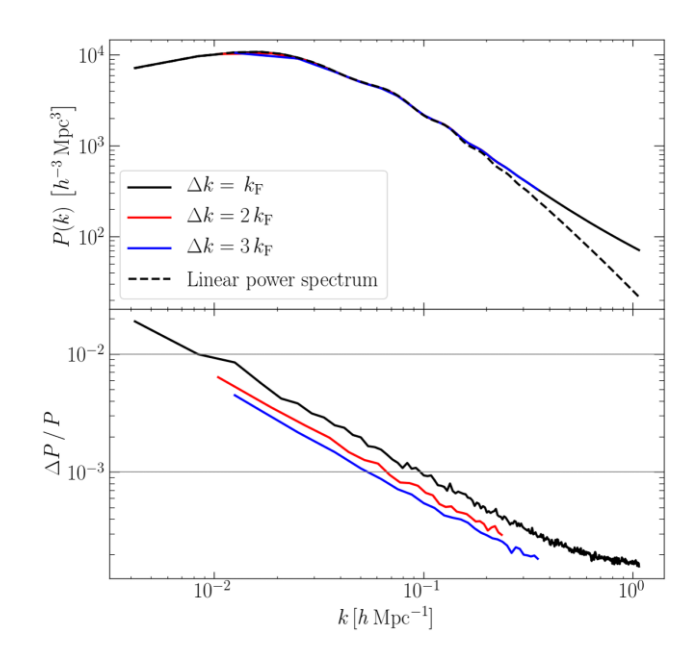


**Figure 1.** The mean power spectrum extracted from the MINERVA simulations (top) and the corresponding statistical uncertainty (bottom).

precise approach to the problem<sup>4</sup> consists of averaging the theoretical predictions over the same set of configurations as it is done for the estimators (21) and (22). Taking these averages, however, is computationally demanding, at least for the bispectrum. A considerable speedup (at the expense of accuracy) can be achieved by computing the model predictions for one characteristic configuration per triangle bin. For instance, Sefusatti, Crocce & Desjacques (2010) considered the average value of the triplet  $(k_1, k_2, \text{ and } k_3)$  in a bin that from now on we refer to as the 'effective' triangle of a bin. In what follows, we always use the full average of the theoretical predictions for the power spectrum and the tree-level bispectrum. On the other hand, due to the computational demand, we average the loop corrections for B only for triangle bins with  $k_1 \lesssim 0.14 \ h \, \mathrm{Mpc}^{-1}$ . In all the other cases, we evaluate the corrections using one effective triangle per bin (after checking that this approximation differs from the exact prediction by less than the standard error on the mean on the larger scales for which we have the average).

#### 4.2 Goodness of fit

In order to quantify the goodness of fit of the different models, we assume Gaussian errors and rely on the  $\chi^2$  test. Schematically, given the mean measurements from the simulations,  $\langle D_i \rangle$ , and the

<sup>&</sup>lt;sup>4</sup>With the exception of point-by-point comparisons on individual realizations (Roth & Porciani 2011; Taruya et al. 2012; Taruya, Nishimichi & Jeong 2018; Steele & Baldauf 2021).

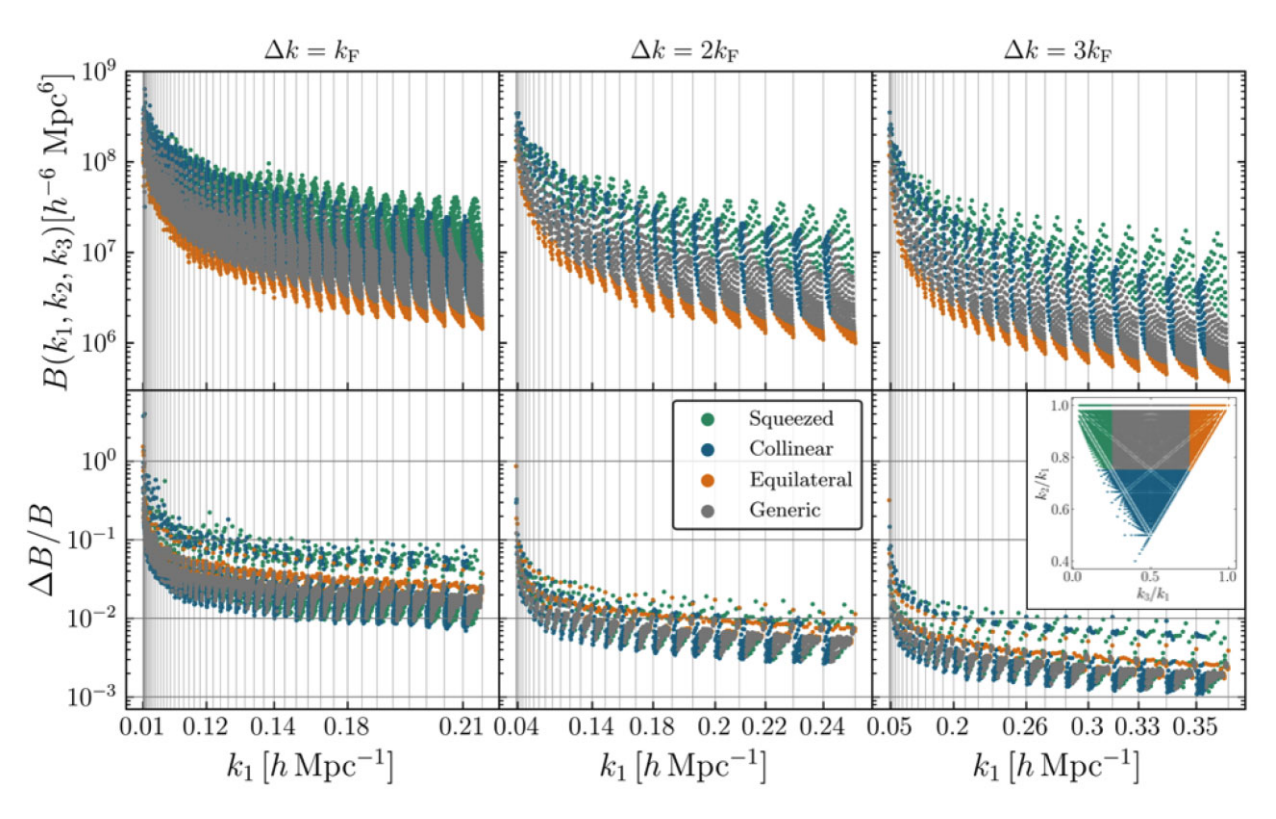


**Figure 2.** The mean bispectrum extracted from the MINERVA simulations (top) and its statistical uncertainty (bottom). Results are plotted by ordering the triangular configurations as in Oddo et al. (2020). In between two consecutive vertical lines, all points correspond to triangle bins with the same longest side  $k_1$ , whereas  $k_2$  and  $k_3$  take all allowed values. The colour of the symbols indicates different triangular shapes as illustrated in the bottom middle and right-hand panels.

corresponding model predictions,  $M_i$ , we compute the statistic

$$\chi_{\rm m}^2 = \frac{\chi_{\rm tot}^2}{\nu} = \frac{1}{\nu} \sum_{i,j} (M_i - \langle D_i \rangle) C_{ij}^{-1} (M_j - \langle D_j \rangle),$$
(24)

where  $\nu$  indicates the number of degrees of freedom (i.e. the number of data points N minus the number of adjusted parameters), the indices i and j run over all possible configurations, and  $C_{ij}$  denotes the elements of the covariance matrix for the adopted estimators (or some approximation thereof).

Since we only consider relatively large scales, we use the socalled Gaussian contribution to the covariance matrix for the powerspectrum estimates, (Feldman, Kaiser & Peacock 1994; Meiksin & White 1999)

$$C_{ij} = \frac{2 P_i^2}{N_P} \delta_{ij},\tag{25}$$

with  $P_i$  the expected power spectrum in the  $i^{th}$  bin and  $\delta_{ij}$  the Kronecker symbol. In order to prevent that the covariance is informed about the noise in our realizations, we use a smooth function to compute  $P_i$  in the expression above. This is obtained by fitting the outcome of the MINERVA simulations with the expression (Cole et al. 2005)

$$P_{\rm NL}(k) = P_{\rm L}(k) \left( \frac{1 + Qk^2}{1 + Ak} \right),$$
 (26)

where Q and A are free parameters. We find that setting  $Q \approx 4 \, h^{-2} \, \mathrm{Mpc^2}$  and  $A \approx 0.37 \, h^{-1} \, \mathrm{Mpc}$  provides a fit that agrees with the measurements to better than 1 per cent at all the scales considered in this work.

For the bispectrum, we find that, even at large scales, the Gaussian approximation underestimates the sample variance from numerical simulations in a shape-dependent manner, reaching a difference of order 50 per cent for some squeezed-triangle configurations (see also Chan & Blot 2017; Colavincenzo et al. 2019; Gualdi & Verde 2020). For this reason, we use the approximate expression

$$C_{ij} = [(PPP)_i + 2(BB)_i] \delta_{ij},$$
 (27)

where

$$(PPP)_i \simeq \frac{6 L_{\text{box}}^3}{N_P} \overline{P_{\text{NL}}(k_1) P_{\text{NL}}(k_2) P_{\text{NL}}(k_3)}$$
 (28)

denotes the Gaussian part and the overline indicates the average over all the configurations contributing to the i<sup>th</sup> triangle bin while

$$(BB)_i \simeq (B_{\rm NL}^{\rm eff})^2 \left[ \frac{1}{N_P(k_1)} + \frac{1}{N_P(k_2)} + \frac{1}{N_P(k_3)} \right],$$
 (29)

where  $B_{\rm NL}^{\rm eff}$  denotes the tree-level bispectrum in SPT evaluated at the effective wavenumbers using  $P_{\rm NL}$  instead of  $P_{\rm L}$ . The  $(BB)_i$  term approximates the actual non-Gaussian contribution due to configurations that share one k-bin (see e.g. Sefusatti et al. 2006). The factor of two in equation (27) approximately accounts for contributions to the covariances that scale as the product of the power spectrum and the trispectrum. This is justified as the two terms are expected to be of the same order of magnitude, as shown in recent studies of the covariance matrix (Barreira 2019; Sugiyama et al. 2020).

In order to assess the accuracy of these approximations to the diagonal elements of the covariance matrices for  $\hat{P}$  and  $\hat{B}$ , we use

the statistic

$$\chi_s^2 = \frac{1}{N} \operatorname{Tr}(\mathbf{SC}^{-1}), \tag{30}$$

where **S** denotes the sample covariance matrix of the measurements from the MINERVA simulations and **C** is our model covariance. It is possible to show that, for Gaussian errors with covariance matrix **C**, the statistic  $N\chi_s^2$  follows a chi-square distribution with N degrees of freedom (Porciani). Therefore, our approximations for the covariance matrix should be considered inaccurate if  $\chi_s^2$  strongly departs from unity. In this case, any conclusion on the accuracy of the models based on  $\chi_m^2$  should be disregarded. Note that our approximations for the covariance matrices are diagonal, implying that

$$\chi_{\rm s}^2 = \frac{1}{N} \sum_{i=1}^{N} \frac{S_{\rm ii}}{C_{\rm ii}}.$$
 (31)

i.e.  $\chi_s^2$  gives the average ratio between the measured and assumed variances of the different data points. More complex statistics can be used to test approximations to the covariance matrix in the general non-diagonal case (Porciani, in preparation).

Before moving on, it is important to note that we do not account for the so-called 'theoretical errors' – i.e. uncertainties on the perturbative predictions reflecting the estimated size of the higher-order terms that are neglected – as advocated by some authors (e.g. Baldauf et al. 2016; Steele & Baldauf 2021; Chudaykin, Ivanov & Simonović 2021). The reason is very simple. We are not trying to determine the domain of validity of the full perturbative expansion (we are actually agnostic regarding its convergence). More pragmatically, we simply want to find out the range of scales for which the one-loop formulae provide an accurate match to *N*-body simulations.

In the remainder of this paper, we distinguish between the concepts of accuracy and validity: the former indicates how closely a perturbative expansion reproduces the exact answer while the latter refers to the consistency of all the assumptions of the theory. Therefore, the domain of accuracy and the range of validity of the models should not be confused. For instance, a model could still provide a good approximation to the truth on a range of scales although its assumptions are not valid.

#### 5 RESULTS

In this section, we determine the domain of accuracy of the perturbative models for the matter power spectrum and bispectrum we have introduced in Section 2 by comparing them against *N*-body simulations. To start with, we pay particular attention to discussing how we fix the EFT parameters that determine the amplitude of the counterterms. Subsequently, we present results as a function of the total volume used to measure *P* and *B*. As a final step, we discuss the impact of systematic errors introduced by the *N*-body technique.

#### 5.1 EFT parameters

As mentioned in Section 2.5, the EFT parameters related to the counterterms need to be determined from the simulation data. In doing so, we do not distinguish between the actual counterterms and the renormalized contributions. Therefore, the coefficients we obtain should be interpreted as simple 'matching coefficients' and not given any particular physical interpretation. Following a common trend in the literature, we will keep referring to these coefficients as counterterms.

The EFT power spectrum at one loop only contains the parameter  $c_0$  for which, following Baldauf et al. (2015b), we can build an

estimator starting from equations (12) and (13),

$$\hat{c}_0(k) = -\frac{\langle \hat{P}(k) \rangle - P_{\text{SPT}}(k)}{2 k^2 P_{\text{L}}(k)}.$$
(32)

In the left-hand panel of Fig. 3, we show how  $\hat{c}_0$  depends on kwhen we use the mean power spectrum extracted from the MINERVA simulations. Within the EFT framework,  $c_0$  is a scale-independent parameter but our data show that  $\hat{c}_0$  significantly deviates from its low-k limit when  $k > 0.14 h \, \mathrm{Mpc}^{-1}$ . This is usually interpreted as a signal that the truncated perturbative expansion breaks down beyond this scale and higher-order corrections become important (Foreman, Perrier & Senatore 2016). In the right-hand panel of Fig. 3, we determine  $c_0$  by fitting  $P_{\text{EFT}}$  (with and without IR resummation) to the mean power spectrum extracted from the MINERVA simulations. Our results are shown as a function of the maximum wavenumber used in the fit,  $k_{\rm fit}$ . The orange line represents the best-fitting value for the EFT model and the shaded region around it marks the 68 per cent confidence region of the fit. Not surprisingly, it resembles a smoothed version of the results shown in the left-hand panel. Considering subsets of 23 MINERVA boxes (which cover the same total volume as the EOS simulations) only increases the scatter of the estimates (blue shaded region). Accounting for the IR resummation (green line) removes the oscillations in the region of the baryonic acoustic features but does not attenuate the overall scale dependence for  $k > 0.14 \, h \, \text{Mpc}^{-1}$ . Based on these results, we conclude that the domain of validity of the one-loop EFT expressions for the power spectrum at z = 1 is  $k < 0.14 \, h \, \mathrm{Mpc}^{-1}$ . Our results are consistent with fig. 14 of Baldauf et al. (2015b), even though our analysis is performed at z = 1 instead of z = 0. Remarkably, the limiting value we find is also consistent with the blinded challenge presented in Nishimichi et al. (2020), which uses a total simulation volume of  $566 h^{-3} \text{ Gpc}^3$  (about half of the volume covered by the MINERVA suite) at z = 0.61 to test the constraining power for cosmology of the EFT predictions for the galaxy power spectrum in redshift space. In this case, the recovered cosmological parameters show a bias whenever the mock data sets are extended beyond  $k_{\text{max}} = 0.14 \ h \, \text{Mpc}^{-1}$ . In the remainder of this paper, we use the bestfitting value of  $c_0$  using  $k_{\text{fit}} = 0.14 \ h \, \text{Mpc}^{-1}$  as the default option for  $P_{\rm EFT}$ . This gives  $c_0 = 0.581 \pm 0.009 \, h^{-2} \, \rm Mpc^2$ . If we simply rescale this value by  $[D(z = 1)]^{-2}$  (thus ignoring any intrinsic time dependence of  $c_0$ ), we obtain 1.525 which closely matches the results previously obtained at z = 0 using slightly different cosmological models, methods, and scales (Carrasco et al. 2014b; Angulo et al. 2015; Baldauf et al. 2015c).

The EFT bispectrum at one loop contains four unknown parameters and different strategies have been developed in the literature to determine them. For instance, it is possible to express  $c_1$ ,  $c_2$ , and  $c_3$  as a function of  $c_0$  by imposing renormalization conditions and then fix  $c_0$  from a fit to the power spectrum (Angulo et al. 2015; Baldauf et al. 2015c). An alternative line of attack – which we follow here - is to treat (at least some of) the EFT parameters as fit parameters for the bispectrum, trying to avoid overfitting. The recent and comprehensive study by Steele & Baldauf (2021) gives evidence supporting the second approach. Two options are available when fitting  $c_0$ : we can either use the best-fitting value for the power spectrum or determine it together with the other EFT parameters only using the bispectrum. We compare these alternatives in Fig. 4, where we show the dependence of the best-fitting EFT parameters on the maximum wavenumber considered in the fit. In all cases, we use the IR resummed model. Focusing on  $c_0$ , we notice that the fit based on the power spectrum is much more stable and less uncertain at large scales. It is also worth stressing that the best-

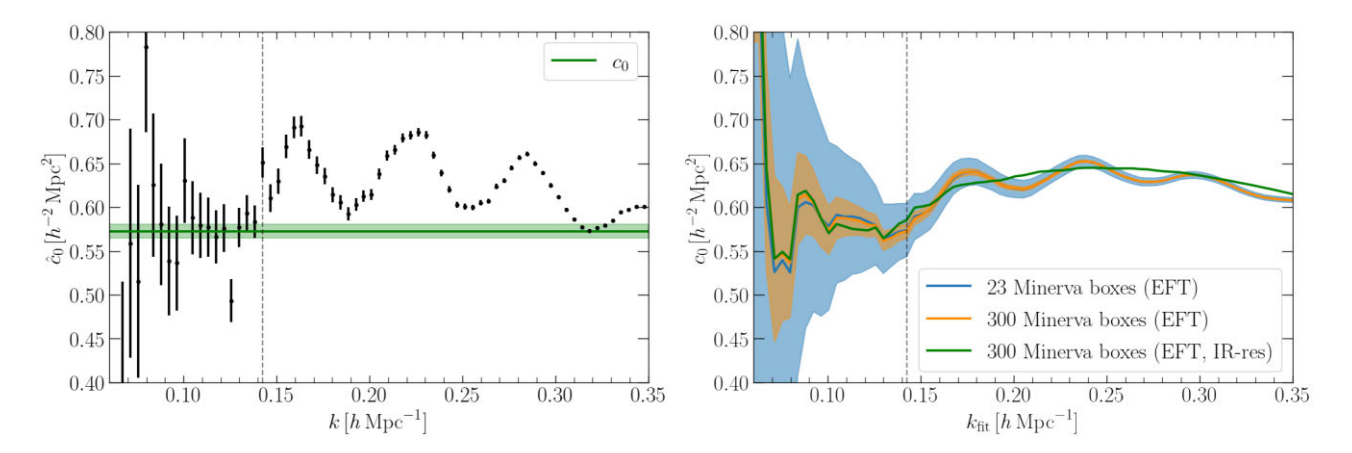
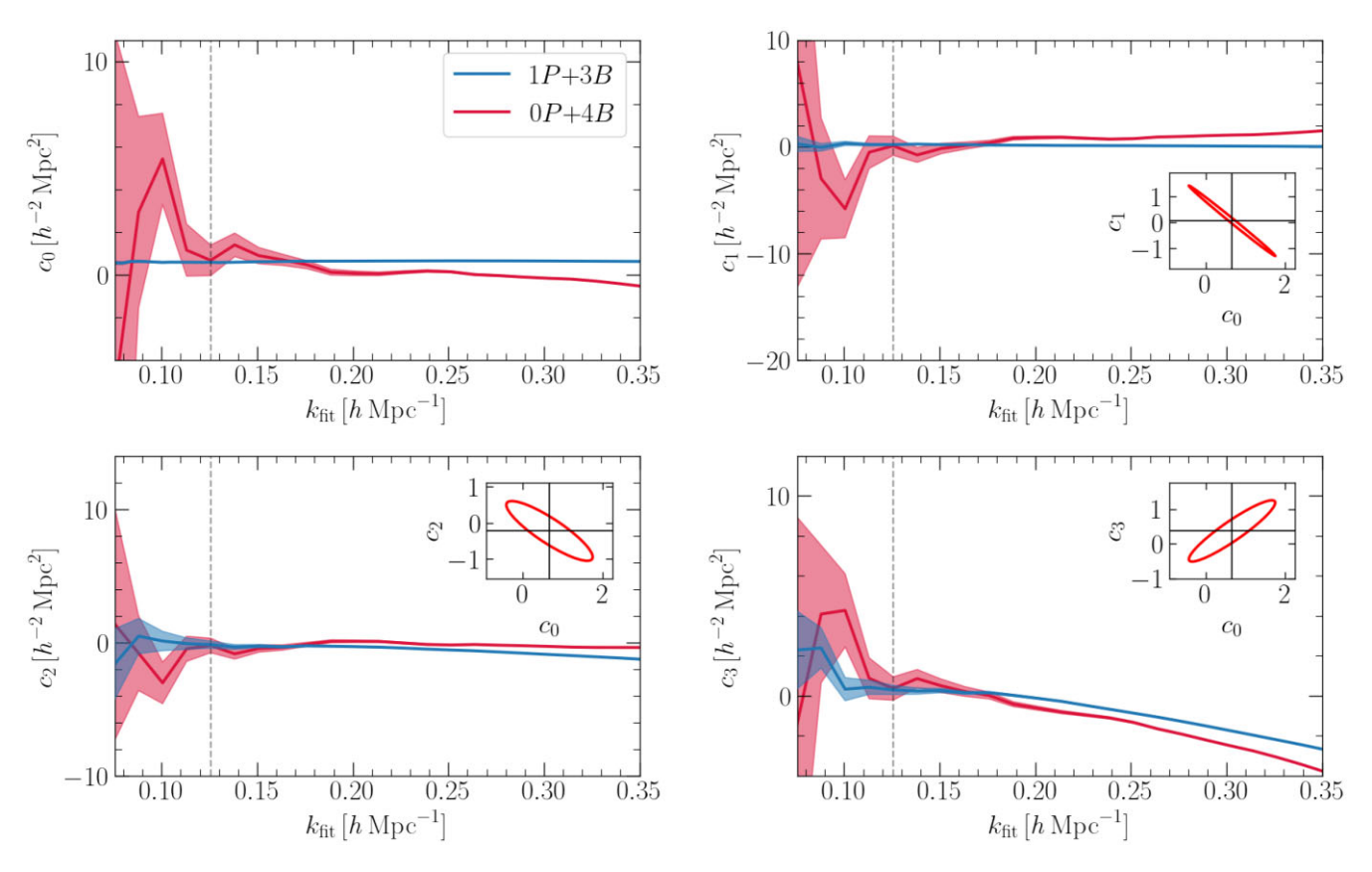


Figure 3. The EFT parameter  $c_0$  obtained by matching the model for the power spectrum at one loop to the MINERVA simulations. In the left-hand panel, we use the estimator given in equation (32), while, in the right-hand panel, we fit the model to the numerical data for  $k < k_{\rm fit}$ . Shown are the best-fitting values (solid lines) and their uncertainty (68 per cent confidence interval, shaded regions). As indicated in the legend, different colours distinguish results obtained with and without accounting for IR resummation or by considering subsamples of the MINERVA simulations. To improve readability, we do not plot the shaded region for the IR-resummed EFT case. The vertical line indicates the scale at which a statistically significant departure from the low-k limit is detected for the full data set. The horizontal line in the left-hand panel shows the result of the fit in the right-hand panel for  $k_{\rm fit} = 0.14 \, h \, {\rm Mpc}^{-1}$ .



**Figure 4.** The best-fitting values (solid lines) and the uncertainties (shaded regions) of the EFT parameters that influence the matter bispectrum at one loop are shown as a function of the maximum wavenumber of the measurements extracted from the MINERVA simulations. We consider two cases: (i) we fix  $c_0$  using the power spectrum (Fig. 3) and the other three parameters using the bispectrum (blue) and (ii) we fit all four parameters using the bispectrum measurements (red). The vertical dashed lines indicate the default value of  $k_{\rm fit} = 0.125~h~{\rm Mpc}^{-1}$  we use in the remainder of the paper. The insets show the joint 68 per cent confidence regions for two EFT parameters evaluated for  $k_{\rm fit} = 0.125~h~{\rm Mpc}^{-1}$ . The cross indicates the best-fitting values of these parameters.

fitting values are sometimes negative while  $c_0 \ge 0$  in the theory. However, we do not give much weight to this consideration since we do not fit the renormalized counterterms. We also notice that  $c_0$  and the other EFT parameters are strongly correlated when they are simultaneously fit from the bispectrum. Their trend with  $k_{\rm fit}$  in

Fig. 4 clearly shows that this happens at all scales. Such degeneracy is investigated in more detail in the three insets where we show the joint 68.3 per cent confidence region for  $c_0$  and a second parameter estimated at  $k_{\rm fit} = 0.125~h~{\rm Mpc}^{-1}$  while keeping the remaining two fixed at their best-fitting values. The cross-correlation coefficients

between  $c_0$  and the other parameters are as high as -0.997 ( $c_1$ ), -0.872 ( $c_2$ ), and 0.922 ( $c_3$ ) indicating that the bispectrum data cannot isolate the contributions from the different counterterms. We believe that the large-scale fluctuations of the EFT parameters are largely influenced by this degeneracy. The fluctuations are, in fact, greatly suppressed by fixing  $c_0$  to the best-fitting value from the power spectrum. In this case, the four EFT parameters assume consistent values for  $k_{\text{fit}} < 0.14 \, h \, \text{Mpc}^{-1}$  (which is basically determined by *P*). On the contrary, considering smaller scales generates deviations, especially for  $c_2$  and  $c_3$ . All this suggests that  $k = 0.14 h \,\mathrm{Mpc}^{-1}$  also approximately delimits the domain of validity of the one-loop model for the bispectrum at z = 1. However, the two fitting methods (i.e. fitting three or four counterterms with the bispectrum) do not provide fully consistent results for all parameters at  $k_{\rm fit} \approx 0.14 \, h \, {\rm Mpc}^{-1}$ while they do at  $k_{\rm fit} \approx 0.125 \, h \, {\rm Mpc}^{-1}$  (the actual values are listed in Table 3). For this reason, unless explicitly stated otherwise, from now on we fix the EFT parameters for  $B_{\text{EFT}}$  to the best-fitting values at this scale using the power spectrum to determine  $c_0$  and the bispectrum to measure  $c_1$ ,  $c_2$ , and  $c_3$ . Note that, in spite of our unprecedentedly large data set, only  $c_0$  is precisely determined while  $c_1$ ,  $c_2$ , and  $c_3$  are compatible with being zero within a few standard deviations. This suggests that it might be quite challenging to fix the EFT counterterms for the bispectrum from actual observational data and all what could be done is to marginalize over them in a Bayesian fashion, possibly reducing the constraining power for cosmology of the data.

#### 5.2 Power spectrum

If we assume for the moment that the *N*-body technique does not introduce any systematic shifts, we can determine the domain of accuracy of the perturbative models for the matter power spectrum by directly comparing their predictions to the measurements extracted from the numerical simulations. The huge volume covered by the MINERVA simulations results in sub-per cent statistical uncertainties for the average power spectrum (see Fig. 1). Getting agreement to this precision would be a major achievement for the models.

In the top panel of Fig. 5, we show the mean power spectrum extracted from the MINERVA simulations using  $\Delta k = k_F$  (symbols with error bars) and the corresponding bin-averaged models (solid lines with different colours as indicated by the label). In order to reduce the span of the data and improve readability, we plot the deviation from the linear power spectrum in per cent points. Similarly, in the second panel from the top, we show the same measurements and models but in terms of their deviation with respect to  $P_{\rm EFT}$  which provides a better fit to the numerical data. The third panel, instead, shows the  $\chi_m^2$  statistic evaluated for the different models as a function of  $k_{\text{max}}$ . This quantity gives a measure of the goodness of fit. In order to have a reference scale, we highlight the regions bounded by the one-sided upper and lower 95 per cent confidence limits for the  $\chi^2$ statistic (with the appropriate number of degrees of freedom) with a grey shaded region. Basically, a model should be rejected at 95 per cent confidence when its  $\chi^2_{m}$  lies outside the shaded region. In practice, we determine the domain of accuracy of the models as follows: moving from left to right, we look for the first  $k_{max}$  at which  $\chi_{\rm m}^2$  lies outside the shaded region. Finally, the bottom panel shows the  $\chi_s^2$  statistic as a function of  $k_{\text{max}}$  together with the corresponding 95 per cent confidence limits that can be used to evaluate the quality of our approximation for the covariance matrix.

Coming to the specific outcome of this comparison, Fig. 5 indicates that, although equation (25) systematically overestimates the variance of our measurements by a few percent, this discrepancy is hardly statistically significant in the range of scales we consider.

Moreover, by examining the  $\chi_m^2$  curves as a function of  $k_{max}$ , it is evident that, when a model begins to break down,  $\chi_m^2$  increases very steeply so that the inferred reach is quite insensitive to small deviations in the size of the error bars. Therefore, we can proceed further with analysing the  $\chi^2_m$  curves knowing that this statistic will be only very slightly underestimated. This provides a clear ranking for the models based on their domain of accuracy. Not surprisingly, the first model to break down is  $P_L$  which fits the MINERVA simulations only for  $k_{\text{max}} < 0.035 \, h \, \text{Mpc}^{-1}$ , followed by SPT  $(k_{\text{max}} < 0.06 \, h \, \text{Mpc}^{-1})$ . Since on these relatively large scales RegPT and RLPT essentially coincide with SPT, they also fail at the same  $k_{\text{max}}$ . Contrary to SPT, however, they agree with the simulations to better than 1 per cent up to  $k \simeq 0.15 \, h \, \mathrm{Mpc}^{-1}$ . The best agreement is found with the EFT model which fits the MINERVA simulations accurately for  $k_{\text{max}} < 0.14 \, h \, \text{Mpc}^{-1}$  (and never shows per cent deviations within the explored range of wavenumbers). Consistently with previous work (e.g. Baldauf et al. 2015a), we find that IR-resummation improves the fit only beyond its nominal range of accuracy. One issue worth investigating is that the value of  $\chi_{\rm m}^2$  rises sharply around  $k \approx 0.125$  and 0.14  $h\,{\rm Mpc}^{-1}$ , which causes the EFT models to get rejected on slightly larger scales than perhaps expected (based on visual inspection of the top panel in Fig. 5). This is caused by the statistically significant deviation of two simulation data points around those scales which are clearly distinguishable in the second panel (from the top) of Fig. 5. After carefully inspecting individual simulations to understand the origin of these deviations, we could not reach any clear conclusion. However, upon re-measuring the power spectrum using narrower bins in that region, we notice that the deviations form coherent features within a range of k-values and are not simply due to random

To cross check our results and also test the models under less demanding standards, we repeat our analysis using the EOS simulations which cover a smaller volume (roughly corresponding to 23 MINERVA boxes) and thus give larger statistical error bars. For simplicity, we only consider the EFT models with and without IR-resummation. In order to properly compare results obtained using the MINERVA and EOS suites, we proceed as follow: (i) we random sample 23 MINERVA boxes from the full set; (ii) we fit the EFT parameter  $c_0$  to the mean power spectrum of the subset using  $k_{\text{max}} = 0.14 \, h \, \text{Mpc}^{-1}$ ; and (iii) we compute the  $\chi_{\text{m}}^2$  statistic as a function of  $k_{\text{max}}$  for the best-fitting  $c_0$ . Our results are shown in Fig. 6 where the solid lines represent the mean  $\chi_m^2$  obtained from the MINERVA subsets and the shaded regions around them show the corresponding standard deviation. Overall, these findings are in very good agreement with the  $\chi^2_{\text{m}}$  curves derived from the EOS simulations (dot-dashed lines). Due to the larger statistical error bars, the nominal reach of the EFT models slightly increases with respect to the analysis performed with the full MINERVA set. We find  $k_{\text{max}} < 0.16^{+0.05}_{-0.01} \, h \, \text{Mpc}^{-1}$  for standard EFT and  $k_{\text{max}} <$  $0.17^{+0.06}_{-0.02} h \,\mathrm{Mpc^{-1}}$  for IR-resummed EFT. Note that this extends beyond the minimum scale for which  $c_0$  can be assumed to be constant.

#### 5.3 Bispectrum

In Fig. 7, we investigate the goodness of fit of the different models for the matter bispectrum by plotting the  $\chi_{\rm m}^2$  and  $\chi_{\rm s}^2$  statistics as a function of  $k_{\rm max}$  for various bin sizes. In the bottom panels, we show two curves: the solid one considers our approximation to the covariance matrix given in equation (27) while the dashed one

**Table 3.** Best-fitting values and uncertainties of the EFT parameters derived with  $k_{\rm fit} = 0.125 \, h \, {\rm Mpc}^{-1}$  in Fig. 4. The  $\chi^2_{\rm m}$  statistic for the best fit is expressed in terms of  $\chi^2_{\rm tot}$  and  $\nu$  as in equation (24).

Fit	$\chi_{m}^{2}$	$(h^{-2} \operatorname{Mpc}^2)$	$(h^{-2} \operatorname{Mpc}^2)$	$(h^{-2} \operatorname{Mpc}^2)$	$(h^{-2}\operatorname{Mpc}^2)$
$ \begin{array}{c} 1P + 3B \\ 0P + 4B \end{array} $	171.03/167 171.01/166	$\begin{array}{c} 0.577 \pm 0.013 \\ 0.67 \pm 0.72 \end{array}$	$\begin{array}{c} 0.177 \pm 0.071 \\ 0.06 \pm 0.90 \end{array}$	$-0.16 \pm 0.27$ $-0.22 \pm 0.54$	$0.30 \pm 0.23$ $0.37 \pm 0.58$

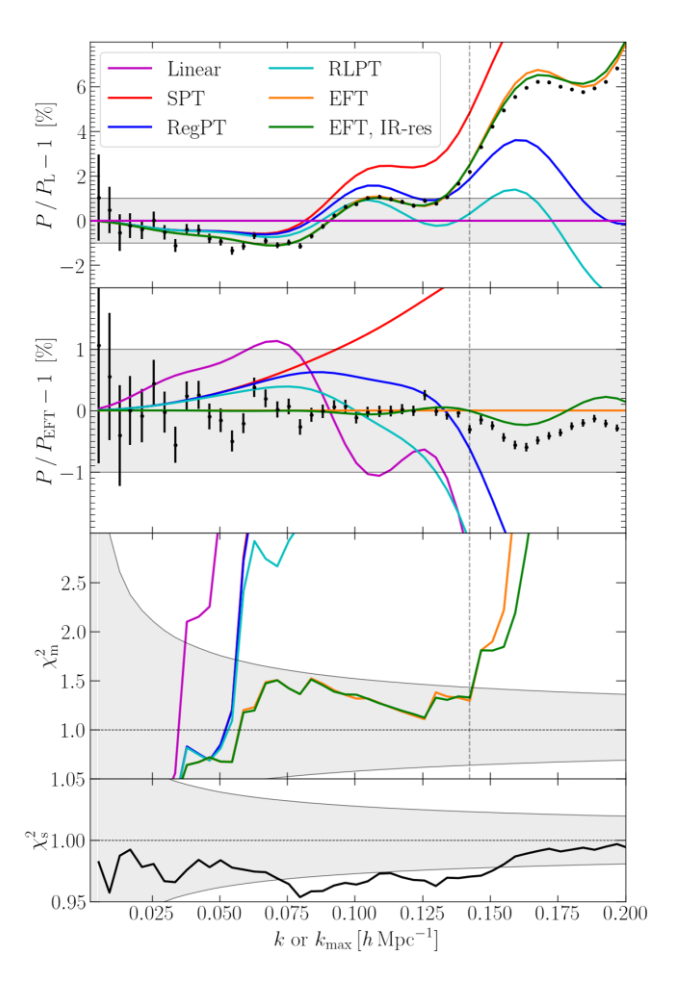


**Figure 5.** Comparison of the perturbative models for the matter power spectrum (solid lines) with the mean measurement extracted from the MINERVA simulations (symbols with error bars) using the bin width  $\Delta k = k_{\rm F}$ . The top two panels compare the different power spectra to  $P_{\rm L}$  and  $P_{\rm EFT}$  whereas the bottom two display the goodness of fit for the models and the covariance matrix (see Section 4.2 for details). The grey shaded areas in the top two panels represent deviations smaller than 1 per cent with respect to the reference models. Those in the bottom two panels, instead, mark the regions bounded by the upper and lower 95 per cent confidence limits for the  $\chi^2$  distribution with the appropriate number of degrees of freedom. The vertical dotted line indicates  $k_{\rm fit} = 0.14 \, h \, {\rm Mpc}^{-1}$ , which is the largest wavenumber used to fit  $c_0$  for the EFT models.

refers to the Gaussian part given in equation (28). It is evident that the Gaussian approximation severely underestimates the variance of the bispectrum measurements already at large scales and especially for broader triangle bins. On the contrary, equation (27) provides average deviations of only a few per cent for all configurations considered in this work. We believe that this is accurate enough to get robust estimates of  $\chi_m^2$ , although, at small scales, the assumed covariance matrix is nominally incompatible with the scatter seen in

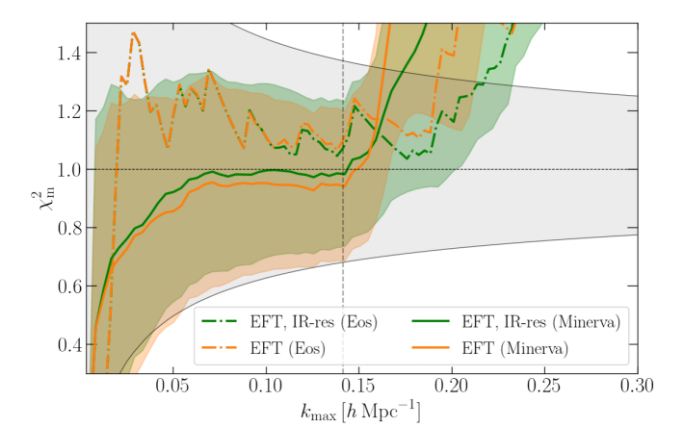


**Figure 6.** The  $\chi_{\rm m}^2$  statistic for the EFT and IR-resummed EFT power spectra evaluated using the EOS suite (dash–dotted) and many different subsets of 23 MINERVA simulations (solid and shaded for mean and standard deviation, respectively). The grey shaded area highlights the region bounded by the (one-sided) upper and lower 95 per cent confidence limits for a  $\chi^2$  distribution function with the appropriate number of degrees of freedom. The vertical dotted line indicates  $k_{\rm fit}$ . Both simulation measurements use bins of width equal to  $k_{\rm F}$ .

the simulations (i.e. the black curve lies outside the shaded region in the plots for  $\chi_s^2$ ).

The variations of  $\chi^2_{\rm m}$  with  $k_{\rm max}$  provide a clear ranking of the models, Independently of the bin width, the tree-level SPT prediction breaks down first and one-loop corrections only slightly improve the range of accuracy of the theory up to  $k_{\rm max} \simeq 0.08\,h\,{\rm Mpc}^{-1}$ . RegPT and RLPT provide substantial improvements and accurately match the MINERVA simulations up to scales between 0.1 and 0.14  $h\,{\rm Mpc}^{-1}$  depending on the bin width. Finally, the counterterms in the EFT bispectra boost the agreement up to  $k_{\rm max} \simeq 0.16-0.19\,h\,{\rm Mpc}^{-1}$ . IR-resummation turns out to be relevant only for  $k\gtrsim 0.15\,h\,{\rm Mpc}^{-1}$  and even marginally for the case of narrow bins, where statistical errors are larger than the deviations between the model and the data at the scales of the BAOs.

As we already did with the power spectrum, in Fig. 8, we verify that using the MINERVA and EOS simulations gives consistent results for the bispectrum as well. It turns out that the reach of the EFT models is a bit reduced for the EOS simulations but this is consistent with random fluctuations. We also note that, for EOS, the EFT models with and without IR-resummation have practically the same domain of accuracy as a consequence of the larger uncertainty of the measurements.

Finally, we test the impact of using the popular EdS approximation for the second-order kernel  $F_2$  instead of the more general scheme we described in Section 2.7. Fig. 9 shows that this modification has very little influence on our results. No changes in the  $\chi^2_{\rm m}$  are visible on large scales where error bars are bigger. The only noticeable differences are: (i) a slight improvement in the reach of SPT when the EdS approximation is adopted and (ii) a similarly sized increase

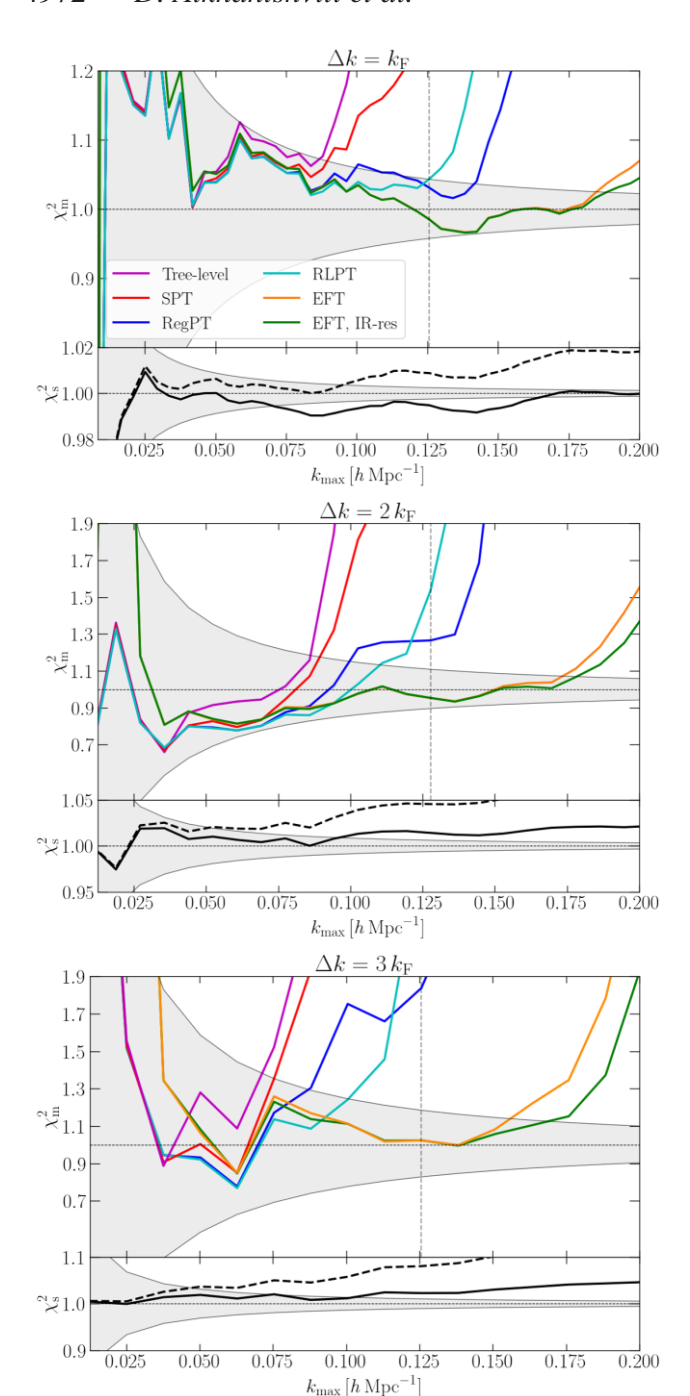


**Figure 7.** As in the bottom two panels of Fig. 5 but for the matter bispectrum. From top to bottom, we consider three different bin widths, namely  $k_{\rm F}$ ,  $2\,k_{\rm F}$ , and  $3\,k_{\rm F}$ . The dashed lines in the plots for  $\chi_{\rm s}^2$  (bottom panels) refer to the Gaussian approximation to the covariance matrix.

in the range of accuracy of EFT when the exact second-order kernel is used. On large scales, the EFT counterterms absorb the differences between the exact second-order kernel and the EdS approximation as indicated by the fact that the two EFT models give the identical  $\chi^2$  values whereas the SPT model fails to do so. We have checked that differences between the two kernels also significantly alter the best-fitting values for the counterterms, especially for  $c_1$  and  $c_2$ . These findings hold true also for wider k-bins.

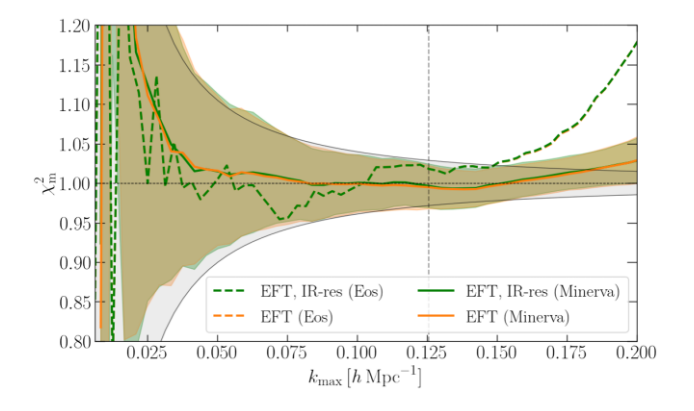
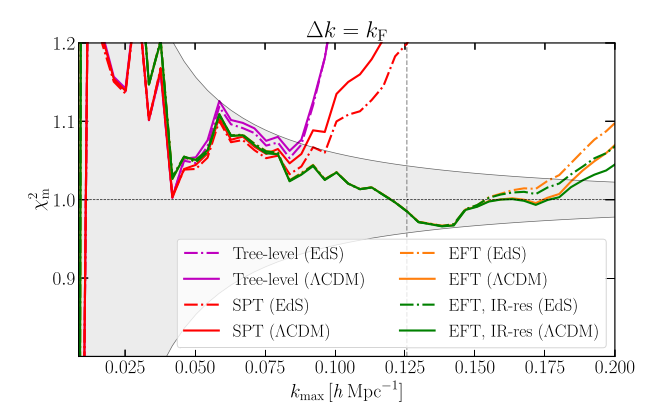


Figure 8. As in Fig. 6 but for the matter bispectrum.



**Figure 9.** As in the top panel of Fig. 7 but comparing models obtained with the exact second-order SPT kernels (ΛCDM) and the popular EdS approximation (see the main text for details).

#### 5.4 Range of accuracy versus surveyed volume

The careful reader might have noticed that our results are more conservative than other estimates in the literature. This is partially due to the fact that we use all bispectrum configurations, but mostly because we use a much larger set of N-body simulations (cf. Angulo et al. 2015). Current surveys of the large-scale structure of the Universe cover volumes which are one to two orders of magnitude smaller than the total volume of the MINERVA simulations. This directly translates into larger statistical uncertainties for summary statistics like the power spectrum and the bispectrum and thus into more extended ranges of accuracy for the models. In this section, we investigate how the reach of the models depends on the volume covered by a survey. In doing so, we also need to account for systematic effects which we have so far neglected. In order to better evaluate their impact on our conclusions, we start with assuming that they are of no consequence (we relax this assumption in the next section).

In the top panels of Figs 10 and 11, we show how the reach of models for P and B changes with the volume over which the measurements are performed. These plots are obtained as follows. (i) We pick a volume V which corresponds to an integer number N of MINERVA boxes. (ii) We randomly select N MINERVA realizations (with no repetitions) and compute  $\langle \hat{P} \rangle$  and  $\langle \hat{B} \rangle$  (using  $\Delta k = k_{\rm F}$  for P and  $3 k_{\rm F}$  for B in order to probe a wider range of scales). (iii) We fit the EFT counterterms to the numerical data using  $k_{\rm fit} = 0.14 h \, {\rm Mpc}^{-1}$  for P and  $k_{\rm fit} = 0.125 h \, {\rm Mpc}^{-1}$  for B. (iv) We evaluate the  $\chi_{\rm m}^2$  statistic as a function of  $k_{\rm max}$  and use it to determine the reach of each

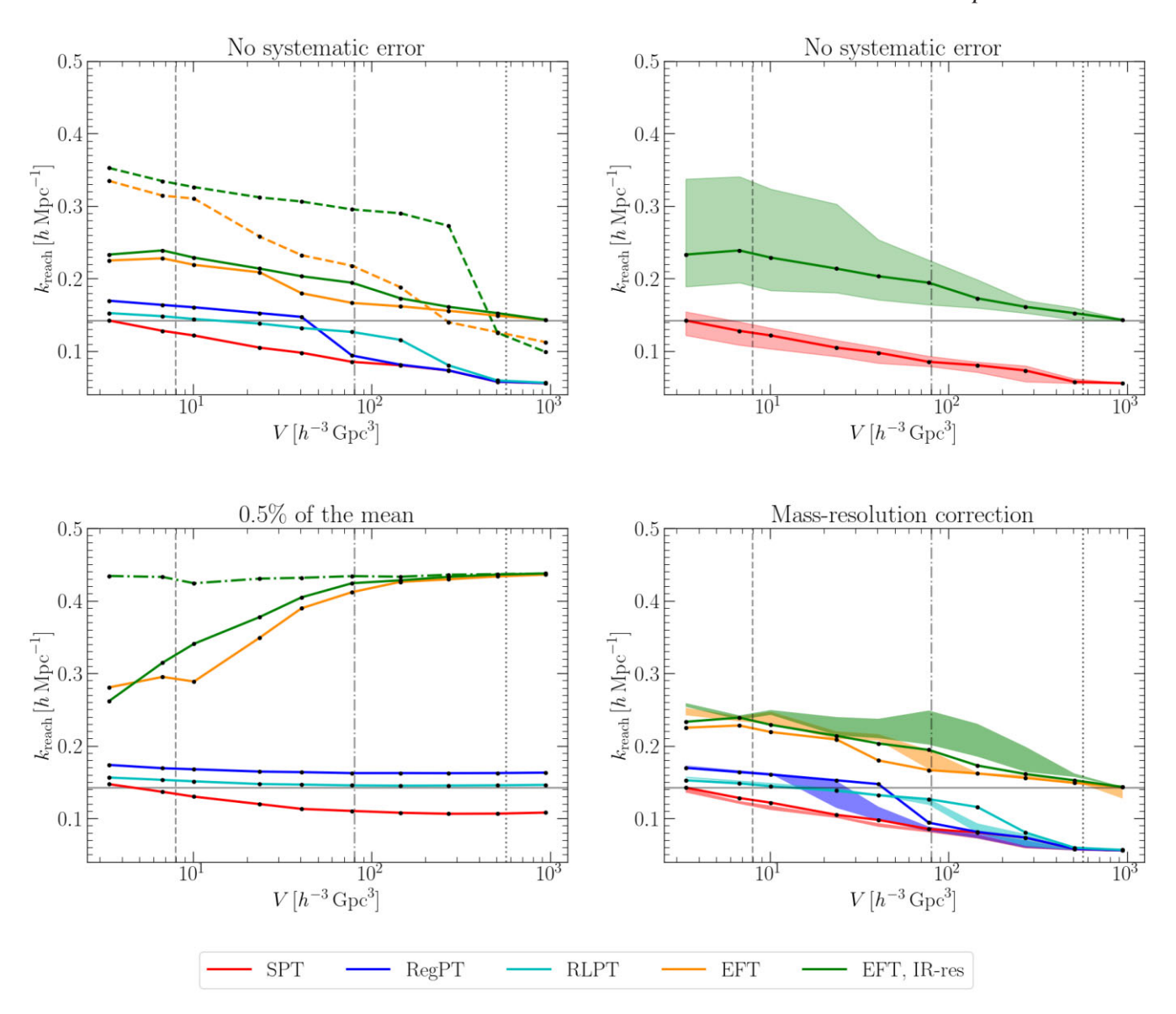


Figure 10. We define the reach of a model for the power spectrum as the minimum  $k_{\text{max}}$  at which the  $\chi^2$  goodness-of-fit test rejects the null hypothesis that the N-body data are consistent with the model predictions at the significance level of 0.05. The top-left panel shows the median reach of 200 subsets of MINERVA simulations each covering a volume V. Different colours refer to different models as indicated in the label. Solid lines are used for the models with no free parameters and for our default EFT models (i.e. with  $k_{\text{fit}} = 0.14 \, h \, \text{Mpc}^{-1}$ , highlighted by a horizontal grey line) while the two dashed lines represent the EFT models with  $k_{\text{fit}} = 0.22 \, h \, \text{Mpc}^{-1}$ . The top-right panel shows the median (solid) and the central 68 per cent range (shaded) of the estimated reach for SPT and the default IR-resummed EFT. The bottom-left panel is analogous to the top-left one but accounts for systematic errors in the simulations by considering an additional 0.5 per cent error added in quadrature to the random contributions. The dot-dashed line refers to the IR-resummed EFT model obtained by averaging  $c_0$  over the 200 subsets. Finally, the bottom-right panel shows the reach of the models after approximately correcting the simulation data for the bias introduced by the finite mass resolution (see the main text for details). The shaded regions encompass the range of variability of the corrections while the solid lines are taken from the top-left panel and are given as a reference. All panels show three vertical lines indicating: (i) the volume of a redshift bin of width  $\Delta z = 0.2$  centred at z = 1 for a Euclid-like survey (dashed); (ii) the total volume of the EOS simulations (dot-dashed); and (iii) the volume of the PT-challenge simulations in Nishimichi et al. (2020, dotted). Measurements and models are compared using a bin width of  $\Delta k = k_{\rm F}$ .

model based on the (one-sided) 95 per cent confidence limits for the chi-squared distribution. (v) We repeat the procedure from step (ii) onward 200 times. (vi) We plot the median value of the reach (top-left panels) and its scatter (top-right panels) as a function of V.

In order to ease the interpretation of our results and facilitate comparison with the literature, we draw vertical lines marking three characteristic volumes. From left to right, they are: (i)  $V = 7.94 h^{-3}$  Gpc<sup>3</sup> which corresponds to a redshift bin centred at z = 1 and of width  $\Delta z = 0.2$  of a Euclid-like survey (Euclid Collaboration

2020); (ii)  $V = 80 h^{-3} \text{ Gpc}^3$  which coincides with the total volume of the EOS simulations (and is approximately a factor 1.5 larger than the volume of the simulations used in Baldauf et al. 2015b, c; Steele & Baldauf 2021); (iii)  $V = 566 h^{-3} \text{ Gpc}^3$  which is the volume of the simulation used in the blinded challenge paper of Nishimichi et al. (2020).

We are now ready to discuss the results presented in the top-left panels of Figs 10 and 11. As expected, the domain of accuracy of the models decreases with increasing V. The only exception

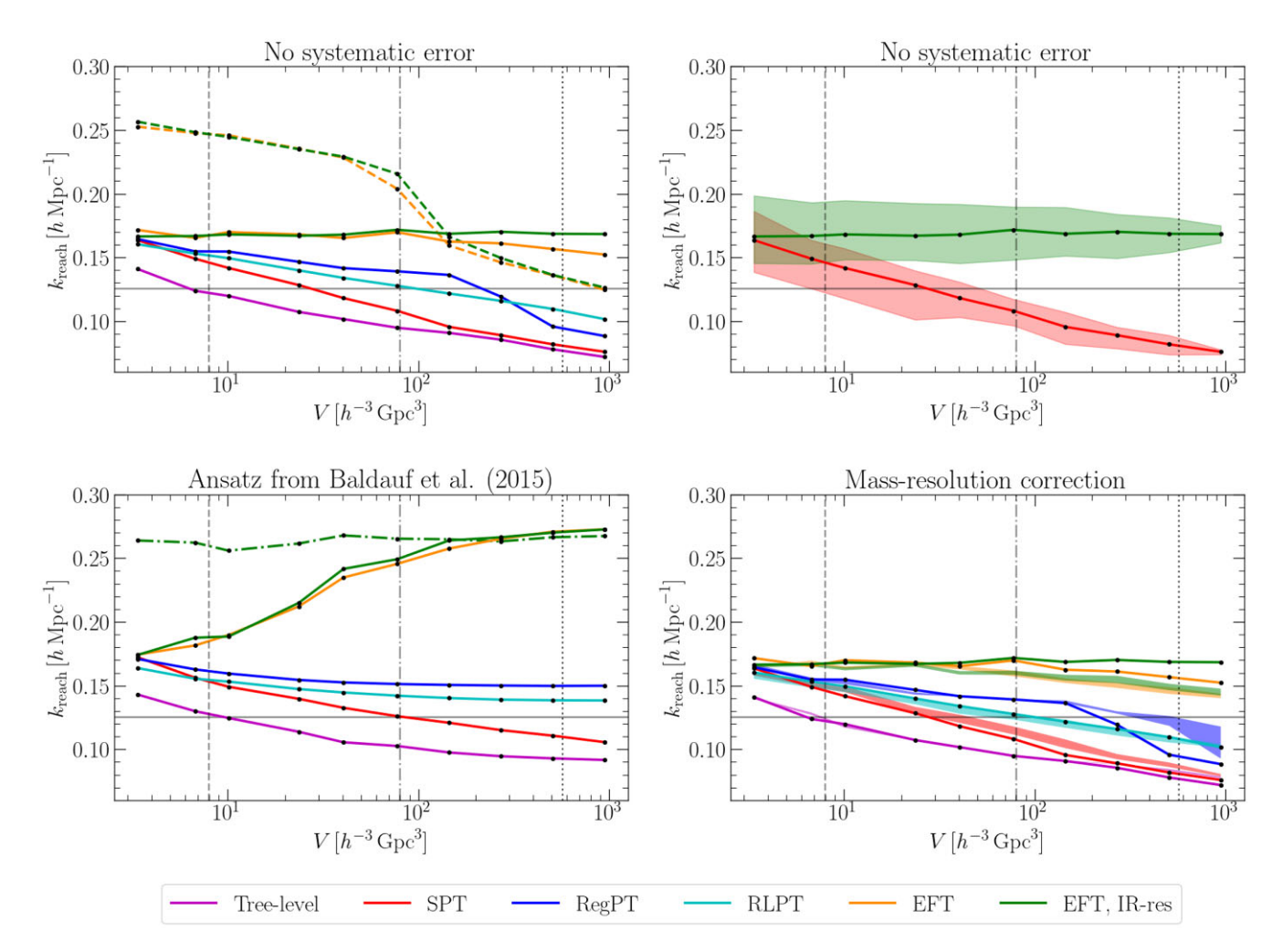


Figure 11. As in Fig. 10 but for the bispectrum models and using  $\Delta k = 3 k_{\rm F}$ . In the bottom-left panel, systematic errors were added in quadrature to the statistical errors of the measurements following the ansatz of Baldauf et al. (2015c).

is the case of the EFT bispectrum for which the reach turns out to be independent of the simulation volume and corresponds to approximately  $0.17\,h\,\mathrm{Mpc^{-1}}$ . The ranking of the models is pretty much independent of V, with SPT always being the first to break down and EFT the last. However, RegPT does better than RLPT for small V while the order is reversed for large V. It is also worth noticing that, while RegPT quite significantly extends the reach of SPT for the power spectrum for  $V \simeq 8\,h^{-3}\,\mathrm{Gpc^3}$ , it gives much smaller improvements for the bispectrum.

The nominal range of accuracy of EFT always extends beyond  $k_{\rm fit}$  (indicated with horizontal grey lines in the figures). This is not surprising because, when the  $\chi^2_{\rm m}$  statistic suggests a good fit at  $k_{\rm fit}$ , our definition of the reach will automatically pick a larger wavenumber. Essentially, what this means is that the EFT fits at  $k_{\rm fit}$  are good (or even too good) in terms of  $\chi^2_{\rm m}$ . We remind the reader that the values for  $k_{\rm fit}$  we use are chosen in Section 5.1 based on two criteria: (i) avoiding that the best-fitting EFT parameters run with  $k_{\rm fit}$  and (ii) requiring consistency between the results obtained from P and B. However, since Section 5.1 takes into consideration the full MINERVA set, our selected values might be considered 'conservative' when V is reduced (although we believe we should always perform the most challenging test for the theory, i.e. use the largest possible volume to test its basic assumptions like the scale-independence of the free parameters). For comparison, in the top-left panels of Figs 10 and

11, we also show the range of accuracy one would obtain by fitting the EFT parameters up to  $k_{\rm fit} = 0.22 \, h \, {\rm Mpc}^{-1}$  (yellow and green dashed lines). This vastly increases the reach at small V (for both P and B) but reduces it at large V. In particular, for large enough volumes, the estimated reach becomes smaller than  $k_{\rm fit}$  meaning that it is impossible to get a good fit to the numerical data.

So far we have concentrated on the median range of accuracy of each model. For this reason, in the top-right panels of Figs 10 and 11, we plot the statistical uncertainty of the estimated reach as a function of V. In this case, we only consider SPT and IR-resummed EFT to improve readability. The shaded areas indicate the central 68 per cent region<sup>5</sup> among the 200 sets of simulations with volume V. It turns out that the error on the reach is by no means negligible, particularly for EFT which contains free parameters. It is therefore important to take this into account when comparing studies based on different simulations. In Fig. 12, we show how the distribution of the best-fitting amplitudes for the counterterms varies with V. We consider the IR-resummed EFT model for the bispectrum, fit  $c_0$  from P and the other counterterms from B, and

<sup>&</sup>lt;sup>5</sup>Obviously, this statistic underestimates the actual scatter when *V* approaches the total volume of the MINERVA simulations as the different samples mostly overlap.

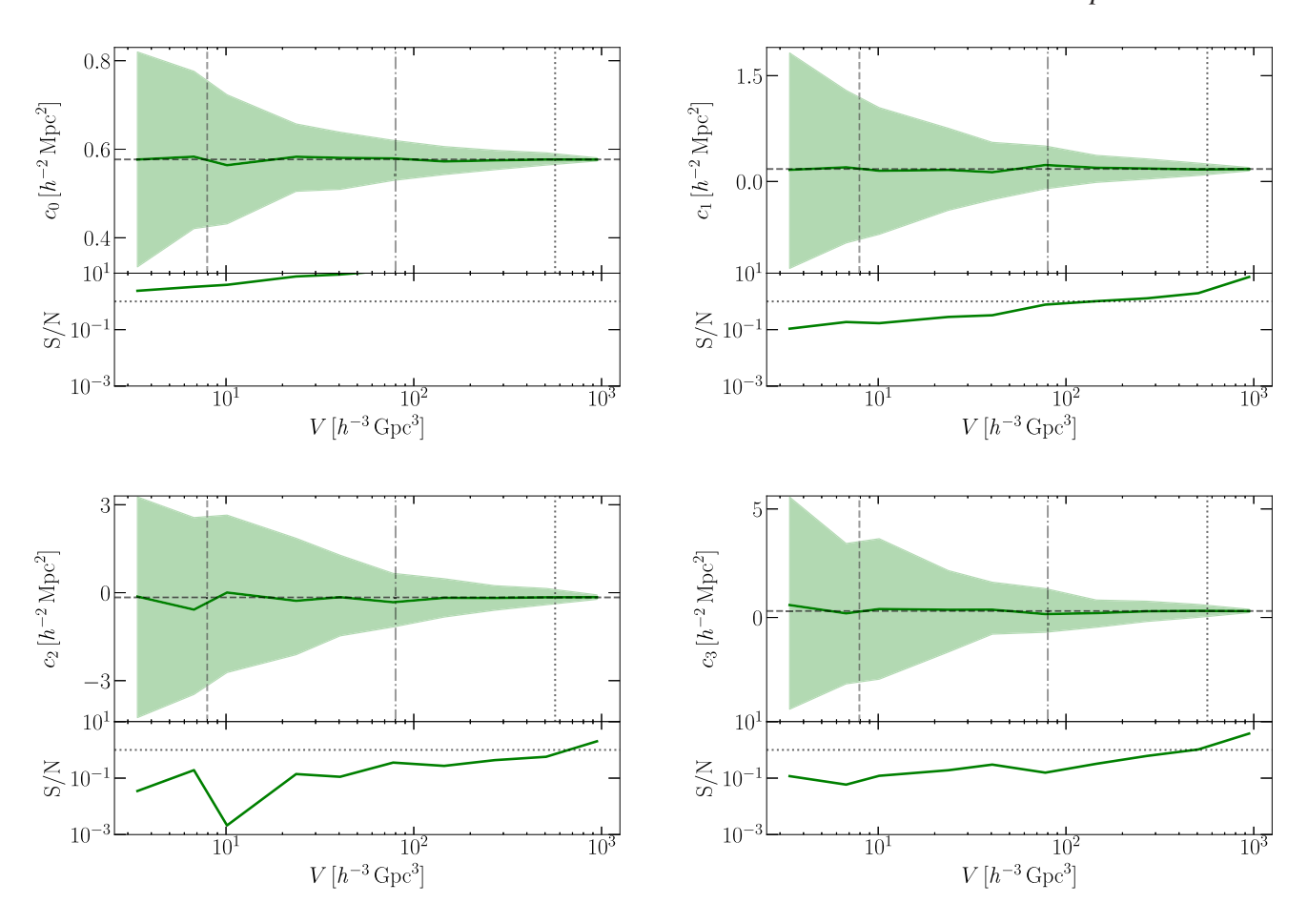


**Figure 12.** Distribution of the best-fitting EFT parameters as a function of the volume V used to measure the power spectrum and the bispectrum. The data refer to the counterterms of the IR-resummed EFT model with  $k_{\rm fit} = 0.125 \, h\,{\rm Mpc}^{-1}$ . The parameter  $c_0$  is derived from the power spectrum while  $c_1$ ,  $c_2$ , and  $c_3$  are determined from the bispectrum. The top panels show the median (solid) and the central 68 per cent region (shaded) over 200 realisations. The horizontal dashed lines indicate the values obtained from the full MINERVA simulation suite and given in Table 3. The three vertical lines mark the same volumes as in Figs 10 and 11. The bottom panels show the signal-to-noise ratio defined as the ratio between the median and and half the central 68 per cent interval.

use  $k_{\rm fit} = 0.125 \, h \, {\rm Mpc}^{-1}$ . It is important to notice that, while the median values of the EFT parameters approximately coincide with those in Table 3, the scatter around them strongly depends on V. For the redshift shell in a Euclid-like survey,  $c_1$ ,  $c_2$ , and  $c_3$  show a tremendous variability meaning that they cannot be accurately measured from a single realization. In order to get a signal-to-noise ratio of order unity for them, it is necessary to consider volumes  $V > 500 \, h^{-3} \, \mathrm{Gpc}^3$ . As a means to further investigate the impact of the fitting strategy for the counterterms, in Fig. 13, we consider four methods in which the EFT parameters are determined in different ways as indicated in Table 4. For the full MINERVA data set, our standard choice (1P + 3B) corresponds to the largest reach, while the one-parameter fit 1P + 0B performs best for  $V < 50 h^{-3}$  Gpc<sup>3</sup> suggesting that there is no need to use three counterterms when the surveyed volume is small and the error bars of the measurements are large. Angulo et al. (2015) reached similar conclusions using  $V = 27 h^{-3} \,\mathrm{Gpc}^3$  and  $k_{\mathrm{fit}} = 0.1 \,h\,\mathrm{Mpc}^{-1}$  (conjecturing that the other counterterms give contributions comparable in size to two-loop corrections). In Fig. 13, there is nothing surprising about the fact that models with less free parameters can have a larger reach given that the EFT counterterms are determined using  $k_{\rm fit} = 0.125 \, h \, {\rm Mpc}^{-1}$  and the estimated reach is substantially larger than that. It is interesting to try to understand why it is preferable to set  $c_1 = c_2 = c_3 =$ 0 for small V. We believe that the reason is related to the fact

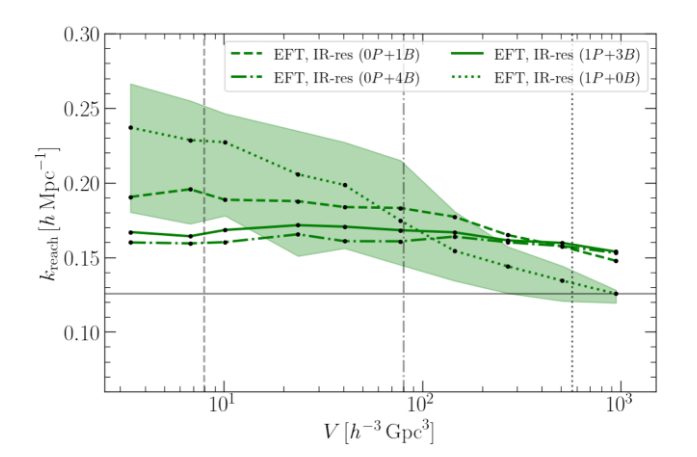


**Figure 13.** As in the top-left and top-right panels of Fig. 11 but for the IR-resummed EFT model with the counterterms determined as described in Table 4.

that the expected values given in Table 3 are much smaller than the scatter seen in Fig. 12. Basically, the fit picks large 'random' counterterms in each realization in order to adjust to the specific noise features.

**Table 4.** Schematic description of the methods used to fit the EFT counterterms in Fig. 13. The symbols P and B denote parameters determined by fitting (up to  $k_{\rm fit} = 0.125 \, h \, {\rm Mpc}^{-1}$ ) the power spectrum or the the bispectrum, respectively. The number 0 indicates that the parameter is set to zero.

Method	$c_0$	$c_1$	$c_2$	<i>c</i> <sub>3</sub>
1P + 0B	P	0	0	0
1P + 3B	P	B	B	B
0P + 1B	B	0	0	0
0P + 4B	B	B	B	B

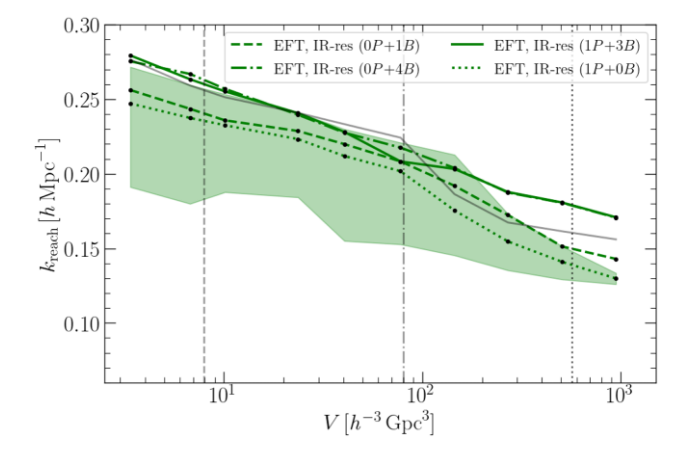


**Figure 14.** As in Fig. 13 but considering a volume-dependent  $k_{\rm fit}$  (grey line for the 1P + 3B case, see the main text for details).

Following a suggestion by the reviewer, we also investigate the case in which  $k_{\rm fit}$  is uniquely determined from the simulation volume. This is motivated by the fact that, in practical applications of the PT models, one first determines  $k_{\text{fit}}$  by testing the performance of the models against mock catalogues with the same volume as the actual survey. Since the counterterms determined from fitting the models to the measurements extracted from smaller volumes have larger uncertainties, the scale dependence of the EFT parameters will become apparent at higher  $k_{\rm fit}$  values. Thus, instead of using the fixed value of  $k_{\rm fit} = 0.125 \ h \, {\rm Mpc}^{-1}$  as above, we now calculate  $k_{\rm fit}$  for each considered volume by fitting constants to the curves given in Fig. 4 and determining the scale at which the  $\chi^2$  test rejects the fit with 68 per cent confidence. As expected, the value of  $k_{\rm fit}$ drops as larger and larger volumes are considered (see the grey solid line in Fig. 14 which shows  $k_{\rm fit}$  for the 1P + 3B case). The other curves in Fig. 14 show the variations of  $k_{\text{reach}}$  for the EFT models with the variable  $k_{\rm fit}$ . Compared to the case with fixed  $k_{\rm fit}$ (Fig. 13), we observe a dramatic increase of  $k_{\text{reach}}$  for the models with extra 3 counterterms for small and intermediate volumes. For  $V \simeq 8 \, h^{-3} \, \mathrm{Gpc^3}$  (representative of a Euclid-like survey), the formal  $k_{\text{reach}}$  of these models is 0.28 h Mpc<sup>-1</sup>. Indeed, the combination of larger statistical errors with the higher value of  $k_{\rm fit}$  results in a better agreement with the simulation data on small scales. Note, however, that, in this case,  $k_{\text{fit}}$  is pushed beyond the value for which the theory is self consistent.

In conclusion, the peculiarity of the EFT approach is the presence of free parameters in the counterterms that need to be determined from the measurements. Our results show that the methodology used to fix the EFT parameters heavily influences the range of accuracy of the theory. Basically, when the V is small, error

bars are large, and the counterterms are poorly determined, the resulting freedom in the EFT parameters boosts the apparent reach of the models. Care should then be taken to ensure that results from different studies are properly compared. Moreover, future studies should carefully investigate if and how the freedom in the counterterms impacts the estimation of cosmological parameters from the galaxy bispectrum that will be measured by the forthcoming generation of redshift surveys (Oddo et al. 2021).

#### 5.5 Systematic errors

Just like any other numerical method, *N*-body simulations do not provide the exact solution to the problem of gravitational instability and perturbation growth. Modern codes are optimized based on a trade-off between computation speed and accuracy. Their finite mass and force resolution, the time-stepping criterion, the integration method, the way initial conditions are set, and forces are computed generate small systematic deviations from the exact solution.

Several studies try to quantify the impact of these imperfections on various summary statistics (e.g. Takahashi et al. 2008; Nishimichi et al. 2009; Baldauf et al. 2015c; Schneider et al. 2016). However, the current understanding is not mature enough yet to provide a robust method for correcting goodness-of-fit statistics such as our  $\chi_m^2$ . Therefore, simplified approaches are necessary. The most elementary consists of adding small uncorrelated systematic errors to the statistical error budget. We follow this approach in the bottomleft panels of Figs 10 and 11. For the power spectrum, we add a 0.5 per cent systematic error in quadrature to the statistical error in order to approximately match the numerical results of Schneider et al. (2016). For the bispectrum, instead, we adopt two different approaches. First, following Angulo et al. (2015), we consider a shape- and scale-independent systematic contribution at the 2 per cent level (again summed in quadrature to the random error). As a second option, we use the scale-dependent ansatz by Baldauf et al. (2015c), which provides a fit to the systematic deviations measured among N-body simulations with different characteristics. In this case, the (relative) systematic error is

$$\frac{\Delta B}{B} = 0.01 + 0.02 \left( \frac{k_1}{0.5 \, h \, \text{Mpc}^{-1}} \right),\tag{33}$$

where, as always,  $k_1$  denotes the largest side of the triangular configuration. Since both approaches give very similar results, in Fig. 11 we only show those obtained with the scale-dependent ansatz. We are now ready to present our findings. For the models with no free-parameters, adding small systematic errors only changes the reach for large values of V, i.e. in every case in which the statistical errors are smaller than the additional systematic contributions. As a consequence, the resulting ranges of accuracy show little variations with V and RegPT turns out to consistently have the largest reach for all values of V. Conversely, the range of accuracy of EFT is strongly affected by the inclusion of systematic errors for all V. What is perhaps more surprising is that the reach of the EFT models increases with V. This happens because the values assigned to the EFT parameters scatter among the 200 subsets of simulations. In particular, when V is small, the EFT parameters have big uncertainties and the models cannot provide a good fit to the numerical data for large  $k_{\text{max}}$ . To clarify this further, we investigate what happens when we use the same EFT parameters for all simulation subsets. In this case, we use the mean of the values obtained from the individual sets. Our results are shown with dot-dashed lines in the bottomleft panels of Figs 10 and 11. The reach for the power spectrum and bispectrum are extended to roughly 0.43 and  $0.26 h \,\mathrm{Mpc}^{-1}$ , respectively, independently of V. Note, however, that the calibration of the EFT parameters without using the data is not doable in practical applications to observational surveys.

Systematic errors affect the accuracy and not the precision of measurements. Therefore, it is somewhat unnatural to model them as random uncorrelated errors. For example, it is well known that the finite mass resolution of N-body simulations leads to the suppression of density fluctuations on small scales (e.g. Heitmann et al. 2010; Schneider et al. 2016). In what follows, we propose a simple parametrization of this effect which allows us to include it in our error budget as a 'perfectly correlated' error. Let us consider an N-body simulation with particle density  $\bar{n}$  and make the educated guess that, due to the finite mass resolution,  $\delta_{\bar{n}}(\mathbf{k}) = \delta_{\infty}(\mathbf{k}) R_{\bar{n}}(k)$  where  $\delta_{\infty}(\mathbf{k})$  denotes the ideal continuum case. It follows that

$$P_{\bar{n}}(k) = P_{\infty}(k) R_{\bar{n}}^{2}(k), \tag{34}$$

and

$$B_{\bar{n}}(k_1, k_2, k_3) = B_{\infty}(k_1, k_2, k_3) R_{\bar{n}}(k_1) R_{\bar{n}}(k_2) R_{\bar{n}}(k_3). \tag{35}$$

In order to constrain the shape of the function  $R_{\bar{n}}(k)$  at z=1, we use the power spectra extracted from 30 realizations of the Quijote simulations (Villaescusa-Navarro et al. 2020) at three different resolutions, i.e. using 256<sup>3</sup>, 512<sup>3</sup>, and 1024<sup>3</sup> particles within a box of 1  $h^{-3}$  Gpc<sup>3</sup>. We find that the following parametrization:

$$R_{\bar{n}}(k) = \frac{1}{1 + A(\bar{n})\,\epsilon(k)}\tag{36}$$

with

$$\epsilon(k) = \frac{k}{h \,\mathrm{Mpc}^{-1}} + \alpha \,\left(\frac{k}{h \,\mathrm{Mpc}^{-1}}\right)^2 + \beta \,\left(\frac{k}{h \,\mathrm{Mpc}^{-1}}\right)^3, \tag{37}$$

accurately reproduces the numerical data up to  $k_{\rm max}=0.3\,h\,{\rm Mpc}^{-1}.$  The ratio between two power spectra obtained with different mass resolution is

$$\frac{P_{\bar{n}_1}(k)}{P_{\bar{n}_2}(k)} = \frac{R_{\bar{n}_1}^2(k)}{R_{\bar{n}_2}^2(k)} \simeq 1 + 2 \Delta A \, \epsilon(k),\tag{38}$$

where  $\Delta A = A(\bar{n}_2) - A(\bar{n}_1)$  and we have Taylor expanded the final result to first order assuming that the corrections are small on the scales of interest. From the Quijote power spectra, we obtain  $\alpha = -0.35$  and  $\beta = 0.39$ . In order to estimate  $A(\bar{n}_{\text{MINERVA}})$ , we assume that the correction is negligible at the highest Quijote resolution and interpolate  $\Delta A$  (note that  $\bar{n}_{\text{MINERVA}} = 0.296 \, h^3 \, \text{Mpc}^{-3}$  while the Quijote simulations have  $\bar{n} = 0.017, 0.134$ , and  $1.074 \, h^3 \, \text{Mpc}^{-3}$ ). We obtain  $A(\bar{n}_{\text{MINERVA}}) = 0.0188$  that corresponds to sub-per cent corrections over all scales of interest. Eventually, we write the systematic error (bias) in the summary statistics extracted from an N-body simulation as

$$\Delta P = P_{\bar{n}} - P_{\infty} = P_{\bar{n}} \left( 1 - \frac{1}{R_{\bar{n}}^2(k)} \right) \approx -2 P_{\bar{n}} A(\bar{n}) \epsilon(k),$$
 (39)

$$\Delta B = B_{\bar{n}} - B_{\infty} \approx -B_{\bar{n}} A(\bar{n}) \left[ \epsilon(k_1) + \epsilon(k_2) + \epsilon(k_3) \right]. \tag{40}$$

In order to apply this result to the MINERVA simulations, we re-scale our estimate for  $A(\bar{n}_{\text{MINERVA}})$  by a factor  $\gamma$  for which we consider three possible values, namely 0.5, 1.0, and 1.5. Although these values may not exactly describe the correction due to the finite mass resolution in the MINERVA runs, they allow us to conceptually investigate the effect of a scale- and shape-dependent bias. We thus re-compute the  $\chi^2_m$  statistic after shifting the measurements from the simulations

according to the corrections given in equations (39) and (40). Our results for the reach of the models are displayed in the bottom-right panels of Figs 10 and 11, where the coloured bands indicate the range of variability induced by  $\gamma$  and the solid lines reproduce the curves from the top-left panel to emphasize changes. Overall, the impact of the corrections is rather minor. None the less, a few changes are worth noticing. For the power spectrum, the IR-resummed EFT at intermediate volumes shows the most marked improvement. For the bispectrum, accounting for the bias improves the reach of RegPT for large V and deteriorates it for both EFT models. Perhaps, the most important conclusion that one can draw from this test is that its results are very different from those obtained by simply inflating the random errors to account for systematics (as routinely done in the literature). The latter approach, in fact, artificially boosts the reach of models with free parameters as in the case of EFT. Our study calls for a better understanding of random and systematic errors in N-body simulations.

#### 6 SUMMARY

Perturbative techniques based on fluid dynamics are widely used to study the growth of the large-scale structure of the Universe. In fact, they often are the only method of obtaining predictions with analytical control. The convergence properties of perturbation theory are still a matter of debate but there is mounting evidence that the resulting expressions for large-scale observables are actually asymptotic, i.e. only the truncated series expansion (including just the first few terms) provides an accurate approximation to the exact solution (e.g. Pajer & van der Woude 2018; Konstandin et al. 2019, and references therein).

Modern perturbative approaches come in a plethora of flavours and sometimes contain free parameters. It is thus imperative to identify their regime of validity and accuracy before applying them to practical situations. *N*-body simulations of collisionless dark matter in a cosmological background are the standard test bed for inferring the reach of the different models.

The purpose of this study is threefold. First, we use a very large set of *N*-body simulations (the MINERVA suite) to test the NLO expansions for the matter power spectrum and bispectrum in five different implementations of perturbation theory, namely SPT, RegPT, RLPT, EFT, and IR-resummed EFT. Secondly, we try to draw the line that demarcates general results from those affected by the method used to determine the reach of the models with free parameters (i.e. EFT and IR-resummed EFT). Thirdly, we explore a novel way to account for the systematic errors introduced by the finite mass resolution of *N*-body simulations.

Specifically, we study how well the different models match the measurements from the simulations as a function of the maximum wavenumber considered,  $k_{\rm max}$ . Having in mind the forthcoming generation of surveys, such as those that will be conducted by DESI and the Euclid mission, we only consider data at z=1. We define the reach of a model as the minimum  $k_{\rm max}$  at which the  $\chi^2$  goodness-of-fit test rejects the null hypothesis that the N-body data are consistent with the model predictions at the significance level of 0.05. This requires making some assumptions about the covariance matrix of the measurements. We use the Gaussian approximation given in equation (25) for the power spectrum and a more sophisticated expression for the bispectrum – see equation (27). In both cases, we use a dedicated version of the  $\chi^2$  test to verify that these expressions closely approximate the covariance matrix of the measurements extracted from the simulations.

#### 4978 D. Alkhanishvili et al.

In the first part of our study, we consider the full MINERVA suite and neglect systematic errors in the simulations. Our main findings are as follows.

- (i) By fitting the EFT parameters that determine the amplitude of the counterterms to the simulation data as a function of  $k_{\rm max}$ , we find that they remain stable until a maximum wavenumber and change beyond that (Figs 3 and 4). The stability region ends at  $k_{\rm max} = 0.14 \, h \, {\rm Mpc}^{-1}$  for the power spectrum and  $0.125 \, h \, {\rm Mpc}^{-1}$  for the bispectrum. We use these values to define the default range of scales ( $k < k_{\rm fit}$ ) over which we fit the EFT parameters.
- (ii) The  $\chi^2$  goodness-of-fit test for the power spectrum (Fig. 5) shows that EFT and IR-resummed EFT accurately match the simulations up to  $k_{\rm max} = 0.14 \, h \, {\rm Mpc}^{-1}$  while all the models without free parameters fail at much larger scales, i.e.  $k_{\rm max} = 0.06 \, h \, {\rm Mpc}^{-1}$ .
- (iii) Repeating the test for the bispectrum (Fig. 7) provides a clear ranking for the models based on their reach. The EFT models have the largest range of accuracy ( $k_{\rm max} \simeq 0.16$ –0.19  $h\,{\rm Mpc}^{-1}$ , depending on the binning of the data) followed by RegPT and RLPT ( $k_{\rm max} \simeq 0.10$ –0.14  $h\,{\rm Mpc}^{-1}$ ) and SPT ( $k_{\rm max} \simeq 0.08\,h\,{\rm Mpc}^{-1}$ ). Note that the nominal reach of EFT extends beyond  $k_{\rm fit}$ , meaning that the model with the counterterms fixed using triangle configurations with  $k < k_{\rm fit} = 0.125\,h\,{\rm Mpc}^{-1}$  continues to provide a good fit on (slightly) smaller scales.

Next, by sub-sampling the MINERVA suite, we investigate how the reach of the models depends on the total volume covered by the simulations used in our tests. This is particularly useful when comparing different results in the literature and also to gauge the range of scales that can be robustly probed in an actual galaxy redshift survey. In this analysis, we approximately account for systematic effects introduced by the *N*-body technique using different methods. Our key results are as follows.

- (iv) Obviously, the reach of the models improves for smaller volumes as the statistical error bars become larger and it is easier to fit the data. Considering a redshift bin of width  $\Delta z = 0.2$  centred at z = 1 for a Euclid-like survey, gives a median reach for SPT of approximately  $0.12\,h\,\mathrm{Mpc^{-1}}$  for the power spectrum and  $0.15\,h\,\mathrm{Mpc^{-1}}$  for the bispectrum. On the other hand, for IR-resummed EFT we obtain  $0.25\,h\,\mathrm{Mpc^{-1}}$  for the power spectrum and  $0.18\,h\,\mathrm{Mpc^{-1}}$  for the bispectrum. All the other models lie in between these extremes (Figs 10 and 11). It is also important to mention that the scatter of the reach between different realizations with the same volume becomes rather large for the models that have free parameters (the central 68 per cent range for EFT extends from 0.19 to  $0.34\,h\,\mathrm{Mpc^{-1}}$  in the case of the power spectrum). This should be taken into account when comparing results from different studies.
- (v) The estimated range of accuracy of the EFT predictions is heavily influenced by the procedure adopted to fit the counterterms. For the volume of the Euclid-like shell, using  $k_{\rm fit}=0.22\,h\,{\rm Mpc}^{-1}$  extends the median reach of the IR-resummed EFT model to 0.33 and 0.25  $h\,{\rm Mpc}^{-1}$  for the power spectrum and the bispectrum, respectively, but degrades it for the full MINERVA set. For the bispectrum, fitting only  $c_0$  from the power spectrum and setting the other three counterterms to zero gives the largest reach for  $V<100\,h^{-3}{\rm Mpc}^3$ . Fitting all the four parameters are instead preferred for larger volumes (Fig. 13). Therefore, it is difficult to unequivocally define a reach for the models with free parameters.
- (vi) The results above are only slightly affected (less than 10 per cent change) by accounting for a scale- and shape-dependent bias due to the finite mass resolution of the *N*-body simulations.

(vii) The situation is very different when uncorrelated systematic errors are added in quadrature to the statistical uncertainties, as assumed in Baldauf et al. (2015c) and Angulo et al. (2015). In this case, the reach of EFT is dramatically extended thanks to the freedom provided by the counterterms. For example, considering the whole MINERVA suite, we obtain that the IR-resummed EFT model provides a good fit until 0.40 and  $0.27 h \, \mathrm{Mpc}^{-1}$  for the power-spectrum and the bispectrum, respectively. More modest changes are seen for the models with no fixed parameters at large V.

In order to constrain the cosmological parameters from the galaxy bispectrum, it is necessary to model galaxy biasing, discreteness effects, and redshift-space distortions on top of the non-linearities of the matter density field. It is very well possible that the additional terms in the expressions for the galaxy bispectrum to NLO will be degenerated with higher-order terms in the matter models and thus extend the reach of the more complex mathematical descriptions beyond the scales determined in this work. Yet, it is pivotal to retain control over the extent to which this is happening, especially if one wants to assign a physical meaning to the additional (e.g. bias and shot-noise) parameters. This is why we believe our work is important.

#### **ACKNOWLEDGEMENTS**

We are grateful to Claudio Dalla Vecchia and Ariel Sanchez for running and making available the MINERVA simulations, performed and analysed on the Hydra and Euclid clusters at the Max Planck Computing and Data Facility (MPCDF) in Garching. We thank Martin Crocce, Alex Eggemeier, Azadeh Moradinezhad, Roman Scoccimarro, and Zvonimir Vlah for useful discussions. We acknowledge the hospitality of the Institute for Fundamental Physics of the Universe in Trieste, where a part of this work was carried out in October 2019. DA acknowledges partial financial support by the Shota Rustaveli National Science Foundation of Georgia (GNSF) under the grant FR-19-498. ES is partially supported by the Istituto Nazionale di Fisica Nucleare (INFN) INDARK PD51 grant and acknowledges support from PRIN MIUR 2015 Cosmology and Fundamental Physics: illuminating the Dark Universe with Euclid. MB acknowledges support from the Netherlands Organization for Scientific Research (NWO), which is funded by the Dutch Ministry of Education, Culture and Science (OCW), under VENI grant 016. Veni. 192. 210. MB also acknowledges support from the NWO under the project 'Cosmic Origins from Simulated Universes' for the computing time allocated to run a subset of the EOS Simulations on CARTESIUS, a supercomputer which is a part of the Dutch National Computing Facilities. AL acknowledges funding by the LabEx ENS-ICFP: ANR-10-LABX-0010/ANR-10-IDEX-0001-02 PSL\*. VY acknowledges funding from the European Research Council (ERC) under the European Union's Horizon 2020 research and innovation programme (grant agreement no. 769130).

#### DATA AVAILABILITY

The data underlying this article will be shared on reasonable request to the corresponding author.

#### REFERENCES

Agarwal N., Desjacques V., Jeong D., Schmidt F., 2021, J. Cosmol. Astropart. Phys., 2021, 021

Angulo R. E., Foreman S., Schmittfull M., Senatore L., 2015, J. Cosmol. Astropart. Phys., 10, 039

- Baldauf T., Mercolli L., Mirbabayi M., Pajer E., 2015c, J. Cosmol. Astropart. Phys., 2015, 007
- Baldauf T., Mercolli L., Zaldarriaga M., 2015b, Phys. Rev. D, 92, 123007
- Baldauf T., Mirbabayi M., Simonović M., Zaldarriaga M., 2015a, Phys. Rev. D, 92, 043514
- Baldauf T., Mirbabayi M., Simonović M., Zaldarriaga M., 2016, preprint (arXiv:1602.00674)
- Barreira A., 2019, J. Cosmol. Astropart. Phys., 03, 008
- Barreira A., 2020, J. Cosmol. Astropart. Phys., 2020, 031
- Baumann D., Nicolis A., Senatore L., Zaldarriaga M., 2012, J. Cosmol. Astropart. Phys., 2012, 051
- Bernardeau F., Colombi S., Gaztañaga E., Scoccimarro R., 2002, Phys. Rep., 367, 1
- Bernardeau F., Crocce M., Scoccimarro R., 2008, Phys. Rev. D, 78, 103521
- Bernardeau F., Crocce M., Scoccimarro R., 2012, Phys. Rev. D, 85, 123519 Biagetti M., Lazeyras T., Baldauf T., Desjacques V., Schmidt F., 2017,
- MNRAS, 468, 3277
  Blas D., Garny M., Ivanov M. M., Sibiryakov S., 2016, J. Cosmol. Astropart.
- Phys., 2016, 028
- Blas D., Garny M., Konstandin T., 2014, J. Cosmol. Astropart. Phys., 2014, 010
- Blas D., Lesgourgues J., Tram T., 2011, J. Cosmol. Astropart. Phys., 2011, 034
- Carlson J., Reid B., White M., 2013, MNRAS, 429, 1674
- Carlson J., White M., Padmanabhan N., 2009, Phys. Rev. D, 80, 043531
- Carrasco J. J. M., Foreman S., Green D., Senatore L., 2014a, J. Cosmol. Astropart. Phys., 7, 56
- Carrasco J. J. M., Foreman S., Green D., Senatore L., 2014b, J. Cosmol. Astropart. Phys., 7, 57
- Carrasco J. J. M., Hertzberg M. P., Senatore L., 2012, J. High Energy Phys., 2012, 82
- Catelan P., 1995, MNRAS, 276, 115
- Chan K. C., Blot L., 2017, Phys. Rev. D, 96, 023528
- Chudaykin A., Ivanov M. M., 2019, J. Cosmol. Astropart. Phys., 2019, 034
- Chudaykin A., Ivanov M. M., Simonović M., 2021, Phys. Rev. D, 103, 043525
- Colavincenzo M. et al., 2019, MNRAS, 482, 4883
- Cole S. et al., 2005, MNRAS, 362, 505
- Crocce M., Pueblas S., Scoccimarro R., 2006, MNRAS, 373, 369
- Crocce M., Scoccimarro R., 2006a, Phys. Rev. D, 73, 063519
- Crocce M., Scoccimarro R., 2006b, Phys. Rev. D, 73, 063520
- Crocce M., Scoccimarro R., 2008, Phys. Rev. D, 77, 023533
- Crocce M., Scoccimarro R., Bernardeau F., 2012, MNRAS, 427, 2537
- d'Amico G., Gleyzes J., Kokron N., Markovic K., Senatore L., Zhang P., Beutler F., Gil-Marín H., 2020, J. Cosmol. Astropart. Phys., 2020, 005
- DESI Collaboration, 2016, preprint (arXiv:1611.00036)
  Eggemeier A., Scoccimarro R., Smith R. E., Crocce M., Pezzotta A., Sánchez
- Eggemeier A., Scoccimarro R., Smith R. E., Crocce M., Pezzotta A., Sanchez A. G., 2021, Phys. Rev. D, 103, 123550
- Euclid Collaboration, 2020, A&A, 642, A191
- Feldman H. A., Kaiser N., Peacock J. A., 1994, ApJ, 426, 23
- Fisher K. B., Nusser A., 1996, MNRAS, 279, L1
- Foreman S., Perrier H., Senatore L., 2016, J. Cosmol. Astropart. Phys., 2016, 027
- Foreman S., Senatore L., 2016, J. Cosmol. Astropart. Phys., 2016, 033
- Fry J. N., 1984, ApJ, 279, 499
- Gaztanaga E., 1994, MNRAS, 268, 913
- Gaztañaga E., Norberg P., Baugh C. M., Croton D. J., 2005, MNRAS, 364, 620
- Gil-Marín H. et al., 2015b, MNRAS, 452, 1914
- Gil-Marín H., Noreña J., Verde L., Percival W. J., Wagner C., Manera M., Schneider D. P., 2015a, MNRAS, 451, 539
- Gil-Marín H., Percival W. J., Verde L., Brownstein J. R., Chuang C.-H., Kitaura F.-S., Rodríguez-Torres S. A., Olmstead M. D., 2017, MNRAS, 465, 1757
- Goroff M. H., Grinstein B., Rey S. J., Wise M. B., 1986, ApJ, 311, 6
- Grieb J. N., Sánchez A. G., Salazar-Albornoz S., Dalla Vecchia C., 2016, MNRAS, 457, 1577
- Gualdi D., Gil-Marín H., Manera M., Joachimi B., Lahav O., 2019, MNRAS, 484, L29

- Gualdi D., Verde L., 2020, J. Cosmol. Astropart. Phys., 2020, 041

  Hahn C. Villaescusa-Navarro F. 2021, J. Cosmol. Astropart. Phys. 202
- Hahn C., Villaescusa-Navarro F., 2021, J. Cosmol. Astropart. Phys., 2021, 029
- Heinrich C., Doré O., 2020, Phys. Rev. D, 102, 123549
- Heitmann K., White M., Wagner C., Habib S., Higdon D., 2010, ApJ, 715, 104
- Hertzberg M. P., 2014, Phys. Rev. D, 89, 043521
- Howlett C., Lewis A., Hall A., Challinor A., 2012, J. Cosmol. Astropart. Phys., 2012, 027
- Ivanov M. M., Sibiryakov S., 2018, J. Cosmol. Astropart. Phys., 2018, 053
  Ivanov M. M., Simonović M., Zaldarriaga M., 2020, J. Cosmol. Astropart.
  Phys., 2020, 042
- Konstandin T., Porto R. A., Rubira H., 2019, J. Cosmology Astropart. Phys., 2019, 027
- Kulkarni G. V., Nichol R. C., Sheth R. K., Seo H.-J., Eisenstein D. J., Gray A., 2007, MNRAS, 378, 1196
- Laureijs R. et al., 2011, preprint (arXiv:1110.3193)
- Lazanu A., Giannantonio T., Schmittfull M., Shellard E. P. S., 2016, Phys. Rev. D, 93, 083517
- Lewis A., Challinor A., Lasenby A., 2000, ApJ, 538, 473
- Matarrese S., Pietroni M., 2007, J. Cosmol. Astropart. Phys., 2007, 026
- Matsubara T., 2008, Phys. Rev. D, 77, 063530
- McBride C. K., Connolly A. J., Gardner J. P., Scranton R., Newman J. A., Scoccimarro R., Zehavi I., Schneider D. P., 2011, ApJ, 726, 13
- Meiksin A., White M., 1999, MNRAS, 308, 1179
- Meiksin A., White M., Peacock J. A., 1999, MNRAS, 304, 851
- Moradinezhad Dizgah A., Biagetti M., Sefusatti E., Desjacques V., Noreña J., 2021, J. Cosmol. Astropart. Phys., 2021, 015
- Moutarde F., Alimi J. M., Bouchet F. R., Pellat R., Ramani A., 1991, ApJ, 382, 377
- Nishimichi T. et al., 2009, PASJ, 61, 321
- Nishimichi T., D'Amico G., Ivanov M. M., Senatore L., Simonović M., Takada M., Zaldarriaga M., Zhang P., 2020, Phys. Rev. D, 102, 123541
- Oddo A., Rizzo F., Sefusatti E., Porciani C., Monaco P., 2021, J. Cosmol. Astropart. Phys., 2021, 038
- Oddo A., Sefusatti E., Porciani C., Monaco P., Sánchez A. G., 2020, J. Cosmol. Astropart. Phys., 2020, 056
- Osato K., Nishimichi T., Bernardeau F., Taruya A., 2019, Phys. Rev. D, 99, 063530
- Pajer E., van der Woude D., 2018, J. Cosmol. Astropart. Phys., 2018, 039
- Pan J., Szapudi I., 2005, MNRAS, 362, 1363
- Pearson D. W., Samushia L., 2018, MNRAS, 478, 4500
- Peebles P. J. E., Groth E. J., 1975, ApJ, 196, 1
- Pietroni M., 2008, J. Cosmol. Astropart. Phys., 2008, 036
- Porto R. A., Senatore L., Zaldarriaga M., 2014, J. Cosmol. Astropart. Phys., 5, 22
- Pueblas S., Scoccimarro R., 2009, Phys. Rev. D, 80, 043504
- Rampf C., Wong Y. Y. Y., 2012, J. Cosmol. Astropart. Phys., 6, 18
- Roth N., Porciani C., 2011, MNRAS, 415, 829
- Samushia L., Slepian Z., Villaescusa-Navarro F., 2021, MNRAS, 505, 628
- Schneider A. et al., 2016, J. Cosmol. Astropart. Phys., 2016, 047
- Scoccimarro R., 1997, ApJ, 487, 1
- Scoccimarro R., Colombi S., Fry J. N., Frieman J. A., Hivon E., Melott A., 1998, ApJ, 496, 586
- Scoccimarro R., Feldman H. A., Fry J. N., Frieman J. A., 2001, ApJ, 546, 652
- Sefusatti E., Crocce M., Desjacques V., 2010, MNRAS, 406, 1014
- Sefusatti E., Crocce M., Pueblas S., Scoccimarro R., 2006, Phys. Rev. D, 74, 023522
- Sefusatti E., Crocce M., Scoccimarro R., Couchman H. M. P., 2016, MNRAS, 460, 3624
- Sefusatti E., Scoccimarro R., 2005, Phys. Rev. D, 71, 063001
- Senatore L., Zaldarriaga M., 2015, J. Cosmol. Astropart. Phys., 2015, 013
- Slepian Z. et al., 2017a, MNRAS, 468, 1070
- Slepian Z. et al., 2017b, MNRAS, 469, 1738
- Slepian Z. et al., 2018, MNRAS, 474, 2109
- Springel V., 2005, MNRAS, 364, 1105

(B8)

Steele T., Baldauf T., 2021, Phys. Rev. D, 103, 023520

Sugiyama N. S., Saito S., Beutler F., Seo H.-J., 2020, MNRAS, 497, 1684

Takahashi R. et al., 2008, MNRAS, 389, 1675

Takahashi R., 2008, Prog. Theor. Phys., 120, 549

Taruya A., Bernardeau F., Nishimichi T., Codis S., 2012, Phys. Rev. D, 86,

Taruya A., Nishimichi T., Jeong D., 2018, Phys. Rev. D, 98, 103532

Taruya A., Nishimichi T., Saito S., Hiramatsu T., 2009, Phys. Rev. D, 80,

Taylor A. N., Hamilton A. J. S., 1996, MNRAS, 282, 767

Verde L. et al., 2002, MNRAS, 335, 432

Villaescusa-Navarro F. et al., 2020, ApJS, 250, 2

Vlah Z., Seljak U., Yat Chu M., Feng Y., 2016, J. Cosmol. Astropart. Phys., 2016, 057

Yankelevich V., Porciani C., 2019, MNRAS, 483, 2078

Zel'dovich Y. B., 1970, A&A, 5, 84

#### APPENDIX A: SPT

The one-loop correction to the matter power spectrum in SPT is

$$P_{\text{SPT}}^{1-\text{loop}}(k, z) = P_{13}(k, z) + P_{22}(k, z),$$
 (A1)

$$P_{13}(k,z) = 6 [D(z)]^4 P_{L}(k) \int_{\mathbf{q}} F_3(\mathbf{k}, \mathbf{q}, -\mathbf{q}) P_{L}(q),$$
 (A2)

$$P_{22}(k,z) = 2 [D(z)]^4 \int_{\mathbf{q}} [F_2(\mathbf{q}, \mathbf{k} - \mathbf{q})]^2 P_{L}(|\mathbf{k} - \mathbf{q}|) P_{L}(q), \quad (A3)$$

and  $\int_{\mathbf{q}}$  denotes  $\int \frac{d^3\mathbf{q}}{(2\pi)^3}$ . Similarly, for the bispectrum, we have:

$$B_{\text{SPT}}^{\text{1-loop}} = B_{222} + B_{321}^{I} + B_{321}^{II} + B_{411}, \tag{A4}$$

$$B_{222}(k_1, k_2, k_3, z) = 8 [D(z)]^6 \int_{\mathbf{q}} P_{L}(q) P_{L}(|\mathbf{k}_2 - \mathbf{q}|)$$

$$\times P_{L}(|\mathbf{k}_3 + \mathbf{q}|) F_{2}(-\mathbf{q}, \mathbf{k}_3 + \mathbf{q})$$

$$\times F_{2}(\mathbf{k}_3 + \mathbf{q}, \mathbf{k}_2 - \mathbf{q}) F_{2}(\mathbf{k}_2 - \mathbf{q}, \mathbf{q})$$
(A5)

$$B_{321}^{I}(k_{1}, k_{2}, k_{3}, z) = 6 [D(z)]^{6} P_{L}(k_{3}) \int_{\mathbf{q}} P_{L}(|\mathbf{k}_{2} - \mathbf{q}|) P_{L}(q)$$

$$\times F_{3}(-\mathbf{q}, -\mathbf{k}_{2} + \mathbf{q}, -\mathbf{k}_{3})$$

$$\times F_{2}(\mathbf{k}_{2} - \mathbf{q}, \mathbf{q}) + 5 \text{ perms.}$$
(A6)

$$B_{321}^{II}(k_1, k_2, k_3, z) = 6 [D(z)]^6 P_{L}(k_2) P_{L}(k_3) F_2^{(s)}(\mathbf{k}_2, \mathbf{k}_3)$$

$$\times \int_{a} P_{L}(q) F_{3}(\mathbf{k}_{3}, \mathbf{q}, -\mathbf{q}) + 5 \text{ perms.}$$
 (A7)

$$B_{411}(k_1, k_2, k_3, z) = 12 [D(z)]^6 (z) P_L(k_2) P_L(k_3)$$

$$\times \int_{\mathbf{q}} P_{L}(q) F_{4}(\mathbf{q}, -\mathbf{q}, -\mathbf{k}_{2}, -\mathbf{k}_{3}) + 2 \text{ perms.}.$$
(A8)

#### APPENDIX B: REGPT

The (p+1)-point propagator,  $\Gamma^{(p)}(\mathbf{k}_1,\ldots,\mathbf{k}_p,z)$ , is defined as

$$\frac{1}{p!} \left\langle \frac{\delta^p \delta(\mathbf{k}, z)}{\delta \delta_{\mathbf{L}}(\mathbf{k}_1) \cdots \delta \delta_{\mathbf{L}}(\mathbf{k}_p)} \right\rangle = \frac{\delta_{\mathbf{D}}(\mathbf{k} - \mathbf{k}_{1 \cdots p})}{(2\pi)^{3(p-1)}} \, \Gamma^{(p)}, \tag{B1}$$

and can be expanded using equations (4) and (B1) as

$$\Gamma^{(p)} = \Gamma_{\text{tree}}^{(p)} + \sum_{n=1}^{\infty} \Gamma_{n-\text{loop}}^{(p)}.$$
(B2)

$$\Gamma_{\text{tree}}^{(p)}(\mathbf{k}_1,\ldots,\mathbf{k}_p,z) = [D(z)]^p F_p(\mathbf{k}_1,\ldots,\mathbf{k}_p)$$
 and

$$\Gamma_{n-\text{loop}}^{(p)}(\mathbf{k}_{1},\ldots,\mathbf{k}_{p},z) = [D(z)]^{(2n+p)} C_{p}^{2n+p} (2n-1)!!$$

$$\times \int \frac{\mathrm{d}^{3}\mathbf{q}_{1}\cdots\mathrm{d}^{3}\mathbf{q}_{n}}{(2\pi)^{3n}} F_{2n+p}$$

$$\times (\mathbf{q}_{1},-\mathbf{q}_{1},\ldots,\mathbf{q}_{n},-\mathbf{q}_{n},\mathbf{k}_{1},\ldots,\mathbf{k}_{p})$$

$$\times P_{L}(q_{1})\cdots P_{L}(q_{n}) \equiv [D(z)]^{(2n+p)}$$

$$\times \overline{\Gamma}_{n-\text{loop}}^{(p)}(\mathbf{k}_{1},\ldots,\mathbf{k}_{p}), \tag{B3}$$

where  $C_p^{2n+p}$  denotes the binomial coefficient. Resumming the subset of terms that provide the dominant contribution at small scales gives (Crocce & Scoccimarro 2006b; Bernardeau et al. 2008)

$$\Gamma^{(p)}(\mathbf{k}_1, \dots, \mathbf{k}_p, z) \xrightarrow{k \to \infty} \exp\left\{-\frac{k^2 [D(z)]^2 \sigma_d^2}{2}\right\} \Gamma_{\text{tree}}^{(p)}.$$
 (B4)

$$\sigma_{\rm d}^2 = \frac{1}{3} \int \frac{{\rm d}^3 \mathbf{q}}{(2\pi)^3} \frac{P_{\rm L}(q)}{q^2}$$
 (B5)

is the rms value of the 1D linear displacement field. Up to one-loop order, the regularized propagators which interpolate between the two asymptotic regimes are (Bernardeau et al. 2012; Taruya et al. 2012)

$$\Gamma_{\text{reg}}^{(1)}(k,z) = D(z) \left\{ 1 + \frac{k^2 [D(z)]^2 \sigma_d^2}{2} + [D(z)]^2 \overline{\Gamma}_{1-\text{loop}}^{(1)}(k) \right\} \\
\times \exp \left\{ -\frac{k^2 [D(z)]^2 \sigma_d^2}{2} \right\}$$
(B6)
$$\Gamma_{\text{reg}}^{(2)}(\mathbf{k}_1, \mathbf{k}_2, z) = [D(z)]^2 \left( F_2(\mathbf{k}_1, \mathbf{k}_2) \left\{ 1 + \frac{k^2 [D(z)]^2 \sigma_d^2}{2} \right\} \right. \\
+ [D(z)]^2 \overline{\Gamma}_{1-\text{loop}}^{(2)}(\mathbf{k}_1, \mathbf{k}_2) \right) \\
\times \exp \left\{ -\frac{k^2 [D(z)]^2 \sigma_d^2}{2} \right\},$$
(B7)
$$\Gamma_{\text{reg}}^{(3)}(\mathbf{k}_1, \mathbf{k}_2, \mathbf{k}_3, z) = [D(z)]^3 F_3 \mathbf{k}_1, \mathbf{k}_2, \mathbf{k}_3)$$

In this formalism, the matter power spectrum and bispectrum up to one-loop corrections can be expressed as (Bernardeau et al. 2008)

 $\times \exp\left\{-\frac{k^2 [D(z)]^2 \sigma_{\rm d}^2}{2}\right\}.$ 

$$P(k, z) = [\Gamma^{(1)}(k, z)]^{2} P_{L}(k)$$

$$+ 2 \int_{\mathbf{q}} [\Gamma^{(2)}(\mathbf{q}, \mathbf{k} - \mathbf{q}, z)]^{2} P_{L}(q) P_{L}(|\mathbf{k} - \mathbf{q}|),$$
 (B9)

$$\begin{split} B(\mathbf{k}_1,\,\mathbf{k}_2,\,\mathbf{k}_3,\,z) &= 2\,\Gamma^{(2)}(\mathbf{k}_1,\,\mathbf{k}_2,\,z)\,\,\Gamma^{(1)}(k_1,\,z)\,\,\Gamma^{(1)}(k_2,\,z) \\ &\times P_{\rm L}(k_1)\,\,P_{\rm L}(k_2) + 2\,\,{\rm perms}. \\ &+ \left[ 8\,\int_{\mathbf{q}} \Gamma^{(2)}(\mathbf{k}_1+\mathbf{q},\,-\mathbf{q},\,z)\,\Gamma^{(2)}(-\mathbf{k}_1-\mathbf{q},\,\mathbf{q}-\mathbf{k}_2,\,z) \right. \\ &\times \Gamma^{(2)}(\mathbf{k}_2-\mathbf{q},\,\mathbf{q},\,z)P_{\rm L}(|\mathbf{k}_2-\mathbf{q}|)P_{\rm L}(|\mathbf{k}_1+\mathbf{q}|)P_{\rm L}(q) \right] \\ &+ \left[ 6\,\Gamma^{(1)}(\mathbf{k}_3,\,z)\,P_{\rm L}(k_3)\int_{\mathbf{q}} \Gamma^{(3)}(\mathbf{q}-\mathbf{k}_2,\,-\mathbf{k}_3,\,-\mathbf{q},\,z) \right. \\ &\times \Gamma^{(2)}(\mathbf{q},\,\mathbf{k}_2-\mathbf{q},\,z)P_{\rm L}(|\mathbf{k}_2-\mathbf{q}|)P_{\rm L}(q) + 5\,\,{\rm perms.} \right]. \end{split} \tag{B10}$$

#### APPENDIX C: RLPT

By combining the Lagrangian perturbative expansion with equations (9) and (10), one obtains the following expressions at one loop (Matsubara 2008; Rampf & Wong 2012):

$$\begin{split} P_{\text{RLPT}}(k) &= \left[ P_{\text{L}} + P_{\text{SPT}}^{\text{1-loop}} + \frac{k^2}{6\pi^2} P_{\text{L}} \int \mathrm{d}q \; P_{\text{L}}(q) \right] \\ &\times \exp \left[ -\frac{k^2}{6\pi^2} \int \mathrm{d}q \; P_{\text{L}}(q) \right], \end{split} \tag{C1} \\ B_{\text{RLPT}}(k_1, k_2, k_3) &= \left[ B_{\text{SPT}}^{\text{tree}} \left\{ 1 + \frac{k_1^2 + k_2^2 + k_3^2}{12\pi^2} \int \mathrm{d}q \; P_{\text{L}}(q) \right\} \\ &+ B_{\text{SPT}}^{\text{1-loop}} \right] \exp \left[ -\frac{k_1^2 + k_2^2 + k_3^2}{12\pi^2} \int \mathrm{d}q \; P_{\text{L}}(q) \right]. \end{split} \tag{C2}$$

This paper has been typeset from a TEX/IATEX file prepared by the author.

# A.2 Window function convolution with deep neural network models

#### LETTER TO THE EDITOR

### Window function convolution with deep neural network models

D. Alkhanishvili<sup>1</sup>, C. Porciani<sup>1</sup>, and E. Sefusatti<sup>2,3,4</sup>

- Argelander Institut für Astronomie der Universität Bonn, Auf dem Hügel 71, 53121 Bonn, Germany e-mail: daalkh@astro.uni-bonn.de
- <sup>2</sup> Istituto Nazionale di Astrofisica, Osservatorio Astronomico di Trieste, Via Tiepolo 11, 34143 Trieste, Italy
- <sup>3</sup> Istituto Nazionale di Fisica Nucleare, Sezione di Trieste, Via Valerio 2, 34127 Trieste, Italy
- <sup>4</sup> Institute for Fundamental Physics of the Universe, Via Beirut 2, 34151 Trieste, Italy

Received 6 October 2022 / Accepted 6 December 2022

#### **ABSTRACT**

Traditional estimators of the galaxy power spectrum and bispectrum are sensitive to the survey geometry. They yield spectra that differ from the true underlying signal since they are convolved with the window function of the survey. For the current and future generations of experiments, this bias is statistically significant on large scales. It is thus imperative that the effect of the window function on the summary statistics of the galaxy distribution is accurately modelled. Moreover, this operation must be computationally efficient in order to allow sampling posterior probabilities while performing Bayesian estimation of the cosmological parameters. In order to satisfy these requirements, we built a deep neural network model that emulates the convolution with the window function, and we show that it provides fast and accurate predictions. We trained (tested) the network using a suite of 2000 (200) cosmological models within the cold dark matter scenario, and demonstrate that its performance is agnostic to the precise values of the cosmological parameters. In all cases, the deep neural network provides models for the power spectra and the bispectrum that are accurate to better than 0.1% on a timescale of 10 µs.

**Key words.** large-scale structure of Universe – methods: statistical – methods: data analysis

#### 1. Introduction

The most common approach to extract cosmological information from a galaxy redshift survey involves measuring the power spectrum and/or the bispectrum of the galaxy distribution. In the majority of cases, the spectra are derived using traditional estimators (Yamamoto et al. 2006; Bianchi et al. 2015; Scoccimarro 2015) based on the ideas originally introduced by Feldman et al. (1994, hereafter FKP). One drawback of this method is that the survey geometry leaves an imprint on the measured spectra, which is difficult to model. The observed galaxy overdensity field  $\delta_{\rm obs}(x)$  does not coincide with the actual fluctuations  $\delta(x)$ . The reasons are twofold. First, galaxy surveys cover only finite sections of our past light cone. Second, tracers of the large-scale structure need to be weighted based on the selection criteria of the survey. In compact form we write  $\delta_{\text{obs}}(x) = W(x) \, \delta(x)$ , where W(x) denotes the window function of the survey. It follows that the observed power spectrum and the underlying true power P(k)satisfy the relation (Peacock & Nicholson 1991; FKP)

$$P_{\text{obs}}(\mathbf{k}) = \int |\tilde{W}_2(\mathbf{k} - \mathbf{q})|^2 P(\mathbf{q}) \frac{d^3 q}{(2\pi)^3},$$
 (1)

where  $\tilde{W}_n(k)$  denotes the Fourier transform of the function W(x) normalised such that

$$\tilde{W}_n(\mathbf{k}) = \frac{\int W(\mathbf{x}) e^{i \mathbf{k} \cdot \mathbf{x}} d^3 x}{\left\{ \int [W(\mathbf{x})]^n d^3 x \right\}^{1/n}}.$$
(2)

Similarly, for the bispectrum we obtain

$$B_{\text{obs}}(\mathbf{k}_{1}, \mathbf{k}_{2}, \mathbf{k}_{3}) = \int \tilde{W}_{3}(\mathbf{k}_{1} - \mathbf{q}) \, \tilde{W}_{3}(\mathbf{k}_{2} - \mathbf{p}) \, \tilde{W}_{3}(\mathbf{k}_{3} + \mathbf{q} + \mathbf{p})$$

$$B(\mathbf{q}, \mathbf{p}, -\mathbf{q} - \mathbf{p}) \, \frac{\mathrm{d}^{3} \mathbf{q}}{(2\pi)^{3}} \, \frac{\mathrm{d}^{3} \mathbf{p}}{(2\pi)^{3}}. \tag{3}$$

The convolution in Eq. (1) mixes Fourier modes with different wavevectors and modifies the power<sup>1</sup> significantly on large scales. Since the survey window is generally not spherically symmetric, it also creates an anisotropic signal in addition to redshift-space distortions and the Alcock-Paczynski effect. These consequences need to be accounted for in order to fit theoretical models to the observational data, in particular when trying to constrain the level of primordial non-Gaussianity (e.g., Castorina et al. 2019) or general relativistic effects (e.g., Elkhashab et al. 2022). Two approaches are possible: by trying to remove the effect from the data (e.g., Sato et al. 2011) or accounting for the window in the models (e.g., de Laix & Starkman 1998; Percival et al. 2001; Ross et al. 2013). This second line of attack is much more popular: starting from an estimate for the window function, a model for

 $<sup>^\</sup>star$  Member of the International Max Planck Research School (IMPRS) for Astronomy and Astrophysics at the Universities of Bonn and Cologne.

<sup>&</sup>lt;sup>1</sup> A different class of estimators based on pixelised maps of the galaxy density is immune to this problem and directly provides noisy measurements of the unwindowed spectra (see e.g., the so-called quadratic estimators for the power spectrum in Tegmark et al. 1998 and Philcox 2021b and the cubic estimator for the bispectrum in Philcox 2021a). However, these estimators are sub-optimal on small scales. Moreover, at the moment, there is no such estimator for the anisotropic bispectrum in redshift space.

 $P_{\rm obs}(k)$  is obtained by solving the convolution integral numerically. Developing numerical procedures for fast likelihood evaluation is pivotal in multivariate Bayesian inference. For this reason, Blake et al. (2013) reformulated the convolution integrals as matrix multiplications and made use of pre-computed 'mixing matrices' to evaluate the impact of the survey window on the power spectra averaged within wavector bins. A computationally efficient way to evaluate the effect of the window function on the multipole moments of the power spectrum in the distantobserver approximation is presented by Wilson et al. (2017) and generalised by Beutler et al. (2017) to the local plane-parallel case (in which the line of sight varies with the galaxy pair). In this approach the convolution is cast in terms of a sequence of one-dimensional Hankel transforms that are performed using the FFTlog algorithm (Hamilton 2000). The key idea is to compress the information about the window function into a finite number of multipole moments of its autocorrelation function (see also Beutler et al. 2014). Further extensions account for wide-angle effects (e.g., Castorina & White 2018; Beutler et al. 2019).

Evaluating the impact of the survey window on the bispectrum has only recently received attention in the literature. From a computational perspective, performing the six-dimensional convolution integral in Eq. (3) is a challenging task that cannot form the basis of a toolbox for Bayesian inference. It is thus necessary to develop faster techniques. Inspired by perturbation theory at leading order, Gil-Marín et al. (2015) proposed an approximation where the monopole moment of the convolved bispectrum is given by the linear superposition of products of two convolved power spectra given by Eq. (1). Although this approximation is accurate enough for the BOSS survey (barring squeezed triangular configurations, which are excluded from the analysis by Gil-Marín et al. 2015), it would likely introduce severe biases in the analysis of the next generation of wide and deep surveys such as *Euclid* (Laureijs et al. 2011) or DESI (DESI Collaboration 2016), which will provide measurements with much smaller statistical uncertainties (see e.g., Yankelevich & Porciani 2019). Sugiyama et al. (2019) introduced a new bispectrum estimator based on the tri-polar spherical harmonic decomposition with zero total angular momentum and showed, in this case, that it is possible to compute the models for the convolved bispectrum following a FFT-based approach. The issue of developing a similar method for more traditional estimators of the bispectrum multipoles (Scoccimarro 2015) has been recently addressed by Pardede et al. (2022), who derived an expression based on two-dimensional Hankel transforms that can be computed using the 2D-FFTlog method (Fang et al. 2020). In this case the survey window is described in terms of the multipoles of its three-point correlation function. Developing optimal estimators for these quantities is still an open problem.

In this Letter we propose employing deep learning as a method to compute the impact of the survey window function on theoretical models for the power spectrum and bispectrum. Specifically, we use a deep neural network (DNN) to approximate the mapping from the unconvolved to the convolved spectra. This technique allows us to consider multiple cosmological models, while drastically reducing computer-memory demands and the wall-clock time of computation with respect to performing the convolution integrals numerically. All these features are key for building efficient Bayesian inference samplers and determining the posterior distribution of cosmological parameters. The structure of the Letter is as follows. In Sect. 2 we briefly describe the architecture of our DNN models and introduce the data sets we employ for training and testing them. Our

results are presented in Sect. 3. We draw our conclusions in Sect. 4.

#### 2. Methods

#### 2.1. Philosophy and goals

It is well known that artificial neural networks are able to approximate any arbitrary continuous function of real variables (Cybenko 1989; White 1990; Hornik 1991). They learn how to map some inputs (features, in machine learning jargon) to outputs (labels) from examples in a training data set. The training process consists of fitting the parameters of the machine (weights and biases of the neurons) by minimising a loss function that quantifies how good the prediction is with respect to the correct result. After the training the accuracy of the model is determined using the testing data.

In our applications the features that form the input of the DNN are the spectra P(k) and  $B(k_1, k_2, k_3)$  evaluated at specific sets of wavevectors. Different options are available when choosing these sets. For instance, we could use many closely separated wavevectors around the output configurations. In this case the DNN would learn how the convolution integrals mix the contributions coming from different configurations. At the opposite extreme, we could consider inputs and outputs evaluated for the very same set of configurations, so that, in some sense, the DNN model also interpolates among the sparser inputs. We opted for this second approach, which is more conducive to a simpler machine learning set-up: choosing a smaller size of features requires fewer model parameters to be tuned, and the trained model is evaluated more quickly. The only implicit assumption here is that the input power spectrum is smooth between the sampled configurations. In our implementation the machine learns to predict the functions

$$R_{\rm P}(\mathbf{k}) = \frac{P_{\rm obs}(\mathbf{k})}{P(\mathbf{k})}$$
 and  $R_{\rm B}(\mathbf{k}_1, \mathbf{k}_2, \mathbf{k}_3) = \frac{B_{\rm obs}(\mathbf{k}_1, \mathbf{k}_2, \mathbf{k}_3)}{B(\mathbf{k}_1, \mathbf{k}_2, \mathbf{k}_3)}$  (4)

evaluated at the same arguments of the input.

Since this Letter is about giving a proof of concept, for simplicity we only predict the effect of window function on the linear matter power spectrum and the so-called tree-level bispectrum, which can be trivially computed using the linear power spectrum (e.g., Fry 1984), neglecting redshift-space distortions in both cases. Moreover, as an example, we consider a spherically symmetric top-hat window function which assumes the value of one for distances smaller than the radius R and zero otherwise. In Fourier space this corresponds to

$$\tilde{W}_n(k) = \frac{4\pi (kR)^2 j_1(kR)}{k^3 V^{1/n}},\tag{5}$$

where the symbol  $j_v(x)$  denotes the spherical Bessel functions of the first kind and  $V = 4\pi R^3/3$  is the comoving volume enclosed by the window function. Basically,  $\tilde{W}_n(k)$  rapidly oscillates (see Fig. 1) which makes it challenging to numerically compute the integrals in Eqs. (1) and (3). The oscillations are damped, and the main contribution to the convolution comes from the first peak at k = 0, which mixes Fourier modes within a shell of width  $\Delta k \simeq R^{-1}$ . Given our assumptions,  $R_P(k)$  and  $R_B(k_1, k_2, k_3)$  only depend on the modulus of the wavevectors.

#### 2.2. Deep learning models

Since the power spectrum is a smooth function of k, we adopt the convolutional neural network (CNN) architecture to model

 $R_{\rm P}(k)$ . The first layer of the network applies a convolution to the input with 16 trainable filters (kernel size 3) and a rectified linear unit (ReLU) activation function, defined as  $f(x) = \max(0, x)$ . This is followed by a dropout layer with a rate of 0.5, which acts as a regulariser and prevents overfitting (Goodfellow et al. 2016). The final layer is a dense one in which the number of neurons matches the length of the output data vector. Since the convolved power spectrum must be positive, the last layer is processed through a softplus activation function of the form  $f(x) = \ln(1 + e^x)$ .

For the bispectrum, we opt for a different CNN architecture. We chose this because we organise the data in a one-dimensional array where each entry corresponds to a different triangular configuration. As a consequence, the sequence of data is not necessarily smooth and we prefer to use a model that can detect features on multiple scales. The network we chose is based on the U-Net architecture (Ronneberger et al. 2015), which consists of a contracting path (encoder) followed by an expansive path (decoder). The former combines convolutional and pooling layers to down-sample the original data, and thus builds a compressed representation of them. The latter decompresses the compact representation to construct an output of the desired size. We include two down-sampling and two up-sampling steps, followed by a dropout layer with a rate of 0.5 and a dense layer in which the number of neurons matches the length of the output data vector.

For building and training the neural networks, we use the Keras library (Chollet 2015) under the TensorFlow framework (Abadi et al. 2015). During the training phase, the parameters of the machine are adjusted to minimise a loss function L, which we identify with the mean absolute error (MAE)  $L = N^{-1} \sum_{i=1}^{N} |y_i^{\text{pred}}/y_i^{\text{truth}} - 1|$ , where  $y_i^{\text{pred}}$  denotes the DNN prediction,  $y_i^{\text{truth}}$  is the corresponding item in the training data set, and N is the number of entries in these data vectors. The minimisation of this loss function (one of the most popular choices for regression problems) is controlled by the Adam Optimizer (based on the stochastic gradient descent method, Kingma & Ba 2014) with an initial learning rate of 0.001, which is reduced as the training progresses using the inverse time decay schedule of TensorFlow. In order to prevent overfitting, five per cent of the training data are set aside as a validation set (i.e., these data are not used to fit the network parameters), and training is automatically stopped early if the validation loss starts to increase. This step makes sure that the network predicts previously unseen data more accurately.

#### 2.3. Training and testing data sets

We used the suite of 2000 linear power spectra in the Quijote database (Villaescusa-Navarro et al. 2020) to build the training set for our DNNs. These spectra are obtained by sampling five cosmological parameters on a Latin hypercube over the ranges defined in Table 1.

For the power-spectrum analysis, we use 47 linearly spaced wavenumbers in the range  $[0.004, 0.2] h \,\mathrm{Mpc}^{-1}$ . The corresponding values for  $P_{\mathrm{obs}}(k)$  are computed using the 3D FFT method to evaluate Eq. (1) employing a top-hat window, which covers a comoving volume of  $V = 700^3 \, h^{-3} \,\mathrm{Mpc}^3$  (i.e.,  $R = 434.25 \, h^{-1} \,\mathrm{Mpc}$ ).

For the bispectrum we compute the tree-level expression from the linear power spectra in the Quijote suite. We consider 564 triangular configurations in which the three sides span the range  $[0.01, 0.2] h \,\mathrm{Mpc}^{-1}$ . In this case the integration in Eq. (3)

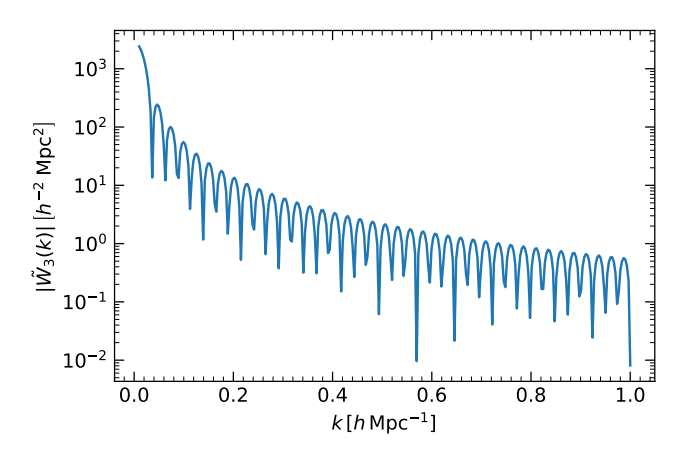


**Fig. 1.** Top-hat window function with  $V = 200^3 h^{-3} \text{ Mpc}^3$ .

is carried out in six dimensions using the VEGAS routine of the Cuba library (Hahn 2005). To facilitate the convergence of the numerical integrals, we consider a top-hat window with  $V = 200^3 h^{-3} \,\mathrm{Mpc}^3 \,(R = 124.07 \,h^{-1} \,\mathrm{Mpc})$ .

We generate the test data set by randomly generating 200 sets of cosmological parameters with Latin hypercube sampling. Since the Quijote database spans a broader region of parameter space compared with that allowed by current observational constraints, our test data are sampled within a narrower region mimicking the actual constraints from Planck Collaboration VI (2020); see the bottom row of Table 1. For each set we compute the linear matter power spectrum using CAMB (Lewis et al. 2000; Howlett et al. 2012) and employ the same procedure used for the training data set to obtain the convolved power spectra and bispectra.

#### 3. Results

In the top panels of Fig. 2 we consider one of the test samples for the power spectrum. The orange triangles in the left panel show the function  $R_P(k)$  computed using Eq. (1): the convolution with the window function flattens out the power spectrum on large scales and changes the amplitude of the baryonic acoustic oscillations by a few per cent. Although the window function considered here is arbitrary, similarly sized (and measurable) corrections are expected for the next generation of galaxy redshift surveys (see e.g., Fig. 6 in Elkhashab et al. 2022), which should deliver per cent accuracy for the power spectrum. The black dots indicate the output of the trained DNN model. The right panel shows the relative error between the DNN prediction and the true signal, which is always smaller than 0.1%. To assess the overall performance of the DNN model, in the bottom panels of Fig. 2 we plot the MAEs for each test sample (left) and error percentiles over the test samples as a function of the wavenumber. The residual mean inaccuracy of the model is well below the per

The effect of the window function on the bispectrum is much more pronounced than for the power spectrum and the ratio  $R_{\rm B}(k_1,k_2,k_3)$  assumes values below 0.5 for some triangle configurations (top left panel in Fig. 3). The DNN model predicts the corrections accurately in all cases (top right and bottom panels) and vastly outperforms the approximated method introduced by Gil-Marín et al. (2015), which, for the compact survey volume considered here, does not accurately reproduce the amplitude of the convolved bispectrum (green circles in the top left panel).

**Table 1.** Parameter spaces spanned by the training and testing data sets.

Data set	$\Omega_{\mathrm{m}}$	$\Omega_{\mathrm{b}}$	h	$n_{\rm s}$	$\sigma_8$
Training	[0.1, 0.5]	[0.03, 0.07]	[0.5, 0.9]	[0.8, 1.2]	[0.6, 1.0]
Testing	[0.2, 0.4]	[0.03, 0.06]	[0.6, 0.8]	[0.9, 1.1]	[0.7, 1.0]

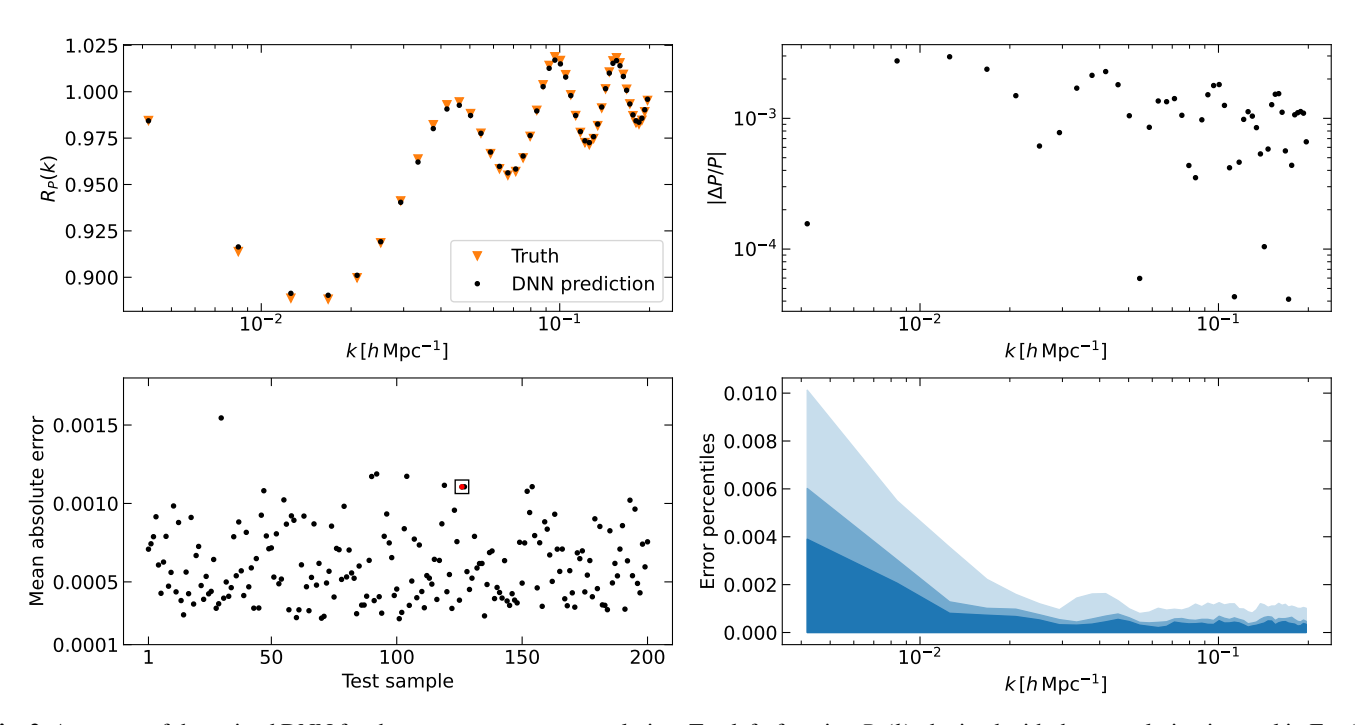


**Fig. 2.** Accuracy of the trained DNN for the power spectrum convolution. Top left: function  $R_P(k)$  obtained with the convolution integral in Eq. (1) (orange triangles) compared with the DNN model (black dots) for one test sample. Top right: relative error of the DNN model in the same test sample used in the left panel. Bottom left: MAEs for all the test samples (the one used in the top panels is highlighted in red and surrounded by a square). Bottom right: 50th, 68th, and 95th error percentiles of the DNN model as a function of k. Generally, the DNN model yields sub-per cent accuracy.

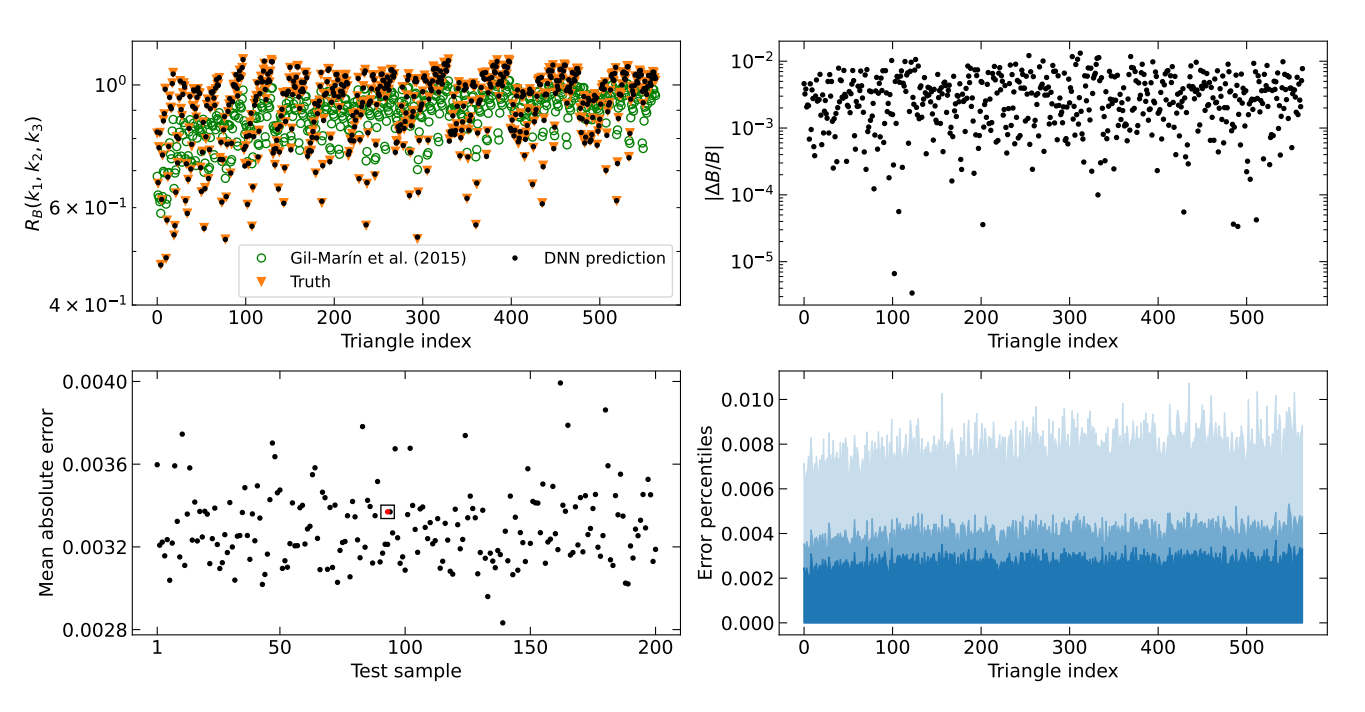


**Fig. 3.** As in Fig. 3, but for the bispectrum. The triangular configurations in the top and bottom right panels satisfy the constraint  $k_1 \ge k_2 \ge k_3$  and are ordered so that first  $k_3$  increases (at fixed  $k_1$  and  $k_2$ ), then  $k_2$  (at fixed  $k_1$ ), and finally  $k_1$ . For reference, in the top left panel, the ratio  $R_B(k_1, k_2, k_3)$  is also plotted, computed according to the approximated method introduced by Gil-Marín et al. (2015; green circles).

#### 4. Conclusions

In this Letter we employed a DNN model to predict the impact of the window function on the power spectrum and the bispectrum measured in a galaxy redshift survey. Overall, the trained DNN models show very promising results with sub-per cent MAEs for all test samples (well below the statistical uncertainty expected from the next generation of surveys). These errors can be further reduced by increasing the size of the training data set

Our DNN model is meant as a proof of concept and, for this reason, we made some simplifications in our study. First, we used the linear power spectrum and the tree-level bispectrum for matter fluctuations. Second, we considered a top-hat window function with a fixed volume in which the number density of tracers does not vary with the radial distance from the observer. Although this is an ideal case, we do not see a reason why a DNN model should not be able to accurately predict the effect of more realistic survey masks, given an appropriately sized training sample.

It takes less than 10 microseconds to generate a complete sample for either  $R_P(k)$  or  $R_B(k_1, k_2, k_3)$  with the trained DNN. This is ideal for sampling posterior probabilities in Bayesian parameter estimation. Our method can be straightforwardly generalised to the multipoles of the spectra, and could also be combined with emulators that make predictions for the true clustering signal (including galaxy biasing) based on perturbation theory (e.g., Donald-McCann et al. 2023; DeRose et al. 2022; Eggemeier et al. 2022). Additional corrections due to binning the theory predictions in exactly the same way as done for the measurements (see e.g., Sect. 3.2 in Oddo et al. 2020 and Sect. 4.1 in Alkhanishvili et al. 2022) can be computed by suitably averaging the output of the DNN model or, more efficiently, can be accounted for in the model. Since in this Letter we do not perform a Bayesian inference for cosmological parameters, we skipped this step when we generated the training sample.

The bottleneck operation in the DNN approach is the creation of the training data set, which requires a significant time investment in the case of the bispectrum (in our case, the calculation of the 2000 convolved bispectra with 64 processor cores took approximately one month of wall-clock time). This step can be sped up using massive parallelisation and, possibly, by relying on more computationally friendly formulations of the convolution integral (e.g., Pardede et al. 2022). It is also conceivable that using larger input vectors that densely sample the wavenumbers within shells of size  $\Delta k$  around the output configurations might facilitate the task of the machine, and would thus help to reduce the training data. The time required to build the training set is not a good reason to dismiss the DNN approach. Even for the simple case of the isotropic bispectrum of matter-density fluctuations in real space, sampling the posterior distribution of the five cosmological parameters we considered would require many more than 2000 evaluations of the window-convolved signal. Thus, using the DNN model would lead in any case to a notable speed up. In any practical application, accounting for redshift-space distortions, shot noise, and perturbative counterterms would substantially increase the number of adjustable coefficients in the perturbative model for the bispectrum (and, correspondingly, the number of likelihood evaluations needed to constrain them from experimental data). We thus conclude that using the DNN model would be advantageous as long as the size of the necessary training set is substantially smaller than the number of the required likelihood evaluations in the Bayesian estimation of the model parameters.

Acknowledgements. We thank Alexander Eggemeier and Héctor Gil-Marin for useful discussions. D.A. acknowledges partial financial support by the Shota Rustaveli National Science Foundation of Georgia (GNSF) under the grant FR-19-498.

```
References
Abadi, M., Agarwal, A., Barham, P., et al. 2015, TensorFlow: Large-Scale
   Machine Learning on Heterogeneous Systems, software available from ten-
Alkhanishvili, D., Porciani, C., Sefusatti, E., et al. 2022, MNRAS, 512, 4961
Beutler, F., Saito, S., Seo, H.-J., et al. 2014, MNRAS, 443, 1065
Beutler, F., Seo, H.-J., Saito, S., et al. 2017, MNRAS, 466, 2242
Beutler, F., Castorina, E., & Zhang, P. 2019, J. Cosmol. Astropart. Phys., 2019,
Bianchi, D., Gil-Marín, H., Ruggeri, R., & Percival, W. J. 2015, MNRAS, 453,
   L11
Blake, C., Baldry, I. K., Bland-Hawthorn, J., et al. 2013, MNRAS, 436, 3089
Castorina, E., & White, M. 2018, MNRAS, 476, 4403
Castorina, E., Hand, N., Seljak, U., et al. 2019, J. Cosmol. Astropart. Phys., 2019,
Chollet, F. 2015, Keras, https://keras.io
Cybenko, G. 1989, Math. Control Signals Syst., 2, 303
de Laix, A. A., & Starkman, G. 1998, ApJ, 501, 427
DeRose, J., Chen, S.-F., White, M., & Kokron, N. 2022, J. Cosmol. Astropart.
   Phys., 2022, 056
DESI Collaboration (Aghamousa, A., et al.) 2016, ArXiv e-prints
   [arXiv:1611.00036]
Donald-McCann, J., Koyama, K., & Beutler, F. 2023, MNRAS, 518, 3106
Eggemeier, A., Camacho-Quevedo, B., Pezzotta, A., et al. 2022, MNRAS,
   accepted [arXiv:2208.01070]
Elkhashab, M. Y., Porciani, C., & Bertacca, D. 2022, MNRAS, 509, 1626
Fang, X., Eifler, T., & Krause, E. 2020, MNRAS, 497, 2699
Feldman, H. A., Kaiser, N., & Peacock, J. A. 1994, ApJ, 426, 23
Fry, J. N. 1984, ApJ, 279, 499
Gil-Marín, H., Noreña, J., Verde, L., et al. 2015, MNRAS, 451, 539
Goodfellow, I., Bengio, Y., & Courville, A. 2016, Deep Learning (MIT Press)
Hahn, T. 2005, Comput. Phys. Commun., 168, 78
Hamilton, A. J. S. 2000, MNRAS, 312, 257
Hornik, K. 1991, Neural Netw., 4, 251
Howlett, C., Lewis, A., Hall, A., & Challinor, A. 2012, J. Cosmol. Astropart.
   Phys. 1204, 027
Kingma, D. P., & Ba, J. 2014, ArXiv e-prints [arXiv:1412.6980]
Laureijs, R., Amiaux, J., Arduini, S., et al. 2011, ArXiv e-prints
  [arXiv:1110.3193]
Lewis, A., Challinor, A., & Lasenby, A. 2000, ApJ, 538, 473
Oddo, A., Sefusatti, E., Porciani, C., Monaco, P., & Sánchez, A. G. 2020, J.
   Cosmol. Astropart. Phys., 2020, 056
Pardede, K., Rizzo, F., Biagetti, M., et al. 2022, J. Cosmol. Astropart. Phys.,
Peacock, J. A., & Nicholson, D. 1991, MNRAS, 253, 307
Percival, W. J., Baugh, C. M., Bland-Hawthorn, J., et al. 2001, MNRAS, 327,
Philcox, O. H. E. 2021a, Phys. Rev. D, 104, 123529
Philcox, O. H. E. 2021b, Phys. Rev. D, 103, 103504
Planck Collaboration VI. 2020, A&A, 641, A6
Ronneberger, O., Fischer, P., & Brox, T. 2015, ArXiv e-prints
   [arXiv:1505.04597]
Ross, A. J., Percival, W. J., Carnero, A., et al. 2013, MNRAS, 428, 1116
Sato, T., Hütsi, G., & Yamamoto, K. 2011, Progr. Theoret. Phys., 125, 187
Scoccimarro, R. 2015, Phys. Rev. D, 92, 083532
Sugiyama, N. S., Saito, S., Beutler, F., & Seo, H.-J. 2019, MNRAS, 484, 364
Tegmark, M., Hamilton, A. J. S., Strauss, M. A., Vogeley, M. S., & Szalay, A. S.
   1998, ApJ, 499, 555
Villaescusa-Navarro, F., Hahn, C., Massara, E., et al. 2020, ApJS, 250, 2
White, H. 1990, Neural Netw., 3, 535
Wilson, M. J., Peacock, J. A., Taylor, A. N., & de la Torre, S. 2017, MNRAS,
```

Yamamoto, K., Nakamichi, M., Kamino, A., Bassett, B. A., & Nishioka, H. 2006,

Yankelevich, V., & Porciani, C. 2019, MNRAS, 483, 2078

464, 3121

PASJ, 58, 93

# **List of Figures**

1.1	An image of the galaxy cluster known as "El Gordo" taken by the James Webb Space Telescope. El Gordo acts as a gravitational lens, distorting and magnifying the light from distant background galaxies. Credit: NASA, ESA, CSA.	3
2.1	The original recession-velocity-versus-distance plot done by Hubble (1929). Plotted are galaxies (originally referred to as 'extragalactic nebulae') whose velocity has been inferred from the spectroscopy. The distances were estimated using the variable cepheid stars via their period-luminosity relation by relating the period of their pulsations to the distance modulus. The solid line is a linear fit to the filled circles that represent individual galaxies. The dashed line is a fit to the empty circles representing galaxies grouped together. The slope of the lines indicates the Hubble constant	8
2.2	The Great Wall: in redshift surveys of galaxies with radial velocities of $cz \le 1500$ km/s, a large galaxy structure was discovered located at a redshift of $cz \sim 6000$ km/s. Each dot on this wedge diagram represents a galaxy. The polar angle denotes the rectascension, whereas the radial coordinate denotes the redshift of the galaxies, which measures their distances according to Hubble's law. Source: Geller	
2.3	and Huchra (1989)	13 19
2.4	The maps of the galaxy distribution observed by SDSS and the one extracted from the Bolshoi simulation. Credit: Bettoni (2013).	21
2.5	Visual representations of triangles forming the bispectrum, $B(k_1, k_2, k_3)$ , with various combinations of triangles satisfying $k_3 \le k_2 \le k_1$ . Source: Jeong and Komatsu (2009)	
2.6	Tree diagrams for bispectrum (left diagram) and trispectrum (right diagram) or three-point and four-point functions in a real space. Here dots represent the density fields and lines represent the power spectrums (two-point function in a real space).	
2.7	Source: Bernardeau et al. (2002)	28
	in the square brackets represent one-loop correction terms given by Eqs. (2.77) and (2.78). Source: Bernardeau et al. (2002)	29

2.8	Diagrams for the three-point correlation or bispectrum one-loop corrections. Source: Bernardeau et al. (2002)	29
5.1	The artist's view of the ESA medium class astronomy and astrophysics space mission <i>Euclid</i> . Credit: ESA	46
5.2	The galaxy power spectrum extracted from the Flagship 1 simulation (top) and corresponding relative statistical uncertainty (bottom). The colour gradient indicates the different redshifts of the snapshots. The shaded areas indicate the assumed statistical errors of the measurements and the horizontal dashed lines indicate the Poissonian shot noise.	49
5.3	The galaxy bispectrum extracted from the Flagship 1 simulation (top) and its relative statistical uncertainty (bottom). Results are plotted by ordering the triangular configurations according to condition $k_1 \ge k_2 \ge k_3$ . In between the two consecutive vertical lines all dots correspond to triangle bins with the same longest side $k_1$ , whereas $k_2$ and $k_3$ take all allowed values.	50
5.4	The bias relations described in Sect. 5.5. Here blue and red contours depict marginalised posterior contours obtained from fitting to HOD1 and HOD3 Flagship simulation mock galaxy catalogues. The same-coloured bands mark the $1\sigma$ and $2\sigma$ errors of the fiducial $b_1$ obtained by fitting the linear spectrum to the large-scale limit of the measured power spectrum from these catalogues	57
5.5	The goodness of fit test of galaxy $P + B$ model (with fixed cosmology) against the Flagship simulation mock galaxy catalogues HOD1 and HOD3. Each panel indicates a different snapshot of the simulation and on the $x$ and $y$ -axis, we indicate the assumed scale cuts on the data vectors. The colours represent the corresponding $p$ -values (top panels) and FoB with respect to parameter $b_1$ (bottom panels). If the $p$ -value is less than 0.05, the model is a bad fit to the data and we do not plot the corresponding $p$ -value. Similarly, if the FoB is above $2\sigma$ critical level, we do not plot the corresponding value.	60
5.6	First row: comparison of bias parameter $b_1$ obtained by fitting the galaxy $P+B$ model (with fixed cosmology) assuming various bias relations, which are indicated using different colours and error bars depict the 68 percent credibility intervals. The grey bands mark the 1 and $2\sigma$ regions of the fiducial $b_1$ obtained by fitting the linear spectrum to the large-scale limit of the measured power spectrum. Second row: the fitted values of the bispectrum Poisson shot noise correction $\alpha_2$ and corresponding 68 percent credibility intervals when fitting the maximal model i.e. the model with only the cosmological parameters fixed. Third row: the difference in DIC with respect to the reference maximal model with nine parameters when assuming the various bias relations. The difference $\Delta DIC < -5$ indicates a strong preference against the reference model. Fourth row: the effective number of parameters $p_V$ that is constrained by the chain when imposing bias relations. The horizontal dotted lines indicate the actual number of parameters 9 and 8 with and without imposed bias	(2)
- 7	relation, respectively. For reference, we also plot the model with $\alpha=0$ in violet	62
5.7	Same as in Fig. 5.6 but for the HOD3 mock catalogue case	63

5.8	Cosmological parameters $A_s$ , $h$ and $\omega_c$ (top three rows) obtained by fitting the galaxy	
	P + B to the same statistics measured from the HOD1 snapshot as a function of the	
	scale cut imposed on the power spectrum, $k_{\text{max}}^{P}$ . The performance metrics - goodness	
	of fit (in terms of $p$ -values), figure of bias, and figure of merit are plotted in the	
	bottom three panels, respectively. The last two metrics were computed with respect	
	to the parameters $A_s$ , $h$ , and $\omega_c$ . The color gradient indicates the different scale cut	
	on the bispectrum, $k_{\text{max}}^B$ . The grey band in the p-value indicates the critical value of	
	0.05 below which the model is rejected as a good fit to the data. The same bands	
	in FoB panels represent the 68 and 95 percentiles of the corresponding distribution,	
	indicating 1 and 2 $\sigma$ deviations of the fitted cosmological parameters from the actual	
	their values. The FoM panels show the figure of merit normalized to the one computed	
	at $k_{\text{max}}^P = 0.1  h  \text{Mpc}^{-1}$ and $k_{\text{max}}^B = 0.08  h  \text{Mpc}^{-1}$	64
5.9	Same as in Fig. 5.8 but for the HOD3 catalogue	65
5.10	Cosmological parameters $h$ and $\omega_{\rm c}$ (top two rows) obtained by fitting the galaxy $P$	
	and $P + B$ to the same statistics measured from the HOD3 catalogue snapshots as	
	a function of the scale cut $k_{\text{max}}^P$ imposed on the power spectrum while the scale cut	
	on the bispectrum $k_{\text{max}}^B = 0.12 \ h \text{Mpc}^{-1}$ . The performance metrics - goodness of fit	
	(in terms of <i>p</i> -values), figure of bias, and figure of merit are plotted in the bottom	
	three panels, respectively. The last two metrics were computed with respect to the	
	parameters $h$ , and $\omega_c$ . The grey bands in the $p$ -value panels indicate the critical value	
	of 0.05 below which the model is rejected as a good fit to the data. The same bands	
	in FoB panels represent the 68 and 95 percentiles of the corresponding distribution,	
	indicating 1 and 2 $\sigma$ deviations of the fitted cosmological parameters from the actual	
	all a transfer and	

# **List of Tables**

2.1	Cosmological parameters as measured from the CMB (Planck Collaboration et al.,	
	2020a) and SNeIa (Brout et al., 2022) observations	10
5.1	Cosmological and structural parameters of Flagship I simulation	47
5.2	Specifications for the HOD galaxy samples used in this analysis. The table lists the	
	total number of objects $N_{\rm g}$ and the mean number density $\bar{n}$ of the sample. All the	
	considered samples share the same volume, which coincides with the one of the	
	Flagship I comoving outputs, i.e., $3780 h^{-3} \text{ Mpc}^3$	48
5.3	The list of model parameters and assumed uniform prior ranges	56
5.4	Marginalised mean values of the linear bias $b_1$ and the shot-noise parameter $\alpha_P$	
	measured using the large-scale limit of the ratio $P_{-}/P_{-}$ presented in equation (5.32).	59

## **Acronyms**

```
ΛCDM Λ Cold Dark Matter. 2, 10, 11, 37
BAO Baryon-acoustic-oscillation. 7, 53, 54
CDM cold dark matter. 12, 27, 39
CMB Cosmic Microwave Background. 2, 7, 10, 25, 58, 121
CP Cosmological Principle. 5, 6, 12, 33
DIC Deviance Information Criterion. 61
DM dark matter. 2, 10, 11, 20, 25, 27, 32, 33, 37
DNN deep neural network. 37, 43, 44, 72
EdS Einstein-de Sitter. 16–18, 20
EFEs Einstein Field Equations. 6
EFT Effective Field Theory. 30, 31, 37, 39–41, 53, 68, 71
ESA European Space Agency. 45
FoB figure of bias. 59, 61, 64–68, 119
FOF friend-of-friend. 48
FoM figure of merit. 64–66, 68, 119
GR General Relativity. 5, 7, 12, 45
HOD halo occupation distribution. 48, 55, 58, 61, 68, 121
IC initial conditions. 33, 34
LPT Lagrangian Perturbation Theory. 34
```

```
LSS large scale structure. 5, 12, 20, 22, 25, 40
```

MCMC Markov Chain Monte Carlo. 36, 58, 65

**PT** perturbation theory. 17, 28, 58, 61

**SPT** standard perturbation theory. 5, 16, 18, 25, 28, 30, 31, 40

### **Acknowledgements**

First and foremost, I would like to express my deepest gratitude to my supervisor, Cristiano Porciani. Thank you for giving me the opportunity to pursue a doctoral degree within your group. Your careful guidance and countless insightful conversations have been invaluable over the years. I am especially grateful for your constant motivation, encouraging me to persevere through the challenges along the way.

When I arrived in Germany many years ago as a complete stranger, I was fortunate enough to make wonderful friends who enriched my journey. I want to give special mention to my dear friends Sven, Jonathan, and Marcus, who have been with me since day one. Sven, in particular, I cherish the amazing moments we shared, especially the time we spent living together during our studies and navigating the pandemic. Those experiences will remain precious memories that I will hold onto for years to come. I am also deeply grateful for your help in reading my thesis and providing invaluable feedback - your support is greatly appreciated. I would also like to acknowledge my friends Sandra, Devika, Hannah, Heba, Xhona, Vakho, Lado and many others. The adventures and positivity we shared helped keep my spirits high, and although I cannot list every moment, please know how much they all mean to me.

I would also like to thank my office mates - Anna, Yvonne, Benedetta, Yousry, Mandar, Prachi, Alex, Matteo, and Emilio - for making the daily ups and downs of work so much more enjoyable. Special thanks go to Alex, whose help during the final stages of my research was crucial. Your attention to detail and hard-working attitude have always been an inspiration to me. Lastly, I would like to extend my gratitude to all the members of the Argelander Institute of Astronomy. You made me feel at home every day and supported me in every possible way. I will deeply miss that sense of community.

I would also like thank Internation Max Planck Research School for the provided support and opportunities for knowledge exchange with my peers.

I am profoundly grateful to my partner and best friend, Sara. Thank you for coming into my life and providing all the love and care one could ask for, as well as for all the beautiful memories we've created together and those yet to come. You've always been there to lift me up when I was down and inspire me to challenge myself.

Finally, I want to express my heartfelt thanks to my family - especially my parents and my brother Oto. Your unwavering support and love have allowed me to stand where I am today. Needless to say, completing this thesis would have been impossible without you.